Structure Property Relationships in Nanoporous Materials for Hydrogen Storage

Noguera Díaz, Antonio Noguera

Award date:
2016

Awarding institution:
University of Bath

Structure Property Relationships in Nanoporous Materials for Hydrogen Storage

Submitted by Antonio José Noguera Díaz
for the degree of Doctor in Philosophy

University of Bath
Department of Chemical Engineering
February 2016

Signed:

Date: 15/02/2016

Authorship Declaration

The author was funded by a University of Bath Research Studentship (URS) attached to the Hydrogen and Fuel Cell SUPERGEN Hub, United Kingdom. EPSRC grant reference EP/J016454/1.

The work presented in this thesis, except where otherwise noted, was done by the author with supervision and guidance from his academic supervisor, Dr Timothy J Mays, Head of Department in the Department of Chemical Engineering at the University of Bath.

Some of the work reported in this thesis has been published in journal articles and presented at conferences, as indicated in the dissemination section.

Abstract

Hydrogen storage is a developing technology that can be used as an energy vector for sustainable energy applications such as fuel cells for transport applications or for supplying power to the grid in moments of high demand. However, before hydrogen can be used as a practical energy vector, hydrogen storage issues, such as low gravimetric storage density, need to be addressed. One possible solution could be using nanoporous materials to physically adsorb hydrogen at low temperatures and moderate pressures.

Hydrogen adsorption excess isotherms in solid-state porous materials can be obtained experimentally. However, the total amount stored in them, a quantity of more practical interest, cannot be measured by experimental techniques. Therefore, a model developed at the University of Bath is used to predict the total amount of hydrogen contained in nanoporous materials from their experimentally derived excess isotherm data. According to inelastic neutron scattering experiments (TOSCA, ISIS, RAL, Oxfordshire), solid-like hydrogen is likely to exist within the pores. The model is applied in this work in order to search for relationships between intrinsic properties of the materials (BET surface area, pore volume and pore size) and the predicted total hydrogen capacity of the materials. The model assumes adsorbed hydrogen at a constant density within the pore (defined as the absolute), also taking bulk hydrogen in the pore (amount that is not considered to be adsorbed by the adsorbent), into account.

Several MOF datasets have been used to search for these relations, since they are the materials that have the highest hydrogen uptake in solid-state adsorption. Different MOFs and MOF families have been tested in order to widen the range of the correlations. Also, different strategies, such as fixing the pore volume when applying the fittings, relying on experimental data, or using high pressure hydrogen isotherm data to increase the robustness of the model have been researched. These MOFs have been either synthesized and characterized at the University of Bath or their datasets obtained from literature. Some of these MOFs with zeolitic structure exhibited unreported flexibility, being their structures further characterized.

Changes on accessible pore size for hydrogen storage were also investigated using C_{60} in IRMOF-1.

The final aim of this work is to find possible correlations between BET surface area, pore volume and pore size to find out what the values of these parameters have to be in a specific material to fulfil the DOE hydrogen storage requirements.

Table of Contents

List of Figures

List of tables

Dissemination

Journal publications

The author has contributed to four manuscripts, being three of them published (1, 2 and 4) and one currently under review (3). Publication 3 contains some of the main results of this thesis, seen in Chapters 3 and 4 while Publication 4 contains some of the results of Chapter 5.

1. N. Bimbo, V. P. Ting, J. E. Sharpe, A. Noguera-Díaz, T. J. Mays. (2014). Isosteric Enthalpies for Hydrogen Adsorbed on Nanoporous Materials at High Pressures. *Adsorption*, 20 (2-3), pp. 373-384.

2. N. Bimbo, V. P. Ting, A. Physick, A. Noguera-Díaz, A. Pugsley, L. Holyfield, T. J. Mays. (2015). High volumetric and energy densities of methane stored on nanoporous materials at ambient temperatures and moderate pressures. *Chemical Engineering Journal*, 272, pp. 38-47.

3. A. Noguera-Díaz, N. Bimbo, L. Holyfield, I.Y Ahmet, V. P. Ting, T. J. Mays. (2015). Structure-property relationships in metal-organic frameworks for hydrogen storage. *Colloids and Surfaces A*, 496, pp. 77–85.

4. V. P. Ting, A. J. Ramirez-Cuesta, N.Bimbo, J. E. Sharpe, A. Noguera-Díaz, Volker Presser, S. Rudic, Timothy J. Mays. (2015). Direct Evidence for Solid-like Hydrogen in Microporous Carbon at Supercritical Temperatures. *ACS Nano*, 9 *(8),* pp. 8249–8254.

Conference and workshop presentations

The author has participated in the following listed conferences and workshops, reporting some of the work mentioned throughout the thesis. The underline indicates the presenter, being chronologically ordered starting from the oldest.

Poster presentations

1. ChemEngDay 2013, London, UK, March 2013.

Hydrogen Energy Research in the Department of Chemical Engineering, University of Bath, UK.

N. Bimbo, S. Owens, J.E. Sharpe, A. Noguera- Díaz, A. Rushworth, M. Smith, M. Berry, P.Hayes, T.J. Mays.

2. 11th International Conference on the Fundamentals of Adsorption, FOA-11, Baltimore, USA, May 2013.

A new generalised model for supercritical sorption in nanoporous materials.

J.E. Sharpe, N. Bimbo, A. Noguera- Díaz, A. Rushworth ,V. P. Ting, T. J. Mays.

3. The Hydrogen & Fuel Cell Research Hub H2FC SUPERGEN Conference, Birmingham, UK, Dec 2013.

Structure-property relationships in nanoporous materials for hydrogen storage.

A. Noguera-Díaz, N. Sánchez-Sánchez, N. Bimbo, J. E. Sharpe, A. Physick, V. P. Ting, T. J. Mays.

4. The Hydrogen & Fuel Cell Research Hub H2FC SUPERGEN Conference, Birmingham, UK, Dec 2013.

Enthalpies of adsorption of hydrogen in carbons and metal-organic frameworks: refining the analysis for improving the design of adsorptive storage systems.

N. Bimbo, J.E. Sharpe, A. Noguera-Díaz, A. Physick, V. P. Ting, T. J. Mays.

5. ChemEngDay 2014, Manchester, UK, April 2014.

Fuel Gas Storage: The Challenge of Hydrogen.

N. Bimbo, J.E. Sharpe, A. Noguera-Díaz, A. Physick, L. Holyfield, J. Rowlandson, W. Xu, A. Ladha, V. P. Ting, T. J. Mays.

6. ChemEngDay 2014, Manchester, UK, April 2014.

Fuel Gas Storage: The Challenge of Methane.

A.Pugsley, N. Bimbo, J.E. Sharpe, A. Noguera-Díaz, A. Physick, L. Holyfield, V. P. Ting, T. J. Mays.

7. Tenth International Symposium on the Characterisation of Porous Solids, COPS-X, Granada, Spain, May 2014.
Structure-property relationships in nanoporous materials for hydrogen storage.
A. Noguera-Díaz, N. Sánchez-Sánchez, N. Bimbo, Sharpe, J. E, A. Physick, V. P. Ting, T. J. Mays.

8. Tenth International Symposium on the Characterisation of Porous Solids, COPS-X, Granada, Spain, May 2014.
Modelling supercritical gases – high pressure adsorption of methane in microporous materials.
N. Bimbo, J. E Sharpe, A. Noguera-Díaz, A. Physick, V. P. Ting, T. J. Mays.

9. Tenth International Symposium on the Characterisation of Porous Solids, COPS-X, Granada, Spain, May 2014.
"Hidden" nanoporosity in activated carbons: reconciling gas sorption with scattering data for pore size determination.
J. Rowlandson, A.J. Physick, A. Noguera-Díaz, J.E. Sharpe, N. Bimbo, T.J. Mays, V.P. Ting

10. Tenth International Symposium on the Characterisation of Porous Solids, COPS-X, Granada, Spain, May 2014.
In-situ investigation of the pore structure and adsorbed hydrogen density profiles in MIL-101 [Cr].
A.J. Physick, A. Noguera-Díaz, J.E. Sharpe, N. Bimbo, T.J. Mays, V.P. Ting

11. UK Energy Research Centre Summer School, Warwick, July 2014.
Structure-property relationships in nanoporous materials for hydrogen storage.
A. Noguera-Díaz, N. Sánchez-Sánchez, N. Bimbo, J. E Sharpe, A. Physick, V. P. Ting, T. J. Mays.

12. The Hydrogen & Fuel Cell Research Hub H2FC SUPERGEN Conference, Birmingham, UK, Dec 2014.
Structure-property relationships in nanoporous materials for hydrogen storage.
A. Noguera-Díaz, N. Sánchez-Sánchez, N. Bimbo, V. P. Ting, T. J. Mays.

13. The Hydrogen & Fuel Cell research hub H2FC Supergen conference, Birmingham, UK, Dec 2014.
Integrating adsorbents for safer high-pressure hydrogen storage: cryocharging and working capacities of hydrogen tanks.
N. Bimbo, J. E Sharpe, L. Holyfield, A. Noguera-Díaz, V. P. Ting, T. J. Mays.

14. ISIS Molecular Spectroscopy Science Meeting 2015, Abingdon, UK, Jan 2015.
Inelastic Neutron Scattering Characterization of Activated Carbons.
A. Noguera-Díaz, N. Bimbo, A. Physick, V. P. Ting, T. J. Mays.

15. Royal Society International Seminar: A UK-Japan meeting on Transforming Framework Materials Chemistry, Chicheley Hall, Milton Keynes, UK, March 2015
Adsorptive storage of methane – high volumetric and energy densities at moderate pressures and temperatures.
N. Bimbo, A.J. Physick, A. Noguera-Díaz, A. Pugsley, L.T. Holyfield, V.P. Ting, T.J. Mays

16. ChemEngDay 2015, Sheffield, UK, April 2014.
Structure-property relationships in nanoporous materials for hydrogen storage.
A. Noguera-Díaz, N. Sánchez-Sánchez, N. Bimbo, V. P. Ting, T. J. Mays.

17. Seventh International Workshop on the Characterization of Porous Materials, Delray Beach, Florida, USA, May 2015.
Structure-property relationships in nanoporous materials for hydrogen storage.
A. Noguera-Díaz, N. Sánchez-Sánchez, N. Bimbo, L. Holyfield, V. P. Ting, T. J. Mays.

18. Seventh International Workshop on the Characterization of Porous Materials, Delray Beach, Florida, USA, May 2015.
Characterisation of methane adsorption in nanoporous materials - tailored porosity for high volumetric and energy densities.
N. Bimbo, A. Physick, A.Pugsley, A. Noguera-Díaz, A. Physick, L. Holyfield, V. P. Ting, T. J. Mays.

Oral presentations

1. ISSHAC-9, 9th International Symposium on Effects of Surface Heterogeneity in Adsorption and Catalysis on Solids, Wroclaw, Poland, July 2015.
Structure-property relationships in metal-organic frameworks for hydrogen storage.
A. Noguera-Díaz, N. Bimbo, L. Holyfield, I.Y Ahmet, V. P. Ting, T. J. Mays.

Acknowledgements

Many people contributed with their expertise and knowledge in the work presented in this thesis. I will always be grateful to them for their help, otherwise this work would have not been possible.

I am most grateful to my supervisor Dr Tim Mays, Dr Valeska Ting (University of Bath Lecturer and Research Fellow) and Dr Nuno Bimbo (University of Bath Postdoctoral Research Officer). Tim has been an excellent supervisor who always guided and advised me during the course of my PhD. I exalt him for accepting me as his PhD student.

Valeska also greatly helped me during my PhD by offering me the opportunity to participate in INS experiments, helping with lab training, suggesting ideas and helping with discussion and analysis of the data. She always went the extra mile, also giving very thorough feedback to my work.

Nuno was also of great help with discussion, analysis and especially, by giving very thorough feedback. He also greatly helped me by guiding me and training me especially at the early stages of my PhD. I will always be in debt with the three of them for all their effort and help in training and guiding me during my PhD.

I am also thankful to the rest of the people in Tim's and Valeska's research groups - Leighton Holyfield, Jemma Rowlandson, Andrew Physick and Dominic Wales for their ideas, suggestions and feedback.

Many thanks to the technicians from the Chemical Engineering Department Fernando Acosta, Dr Daniel Lou-Hing, Dr Alex Ciupa, Robert Brain and Suzanne Barkley for their help in the lab and safety training overall. Furthermore, I would like to thank Gabriele Kociok-Köhn for her invaluable help and training with the X-ray machine and Dr Andrew Burrows for his help with some XRD spectra analysis.

Dr Svemir Rudic (ISIS, Rutherford Appleton Laboratories) was also very helpful with the INS experiments in which I had the chance to participate thanks to Valeska. Thanks also go to Dr Timmy Ramirez-Cuesta (Oak Ridge National Laboratory, US), who provided useful feedback from the INS data. Thanks to MAST Carbon (MAST Carbon International, Basingstoke, UK) for providing the TE7 and TE3 carbon beads, Anderson Company (Anderson Development Company, MI, USA) for providing the AX-21 and to Dr Volker Presser (INM, Leibniz Institut Saarbrücken, Germany) who provided the OLC-1750 carbon.

Dr John Mitchels (University of Bath) was undoubtedly helpful with the Raman spectroscopy measurements and data analysis. Karim Sapag and Jhonny Villaroel are also acknowledged for their collaboration with the gas adsorption experiments in some ZIFs and to Semali Perera and Olivier Camus for providing the zeolite 13X beads and powder and for doing the CO_2 breakthrough experiments.

I would also like to thank Quantachrome for their contribution towards the conference CPM-7 fees and to Claire Feehily and Jackie Dannatt for their invaluable help correcting part of this thesis.

To conclude, I would like to thank my family, friends and girlfriend, who have always been very supportive and encouraging, especially at the end of my PhD.

Acronyms

ASAP	Accelerated Surface Area and Porosity system
BET	Brunauer, Emmett and Teller
BDC	Benzene-1,4-dicarboxylate or terephthalic acid
BJH	Barrett, Joyner and Halenda
BPDC	4,4'-Biphenyl-dicarboxylate
CDC	Carbide derived carbon
CFRP	Carbon fibre reinforced plastic
DFT	Density Functional Theory
DR	Dubinin-Radushkevich
EOS	Equation of state
FRM-II	Forschungsreaktor München II
GPE	Grand potential energy
HGM	Hollow glass microsphere
HK	Horvath-Kawazoe
HKUST	Hong Kong University of Science and Technology
HTP-1	High Temperature and Pressure-1
INS	Inelastic neutron scattering
IRMOF	Isoreticular metal-organic framework
ISO	International Organization for Standardization
IUPAC	International Union of Pure and Applied Chemistry
LINAC	Linear particle accelerator
LLNL	Lawrence Livermore National Laboratory
MIL	Materiaux de l'Institut Lavoisier
MOF	Metal-organic framework
MWCNT	Multi-walled carbon nanotube
NIST	National Institute of Standards and Technology
OLC	Onion-like carbon
PEM	Proton exchange membrane
PIM	Polymer of intrinsic microporosity
PSD	Pore size distribution
PXRD	Powder X-ray diffraction
RAL	Rutherford Appleton Laboratories

RT	Room temperature
SNS	Spallation Neutron Source
STP	Standard conditions for temperature and pressure
RPM	Revolution per minute
SWCNT	Single-walled carbon nanotube
MWCNT	Multi-walled carbon nanotube
TGA	Thermogravimetric analyser
UiO	University of Oslo
US DOE	United States Department of Energy
UV	Ultraviolet
XRD	X-ray diffraction
ZIF	Zeolitic imidazolate framework

Mathematical Nomenclature

θ	Toth pore filling	-
A	Pre-exponential factor	MPa^{-1}
$A1$	Compressibility parameter 1	MPa^{-1}
$A2$	Compressibility parameter 2	MPa^{-2}
$A3$	Compressibility parameter 3	MPa^{-1}
$A4$	Compressibility parameter 4	MPa^{-2}
a_m	molecular cross-sectional area	nm^2
b	Affinity constant	MPa^{-1}
C	BET constant	-
c	Heterogeneity parameter	-
D	Density conversion factor	cm^3 liquid cm^{-3} STP
*HK total V*p	HK total pore volume	$cm^3\ g^{-1}$
I	Intensity	-
D	Interplanar space	Å
Θ	Scattering angle	degrees
2Θ	Diffraction angle	degrees
L	Avogadro constant	mol^{-1}
n_A	Absolute hydrogen uptake	% wt
n_a	Specific amount of adsorbed	$mmol\ g^{-1}$

n_E	Excess hydrogen uptake	% wt
NI	Normalised intensity	-
n_m	Monolayer adsorbed gas	mmol g^{-1}
n_T	Total hydrogen uptake	% wt
P	Absolute pressure	MPa/bar/mmHg
P/*P*o	Relative pressure	-
*P*o	Saturation pressure	MPa/bar/mmHg
ppm	Parts per million (mass based)	mg kg^{-1}
ppmv	Part per million (in volume)	mg L^{-1}
*P*s	Pore size	nm or Å
Q	Heat of adsorption	kJ mol^{-1}
R	Molar gas constant	MPa cm^3 K^{-1} mol^{-1}
T	Temperature	K, °C
t_b	Breakthrough time	h
t_{b350}	Breakthrough time 350 ppm	h
V	Volume adsorbed	cm^3 STP g^{-1}
V_{CUM}	Total cumulative pore volume (HK)	cm^3 g^{-1}
*V*o	Micropore capacity	cm^3 STP g^{-1}
*V*p	Pore volume	cm^3 g^{-1}
V_{ads}	Adsorbed phase volume	cm^3
wt %	Mass of adsorbed gas over dry	
	mass of the adsorbent	%
Z	Compressibility factor	-
β	Affinity constant (DR)	-
B	Constant (DR)	-
θ_A	Langmuir fractional loading	-
ρ_A	Density of the adsorbate	kg m^{-3}
ρ_B	Density of the bulk	kg m^{-3}
m_E	Balance error	g
V_E	HTP-1 pycnometry error	cm^3

Chapter One

Introduction

1 Introduction

1.1 Scope and motivation

Humans have made intensive use of fossil fuels since the industrial revolution (especially petroleum and coal initially), causing a brisk increase in population and wealth, resulting in a corresponding rise in energy consumption as well. Nowadays, fossil fuels are the primary energy sources used worldwide, whose use has induced a constant increase in CO_2 levels in the atmosphere (surpassing 400 ppm in May 2015) [1]. This rise of greenhouse gases (CO_2, H_2O, CH_4, N_2O and O_3, principally CO_2) is directly related to an increase in the Earth's global temperature, which will carry a predicted rise in the oceans' levels, as well as other disasters [2]. In Figure 1.1, the global surface temperature deviations can be observed from 1880 to 2009 [1].

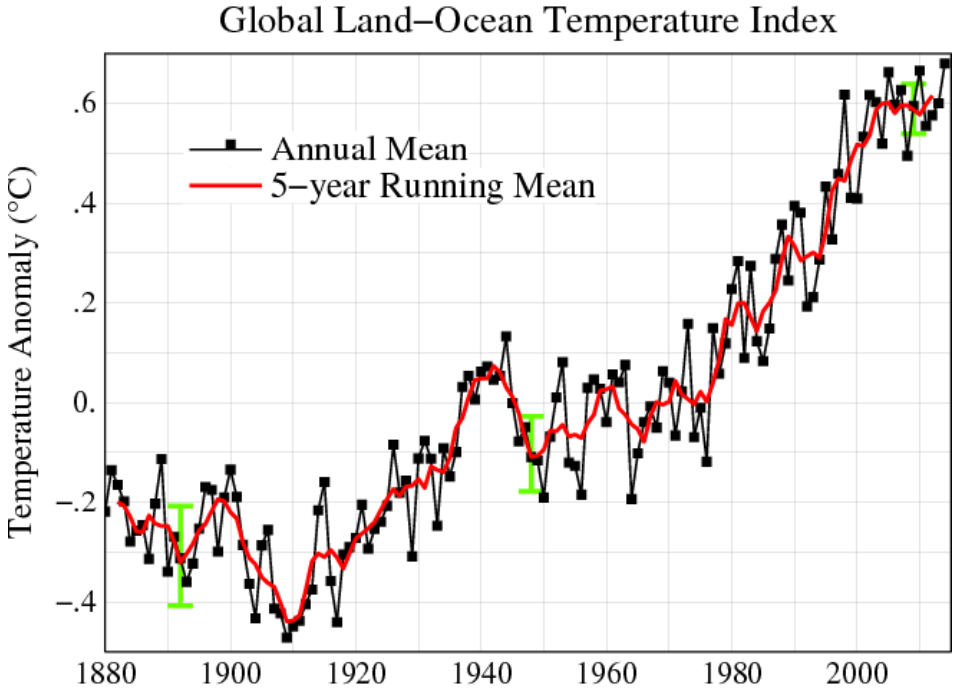

Figure 1.1. Global surface temperature anomalies from 1880 till 2009. Black dots represent the global annual mean temperature while the red line represents 5 year mean global temperature values. Green bars represent 2σ error estimations from incomplete spatial coverage of measurements**.** Reprinted from [1], with permission from John Wiley and Sons.

With the prediction of an increase in energy consumption in the 21st century, society will have to face a process of decarbonisation of their economies, replacing scarce fossil fuels with clean renewable energies to stop contributing to what is known as anthropogenic global warming [3]. This change presents daunting challenges in many areas, emphasizing the need for energy storage due to the intermittent production of some renewable energies such as solar and wind power in order to meet the national electricity grid demands. This also applies to the transport sector, which accounts for 13.1 % of all global greenhouse gas emissions from 2004, being almost completely dependent on oil [4].

Hydrogen has been proposed to be used as an energy vector due to its intrinsic characteristics. Among its features, hydrogen presents a very high energy density per unit mass (the highest after uranium and thorium), being its lower and higher values 120 and 142 MJ kg^{-1} respectively, around three times higher than gasoline and seven times more than coal [5-7]. What is more, hydrogen can be obtained from water, a very abundant resource. However, it presents a very low energy density per unit volume, especially for mobile applications. Compressed and cryogenic hydrogen storage are the existing mature storage technologies. Nevertheless, compressed hydrogen presents safety and compression cost issues, while cryogenic hydrogen exhibit cooling costs issues [8]. A possible solution is to use nanoporous materials in order to physically adsorb the hydrogen. This developing technology does not require temperatures as low as liquefaction and stores hydrogen at lower pressures than compression.

There are several materials that can be used as adsorbents such as metal-organic frameworks (MOFs), activated carbons, zeolites and porous polymers [5]. MOFs are materials made of metal ions or clusters connected by organic molecules. These crystalline materials exhibit the highest hydrogen uptake and surface area, also presenting high costs depending on the metal and linker used [11]. They present many different topologies, being made of open cavities with sizes ranging from micro- to the meso scale [9]. Their synthesis is scalable overall, giving high yields, being usually synthesized using solvothermal methods at relatively mild conditions. Due to their mentioned crystallinity, powder X-ray diffraction can be used to determine the success of the synthesis [7, 12]. Because of their accessible surface area and permanent

porosity, MOFs have become increasingly interesting for applications such as gas storage, separation, and catalysis.

The aim of this work is to predict the hydrogen capacities of these materials from their intrinsic structural properties. A model developed at the University of Bath has been used to predict the total hydrogen capacity of the materials by fitting it to their hydrogen excess isotherms tested at high pressures (up to 18 MPa) and cryogenic temperatures (77 K) [13, 14]. The materials have been characterized and their total hydrogen capacities predicted in order to find correlations between them. These correlations will help predicting the properties a MOF needs to have in order to meet the US DOE (US Department of Energy) given the specifications of the storage tank for mobile applications such as light duty transport vehicles using hydrogen from sustainable sources. The full list of aim and objectives can be found in section 2.8.

1.2 Structure of the thesis

This thesis is divided into eight Chapters. Chapter 1 (Introduction), gives the objectives and motivation for doing the work, focusing on energy, and global warming problems caused because of the heavy use of fossil fuels. Chapter 2 (Background) further describes energy issues we have to face, the available hydrogen storage technologies, principles of adsorption, and the aims and objectives of the thesis. Chapter 3 outlines the materials and methods used for the thesis and a summary of the characterization results of the synthesized materials, as well as data obtained from literature. Both synthesis of the materials and underlying reasons why these materials were chosen are explained. The Chapter also addresses the used laboratory equipment and software, the methodology followed to analyse the results obtained, the model used to predict the total hydrogen capacities, and how the hydrogen properties were obtained from the modelling. Chapter 4 introduces previous studies between the hydrogen uptake of several materials and their intrinsic properties, the experimental hydrogen results obtained, the research about maximum excess and total hydrogen capacity correlations, the found sorbate-induced gate-opening phenomena, further theoretical pore volume studies from the model fittings and model fittings and adsorbate density variations with fixed experimental pore volumes. In Chapter 5, inelastic neutron scattering (TOSCA, Oxfordshire) experiments with activated carbons are shown. Experiments that validate

the model and back up the existence of solid-like hydrogen in different activated carbons are presented. Chapter 6 displays the differences in properties when buckyballs (C_{60}) are introduced in IRMOF-1 (impregnation) with the intention of enhancing its hydrogen properties. Chapter 7 shows the collaboration results obtained throughout the duration of the PhD, where CO_2 breakthrough results of mixed zeolite beads with ZIFs and further tests of several ZIFs with different gases to further research about flexibility features are presented. Chapter 8 contains the concluding remarks and suggests future work.

Chapter Two

Background

2 Background

This section contextualizes the rise of energy consumption over time, climate change, energy distribution and the resulting problems that the world will face in the future. Also, the proposal of hydrogen as an energy vector and state of art of hydrogen storage technologies are explained. The Chapter concludes indicating the aims and objectives of the thesis.

2.1 Energy overview

Petroleum, that important resource that we all depend on nowadays is limited .Without it, our way of life would be impossible. Every day, 88 million barrels (13,992 million litres) are extracted globally, most of which is destined as fuel for the automotive industry [2]. But petroleum is obviously more than a fuel because it is used not only to power vehicles, but also to make synthetic fibres, resins, plastics, and almost everything in our daily lives. Nowadays, most of the primary energy consumed comes from oil, coal and natural gas, demonstrating how dependent today's modern industrialised society is on fossil fuels [2].

In Figure 2.1, the total global proved reserves is shown, being 1700 thousand million barrels, enough to provide 52.5 years of global production at current rates.

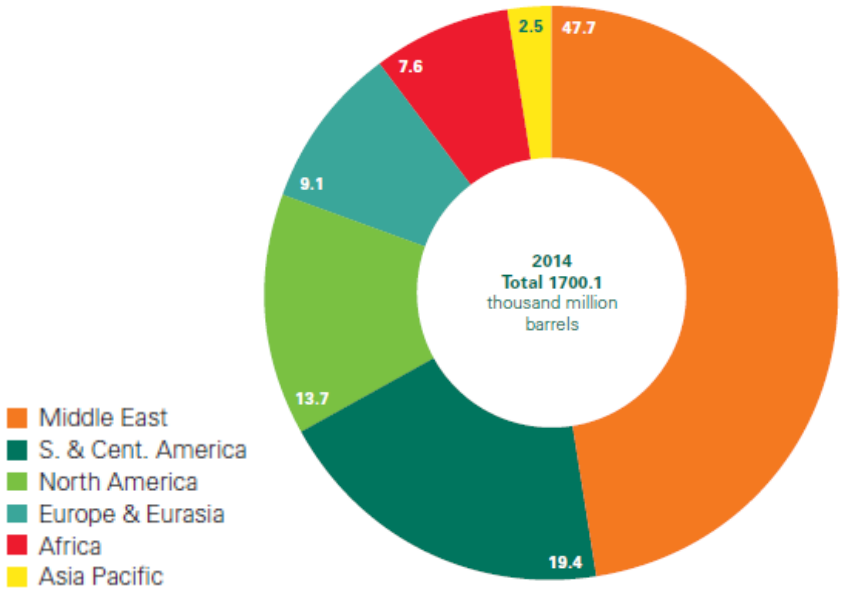

Figure 2.1. Distribution of world proved oil reserves in 2014. Reprinted from [2], with for permission from BP. Copyright 2015.

Experts predict that energy consumption and usage will carry on growing in the 21st century, creating a colossal challenge in the future [5]. However, although other energies are becoming more used, their usage is still modest compared to fossil fuels. Eventually, fossil fuel depletion will prevent us from filling vehicles with diesel or other oil derivatives. The energy needed for heating will no longer come from natural gas. The energy necessary for electricity (such as illumination and devices plugged into the electric power network) will not have the support of thermal power stations (where coal, oil or gas are burned) to be produced.

The major challenges in the future will be the replacement of increasingly scarce fossil fuel energies with renewable energies; the development of these renewable energies to make them competitive; dealing with environmental problems such as greenhouse gases; and substituting conventional fuels in vehicles. According to Orimo *et al.*, the best candidates to substitute fossil fuels are renewable energies based on wind, direct solar conversion and biofuels, supplemented by existing hydropower [11]. However, renewable sources do not stay in a stored form of energy such as gasoline, hence the need of storage technologies. Different available energy storage technologies exist, such as pumped hydro storage, thermal, compressed air, batteries, accumulators, flywheels, superconducting magnets, supercapacitors and hydrogen [3].

2.2 Hydrogen as an energy carrier

One renewable energy carrier which is of enormous importance today is hydrogen. Hydrogen (Figure 2.2) is a tasteless, colourless, odourless and non-toxic molecule whose combustion product is solely water (no CO_2 or any other contaminants are released):

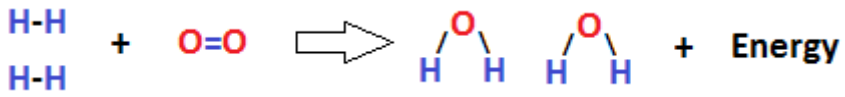

Figure 2.2. Hydrogen combustion reaction.

It is important to point out that free hydrogen does not occur naturally in quantity, so it must be generated from other sources. However, it is a versatile energy vector that converts easily to other forms of energy. Hydrogen can be obtained from water, a very abundant resource on earth (so there is no exclusive access to it). It does not pollute,

has high energy efficiency and there are a number of methods available for producing it [4]. Fossil fuels, on the other hand, are limited and they can only be found in certain parts of the world. In addition, they have major drawbacks that include their market price instability and the fact that different fractions of fossil fuels are needed to power different devices, as opposed to hydrogen. Besides, fossil fuels need to be burned in order to deliver their energy content when used in a motor, causing an inevitable loss in form of heat in automobiles [5].

Therefore, it is envisaged that hydrogen will be an energy carrier molecule in the near future, and it is being proposed as a potential replacement for fossil fuels because of their depletion and the environmental effects they cause. Because of the predicted scarcity of fossil fuels, it would be necessary to produce H_2 from renewable energy sources as a substitute. Hydrogen could be used in vehicles, in the generation of power and heat and for energy storage [6].

Furthermore, hydrogen has good properties as a fuel, being its autoignition temperature 500 °C. In addition, its flammability range is very high (4-75 %), allowing for easy control of the power output from a motor. Its octane number (scale used to measure the anti-knock capacity of a carburant when inside a motor cylinder) is very high, increasing the difficulty of producing unwanted auto ignitions in the combustion chamber of the engine. It has also been confirmed that benchtop and industrial scale production and consumption of hydrogen are viable [5]. However, hydrogen presents storage problems since it has the lowest energy density of common fuels by volume, and can explode violently when in contact with air and an ignition source [7]. Nevertheless, the technology is still not completely developed because of the daunting task of transitioning from a carbon energy system. Despite the remaining challenges, hydrogen is seen as a key solution to the twenty-first century's energy problems.

2.3 Hydrogen storage targets

There exist several technologies for storing hydrogen. Some of them, like compressed hydrogen and liquid hydrogen, are considered mature technologies. Solid state storage is another hydrogen storage technology and, in this specific kind of storage, two different forms can be differentiated: chemical and physical storage.

The US DOE (United States Department of Energy), defined the targets for hydrogen powered vehicles, setting a 300 miles (500 km) driving range on a single fill, meeting packaging, cost, safety and performance requirements in order to be competitive with current vehicles [8]. For this, between 5 and 13 kg would be needed, depending on the technology used to produce energy (fuel cell or combustion engine respectively) as well as its fuel and H_2 losses [9]. A summary of the specific set of targets (2020 and Ultimate) can be seen in Table 2.1:

Table 2.1. Summary of US Department of Energy targets for Light-Duty Fuel Cell Vehicles [9].

Storage Parameter	Units	2020	Ultimate
System Gravimetric Capacity	g H_2 (kg system)$^{-1}$ (kWh kg^{-1})	5.5 1.8	7.5 2.5
System Volumetric Capacity	g H_2 (L system)$^{-1}$ (kWh L^{-1})	40 (1.3)	70 (2.3)
Fuel cost	\$ (kg H_2 stored)$^{-1}$	333	266
Min/max delivery Temperature	°C	-40/85	-40/85
Operational cycle life	Cycles	1500	1500
Min/max delivery pressure from storage system	Bar	5/12	3/12
Onboard efficiency/ "Well to Powerplant Efficiency"*	%	90/60	90/60
System fill time (5 kg)	Min	3.3	2.5
Fuel Quality (from storage)	% H_2	99.97 % (dry basis)	99.97 % (dry basis)
Loss of usable H_2	(g h^{-1}) (kg H_2 stored)$^{-1}$	0.05	0.05

*Onboard efficiency refers to the delivery efficiency from the storage system to the fuel cell power plant. It accounts for any energy required from pumps, compressors, heating, etc. "Well to Powerplant Efficiency" includes both onboard and offboard efficiency (hydrogen production, delivery, liquefaction, compression, dispensing, regeneration of chemical materials, etc, depending of the storage system).

2.4 Conventional hydrogen storage systems

Compressed hydrogen is a mature storage method, as well as liquid hydrogen storage. However, the materials and design used to contain hydrogen in these two technologies can be further developed in order to be more resilient, lighter and have better thermal properties.

2.4.1 High-pressure tanks

High-pressure tank technology consists of compressing gaseous hydrogen to 350 or 700 bar at room temperature, although even pressures of more than 1000 bar are possible [10, 11] . The benefit of this technology is that when hydrogen is compressed, its volume is greatly reduced. As a particular example, one kilogram of hydrogen at 25 °C would require a volume of 12.3 m^3 at 1 bar of pressure. If hydrogen is stored at 350 bar instead, its volume is reduced by 99.6 % [12]. The occupied space can be further decreased if the pressure is raised, although this increases costs and security risks. In Figure 2.3, energy needs for hydrogen compression at different pressures and compressing conditions are shown:

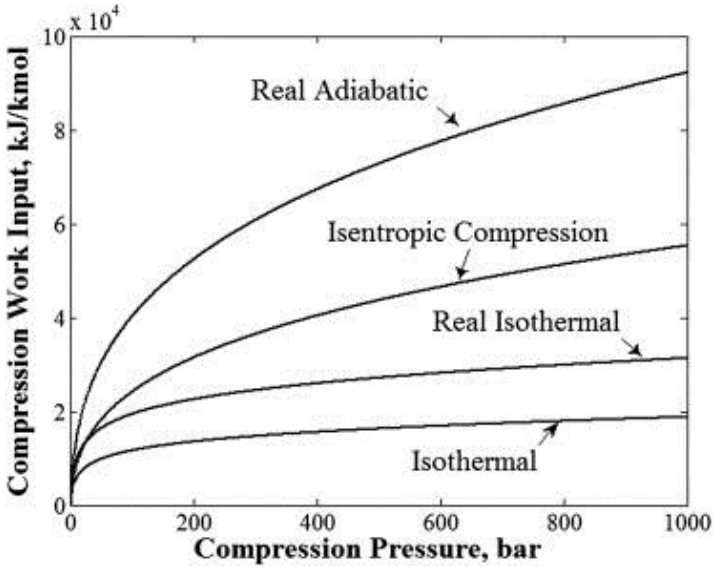

Figure 2.3. Compression work input for different compression conditions. Reprinted from [12] and used with permission from Elsevier.

Calculations were carried out to calculate compression energy costs in terms of % of hydrogen introduced into the cylinder, stating a cost of 9, 10 and 12 % of its energy content if the cylinder was respectively filled at 200, 350 and 700 bar. Calculations assumed a multi-stage compression with real isothermal conditions [13]. Compression

is considered as a relevant mature technology for hydrogen storage since no other technology so far discovered has significantly better output than compressed gaseous hydrogen storage [14]. Figure 2.4 shows the two hydrogen cylinders (700 bar) used to store hydrogen in a Ford C-Max Hydrogen car:

Figure 2.4. 700 bar compressed hydrogen cylinders in a Ford C-Max Hydrogen. Reprinted from [15], asked permission to SAE International. Copyright 2011.

The prime factor of this technology is the material of which tanks are made. It has to fulfil a series of requirements, such as resistance to embrittlement, weight and costs [7, 16]. Initially, tanks were made from aluminium, offering high thermal conductivity. However, these vessels were not strong enough, having switched to a carbon fibre/epoxy composite (carbon fibre reinforced plastic or CFRP) in recent years [7]. However, despite being lightweight and very strong, CFRP tanks have to be below 85 °C at all times because of their sensitivity to high temperatures and fire. If the conditions are not met, there could be a decrease on their mechanical properties and the eventual rupture of the cylinders. Furthermore, the thermal conductivity of carbon reinforced plastic is low, creating problems during the exothermic compression of hydrogen inside the vessel [7]. Currently, the most commonly used tanks are type IV (entirely made of CFRP) and type III (mix of aluminium and CFRP), having the last very high costs. New types of tanks are being researched such as the CFRP tank reinforced with a space-filling skeleton, which would allow the fabrication of lighter and stronger tanks in the future [7].

2.4.2 Capillary storage

Hydrogen can also be stored in capillaries, which consist of glass arrays. Glass capillary arrays (shown in Figure 2.5), are made of quartz and other glasses such as soda, borosilicates and aluminosilicates. These glasses possess interesting properties. As a particular example, quartz is three times more resilient than steel, with some capillaries able to resist up to 1200 bar of pressure. In addition to this, its density is around three times lower that of steel. These two features make this material ideally suited for the building of lightweight storage vessels [17].

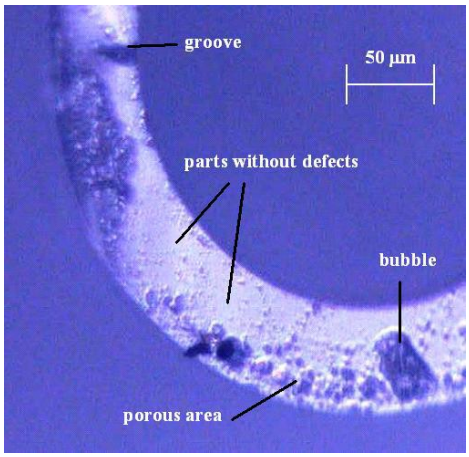

Figure 2.5. Microscope image of a soda capillary loaded with H_2. Reprinted from [17], with permission from BAM Federal Institute for Materials Research and Testing, Germany.

Capillaries are sealed by melting an alloy and cooling it after hydrogen has been stored inside. The other end is molten. In order to release the gas, the alloy must be melted again [17].

One interesting feature of this technology is that it allows multicapillary storage as well as a single capillary. Thus, many vessels can be added to a device, so avoiding the release of high quantities of hydrogen in case one of them breaks, adding further safety to the system. Furthermore, any size and length is possible, allowing the possibility for creating suitable storage systems for any application [17]. Besides, they can be filled at the fuel plant, reducing the infrastructure needed [7].

Conducted tests exhibited a gravimetric storage capacity of around 33 % and a volumetric capacity of 28 % at only 400 bar. These results met the DOE's 2010 target,

and it is hoped that further work will soon achieve the 2020 target, exceeding the DOE targets in many areas but the volumetric one [7, 17]. It has been calculated that gravimetric storage capacities of 50 % are possible at around 1000 bar. This technology seems promising although a great deal of energy is required to release the hydrogen, the capillaries' durability is limited and very high pressures are needed [7]. Also, there are still some properties that need to be tested such as the robustness of capillary arrays, depending on wall thickness, long term storage pressures, mechanical impact and fire treatment [17].

2.4.3 Glass microspheres

Hollow glass microspheres (HGMs) (Figure 2.6) are very small spheres made of glass, as seen in Figure 2.6. These microspheres are very resilient, being able to contain hydrogen at pressures up to 1500 bar, leading to storage capacities of up to 21 wt % [18]. It is also considered a safe method (non-explosive) since every microsphere contains a tiny quantity of hydrogen. In addition, it is efficient, cheap, non-toxic and light [18]. Their diffusivities are temperature dependant, being very low at room temperature (trapping the hydrogen), and high at high temperatures, allowing the gas be released (when hydrogen is needed), or diffused into the HGMs (when filling the microspheres). HGMs can be created using several methods. Probably the most common is "flamed sprayed pyrolysis", although there are others, such as "the droplet method" [18]. The exact composition of the glass, together with the heating method used, are of high importance, as they affect the hydrogen diffusivities of the material [18].

The main problems of technology are the high filling and release temperatures needed (above 300 °C), as well as their limited durability [7, 18]. However, by using different glass composition, the filling temperature could be reduced [18].

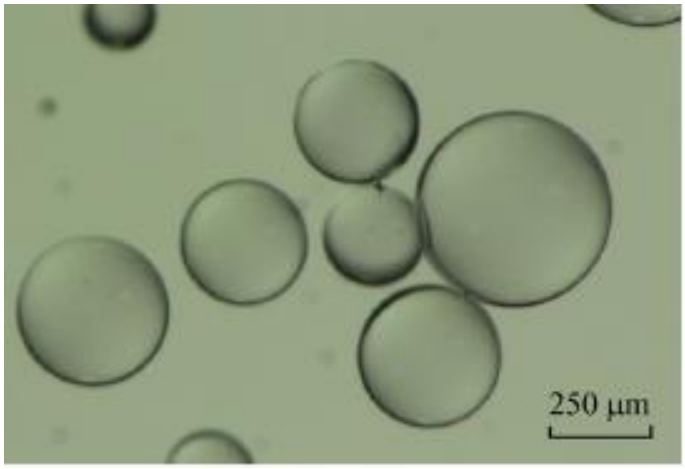

Figure 2.6. Optical photomicrograph of glass microspheres. Reprinted from [18], with permission from Elsevier.

2.5 Cryogenic storage: liquid hydrogen

Hydrogen can also be stored in liquid form below its critical temperature (33.18 K, being 13 bar its critical pressure), a technology known as cryogenic storage [19, 20]. Hydrogen stored in liquid form has a higher energy density compared to compressed hydrogen gas. This value is 2.22 kWh L^{-1} for liquid hydrogen, being 0.69 and 1.39 kWh L^{-1} for compressed hydrogen at 350 and 700 bar respectively [7]. However, this increase in energy density comes with extra costs, since the system needs to be below hydrogen's boiling point (hydrogen is therefore cooled to 20 K before entering the vessel), using 35 % of the fuel's energy. This value is three times higher than that needed to compress hydrogen up to 700 bar, having a dormancy period of 3-5 days (2 weeks to completely evaporate the entire vessel). Due to this need of venting, pressure release valves are needed for safety reasons [7].

A car that uses this technology was launched in 2002, called HydroGen3. It had a PEM fuel cell, and reached a speed up to 160 km h^{-1}, having a driving range of about 400 km and proved to hold up to 4.6 kg of liquid hydrogen. The total mass of the storage system was 90 kg [21].

2.6 Cryocompressed hydrogen

These technologies combine both compression and cryogenic storage of hydrogen. Among these technologies we can differentiate between compressed liquid hydrogen and compressed cryogenic gas.

2.6.1 Compressed liquid hydrogen

Compressed liquid hydrogen consists in storing liquid hydrogen in insulated pressure vessels, taking advantage of the low compressibility of liquid hydrogen. This advantage gives these vessels an increase in hydrogen density, reaching up to 87 g L^{-1} (at 240 bar and 21 K) compared with 70 g L^{-1} (at 1 bar and 21 K) [7, 22]. Also, thanks to the possibility of compressing the hydrogen in the vessel, these tanks increase their safety during dormant periods compared to non-compressed tanks [22].

LLNL and the BMW group have combined cryogenic and high-pressure vessels technology for automotive purposes, creating vessels that contain liquid hydrogen at temperatures as low as 20 K and pressures of around 355 bar [23-25]. This mix of technologies gives the possibility to use smaller and lighter vessels that have greater thermal resistance than normal cryogenic cylinders.

This type of cryogenic tank was placed in a hydrogen-powered Toyota Prius, showing high unrefuelled driving distance and highest dormancy time (maximum time the tank can withstand before being forced to vent the gas if the vehicle is idle) compared to other mechanical hydrogen storage vessels (with 5.6 kg of H_2). It showed a gravimetric capacity of 5.5 wt %, with a theoretical maximum of 9.2 wt % if the shell was made of aluminium, being able to meet the ultimate US DOE target of 7.5 wt %. Nevertheless, the manufacturing cost was two times higher that of the US DOE 2015 targets, not meeting the "well to tank efficiency" either (41.4 % compared to 60 % US DOE target) [7, 22].

In Figure 2.7, H_2 density and volume required to store 5 kg of H_2 at different temperatures is shown: the red dot refers to compressed hydrogen at ambient temperature, the blue dot to liquid hydrogen and the green area to conditions for cryogenic capable pressure vessels.

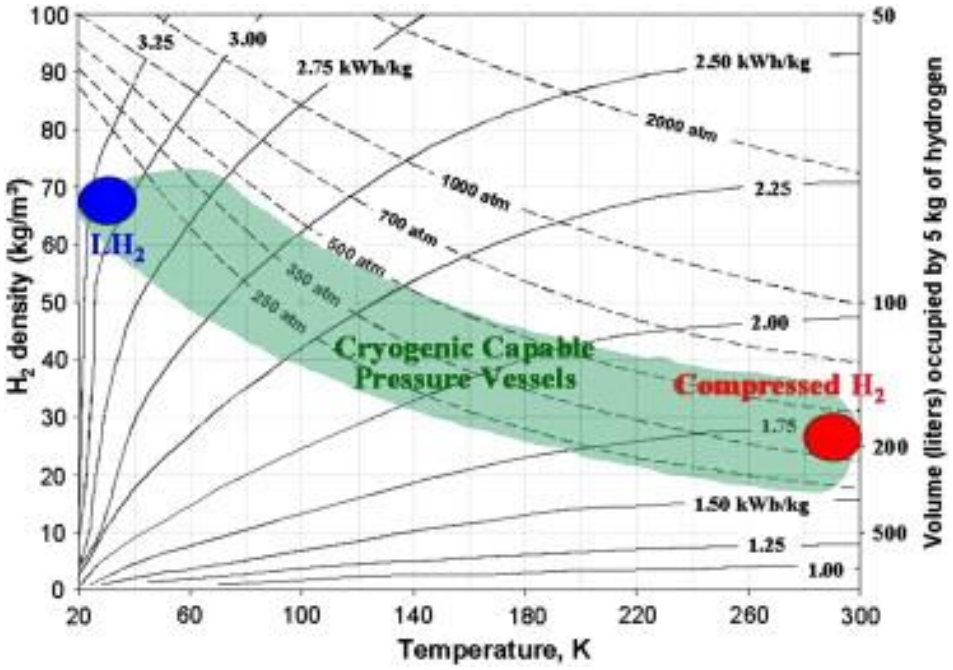

Figure 2.7. Commercial automotive hydrogen storage technologies properties graph for compressed (red), liquid (blue) and cryogenic capable pressure vessels (green) (temperature *vs*. H_2 density and volume occupied by 5 kg of H_2). Solid lines indicate the theoretical minimum work to compress and/or liquefy hydrogen and dotted lines represent the system pressure. Reprinted from [26], with permission from Elsevier.

Figure 2.7 includes different solid curves indicating energy costs of storing hydrogen at various conditions. As can be seen, storage at cryogenic temperatures uses less space but requires a greater amount of energy than storing at high pressures. The shaded green area exhibits the high pressure cryogenic vessel working range, whose systems allow filling the tank at different costs, depending on the desired H_2 density [26].

One of the biggest problems that cryogenic systems have is the gain of thermal energy from the environment due to H_2 storage at low temperatures, forcing the system to vent gas when the dormancy period is reached. This can cause additive losses, when the car is used over short continuous driving distances, and the risk of being stranded when parked for a long term [26]. In Figure 2.8, differences in dormancy periods can be seen between a vessel whose maximum pressure is 6 atm (green) and a vessel whose maximum pressure is 350 atm (green plus red) of a parked car. The car has a conventional LH_2 tank with 140 L internal volume, and is 80 % full with 8 kg of liquid

hydrogen at 20 K and 1 atm. The graph has been simplified so that every square represents 1 Watt day ($86.4 \frac{\text{kJ}}{\text{kg H2}} * \frac{1 \text{ day}}{86400 \text{ sec}}$) of heating [26].

Figure 2.8 shows that the amount of heat necessary to force vent (concluding the dormancy period) is seven times higher (for case 1 it goes from point 1 to 2; and for case 2 it goes from 1 to 3) (8 Watt day in case 1 against 48 Watt day in case 2). Dormancy can be calculated by dividing the Watt days obtained by the heat transfer rate while the car is parked [26].

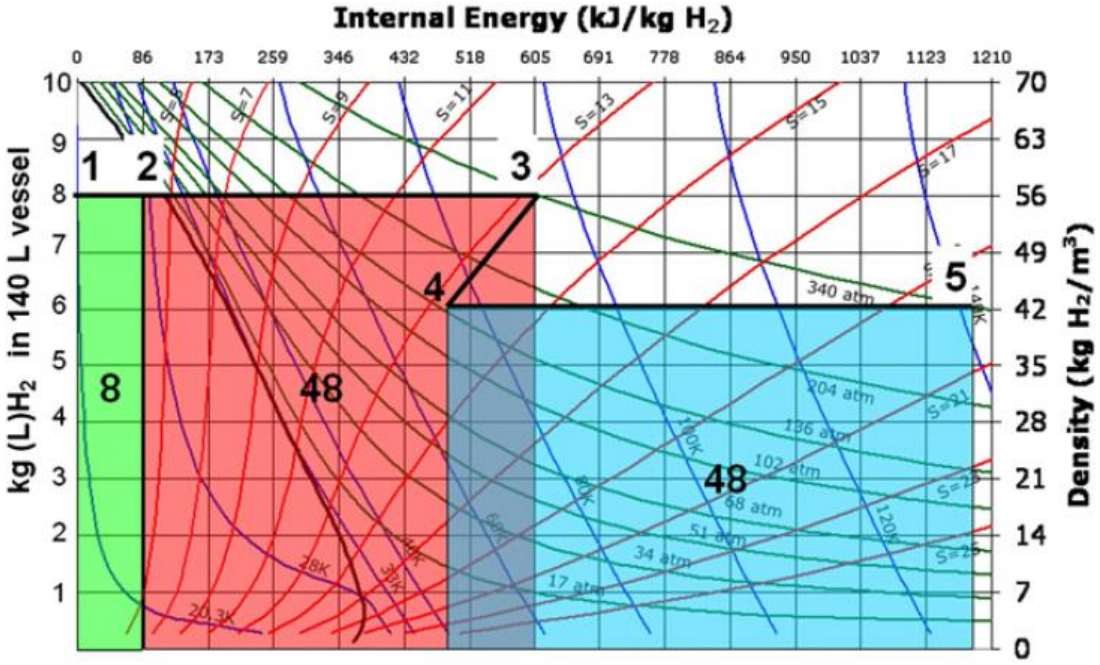

Figure 2.8. Hydrogen phase diagram plotting hydrogen density against internal pressure with lines representing constant pressure (green), temperature (blue) and entropy (red). The figure also shows different areas for a 140 L tank that would store 8 kg of LH_2 at 20 K and 1 bar (in Watt days). The green area represents dormancy for a conventional LH_2 tank while green and red and blue areas refer to a cryogenic capable pressure vessel. Reprinted from [26], with permission from Elsevier.

Furthermore, if the parked vehicle is used at point 3, and 2 kg of hydrogen are consumed, the remaining hydrogen in the tank would expand. This would cause a cooling of the remaining fuel (point 4), allowing the fuel to endure another 48 Watt-days without any loses (point 5) [26].

Although this mix of technologies is a great advance in hydrogen storage, the prototype vessel showed a capacity of 41.8 g H_2 L^{-1}, which meets the DOE 2015 target of 40 g

L^{-1}, but cannot meet the ultimate target of 70 g L^{-1}. The efficiency was 41.4 %, not meeting the well-to-powerplant efficiency DOE target of 60 %. Also, manufacturing and fuel costs were double than the DOE requirements [7, 22]. Compressed liquid hydrogen is one of the most promising physical storage systems which are still being developed [7].

2.6.2 Compressed cryogenic gas

Compressed cryogenic gas consists of storing compressed gaseous hydrogen at low temperatures (usually 77 K by using liquid nitrogen). Since gases are denser at lower temperatures, cooling at 77 K increases the volumetric capacity by three compared with non-cooled hydrogen. Also, it requires less energy than liquid hydrogen storage since it does not need to be cooled down to 20 K. As an example, to store 4.1 kg of hydrogen in a 100 L vessel, 750 bar are needed if compressed at room temperature, whereas only 150 bar would be required at 77 K. However, it also has to be considered that the cryogenic cylinder would be heavier due to the thermal insulation needed [7].

A very important fact is that adsorbent materials (explained in section 2.7.2) can be included in this type of tank, reducing the storage pressure even further. If this tank is filled with activated carbon pellets (AX-21), only 60 bar would be needed to store 4.1 kg of hydrogen in a 100 L tank at 77 K [7, 27]. In a different system it was found a maximum hydrogen adsorption capacity of 5.2 % with AX-21 at 29 bar and 77 K, 1.3 wt % below the Ultimate target. These promising results of combining cryogenic compressed gas with solid-state adsorbents such as MOFs, activated carbons and zeolites is hoped to be brought to US DOE standards [7, 28].

2.7 Solid/liquid state storage

There are two different types of solid/liquid state storage: chemical and physical, which can be distinguished by the strength of the interaction between hydrogen and the material and by the fact that hydrogen does not dissociate in physical storage. Physical solid-state storage materials adsorb hydrogen through a physisorption process whereas hydrogen is chemically bound in case of chemical hydrides. Chemisorption is favoured over physisorption due to the strength of the chemical bond compared with the adsorption of hydrogen on the surface of nanoporous materials. The binding energy for

chemical hydrides is between 193 and 289 kJ mol^{-1} being less than 10 kJ mol^{-1} for physisorbed hydrogen [7, 29]. However, different values have been found in other literature publications for the physisorption of hydrogen (4 to 7 kJ mol^{-1} for metal organic frameworks) [30].

In order to design a storage material that is good enough for this purpose, multiple criteria must be satisfied. Storage materials must have a high capacity, be lightweight and inexpensive, rapidly refuelable, and, most importantly, safe [14].

2.7.1 Chemical Storage: hydrides

Originally, the definition of hydride was reserved only for compounds that contained hydride ions, but its meaning has been extended to include all compounds that involve chemically bound hydrogen. They can store large amounts of hydrogen, although they have the issue of not being able to be recharged in a fuel cell vehicle [7].

There are many different methods for storing hydrogen chemically such as metal hydrides, carbohydrates, synthesized hydrocarbon, liquid organic hydrogen carriers (LOHC), ammonia, amine borane complexes, formic acid, imidazolium ionic liquids, phosphonium borate and carbonite substances. Among this type of materials we can differentiate between metal and non-metal hydrides [7].

2.7.1.1 Metal hydrides

A hydride is a chemical compound in form of a bond between hydrogen and a metal usually found in the first group of the Periodic table [10]. It is usually bonded with a more electropositive element. This type of chemical hydrides can operate at the relatively low temperatures and pressures needed for fuel cells [7].

This sub-group is divided in simple and complex metal hydrides. Simple metal hydrides are divided into two classes: binary metal hydrides and intermetallic hydrides. Binary hydrides contain hydrogen and one metal (with the formula MH_x, where M is the metal), whereas intermetallic hydrides contain two or more metals forming structures such as AB, AB_2. A_2B or AB_5, having at least one of the metals (A) high affinity for hydrogen, while the other/s (B) does/do not interact with hydrogen [7, 31].

Complex metal hydrides contain hydrogen atoms as part of their structure, being partially covalently bound within a polyatomic anion. Depending on the type of atoms present in the material, two different categories can be distinguished: amines and imines (if they contain nitrogen) and borohydrides (if they contain boron) [7].

From these groups, the most important ones are the borohydrides, which can contain up to 18 wt % with materials like $LiBH_4$ and $NaBH_4$ [7]. As a promising case, $LiBH_4$ releases a 13.8 wt %, decomposing itself into LiH and B [32]. When $LiBH_4$ is dehydrogenating at a low heating rate, three desorption peaks are observed, indicating that the process involves intermediate steps [32]. The compound hydrogenation is sluggish and needs high energy conditions, but it can be improved by using a binary LiB_x compound instead of LiH and B separately.

Another interesting metal hydride is $Mg(BH_4)_2$, which releases a 14.9 wt % of H_2 when it is heated at high temperatures (up to 600 °C). The reaction occurring and the steps involved are shown in Equation 1.1 and Figure 2.9 respectively [32]. Although its rehydrogenation conditions are still high, they are not as harsh as for $LiBH_4$ (270 °C at 400 bar for 48 h).

$$Mg(BH_4)_2 \longrightarrow MgH_2 + 2B + 3H_2 \qquad \text{Eq.1.1}$$

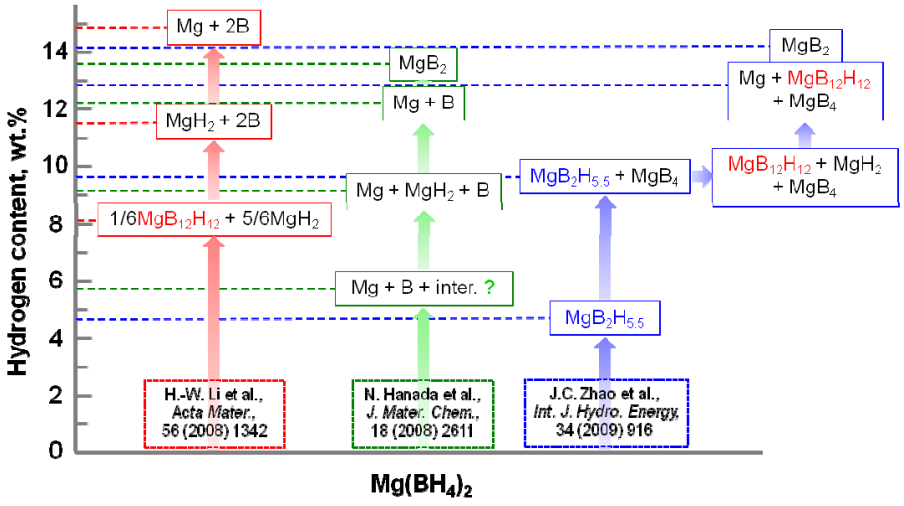

Figure 2.9. Dehydrogenation processes of $Mg(BH_4)_2$ from different reports. Reprinted from [32], used following the terms and conditions of the Creative Commons Attribution license.

Metal hydrides present excellent absorption capacities, although they also present serious difficulties regarding gravimetric density and system costs. Figure 2.10 shows a spider chart summarising metal hydrides achieved properties compared with the 2010 DOE targets, listing the twenty criteria for measuring the capability of materials to be used for hydrogen storage. Because they use expensive elements, system costs are very high. Among others, they also display problems in reversibility (which is typical in some metal hydrides), high weight, on-board efficiency, volumetric density and rehydrogenating conditions [14].

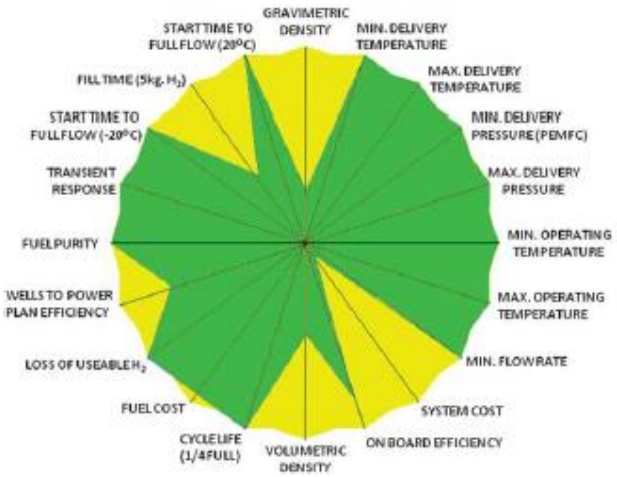

Figure 2.10. Representative spider chart for reversible metal hydrides. Reproduced from [14], with permission of The Royal Society of Chemistry.

2.7.1.2 Non-metal hydrides

Non-metal hydrides are made of boron, carbon, nitrogen or oxygen as well as hydrogen. Among non-metal hydrides we can find hydrocarbons, materials made of carbon and hydrogen. Hydrogen can be produced from both gas and liquid hydrocarbons. However, this poses many problems, since side products from the reactions often poison the fuel cell (sulphur gas or carbon monoxide) [7, 33]. Also, by obtaining hydrogen from hydrocarbons, we would carry on increasing problems related to the release of CO_2 to the atmosphere, such as global warming, poor air quality and the depletion of fossil fuels previously discussed.

Other different types of non-metal hydrides are boron and nitrogen hydrides. A very interesting hydride from this family is ammonia borane, NH_3BH_3, which has a

hydrogen capacity of 19.6 wt % (higher than petrol). However, these hydrides possess slow kinetics and unfavourable thermodynamics, although several different approaches are being researched to increase the reaction rate and decrease of the dehydrogenation and hydrogenation temperatures [7, 34].

Ammonia is a nitrogen based material that also presents interesting hydrogen capacities. NH_3 presents a high hydrogen uptake, 17.7 wt % and its production technology has already been developed [7, 34]. The problem is the nature of the reaction. By being endothermic, high temperatures are necessary to produce fair amounts of hydrogen. The use of catalysts such as ruthenium slightly diminish the temperature needed. The combination of both ammonia and lithium hydride allows the generation of 8.1 wt % at room temperature in a reversible reaction. To revert it, $LiNH_2$ needs to be hydrogenated at 300 °C and 5 bar [7, 34].

2.7.2 Solid State Storage: Physical

Physical solid-state storage materials adsorb hydrogen through a physisorption process, which possess a low enthalpy of adsorption (from 4 to 7 kJ mol^{-1} for MOFs) [30]. This value is related to the interaction between the material and the adsorbed hydrogen, being high values desirable as long as the adsorption is reversible [30].

2.7.2.1 Adsorption

Adsorption occurs whenever a solid surface is exposed to a gas or liquid. It is defined as the enrichment of one or more of the components in the region between two bulk phases. In the context of adsorption in nanoporous materials, the material will be the solid while the other one to be adsorbed, the fluid (gas or liquid) [35].

The adsorptive, the fluid to be adsorbed, is adsorbed by the adsorbent, which is the solid material where the process occurs. Once the adsorptive is adsorbed (designated as adsorbate), it is normally initially confined to a surface monolayer. If the adsorption occurs at relatively high pressures, the process usually occurs in multilayers [35].

If the adsorbent is porous, as exemplified in Figure 2.11, it might have different types of pores and/or roughness. The porosity of the material is defined as the ratio of the

volume of both pores and voids of the material divided by the volume that the solid occupies [35].

Figure 2.11. Cross-section of a hypothetical porous grain showing different types of pores: closed (below R), blind (B), through (T), interconnected (I), together with some roughness (R). Reprinted from [35], with permission from Elsevier.

According to the IUPAC, depending on the pore width of the internal pores of the material, the material can be microporous (lower than 2 nm pore diameter), mesoporous (between 2 and 50 nm pore diameter) or macroporous (higher than 50 nm pore diameter) [35].

The relation at constant temperature between the amount adsorbed in the material and the equilibrium pressure is known as the adsorption isotherm. Again, the IUPAC has an isotherm classification (shown in Figure 2.12) depending on the shape of the experimental adsorption isotherm [35]:

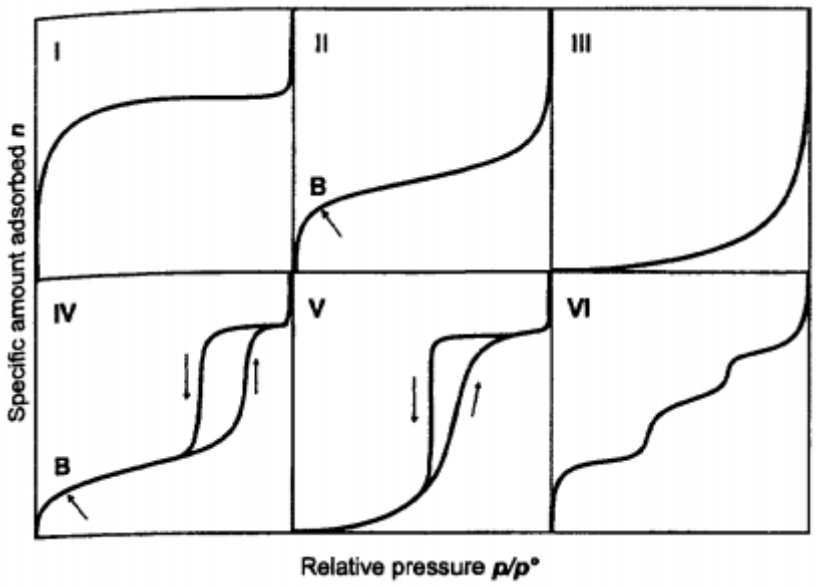

Figure 2.12. The six main types of gas physisorption isotherms according to the IUPAC classification. Reprinted from [35], with permission from Elsevier.

It can be seen in isotherms type IV and V that the amount of adsorbed adsorptive at specific relative pressures while in equilibrium is different in adsorption and desorption. This effect is called hysteresis.

Characteristic features of isotherms are as follows. A type I isotherm is indicative of microporosity in the material and a small amount of multilayer adsorption, while a Type II for example, would normally be associated with monolayer-multilayer adsorption on a material that can be non-porous, macroporous or slightly microporous [35].

2.7.2.2 Carbons

There exist different types of porous carbons: activated carbons and carbon nanotubes. Carbons are a form of synthetic or processed carbons. They are amorphous, and usually have high specific surface areas and low producing costs [4]. These mentioned features, together with the possibility to be mass produced and their moderate uptake have made these materials interesting for hydrogen storage, being the first type of adsorbents to be tested [4]. For activated carbons, one of the best observed excess uptake values is 5 wt % on AX-21 at 77 K and 30-60 bar. Another effective activated carbon is KUA5, which is capable of adsorbing 3.2 wt % excess uptake at 190 bar and 6.8 wt % excess uptake at 500 bar at room temperature. If the temperature is lowered to 77 K, it is able to adsorb 8 wt % excess uptake at only 40 bar [7, 36]. However, a more recent publication shows an outstanding 7.7 wt % excess uptake at 77 K and 12 bar [37].

Other existing types of activated carbons are TE3, TE7 and OLC-1750, which were some of the tested carbons by using inelastic neutron scattering, whose results can be found in Chapter 6. TE7 carbon beads were synthesized from a carbonized phenolic resin-based material, being the material activated at 900 °C under a CO_2 atmosphere. TE3 carbon beads were produced using similar conditions, resulting in a more microporous material. Materials were supplied from MAST Carbon International, UK [38].

OLCs (Onion-like carbons) are spherical carbon nanoparticles consisting of several concentric stacks of graphene-like carbon shells of 2-50 nm in size. There exist

numerous synthesis methodologies, being OLC-1750 particularly synthesized by vacuum annealing of detonated nanodiamond powder for 3 h at 1750 °C (from Ray Technologies Ltd., Israel) [38, 39].

Carbon nanotubes (shown in Figure 2.13) are one-dimensional materials that possess the same diameter range size as fullerenes. They have been recognized as interesting materials with nanometre dimensions, promising exciting new areas of carbon chemistry and physics [40]. They were the first carbon materials to be studied for hydrogen storage, starting in 1997 because of their microporous structure and high surface area [7, 36]. In addition, carbon nanotubes can adsorb hydrogen in both the exterior and interior of their nanostructure, yielding capacities between 0.25 and 11 wt % under different conditions [7, 36]. The theoretical maximum hydrogen uptake on metal doped carbons is 2 wt % per 1000 m^2 g^{-1} of carbon sorbent, but only 0.4 wt % has been obtained experimentally so far [41].

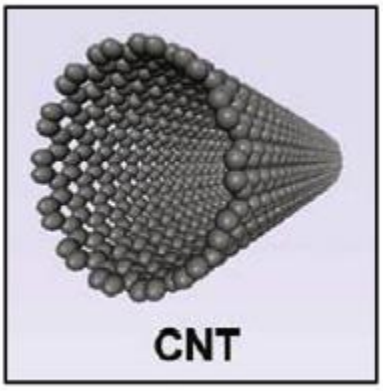

Figure 2.13. Carbon nanotube. Adapted from [7], with permission from Elsevier.

2.7.2.3 Zeolites/Silicalites

Zeolites are mainly alumina-silica crystalline materials widely used in industry [42, 43]. Their name comes from the Greek, whose meaning is “boiling stone”. Many different varieties of this mineral have been found, referring now the word to a family of minerals instead. They can be formed in volcano environments when wind-blown volcanic dusts are deposited in saline lakes, although nowadays they can also be artificially synthesized [42, 43].

Zeolites have numerous applications in industry such as separation, catalysis, domestic water purification, construction, as soil remediation agents and animal feed

supplements due to their intracrystalline structure. A wide range of interconnected pore widths, different shapes and a large quantity of channels and cages in the micropore size range can be found in their structure. They are three dimensional structures of linked silicon and oxygen tetrahedrons. Atoms of Si can be replaced, usually by Al atoms, leaving negative charges in the network that are neutralised by extra-framework ions such as Na^{+} or Ca^{2+}. Zeolites show great adsorption properties when they are neutral or weakly polar, being dependant on their pore size distributions [43, 44].

A systematic investigation in hydrogen storage in zeolites was performed, showing Zeolite X as the zeolite with the best hydrogen uptake [30]. With a BET surface area of 669 m^2 g^{-1}, this particular calcium-exchanged zeolite has a 2.19 wt % at 15 bar and 77 K [41, 45-49].

Silicalites are microporous crystalline polymorphs of silica. They possess a similar structure to that of zeolites. Figure 2.14 shows the structure of ZSM-5, a very well-known silicalite. Its tetrahedral framework contains several five-membered rings of silicon-oxygen tetrahedra, arranged in a three dimensional system defined by 10-rings of oxygen ions in all the three directions [50].

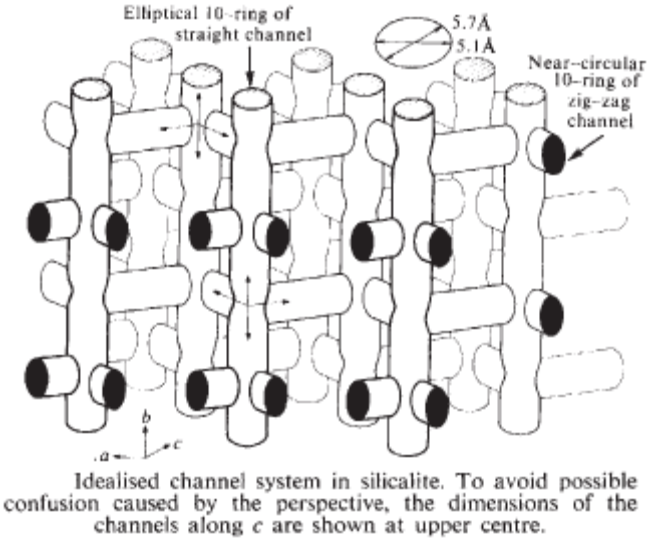

Figure 2.14. Idealised channel system of the ZSM-5. Reprinted with permission from Macmillan Publishers Ltd: [46], copyright 1978.

By removing the ammonium ions from the silicalite precursor, large voids are obtained. This process takes 33% of the total crystal volume, and the resulting channels are

sufficiently big to adsorb, and therefore hold, molecules of up to 0.6 nm in diameter [50].

Nevertheless, silicalites have a relatively low hydrophilicity compared to zeolites. Zeolites' hydrophilicity is explained by the presence of polar groups such as cations and hydroxyl groups in their structure. Because of replacing silicon from the tetrahedral groups by aluminium, its hydrophilicity is increased. Other zeolites whose aluminium and cations have been removed show a decrease in water adsorption [50].

2.7.2.4 Clathrate hydrates

Clathrate hydrates are water-based solids that can hold gas molecules. These molecules are trapped in polyhedral cages, which are made up of hydrogen bonded water molecules. In these structures, water molecules function as hosts while molecular gases act as guests. One of these gas guests can be hydrogen. Therefore, clathrate hydrates can be used as a hydrogen storage method. There are different possible clathrate cage structures found in Figure 2.15: type I, type II and type H. Each structure has different crystallographic characteristics and cavities. However, without the confined gas molecules, the hydrate would collapse into a liquid [51, 52].

These clathrate hydrates can be synthesized with hydrogen molecules as guests at around 2000 bar and low temperatures (around 250 K) [52]. A specific clathrate hydrate can contain a 0.6 wt % (on furan hydrate) at 275.1 K and 415 bar, being up to 4 wt % the theoretical maximum achievable on these materials [53, 54].

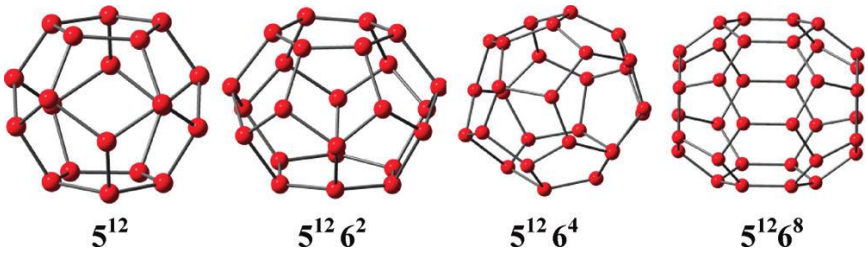

Figure 2.15. Different Clathrate hydrate structures. Reprinted with permission from [52]. Copyright 2010 American Chemical Society.

2.7.2.5 Polymers of intrinsic microporosity

PIMs (polymers of intrinsic microporosity) are amorphous organic microporous materials that possess intrinsic microporosity (Figure 2.16). Intrinsic microporosity can

be defined as a continuous network of interconnected intermolecular voids, which are formed due to the shape and rigidity of the component macromolecules [55-57]. These porous polymers have features such as crosslinking networks or spiro-centres, offering rigidity and avoiding efficient packing and, therefore, conferring large amounts of free volume [30]. However, common polymers tend to minimize void space, condensing themselves in order to increase the interaction between their constituent molecules [55].

Apart from high porosity, PIMs have low density, chemical homogeneity, thermal and chemical stability, and synthetic reproducibility [30]. Uptakes of 1.61 and 3.68 wt % at 1 and 15 bar respectively at 77 K have been reported in literature by the p-DCX/BCMBP hypercrosslinked polymer, exhibiting high BET and Langmuir surface areas (1900 and 3000 m^2 g^{-1} respectively). Examples of PIMs are polyacetylenes, fluorinated polymers and polyimides [30, 58].

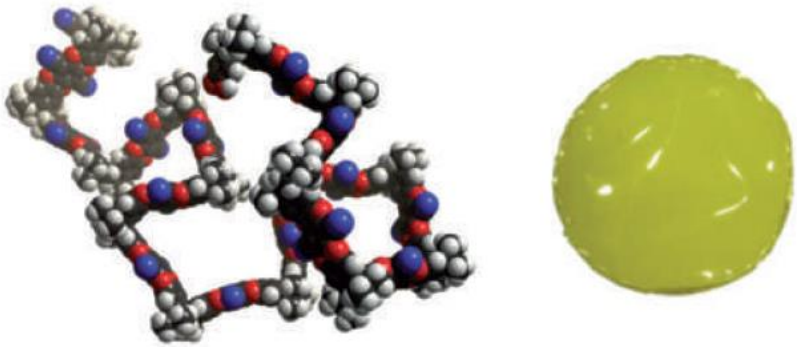

Figure 2.16. Molecular model of a fragment of a polymer of intrinsic microporosity (left), and photograph of an amorphous PIM film (right). Reprinted with permission from Macmillan Publishers Ltd: [59], copyright 2010.

2.7.2.6 Metal-organic frameworks

Metal-organic frameworks, are crystalline materials formed by the connection of metal ions or clusters through organic molecules acting as linkers. These materials can show geometric rigidity, chemical functionality and/or chirality. The preparation of these materials is scalable and generally gives high yields and, by carefully choosing the building blocks, targeted MOFs can be created. They are usually synthesized using solvothermal methodologies at relatively mild conditions. Due to the crystallinity of these materials, powder X-ray diffraction can be used as an effective technique to determine the success of the synthesis [7, 60]. This peculiar type of material has become interesting in applications such as gas storage, separation, and catalysis applications

due to its accessible surface area and permanent porosity [61, 62]. MOFs have open channels or cavities from micro- to meso-scale. However, a large number of MOFs show micropores with low molecular diffusion and mass transfer [61, 62].

MOFs can have very high surface areas. NU-100 exhibits the highest BET surface area to date, with a value of 6143 m^2 g^{-1} [63]. They are also the nanoporous materials that show the highest excess hydrogen uptake, with NU-100 having 9.95 wt % at 70 bar and 77 K (16.4 wt % total H_2 uptake) and other existing MOFs such as DUT-49, which also present high hydrogen adsorption (maximum hydrogen uptake of 8 wt % at 50 bar and 77 K) [64, 65].

Unlike many metal hydrides, MOFs are reversible but need low temperatures in order to operate more effectively [14]. The next figure is a spider graph that shows the 2010 US DOE met criteria for physisorbed hydrogen:

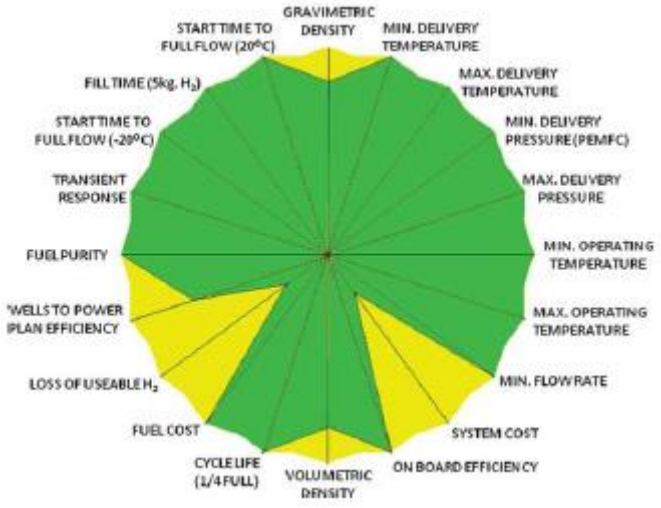

Figure 2.17. Representative spider chart hydrogen sorbent (principally physisorbed, porous systems) assessed against 2010 DOE. Reproduced from [14], with permission of The Royal Society of Chemistry.

There exist different types of MOFs, grouped by different topologies:
IRMOFs are isoreticular MOFs (Figure 2.18). Their topology is that of CaB_6, in which an oxide-centered Zn_4O tetrahedron is connected to six organic linkers (in form of benzene dicarboxylates or similar), giving an octahedron secondary building unit (known as SBU) that reticulates into a 3D cubic porous network [66]. The simplest organic linker that can be used is known as BDC (benzene-1,4- dicarboxylate, also known as terephthalic acid), shown in Figure 2.18. However, their versatility allow

them to use a wider range of carboxylate linkers (including linkers that contain bromine and amino groups for example) to tune their characteristics while maintaining an octahedral cell unit. Because of IRMOFs mentioned tunability, their pore diameter can oscillate between 3.8 to 28.8 Å [66].

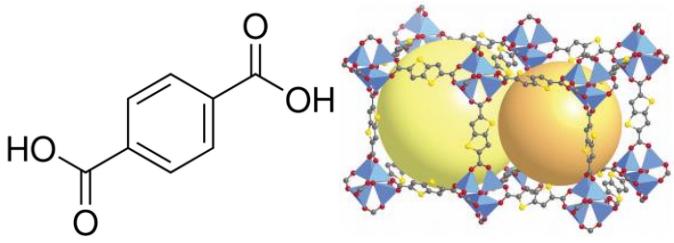

Figure 2.18. Benzene-1,4-dicarboxylate molecule, linker of IRMOF-1 (left) and IRMOF-20 ($Zn_4O(C_8H_2O_4S_2)_3$), a type of MOF (right). The blue tetrahedrons represent zinc, which are the metal ions. The molecules (in yellow and grey) that link the tetrahedra are the organic linkers (thieno[3,2-b]thiophene-2,5-dicarboxylic acid). The yellow and orange approximately spherical spheres represent the pores, which intersect at the apertures. Reprinted with permission from [67]. Copyright 2006 American Chemical Society.

Another group of MOFs are ZIFs (zeolitic imidazolate frameworks), whose crystal structure is the same that of zeolites [68, 69]. As the rest of the MOFs, they are formed by metal ions (e.g., Zn, Co) tetrahedrally-coordinated and connected by specific organic linkers (imidazolates). It is the metal-imidazole angle the one that make ZIFs isomorphs of zeolites, since it is similar to the 145° Si-O-Si angle found in them [68]. Almost 30 different zeolite reported structures (e.g. LTA, ANA, GME, SOD, RHO, DFT, MER, POZ, and MOZ) have also been reported in ZIFs [70, 71]. This resemblance is shown in Figure 2.19:

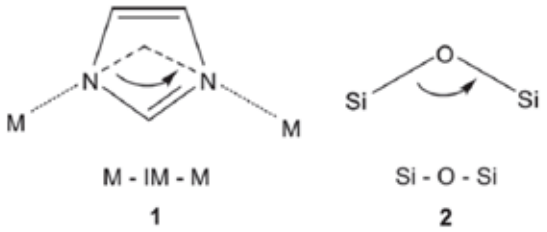

Figure 2.19. ZIFs (1) and zeolites (2) bridging angles. M refers to the metal, IM to the imidazolate linker, Si to silicon and O to oxygen. Reprinted from [68], with permission from PNAS, copyright (2006) National Academy of Sciences, U.S.A.

ZIFs have proven high thermal stability and extraordinary chemical resistance, some of them showing the ability to withstand boiling alkaline water and organic solvents [68, 72]. SOD and RHO (found in ZIF-8 and 11 respectively) are two ZIF topologies that exhibit this outstanding resistance.

The SOD framework is formed of truncated cuboctaedron cages (known as beta cages). These cages are composed of 4 and 6 membered ring windows with 24 Co or Zn atoms per unit cell [68, 70, 71, 73]. Each β cage is connected to six other β cages by sharing double 4 membered ring units as shown in Figure 2.20:

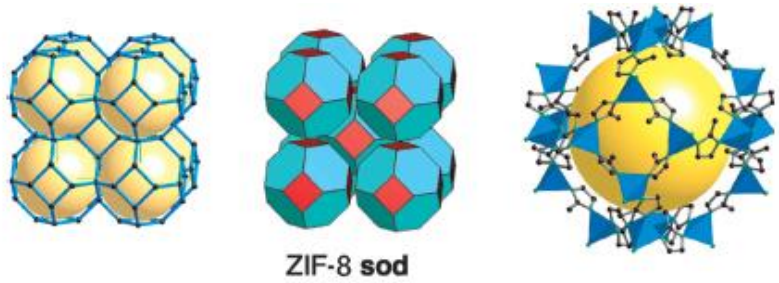

Figure 2.20. Structure of ZIF-8 (SOD) as a stick diagram (first from left), as a tiling (second from left) and a detailed structure of a beta cage from ZIF-8 (last). In the last figure, ZnN_4 is represented as blue tetrahedra and carbons in black. The yellow sphere represents the pore, which intersect at the apertures. Reprinted from [68], with permission from PNAS, copyright (2006) National Academy of Sciences, U.S.A.

The RHO structure is composed of alpha cages, made of 4, 6 and 8 membered windows. 48 Zn or Co ions can be found per unit cell. The framework area cages are constituted of 6 octagons, 8 hexagons and 12 squares. Each alpha cage is connected to six other cages by sharing double 8 membered ring units [70, 71]. RHO topology possesses larger cages connected through polyhedral units (known as D8R), shown in Figure 2.21 [70]:

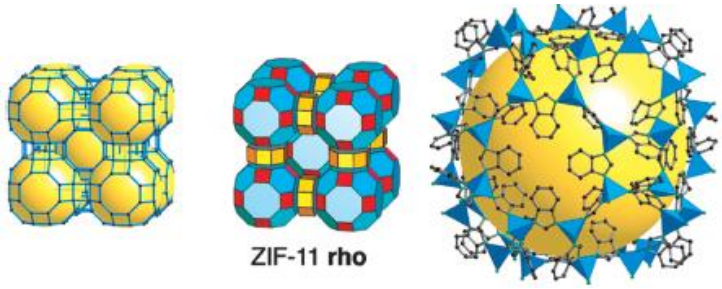

Figure 2.21. ZIF-11 (RHO) as a stick diagram (first from left), as a tiling (second from left) and a detailed structure of an alpha cage of ZIF-11 (last). In the last figure, ZnN_4 metal clusters are represented as blue tetrahedra and carbons as black dots. The yellow sphere represents the pore, which intersect at the apertures. Reprinted from [68], with permission from PNAS, copyright (2006) National Academy of Sciences, U.S.A.

UiOs are MOFs with a different topology, based on Zr that can also be made with increasing length of the linkers. These MOFs have the feature of allowing to increase the scale by choosing different organic linkers without compromising the stability of the material. As an example, UiO-66 (formed of BDC linkers) and UiO-67 (formed of BPDC linkers) have the same decomposition temperature [74]. Figure 2.22 show the structures of UiO-66 and 67 respectively:

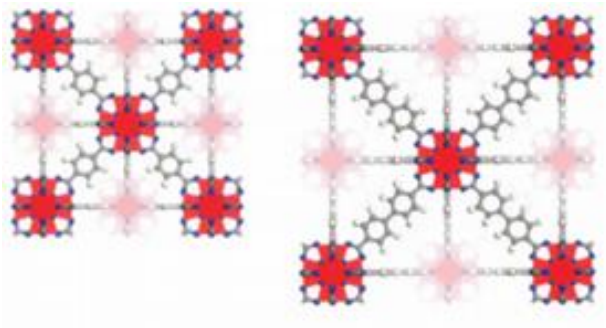

Figure 2.22. Zr MOF with 1,4-benzene-dicarboxylate (BDC) as linker, UiO-66 (left). Zr MOF with 4,4' biphenyl-dicarboxylate (BPDC) as linker, UiO-67. Zirconium, oxygen, carbon and hydrogen atoms are red, blue, gray and white, respectively. Adapted with permission from [75]. Copyright 2008 American Chemical Society.

UiOs are formed by an inner $Zr_6O_4(OH)_4$ core whose triangular faces are alternatively capped by μ3-O and μ3-OH groups (Figure 2.23a). All the edges of the polyhedron are bridged by carboxylate groups ($-CO_2$), which originally come from the dicarboxylic acids of the organic linkers, creating a $Zr_6O_4(OH)_4(CO_2)_{12}$ cluster (Figure 2.23b). Each zirconium atom (red) is eight-coordinated forming a square-antriprismatic coordination (polygon made of 2 squares and 6 triangles) formed of eight oxygen atoms (blue). One

of the squared faces is formed from oxygen atoms that come from the carboxylates (C in grey), while the other squared face is formed by oxygen atoms from the μ3-O and μ3-OH groups (where H is represented in white). This results in a cluster shaped like a Maltese star (Figure 2.23c) [75-77].

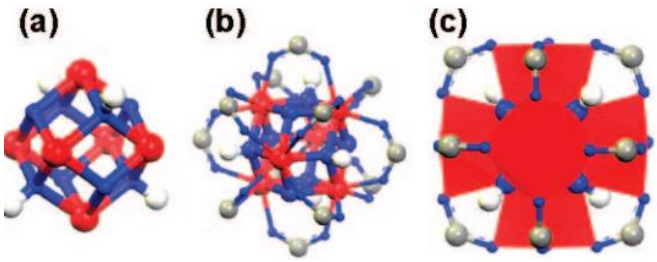

Figure 2.23. Structures *a* to *c* show the inner core Zr_6-cluster in more detail. Zirconium, oxygen, carbon and hydrogen atoms are red, blue, grey, and white, respectively. Adapted with permission from [75]. Copyright 2008 American Chemical Society.

HKUST-1, also known as Cu-BTC, MOF-199 and Basolite™ C300, is a highly porous MOF with the structure $[Cu_3(TMA)_2(H_2O)_3]_n$] [78]. It forms face-centered-cubic crystals that contain an intersecting three dimensional system of large square shaped pores (9x9 Å). The pores contain up to 10 molecules per formula unit, a reasonable thermal stability (up to 240 °C), an electrically neutral framework and the availability to chemically functionalise the channel linings [78].

The framework is formed of dimeric cupric tetracarboxylate units (Figure 2.24), being the Cu-Cu internuclear separation 2.628 Å. The 12 carboxylate oxygens from the two TMA ligands (benzene-1,3,5-tricarboxylate) are bind to four coordination sites for each of the three Cu^{2+} of the formula unit. Each metal completes its pseudooctahedral coordination sphere with an axial aqua ligand opposite to the Cu-Cu vector. HKUST-1 has channels with fourfold symmetry of around 1 nm in size which can be seen in 2.24 [78].

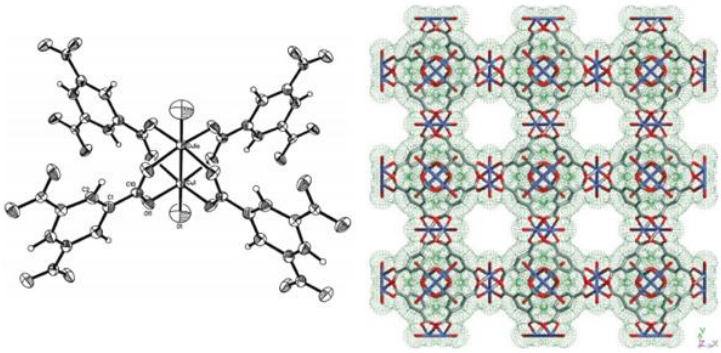

Figure 2.24. Dicopper (II) tetracarboxylate building block for HKUST-1 (left) and n-polymer framework viewed down the direction, showing nanochannels with fourfold symmetry (right). From [78]. Reprinted with permission from AAAS.

MILs are another type of MOFs. MIL-101 (Cr) specifically has terephthalic acid as the organic linker, connecting the chromium metal clusters. In Figure 2.25, a computational model of the units that form the MOF and its structure are shown [79]:

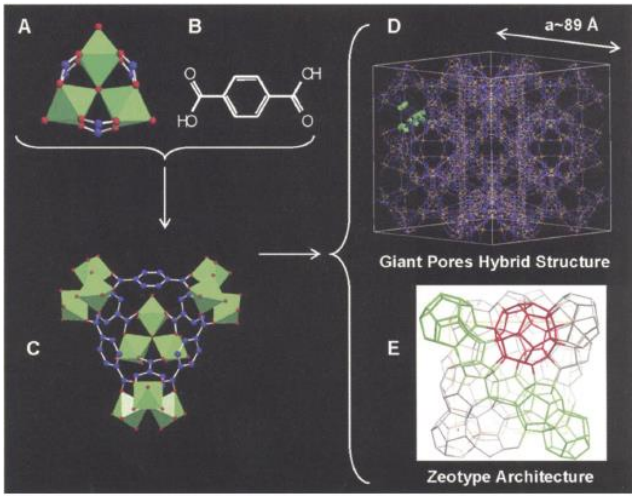

Figure 2.25. A) Building block of MIL-101 (Cr). B) Molecule of the organic linker, terephthalic acid. C) Sub-unit made from building blocks (A). D) Ball and stick representation of an unit cell. A sub unit (C) can be seen coloured on the left side. E) Schematic three dimensional representation of the MOF, differentiating two different cage types (20 tetrahedra in green, 28 tetrahedra in red) in the MOF. Chromium octahedra, oxygen, fluorine and carbon atoms are represented in green, red and blue respectively. From [79]. Reprinted with permission from AAAS.

The two cages are in a 2:1 ratio (marked in E in green and red) and exhibit different pore sizes. The smaller cage (green) is made of 20 tetrahedral units (C) and has a pore size of 29 Å. It is formed by pentagonal windows of 12 Å, allowing access to large molecules. The bigger cages are formed by both pentagonal and hexagonal windows (16 Å X 14.7 Å), creating a bigger cage of 34 Å in pore size. Another literature

publication shows that the small tetrahedral side pockets built up of chromium octahedra connected by 1,3,5-benzene tricarboxylate (BTC) have an inner free diameter of 7 Å, indicating the existence of a third pore size in MIL-101 (Cr) [80].

2.8 Aim and objectives of the thesis

The aim of this thesis is to investigate correlations between the total hydrogen capacity of nanoporous materials (by modelling their hydrogen experimental excess data) and their intrinsic properties at high pressures and cryogenic temperatures to help to select and predict the properties of a material that would meet the US DOE targets.

To meet this aim, the following objectives were set:

I) Research about specific nanoporous materials' properties and measure their hydrogen uptake excess, as well as obtaining more material datasets from literature to investigate relationships between variables and hydrogen adsorption.

II) Correlate intrinsic properties of the materials against their total hydrogen uptake and total hydrogen capacities to help predicting the properties of a material that would meet the DOE targets.

III) Develop methodologies to improve results from model fittings using experimental data to better predict the properties of a material that would meet the DOE targets.

IV) Confirm the existence of solid-like hydrogen adsorbed in nanopores to validate model assumptions and widen the understanding of hydrogen adsorption in nanoporous materials.

V) Study possible strategies to improve hydrogen storage by reducing the available pore size of materials to improve their heat of adsorption and therefore storage capacities.

VI) Design mixed materials for CO_2 removal systems to help improving air quality and purify hydrogen to increase the quality of hydrogen adsorption experiments.

2.9 References

1. Hansen J., R.R., Sato M., Lo K., *Global surface temperature change.* Reviews of Geophysics, 2010. 48(4): p. n/a-n/a.
2. *BP Statistical Review of World Energy June 2012*. 2012.
3. Ibrahim H., I.A., Perron J., *Energy storage systems—Characteristics and comparisons.* Renewable and Sustainable Energy Reviews, 2008. 12(5): p. 1221-1250.
4. Lim K. L., K.H., Yaakob Z., Daud W. R. W., *Solid-state Materials and Methods for Hydrogen Storage: A Critical Review.* Chemical Engineering & Technology, 2010. 33(2): p. 213-226.
5. Mazloomi, K. and C. Gomes, *Hydrogen as an energy carrier: Prospects and challenges.* Renewable & Sustainable Energy Reviews, 2012. 16(5): p. 3024-3033.
6. Makowski P., T.A., Kuhn P., Goettmann F., *Organic materials for hydrogen storage applications: from physisorption on organic solids to chemisorption in organic molecules.* Energy & Environmental Science, 2009. 2(5): p. 480-490.
7. Durbin, D.J. and C. Malardier-Jugroot, *Review of hydrogen storage techniques for on board vehicle applications.* International Journal of Hydrogen Energy, 2013. 38(34): p. 14595-14617.
8. *http://energy.gov/eere/fuelcells/hydrogen-storage. Last accessed 29/06/15.*
9. *http://energy.gov/eere/fuelcells/hydrogen-storage-current-technology. Last accessed 29/06/15.*
10. Eberle, U., M. Felderhoff, and F. Schuth, *Chemical and Physical Solutions for Hydrogen Storage.* Angewandte Chemie-International Edition, 2009. 48(36): p. 6608-6630.
11. Zuttel, A., *Hydrogen storage methods.* Naturwissenschaften, 2004. 91(4): p. 157-172.
12. Hosseini M., D.I., Naterer G. F., Rosen M. A., *Thermodynamic analysis of filling compressed gaseous hydrogen storage tanks.* International Journal of Hydrogen Energy, 2012. 37(6): p. 5063-5071.
13. Di Profio P., A.S., Rossi F., Filipponi M., *Comparison of hydrogen hydrates with existing hydrogen storage technologies: Energetic and economic evaluations.* International Journal of Hydrogen Energy, 2009. 34(22): p. 9173-9180.
14. David, W.I.F., *Effective hydrogen storage: a strategic chemistry challenge.* Faraday Discussions, 2011. 151: p. 399-414.
15. Veenstra, M.J. and B. Hobein, *On-Board Physical Based 70 MPa Hydrogen Storage Systems.* SAE Int. J. Engines, 2011. 4(1): p. 1862-1871.
16. Jorgensen, S.W., *Hydrogen storage tanks for vehicles: Recent progress and current status.* Current Opinion in Solid State and Materials Science, 2011. 15(2): p. 39-43.
17. *K. Holtappels, M. Beckmann-Kluge, M. Gebauer, M. Grüneberg and D. Eliezer. Hydrogen storage in Glass capillary arrays for portable and mobile systems*
18. Qi X.B., G.C., Zhang Z.W., Chen S.F., Li B., Wei S., *Production and characterization of hollow glass microspheres with high diffusivity for hydrogen storage.* International Journal of Hydrogen Energy, 2012. 37(2): p. 1518-1530.
19. *http://webbook.nist.gov/cgi/cbook.cgi?ID=C1333740&Mask=4#Thermo-Phase. Last accessed 29/06/15.*
20. *P.G. Cath, C.A. Crommelin and H. Kamerlingh Onnes. Isothermals of di-atomic substances and their binary mixtures. XIX. A preliminary determination of the critical point of hydrogen.* KNAW, Proceedings, 20 I, Amsterdam, 1918: p. 178-184.
21. Wolf, G.A.a.J., *Liquid Hydrogen for Automotive Application Next generation Fuel for FC and ICE Vehicles.* J.Cryo.Soc.Jpn. (Teion Kogaku), 2005. 40(6).
22. Ahluwalia R. K., H.T.Q., Peng J. K., Lasher S., McKenney K., Sinha J., Gardiner M., *Technical assessment of cryo-compressed hydrogen storage tank systems for automotive applications.* International Journal of Hydrogen Energy, 2010. 35(9): p. 4171-4184.
23. Aceves SM, B.G., Rambach GD., *Insulated pressure vessels for hydrogen storage on vehicles. International Journal of Hydrogen Energy.* 1998. 7: p. 583–91.
24. Aceves, S.M. and G.D. Berry, *Thermodynamics of insulated pressure vessels for vehicular hydrogen storage.* Journal of Energy Resources Technology-Transactions of the Asme, 1998. 120(2): p. 137-142.
25. Aceves S.M., B.G.D., Martinez-Frias J., Espinosa-Loza F., *Vehicular storage of hydrogen in insulated pressure vessels.* International Journal of Hydrogen Energy, 2006. 31(15): p. 2274-2283.
26. Aceves S.M., E.-L.F., Ledesma-Orozco E., Ross T.O., Weisberg A.H., Brunner T.C., Kircher O., *High-density automotive hydrogen storage with cryogenic capable pressure vessels.* International Journal of Hydrogen Energy, 2010. 35(3): p. 1219-1226.

27. Paggiaro, R., P. Bénard, and W. Polifke, *Cryo-adsorptive hydrogen storage on activated carbon. I: Thermodynamic analysis of adsorption vessels and comparison with liquid and compressed gas hydrogen storage.* International Journal of Hydrogen Energy, 2010. 35(2): p. 638-647.
28. Weinberger, B. and F.D. Lamari, *High pressure cryo-storage of hydrogen by adsorption at 77 K and up to 50 MPa.* International Journal of Hydrogen Energy, 2009. 34(7): p. 3058-3064.
29. Zuttel, A. and S. Orimo, *Hydrogen in nanostructured, carbon-related, and metallic materials.* Mrs Bulletin, 2002. 27(9): p. 705-711.
30. Tedds S., W.A., Broom D.P., Book D., *Characterisation of porous hydrogen storage materials: carbons, zeolites, MOFs and PIMs.* Faraday Discussions, 2011. 151: p. 75-94.
31. Jain, I.P., C. Lal, and A. Jain, *Hydrogen storage in Mg: A most promising material.* International Journal of Hydrogen Energy, 2010. 35(10): p. 5133-5144.
32. Li H.W., Y.Y.G., Orimo S., Zuttel A., Jensen C.M., *Recent Progress in Metal Borohydrides for Hydrogen Storage.* Energies, 2011. 4(1): p. 185-214.
33. Cheekatamarla, P.K. and C.M. Finnerty, *Reforming catalysts for hydrogen generation in fuel cell applications.* Journal of Power Sources, 2006. 160(1): p. 490-499.
34. Umegaki T., Y.J.M., Zhang X.B., Shioyama, H., Kuriyama N., Xu Q., *Boron- and nitrogen-based chemical hydrogen storage materials.* International Journal of Hydrogen Energy, 2009. 34(5): p. 2303-2311.
35. Francoise Rouquerol, L.R.a.K.S., *Adsorption by Powders and Porous Solids. Principles, Methodology and Applications.* Academic Press, 1999.
36. Jordá-Beneyto M., S.-G.F., Lozano-Castelló D., Cazorla-Amorós D., Linares-Solano A., *Hydrogen storage on chemically activated carbons and carbon nanomaterials at high pressures.* Carbon, 2007. 45(2): p. 293-303.
37. Chen H., W.H., Xue Z., Yang L., Xiao Y., Zheng M., Lei B., Liu Y., Sun L, *High hydrogen storage capacity of rice hull based porous carbon.* International Journal of Hydrogen Energy, 2012. 37(24): p. 18888-18894.
38. Ting, V.P., Ramirez-Cuesta A.J., Bimbo N., Sharpe, J.E., Noguera-Diaz A., Presser V., Rudic S., Mays, T.J., *Direct Evidence for Solid-like Hydrogen in a Nanoporous Carbon Hydrogen Storage Material at Supercritical Temperatures.* ACS Nano, 2015.
39. Zeiger M., J.N., Aslan M., Weingarth D., Presser V., *Understanding structure and porosity of nanodiamond-derived carbon onions.* Carbon, 2015. 84: p. 584-598.
40. Morinubo Endo, S.H., Mildred S. Dresselhaus, *Carbon Nanotubes.* Elsevier, 1996. Carbon, Vol. 33.
41. Wang, L.F. and R.T. Yang, *Molecular hydrogen and spiltover hydrogen storage on high surface area carbon sorbents.* Carbon, 2012. 50(9): p. 3134-3140.
42. Lu, G.Q.Z., X.S., *Nanoporous Materials - Science and Engineering*. 2006. Chapter 12.6, Adsorption in zeolites: p. 18-19.
43. Buschow, K.H.J.C., Robert W.; Flemings, Merton C.; Ilschner, Bernhard; Kramer, Edward J.; Mahajan, Subhash, *Encyclopedia of Materials - Science and Technology, Volumes 1-11 (2008) (pp 9859-9861).* 2008: p. 9859-9861.
44. Lu, G.Q. and X.S. Zhao, *Nanoporous Materials - Science and Engineering*. 2006, World Scientific. p. 18-19.
45. K. S. Park, Z.N., A. P. Cote, J. Y. Choi, R. D. Huang, F. J. Uribe-Romo, H. K. Chae, and M. O'Keeffe and O. M. Yaghi, *Proc. Natl. Acad. Sci. U. S. A.* 2006(103): p. 10186–10191.
46. C. Baerlocher, L.B.M.a.D.H.O., *Atlas of Zeolite Frameworks.* Elsevier, Amsterdam, 2007. 6th edn.
47. Moore, L.S.a.E., *Solid State Chemistry: An Introduction.* Taylor & Francis Group, Boca Raton, 2005.
48. H. W. Langmi, D.B., A. Walton, S. R. Johnson, M. M. Al-Mamouri, J. D. Speight, P. P. Edwards, I. R. Harris and P. A. Anderson,, *J. Alloys Compd.* 2005. 404: p. 637–642.
49. H. W. Langmi, A.W., M. M. Al-Mamouri, S. R. Johnson, D. Book, J. D. Speight, P. P. Edwards, I. Gameson, P. A. Anderson and I. R. Harris,, *J. Alloys Compd.* 2003. 356: p. 710–715.
50. Flanigen E. M., B.J.M., Grose R. W., Cohen J. P., Patton R. L., Kirchner R. M., Smith J. V., *Silicalite, a new hydrophobic crystalline silica molecular-sieve.* Nature, 1978. 271(5645): p. 512-516.
51. Heine, D.T. *http://transition.jacobs-university.de/node/2245. Last accesed 16/06/15*.
52. Chattaraj, P.K., S. Bandaru, and S. Mondal, *Hydrogen Storage in Clathrate Hydrates.* Journal of Physical Chemistry A, 2011. 115(2): p. 187-193.

53. Tsuda T., O.K., Hashimoto S., Sugahara T., Moritoki M., Ohgaki K., *Storage capacity of hydrogen in tetrahydrothiophene and furan clathrate hydrates.* Chemical Engineering Science, 2009. 64(19): p. 4150-4154.
54. David W. I. F., C.S.K., Jones M. O., Aeberhard P. C., Culligan S. D., Pohl A. H., Johnson S. R., Ryan K. R., Parker J. E., Edwards P. P., Nuttall C. J., Amieiro-Fonseca A., *The structure, thermal properties and phase transformations of the cubic polymorph of magnesium tetrahydroborate.* Physical Chemistry Chemical Physics, 2012. 14(33): p. 11800-11807.
55. McKeown, N.B. and P.M. Budd, *Exploitation of Intrinsic Microporosity in Polymer-Based Materials.* Macromolecules, 2010. 43(12): p. 5163-5176.
56. McKeown, N.B.B., P.M., *InEncyclopedia of Polymer Science and Technology*. Wiley: New York, 2009.
57. Ilinitch, O.M.F., V. B.; Lapkin, A. A.; Okkel, L. G.; Terskikh, V. V.; Zamaraev, K., *I.Microporous Mesoporous Mater.* 1999. 31: p. 97–110.
58. C. D. Wood, B.T., A. Trewin, H. J. Niu, D. Bradshaw, M. J. Rosseinsky, Y. Z. Khimyak, N. L. Campbell, R. Kirk, E. Stockel and A. I. Cooper, *Chem. Mater.* 2007. 19: p. 2034–2048.
59. James r. holst, a.t.a.a.i.c., *Porous organic molecules.* Nature Chemistry, 2010.
60. Rowsell, J.L.C. and O.M. Yaghi, *Strategies for Hydrogen Storage in Metal–Organic Frameworks.* Angewandte Chemie International Edition, 2005. 44(30): p. 4670-4679.
61. Song L. F., Z.J., Sun L. X., Xu F., Li F., Zhang H. Z., Si X. L., Jiao C. L., Li Z. B., Liu S., Liu Y. L., Zhou H. Y., Sun D. L., Du Y., Cao Z., Gabelica Z., *Mesoporous metal-organic frameworks: design and applications.* Energy & Environmental Science, 2012. 5(6): p. 7508-7520.
62. J. R. Long and O. M. Yaghi, C.S.R., 2009, 38, 1213–1214.
63. Farha O. K., Y., A.O., Eryazici I., Malliakas C.D., Hauser B.G., Kanatzidis M.G., Nguyen S.T., Snurr R.Q., Hupp J. T., *De novo synthesis of a metal-organic framework material featuring ultrahigh surface area and gas storage capacities.* Nature Chemistry, 2010. 2(11): p. 944-948.
64. Stoeck U., K.S., Bon V., Senkovska I., Kaskel S., *A highly porous metal-organic framework, constructed from a cuboctahedral super-molecular building block, with exceptionally high methane uptake.* Chemical Communications, 2012. 48(88): p. 10841-10843.
65. Dalebrook A.F., G.W.J., Grasemann M., Moret S., Laurenczy G., *Hydrogen storage: beyond conventional methods.* Chemical Communications, 2013. 49(78): p. 8735-8751.
66. Eddaoudi M., K.J., Rosi N., Vodak D., Wachter J., O'Keeffe M., Yaghi O.M., *Systematic design of pore size and functionality in isoreticular MOFs and their application in methane storage.* Science, 2002. 295(5554): p. 469-472.
67. Rowsell, J.L.C. and O.M. Yaghi, *Effects of functionalization, catenation, and variation of the metal oxide and organic linking units on the low-pressure hydrogen adsorption properties of metal-organic frameworks.* Journal of the American Chemical Society, 2006. 128(4): p. 1304-1315.
68. Park K. S., N.Z., Cote A.P., Choi J.Y., Huang R.D., Uribe-Rom, F.J., Chae H.K., O'Keeffe M., Yaghi O.M., *Exceptional chemical and thermal stability of zeolitic imidazolate frameworks.* Proceedings of the National Academy of Sciences of the United States of America, 2006. 103(27): p. 10186-10191.
69. Phan A., D.C.J., Uribe-Romo F.J., Knobler C.B., O'Keeffe M., Yaghi O.M., *Synthesis, Structure, and Carbon Dioxide Capture Properties of Zeolitic Imidazolate Frameworks.* Accounts of Chemical Research, 2010. 43(1): p. 58-67.
70. He M., Y.J.F., Liu Q., Zhong Z. X., Wang H. T., *Toluene-assisted synthesis of RHO-type zeolitic imidazolate frameworks: synthesis and formation mechanism of ZIF-11 and ZIF-12.* Dalton Transactions, 2013. 42(47): p. 16608-16613.
71. Biswal, B.P., T. Panda, and R. Banerjee, *Solution mediated phase transformation (RHO to SOD) in porous Co-imidazolate based zeolitic frameworks with high water stability.* Chemical Communications, 2012. 48(97): p. 11868-11870.
72. Banerjee R., P.A., Wang B., Knobler C., Furukawa H., O'Keeffe M., Yaghi O. M., *High-throughput synthesis of zeolitic imidazolate frameworks and application to CO2 capture.* Science, 2008. 319(5865): p. 939-943.
73. Ruthven, D.M., *Principles of adsorption & adsorption processes.* 1984.
74. Chavan S., V., J.G., Gianolio D., Zavorotynska O., Civalleri B., Jakobsen S., Nilsen M.H., Valenzano L., Lamberti C., Lillerud K.P., Bordiga S., *H2storage in isostructural UiO-67 and UiO-66 MOFs.* Physical Chemistry Chemical Physics, 2012. 14(5): p. 1614-1626.

75. Cavka J.H., J.S., Olsbye U., Guillou N., Lamberti C., Bordiga S., Lillerud K.P., *A new zirconium inorganic building brick forming metal organic frameworks with exceptional stability.* Journal of the American Chemical Society, 2008. 130(42): p. 13850-13851.
76. Valenzano L., C.B., Chavan S., Bordiga S., Nilsen M.H., Jakobsen S., Lillerud K.P., Lamberti C., *Disclosing the Complex Structure of UiO-66 Metal Organic Framework: A Synergic Combination of Experiment and Theory.* Chemistry of Materials, 2011. 23(7): p. 1700-1718.
77. Katz, M.J., et al., *A facile synthesis of UiO-66, UiO-67 and their derivatives.* Chemical Communications, 2013. 49(82): p. 9449-9451.
78. Chui S.S.Y., L.S.M.F., Charmant J.P.H., Orpen A.G., Williams I.D., *A chemically functionalizable nanoporous material Cu-3(TMA)(2)(H2O)(3) (n).* Science, 1999. 283(5405): p. 1148-1150.
79. Ferey G., M.-D.C., Serre C., Millange F., Dutour J., Surble S., Margiolaki, I., *A chromium terephthalate-based solid with unusually large pore volumes and surface area.* Science, 2005. 309(5743): p. 2040-2042.
80. Streppel, B. and M. Hirscher, *BET specific surface area and pore structure of MOFs determined by hydrogen adsorption at 20 K.* Physical Chemistry Chemical Physics, 2011. 13(8): p. 3220-3222.

Chapter Three

Materials, Methods and Characterization

3 Materials, Methods and Characterization

3.1 Introduction

This section focuses on the materials and methods used in the thesis and characterization results. An explanation about why those materials were chosen, their synthesis, solvent exchange and activation techniques are presented. Following this, an outline of the equipment, software and methodology used is shown. Then, the model and its variables (such as the definitions of excess, absolute and total), are explained. In the latter, the characterization results (XRD, TGA, ASAP 2020 and HTP-1 pycnometry results) are also presented. The reader can refer to the full results and discussion of the individual experiments grouped in the Supplementary Information files C, D and E.

3.2 Synthesis

Initially, different adsorbents were considered for inclusion in this study. It was decided to only use MOFs because more data at very high pressures were found, as well as showing a wide range of properties, topologies, tunability and high hydrogen uptake. With the intention of both strengthening and widening the validity of the final correlations, as many materials as possible from different topologies were synthesized/obtained from literature.

Data from literature includes several IRMOFs, so more IRMOFs (IRMOF-1, IRMOF-3, IRMOF-8 and IRMOF-10) were synthesized to observe changes of intrinsic properties with materials sharing the same topology and metal cluster (Zn). IRMOF-10 was intended to be synthesized to be added to the correlation. However, after several attempts, only IRMOF-9, its interpenetrated version, was obtained. Furthermore, IRMOF-3 and IRMOF-9 hydrogen adsorption data was not found tested at high pressures and very little IRMOF-9 characterization data was found [1]. IRMOF-8 has data at high pressures in various reports in literature [2-4]. However, the datasets did not fully match, the maximum hydrogen uptake of the material was not found at the tested pressures and little characterization data was found [2-4].

Due to their excellent chemical and thermal resistance and different topologies, ZIF-7 (SOD), ZIF-8 (SOD), ZIF-9 (SOD), ZIF-11 (RHO), ZIF-12 (RHO) and ZIF-CoNIm (RHO) were synthesized to form part of the correlation. By characterizing and testing these materials, it is possible to test the effects on different ZIF topologies (SOD and RHO), different metals (Co and Zn) for hydrogen adsorption and, as previously stated, to widen the range of different MOFs used in the correlation. Also, many ZIFs showed synthesis methodologies at RT, they are easily scalable and show higher yields and lower cost solvents than the DEF/DMF solvothermal protocols. These methodologies had difficulties to remove the DMF, sometimes leading to the collapse of the framework because of the large solvent kinetic diameter (5.2–5.5 Å) when compared to the window size of some ZIFs [5].

UiO-66 and UiO-67 present high hydrogen excess uptakes, excellent thermal stabilities (up to 500 °C), both share the same organic linkers as IRMOF-1 and IRMOF-9 and added another topology and metal (Zr) to the correlation [6]. Also, the hydrogen isotherm data from literature was not high enough to give sensible results when fitting the model.

The MILs show high surface areas, high hydrogen uptakes and reasonable stability (up to 180 and 250 °C) as well as adding two more metals to the correlation (Cr and Al) [7].

This section shows all the synthesized materials and the followed methodologies used in the thesis. A list of the used chemicals, their purity, supplier and a description of the equipment and software used can be found respectively in Supplementary Information A and section 3.2. Note that only successfully synthesized batches were included in the thesis.

IRMOF-1

A slightly modified synthesis from Yaghi's *et al.* patent was done in order to synthesize IRMOF-1 [$Zn_4O(BDC)_3(DEF)_7(H_2O)_3$] [8, 9]. Zinc nitrate hexahydrate (0.3570 g, 1.20 mmol) and terephthalic acid (known as 1,4-benzenedicarboxylic acid or H_2BDC) (0.066 g, 0.20 mmol) was dissolved in 10 mL of DEF at 200 RPMs. The mix was placed in a hydrothermal bomb and heated in in the oven at a constant rate of 2 °C min^{-1} to 105

°C for 20 h and then allowed to cool to room temperature. Slightly yellow crystals were obtained from the three produced batches, which were then filtered by gravity and washed with 3 X 5 mL of fresh DEF. Table 3.1 shows the materials and quantities used for the different batches:

Table 3.1. IRMOF-1 materials quantities used for synthesis of batches 1, 2 and 3.

	DEF (mL)	Zinc nitrate hexahydrate (g)	Terepthalic acid (g)
IRMOF-1 (B1)	10	0.3579	0.0686
IRMOF-1 (B2)	10	0.3619	0.0654
IRMOF-1 (B3)	10	0.3641	0.0664

The crystals were stored in DEF in a desiccator to avoid degradation by air or moisture until they were measured in the powder X-ray diffractometer (XRD). After being tested in the powder XRD, samples were merged and solvent exchanged twice with $CHCl_3$ to solvent-exchange the DMF. After one day, the sample was solvent-exchanged again and left under $CHCl_3$ stand for at least 48 h. After that, the samples were dried at room temperature and vacuum (around 200 mbar) for 2 h, enough to dry the $CHCl_3$, trying to avoid any degradation of the crystals.

C_{60} IRMOF-1

A modified synthesis from Yaghi's patent was done in order to synthesize IRMOF-1 C_{60} [8]. 2 mL of DCB (dichlorobenzene) were added to a teflon liner with 0.0500 g of C_{60} in order to dissolve the C_{60}. After that, 8 mL of DEF were added to the mix, followed by 0.0665 g of terepthalic acid (0.400 mmol) and 0.357 g of zinc nitrate hexahydrate. The final mix was stirred at room temperature overnight in order to try to dissolve as much C_{60} as possible. Finally, the 2 prepared batches were put in the oven at 100 °C for 20 hours. Table 3.2 shows the materials and quantities used for the different batches:

Table 3.2. Synthesis materials and quantities for IRMOF-1 C_{60} batches 1 and 2.

	DCB (mL)	DEF (mL)	C_{60} (g)	Zinc nitrate hexahydrate (g)	Terepthalic acid (g)
IRMOF-1 C_{60} (B1)	2	8	0.0502	0.3573	0.0668
IRMOF-1 C_{60} (B2)	2	8	0.0502	0.3578	0.0669

The samples were left to cool down to room temperature and the mother liquor was decanted and washed with DCB (10 mL) and DEF until only the orange/brown crystals (IRMOF-1 C_{60}) remained. The crystals from both batches were stored in DEF in a desiccator to avoid degradation by air or moisture until they were tested in the powder XRD. After being tested in the powder XRD, both samples were merged and solvent exchanged with CCl_4 three times over a period of 48 h. The sample was transferred to an ASAP 2020 tube by using $CHCl_3$ to avoid losses and dried in the oven at RT under vacuum before they were tested.

IRMOF-3

IRMOF-3 [$Zn_4O(NH_2\text{-}BDC)_3(DEF)_7$] was made using the synthesis from Yaghi's patent [8, 9]. Zinc nitrate hexahydrate (0.1790 g, 0.600 mmol) and 2-aminotherephthalic acid (0.0360 g) was dissolved in 9 mL of DEF and 3 mL of ethanol at 200 RPMs. The mix was placed in a hydrothermal bomb and put in the oven at a constant rate 2° C min^{-1} to 105° C for 20 h and it was allowed to cool to room temperature. Yellow crystals were obtained from the produced batches, which were then filtered by gravity and washed with 3 X 5 mL of fresh DEF. Batches 1 and 2 were used for nitrogen characterization and the later synthesized batches 3, 4 and 5 were tested in the HTP-1 because of sample degradation. Table 3.3 shows the materials and quantities used for the different batches:

Table 3.3. IRMOF-3 materials quantities used for synthesis of batches 1 to 5.

	DEF (mL)	Ethanol (mL)	Zinc nitrate hexahydrate (g)	2-Aminoterephthalic acid (g)
IRMOF-3 (B1)	9	3	0.1706	0.0367
IRMOF-3 (B2)	9	3	0.1803	0.0370
IRMOF-3 (B3)	9	3	0.1634	0.0364
IRMOF-3 (B4)	9	3	0.1583	0.0378
IRMOF-3 (B5)	9	3	0.1580	0.0361

The crystals from both batches were stored in DEF in a desiccator to avoid degradation by air or moisture until they were tested in the powder XRD. After being tested in the powder XRD, samples were merged. The samples were solvent exchanged with $CHCl_3$ three times over a period of 48 h. The sample was transferred to an ASAP 2020 tube by using $CHCl_3$ to avoid losses and dried in the oven at RT under vacuum before they were tested.

IRMOF-8

IRMOF-8 [$Zn_4O(2,6\text{-}NDC)_3(DEF)_6$] was made using the synthesis from Yaghi's patent [8, 9]. Zinc nitrate hexahydrate (0.125 g, 0.42 mmol) and 2,6-naphtalene dicarboxylic acid (0.012 g, 0.055 mmol) were dissolved in 10 mL of DEF at 200 RPM. The mix was placed in a hydrothermal bomb and left to stand for 48 h at RT. A very small amount of transparent crystals were obtained from the two batches, which were then filtered by gravity and washed with 3 X 5 mL of fresh DEF. Table 3.4 shows the materials and quantities used for the different batches in the first successful syntheses:

Table 3.4. IRMOF-8 materials quantities used for synthesis, first successful synthesized batches 1 and 2.

	DEF (mL)	Zinc nitrate hexahydrate (g)	2,6-Naphtalene dicarboxylic acid (g)
IRMOF-8 (B1)	10	0.1248	0.0121
IRMOF-8 (B2)	10	0.1283	0.0125

The batches were flushed twice with $CHCl_3$ to solve exchange the DMF and left for another day to change the $CHCl_3$ again and then let it stand for at least 48 h. These crystals decomposed, because the $CHCl_3$ dried out, exposing the samples to air and moisture.

Due to the very low yield obtained from previous synthesis and since the reaction occurs at room temperature, it was thought of scaling the reaction up, maintaining the same molar ratio, in a 150 mL Fisher glass bottle. The scaled synthesis consisted of mixing 0.0600 g (0.275 mmol) of 2,6-naphtalene dicarboxylic acid and 0.625 g (2.1 mmol) of zinc nitrate hexahydrate in 50 mL of DEF. The mix was stirred in a hotplate until both substances were fully dissolved. After that, the mix was allowed stand for 7 days at least in several teflon liner autoclaves in an oven at 25 °C. Unfortunately, scaling up did not result in the synthesis of IRMOF-8, even though the molar ratio and synthesis conditions were the same.

Because of this, it was decided to synthesize 9 independent batches following the original synthesis methodology. The mix was placed in a hydrothermal bomb and left to stand for 7 days at room temperature. The transparent crystals were obtained from some of the batches, which were then filtered by gravity and washed with 3 X 5 mL of fresh DEF. After that, powder XRD was performed to confirm the structure. Once this was done, all the batches were merged and solvent exchanged twice with CCl_4 for at least 48 h before degassing the sample [10]. Table 3.5 shows the materials and quantities used for the different successful synthesized batches:

Table 3.5. IRMOF-8 materials quantities used for synthesis, third attempt, obtaining batches 3 to 6.

	DEF (mL)	Zinc nitrate hexahydrate (g)	2,6-Naphtalene dicarboxylic acid (g)
IRMOF-8 (B3)	10	0.1264	0.0113
IRMOF-8 (B4)	10	0.1246	0.0118
IRMOF-8 (B5)	10	0.1265	0.0119
IRMOF-8 (B6)	10	0.1268	0.0122

IRMOF-9

IRMOF-9 [$Zn_4O(BPDC)_3(DEF)_7(H_2O)_4$] was obtained using a modified using the synthesis from Yaghi's patent [8, 9]. Zinc nitrate hexahydrate (0.110 g, 0.42 mmol) and 4,4'-biphenyldicarboxilic acid (0.08 g, 0.03 mmol) was dissolved in 10 mL of DEF at 200 RPMs. The mix was placed in a hydrothermal bomb and put in the oven at a constant rate 2° C min^{-1} at 100 °C for 48 h and it was allowed to cool to room temperature. Crystals were obtained from the two batches, which were then filtered by gravity and washed with 3 X 5 mL of fresh DEF. Table 3.6 shows the materials and quantities used for the different synthesized batches:

Table 3.6. IRMOF-9 materials quantities used for the synthesis of batches 1 and 2.

	DEF (mL)	Zinc nitrate hexahydrate (g)	BPDC (g)
IRMOF-9 (B1)	10	0.1145	0.0807
IRMOF-9 (B2)	10	0.1104	0.0802

The crystals from both batches were stored in DEF in a desiccator to avoid degradation by air or moisture until they were tested in the powder XRD. After being tested in the powder XRD, samples were merged and solvent exchanged with $CHCl_3$ three times over a period of 48 h. The merged sample was transferred to an ASAP 2020 tube by using $CHCl_3$ to avoid losses and dried in the oven at RT under vacuum for 2 h before they were tested.

ZIF-7

ZIF-7 (SOD) ($Zn(C_7H_2N_2)_2 \cdot (H_2O)_3$) was successfully synthesized twice using a scaled-up protocol to ensure enough sample was obtained [5]. In the original synthesis, 0.1200 g (1 mmol) of bIm (benzimidazole) were dissolved in 6.8 g of ethanol. After, the ammonia hydroxide (28–30% aqueous solution, 0.18 g) and the zinc acetate dihydrate (0.1100 g, 0.5 mmol) were added to the mix. The solution was stirred at RT for 3 hours. Because of the scaled up reactions, capped 150 mL Fisher glass containers were used for the synthesis.

The solution presented a white colour, indicating that a white powder was formed. The liquid was decanted and the white powder was introduced into centrifuge beakers with ethanol in order to wash the material, putting the beakers in the centrifuge 3 times during 10 min at 7000 RPMs. The liquid was then decanted and more ethanol was added each time, repeating the washing process 3 times. After this, the powder was left in ethanol for at least 48 hours to solvent exchange the sample. Once this process was done, the content of all the beakers was put in one and introduced in the oven at room temperature and partial vacuum (around 50 mbar) overnight to remove the remaining ethanol. Table 3.7 shows the materials and quantities used for the different synthesized batches:

Table 3.7. ZIF-7 quantities used for batches 1, 2 and 3.

	bIm (g)	Ethanol (g)	Ammonia hydroxide (g)	Zinc acetate dihydrate (g)
ZIF-7 (B1, scaled X3)	0.3600	20.4	0.18	0.3303
ZIF-7 (B2, scaled X4)	0.4805	27.2	0.24	0.4409
ZIF-7 (B3, scaled X4)	0.4800	27.2	0.24	0.4405

ZIF-8

ZIF-8 (SOD) [$(ZnC_8H_{10}N_4)\cdot 3.33(H_2O)$] was successfully synthesized using a protocol obtained from literature [11]. 1.460 g of zinc nitrate hexahydrate (4.91 mmol) were dissolved in 100 mL of methanol at the same time that 3.15 g of 2-methylimidazole (38.36 mmol) were dissolved in another beaker with 100 mL of methanol. Table 3.8 shows the materials and quantities used for the synthesized batch:

Table 3.8. ZIF-8 quantities used for the synthesized batch.

	Zinc nitrate hexahydrate (g)	2-Methylimidazole (g)	Methanol (mL)
ZIF-8 (B1)	1.4660	3.1505	200

After both substances were fully dissolved, they were poured at the same time in another beaker. The resultant solution was stirred for 1 hour, obtaining a white dispersed precipitate. The resulting solution was put into four 50 mL beakers and centrifuged at 7000 RPMs for 10 min. After this, the resultant solid was separated from

the methanol, which was replaced with fresh methanol. The solid was left for 48 hours under the fresh methanol and after that, centrifuged 3 times at 7000 RPMs to ensure complete separation of the solid. The methanol was again replaced with fresh methanol, repeating this process two more times. After this, the methanol was decanted and the white solid was put in one beaker, being washed again with methanol and centrifuged again 3 times at 7000 RPMs before putting it in the vacuum oven under partial vacuum (around 100 mbar) overnight at 60 °C.

ZIF-9

ZIF-9 (SOD) [$Co(C_7H_5N_2)_2 \cdot (H_2O)$] was successfully synthesized twice using a scaled-up protocol to ensure enough sample was obtained [5]. In the original synthesis, 0.1200 g (1 mmol) of bIm (benzimidazole) were dissolved in 6.9 g of ethanol. After that, the ammonia hydroxide (28–30% aqueous solution, 0.18 g) and the cobalt acetate tetrahydrate (0.1250 g, 0.5 mmol) were added to the mix. The solution was stirred at RT for 3 hours. Because of the scaled up reactions, capped 150 mL Fisher glass containers were used for the synthesis.

The solution presented a purple colour, indicating that a purple solid precipitate was formed. The liquid was decanted and the purple powder was introduced into centrifuge beakers with ethanol in order to wash the material, putting the beakers in the centrifuge 3 times during 10 min at 7000 RPMs. The liquid was then decanted and more ethanol was added each time, repeating the washing process 3 times. After this, the powder was left in ethanol for at least 48 hours to solvent exchange the sample. Once this process was done, the content of all the beakers was put in one and introduced in the oven at room temperature and partial vacuum (around 50 mbar) overnight to remove the remaining ethanol. Table 3.9 shows the materials and quantities used for the different synthesized batches:

Table 3.9. ZIF-9 quantities used for the synthesized batches 1 and 2.

	bIm (g)	Ethanol (g)	Ammonia hydroxide (g)	Cobalt acetate tetrahydrate (g)
ZIF-9 (B1, scaled X4)	0.4800	27.7	0.24	0.5009
ZIF-9 (B2, scaled X6)	0.7207	42.7	0.36	0.7501

ZIF-11

ZIF-11 (RHO structure) ($Zn(C_7H_5N_2)_2 \cdot 0.36(C_7H_8)$) was successfully synthesized twice using a scaled-up protocol to ensure enough sample was obtained [5]. In the original synthesis, 0.1200 g (1 mmol) of bIm (benzimidazole) were dissolved in 6.8 g of ethanol. After that, toluene (4.6 g, 50 mmol), ammonia hydroxide (28–30% aqueous solution, 0.18 g) and the zinc acetate dihydrate (0.1100 g, 0.5 mmol) were added to the mix. The solution was stirred at RT for 3 hours. Because of the scaled up reactions, capped 150 mL Fisher glass containers were used for the synthesis.

The solution presented a white colour, indicating that a white powder was formed. The liquid was decanted and the white powder was introduced into centrifuge beakers with ethanol in order to wash the material, putting the beakers in the centrifuge 3 times during 10 min at 7000 RPMs. The liquid was then decanted and more ethanol was added each time, repeating the washing process 3 times. After this, the powder was left in ethanol for at least 48 hours to solvent exchange the sample. Once this process was done, the content of all the beakers was put in one and introduced in the oven at room temperature and partial vacuum (around 50 mbar) overnight to remove the remaining ethanol. Table 3.10 shows the materials and quantities used for the different synthesized batches:

Table 3.10. ZIF-11 quantities used for the synthesized batches 1 and 2.

	bIm (g)	Ethanol (g)	Toluene (g)	Ammonia hydroxide (g)	Zinc acetate dihydrate (g)
ZIF-11 (B1, scaled X3)	0.3605	20.4	13.8	0.18	0.3300
ZIF-11 (B2, scaled X4)	0.4823	27.7	18.4	0.24	0.4399

ZIF-12

ZIF-12 (RHO) ($Co(C_7H_5N_2)_2$) was successfully synthesized twice using a scaled-up protocol to ensure enough sample was obtained [5]. In the original synthesis, 0.1200 g (1 mmol) of bIm (benzimidazole) were dissolved in 4.8 g of methanol. After that, toluene (4.6 g, 50 mmol), ammonia hydroxide (28–30% aqueous solution, 0.06 g, 1 mmol) and the cobalt acetate dihydrate (0.1250 g, 0.5 mmol) were added to the mix. The solution was stirred at RT for 3 hours. Because of the scaled up reactions, capped 150 mL Fisher glass containers were used for the synthesis.

The solution turned purple, indicating the formation of a purple precipitate. The liquid was decanted and the powder introduced into centrifuge beakers with ethanol in order to wash the material, putting the beakers in the centrifuge 3 times during 10 min at 7000 RPMs. The liquid was then decanted and more ethanol was added each time, repeating the washing process 3 times. After this, the powder was left in ethanol for at least 48 hours to solvent exchange the sample. Once this process was done, the content of all the beakers was put in one and introduced in the oven at room temperature and partial vacuum (around 50 mbar) overnight to remove the remaining ethanol. Table 3.11 shows the materials and quantities used for the different synthesized batches:

Table 3.11. ZIF-12 quantities used for the synthesized batches 1 and 2.

	bIm (g)	Methanol (g)	Toluene (g)	Ammonia hydroxide (g)	Cobalt acetate tetrahydrate (g)
ZIF-12 (B1, scaled X3)	0.3602	14.4	13.8	0.18	0.5009
ZIF-12 (B2, scaled X6)	0.7211	27.2	27.6	0.36	0.7502

ZIF-CoNIm (RHO)

ZIF-CoNIm (RHO) ($C_6H_4CoN_6O_4$, empirical formula) was successfully synthesized several times using a scaled-up protocol to ensure enough sample was obtained [12]. In the original synthesis, 0.056 g (0.49 mmol) of 2-nitroimidazole were dissolved in 2.5 mL of DEF, together with 0.072 g (0.24 mmol) of cobalt nitrate ($Co(NO_3)_2 \cdot 6\ H_2O$) in 1.25 mL of DEF. The mix was stirred together in a hydrothermal bomb and heated up to 120 °C to react solvothermally for 14 h. The resulting red liquid was separated and washed by gravity 5 times, separating pink crystals. Table 3.12 shows the materials and quantities used for the different synthesized batches:

Table 3.12. ZIF-CoNIm (RHO) quantities used for the synthesized batches 1 to 5.

	2-nitroimidazole (g)	Cobalt nitrate (g)	DEF (mL)
ZIF-CoNIm (B1) (scaled X2)	0.1102	0.1499	7.5
ZIF-CoNIm (B2) (scaled X2.5)	0.1456	0.1883	12
ZIF-CoNIm (B3) (scaled X2)	0.1133	0.1449	7.5
ZIF-CoNIm (B4)	0.0551	0.0730	3.75
ZIF-CoNIm (B5)	0.0587	0.0749	3.75

Before and after being tested in the powder XRD, the crystals were kept under DEF and washed two times more before they were solvent-exchanged. The crystals were washed 3 times with a mix of acetone and anhydrous methanol (5 + 5 mL) and left for 48 h. After that, the crystals were washed once more and dried at 120 °C under vacuum to activate the samples before testing them.

UiO-66

UiO-66 ($Zr_6O_4(OH)_4(C_8H_6O_4)_6$) was successfully synthesized several times using a modified literature protocol [13]. 0.053 g (0.227 mmol) of $ZrCl_4$ were mixed with 0.034 (0.227 mmol) of 1,4-benzenedicarboxylic acid in 15 mL of DMF rather than 24.9 g (340 mmol) due to the limited capacity of the teflon liners used for the synthesis (15 mL). The chemicals were stirred in a hotplate at 200 RPMs until the solids had fully dissolved. Then, the three prepared solutions were placed in hydrothermal bombs and placed in the oven at 120 °C for 24 h. Table 3.13 shows the materials and quantities used for the different synthesized batches:

Table 3.13. UiO-66 materials and quantities used for the synthesis of batches 1 to 3.

	$ZrCl_4$ (g)	Terepthalic acid (g)	DMF (mL)
UiO-66 (B1)	0.0509	0.0331	15
UiO-66 (B2)	0.0530	0.0345	15
UiO-66 (B3)	0.0530	0.0345	15

UiO-67

UiO-67 [$Zr_6O_4(OH)_4(BPDC)_6$] was successfully synthesized several times using a modified literature protocol [13, 14]. 0.053 g (0.227 mmol) of $ZrCl_4$ were mixed with 0.0549 (0.227 mmol) of 4.4'-biphenyldicarboxilic acid (BPDC) in 10 mL of DMF rather than 24.9 g (340 mmol) due to the limited capacity of the teflon liners used for the synthesis (15 mL). The chemicals were stirred in a hotplate at 200 RPMs until the solids had fully dissolved. Then, the prepared solutions were placed in hydrothermal bombs and placed in the oven at 120 °C for 24 h. Table 3.14 shows the materials and quantities used for the different synthesized batches:

Table 3.14. UiO-67 materials and quantities used for the synthesis of batches 1 and 2.

	ZrCl4 (g)	BPDC (g)	DMF (mL)
UiO-67 (B1)	0.0514	0.0559	10
UiO-67 (B2)	0.0546	0.0554	10

After that, samples were washed with ethanol and put in the centrifuge three cycles of 10 min at 7000 RPMs three times to exchange the DMF. Samples were left standing in ethanol for at least 48 h in total. This ensured the cleanliness of the framework without altering the observed surface area before testing the samples [15].

MIL-101 (Cr)

Two batches of MIL-101 (Cr) {$[Cr_3OH(H_2O)_2O[O_2C\text{-}C6H4\text{-}(CO_2)]_3 \cdot nH_2O$} were synthesized using a modified synthesis from the Ferey's and co-workers' original protocol [7, 16]. Although quantities were maintained, the reaction temperature was changed from 180 °C to 230 °C. For each batch, 0.8000 g of chromium nitrate (III) and 0.3300 g of terepthalic acid and 10 mL of deionised water were placed in the teflon-lined autoclave and stirred until dissolved. After that, the hydrothermal bombs were heated at 230 °C in the oven during 8 hours. The resulting solution was filtered to separate the excess non-reacted terepthalic acid from the synthesized MIL-101 (Cr). The obtained solution was then put in several centrifuge tubes, topping them at the same level with deionised water.

The beakers were then placed on a centrifuge (2 cycles of 15 min at 7000 RPMs), separating the MOF from the deionised water. After that, the water was drained off and put in the vacuum oven at 40 °C for 21 hours at a partial pressure of 200 mbar. Finally, the sample was activated at 180 °C in the oven for 24 hours at full vacuum. Table 3.15 shows the materials and quantities used for the different batches:

Table 3.15. MIL-101 (Cr) materials quantities used for synthesis of batches 1 and 2.

	Deonised water (mL)	Chromium (III) nitrate nonahydrate (g)	Terepthalic acid (g)
MIL-101 (Cr) (B1)	10	0.7997	0.3303
MIL-101 (Cr) (B2)	10	0.7998	0.3302

NH_2-MIL-101 (Cr)

Two batches of NH_2-MIL-101 (Cr) $\{[Cr_3OH(H_2O)_2O[O_2C\text{-}C_6H_3(NH_2)\text{-}(CO_2)]_3 \cdot nH_2O\}$ were synthesized using the protocol from Jiang et al. [17]. For each batch, 0.4995 g of chromium nitrate (III) and 0.2260 g of 2-aminotherepthalic acid and 10 mL of deionised water were placed in the teflon-lined autoclave, and stirred for 40 minutes. After that, the hydrothermal bomb was heated at 130 °C in the oven during 24 hours. The solution from the autoclave was transferred into centrifuge tubes and topped up to 50 mL with deionized water and placed in a centrifuge. A cycle of 20 minutes at 7000 RPMs was enough to separate the MOF from the deionised water. After that, the water was poured off.

Subsequently, ethanol was added to the NH_2-MIL-101 (Cr) batches in order to solvent exchange the water and activate the samples. The tubes were then topped up with ethanol for 48 h and centrifuged 3 times for 15 minutes at 7000 RPMs to ensure the process. The ethanol was then poured off and the centrifuge tubes were put in the oven at RT and partial pressure (0.2 bar) overnight to dry the sample. Table 3.16 shows the materials and quantities used for the different batches:

Table 3.16. NH_2-MIL-101 (Cr) materials quantities used for synthesis for batches 1 and 2.

	Deonised water (mL)	Chromium (III) nitrate nonahydrate (g)	2-Amino terephthalic acid (g)
NH_2-MIL-101 (Cr) (B1)	10	0.4994	0.2260
NH_2-MIL-101 (Cr) (B2)	10	0.4995	0.2260

3.3 Experimental methods

To weigh chemicals and samples, the scales Sartorius BP1215 and TE1245 (Sartorius AG, Goettingen, Germany) were used. A Binder FD 23 series oven (BINDER Inc., Bohemia, USA) was used together with hydrothermal bombs, formed by a 23 mL teflon liner and a stainless steel carcass (Parr Instrument company, Moline, Illinois) for solvothermal synthesis. Powder XRD measurements were done in flat plate mode at 298 K on wet crystalline samples on a Bruker D8 Advance Diffractometer (Cu-Kα radiation, $\lambda = 1.54184$ Å) (Bruker, Billerica, US) with a lynxeye detector at 40 kV and 40 mA. A step size of 0.041 ° s^{-1} (0.0081996 ° $step^{-1}$ with a time per step of 0.2 seconds) was selected. XRD obtained spectra was corrected using Diffract Eva V 16.0 software and compared against the theoretical structures from CIF files obtained from the Cambridge Crystallographic Database (by using Mercury V 3.3 software) to ensure their correct synthesis. To centrifuge samples, a Jouan C4-22 (Thermo Fisher Scientific, Waltham, USA) was used. In order to predegas and activate the samples, a Heraeus Vacutherm vacuum oven (Thermo Fisher Scientific, Waltham, USA) was used. To investigate the thermal stability of the materials, a Setaram TGA 92 16.18 (Setaram, Caluire, France) was employed. Materials were usually tested at a ramp rate of 5 °C min^{-1} using N_2 as carrier gas from 20 to 600 °C. For CO_2 and N_2 adsorption, a Micromeritics ASAP 2020 (Micromeritics Instrument Corporation, Georgia, USA) at 273 and 77 K respectively was used. The BET method consistent with the BS ISO 9277:2010, which uses the consistency criteria reported by Rouquerol was used to measure the experimental surface area of the materials [18, 19]. The microporous and total pore volume of the materials, Dubinin-Radushkevich (DR) and Horvath-Kawazoe (HK) methodologies were used [20, 21]. Pore size distributions (PSD) were calculated using Density Functional Theory (DFT). All these calculations (BET surface area, pore volumes and pore size distributions) were obtained from the analysis of N_2 isotherms

using MicroActive V 1.01 software (Micromeritics Instrument Corporation, Georgia, USA). Experimental hydrogen excess isotherms (measured at 77 K) were collected at equilibrium in a volumetric Hiden HTP-1 sorption analyser using a liquid nitrogen immersion dewar for temperature control and 2 x 10^{-3}, 10^{-2}, 0.1, 1, 100 and 200 bar absolute pressure transducers ranges (Hiden Isochema, Warrington, UK). An AccuPyc 1330 (Micromeritics Instrument Corporation, Georgia, USA) was used for pycnometry measurements on zeolite 13X beads. A Raman Renishaw DM2500M (Renishaw, Gloucester, UK) was used to explore differences between IRMOF-1 and its impregnated version. An Autosorb 1-MP (Quantachrome, Boynton Beach, USA) was used for some of the ZIF gas measurements found on Chapter 8. The non-linear model fittings and calculations were performed on OriginPro 9.1 (OriginLab, Northampton, Massachusetts, USA), with the nonlinear fitting tool based on the Levenberg–Marquardt algorithm [22]. To assess the goodness of the model fittings, the reduced chi-squared test was used [23]. To evaluate the linear fittings from the correlations in Chapter 5, the standard deviation of the residuals (Root-MSE) was used. Using this Root-MSE ensured a correct comparison of linear fittings since the R^2 does not correctly express the results of the fittings that were forced through the origin because of the elimination of the intercept.

3.4 Methodology used for analysing results

This section further explains which methodology was followed to test and analyse the data.

3.4.1 BET surface area

BET (Brunauer, Emmett and Teller) is a method used to calculate/quantify the surface area of materials [18]. The BET method consists on the determination of the amount of adsorbate needed to cover with a monolayer (monomolecular layer) the external surface and the accessible internal pore surfaces of the tested material. The BET method assumes that gas molecules physically adsorb infinitely in layers on a solid, not existing interaction between each adsorbed layer allowing the Langmuir theory can be applied to each layer.

For this purpose, any gas can be used, as long as it is physically adsorbed by weak bonds to the surface of the material and, at the same time, can be desorbed by decreasing its pressure (at the same temperature as the test was performed). Owing to its boiling point (around 77.3 K), nitrogen is usually the best gas to do the test. If nitrogen is not suitable for a certain material, argon (boiling point of 87.27 K), is usually considered a good alternative (ISO 9277, 2010). The ASAP 2020, was used to calculate this value among others in the tested materials using nitrogen.

3.4.1.1 The BET method

The amount of gas that forms the monolayer can be calculated by applying the BET equation to the adsorption isotherm [24]:

$$\frac{P/Po}{n_a(1-\frac{P}{Po})} = \frac{1}{n_m C} + \frac{C-1}{n_m C}\frac{P}{Po} \qquad \text{Eq.3.1}$$

Where n_a is the specific amount of the absorbed adsorbate (mmol g^{-1}), P and Po are the equilibrium and the saturation pressure of the adsorbate at the temperature of adsorption, P/Po being the relative pressure, n_m the monolayer adsorbed gas quantity (mmol g^{-1}) and C the BET constant (dimensionless).

From the BET test, P/Po and n_a are known and, using Eq. 3.1, a plot can be obtained. The resulting plot should be a straight line type $y = a + bx$, were a, the origin ordinate, must be positive. The slope of the plot, b, can also be calculated by linear regression. Once a and b are calculated, the monolayer amount n_m and C, can also be calculated. The specific surface area per mass (m^2 g^{-1}) of the sample is then calculated by using the following equation:

$$BET_{specific} = n_m \, L \, a_m \qquad \text{Eq.3.2}$$

Where L is the Avogadro constant (6.022×10^{23} mol^{-1}) and a_m the molecular cross-sectional area (0.162 nm^2 recommended for N_2 at 77.3 K).

Note that according the ISO, the BET method is only valid for adsorption isotherms of type II and IV. This is typical of mesoporous solids (pore diameter between 2 nm and 50 nm). Furthermore, any inaccessible pore will be unable to be measured [24].

3.4.1.2 Surface area of microporous materials

As the BET equation is only applicable to non-porous, macro and mesoporous materials (also depending on their isotherm type), it is strictly not applicable for microporous materials. This means that the BET surface area obtained does not show the real surface area of the material, although it is considered a kind of characteristic or equivalent BET area. In the proposed methodology, several conditions have to be met [24, 25]:

-*C* shall be positive

-Any negative interception on the ordinate of the BET means that the *P*/*P*o range chosen for the BET equation is not valid.

-BET equation range should be limited to the pressure range where the term $n_a(Po-P)$ or $n_a(1-P/Po)$ continuously increases with *P*/*P*o (as shown in Figure 3.1).

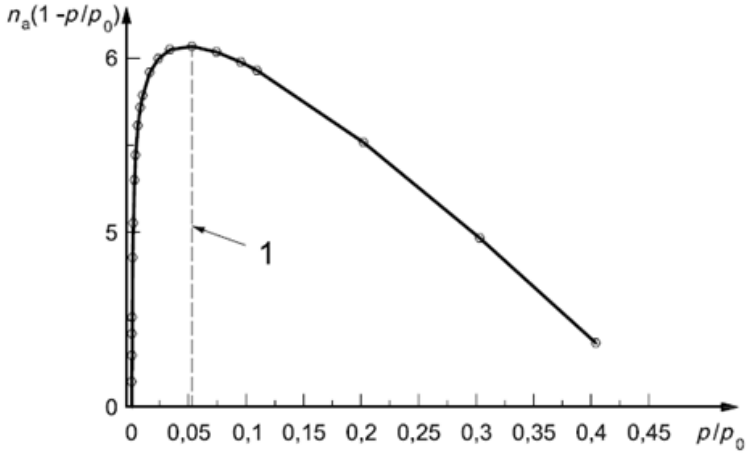

Figure 3.1. Representation of the plot that shows the *P*/*P*o range that can be used for the BET determination of microporous materials (left region to the dotted vertical line).

The settings chosen to calculate the BET have then been chosen according to the most up to date BET ISO (ISO 9277, 2010). The classic 5 point BET determination has also been calculated to help to compare the results with literature.

3.4.1.3 Sample Preparation

According to ISOs 8213 and 14488, samples must be degassed and heated without being degraded. A pressure of approximately 10^{-5} bar or better is stated to be enough. In order to prepare the samples, degassing temperatures were selected from TGA data (Section 3.7 and Supplementary Information E), ensuring the sample would be stable and the framework of the materials would be completely evacuated from possible

contaminants. The maximum degassing pressure available for the equipment, 10^{-6} bar, was used.

3.4.1.4 Measuring method

In this type of test, the amount of gas is introduced into a sample tube, where the adsorption of the gas on the surface and pores of the sample occurs at the adsorption temperature, 77 K. Beforehand, the dead space (space in the sample tube that is not occupied by the sample) must be measured with an inert gas. In the particular case of the ASAP 2020, the free space was measured with He before running the BET analysis. When the BET value comes from a full nitrogen isotherm, the free space was measured after the nitrogen adsorption, in order to avoid He contamination of the sample before measuring the isotherm.

3.4.1.5 Use of reference materials

To make sure the conditions and performance of the device were correct, a reference material was used periodically. For this device, Silica-alumina from the same supplier as the ASAP 2020 (Micromeritics), was used. The ISO considers silica-alumina as a valid reference material. Tests with the reference material were done as stated by the supplier, whose results can be found in Supplementary Information B. From this it was concluded that the ASAP 2020 was correctly calibrated during the period where all the materials were tested/characterized.

3.4.2 Pore volume

Pore volume is another intrinsic property of nanoporous materials. Numerous methodologies exist, which allow to calculate both the total and the micropore pore volumes of the materials. No consensus exists yet of a pore volume methodology especially suitable for metal organic frameworks, which are the materials that form the correlations found in Chapter 4. For the total pore volume, the Horvath-Kawazoe (HK) total pore volume method at 0.99 P/P_o has been used, whereas for the micropore pore volume, the Dubinin-Radushkevich (DR) method has been applied [20, 21]. For some cases, the data has been obtained from literature, always trying to follow the same methodology whenever possible. This approach can bring some uncertainties to this work, since different BET, pore volume and pore size values have been found for the same material in different literature publications. These differences may be due to the

use of different methods/settings to calculate the parameters, inaccuracies during the performance of the tests, impurities, isotherm corrections at high pressures, or different synthesis and/or activation methods. However, HK and DR are recommended for microporous materials, especially for carbons.

3.4.2.1 Total pore volume

As previously stated, in order to calculate the total pore volume (mesopore plus micropore volumes) of a sample, the HK methodology for pore volume was used [20]. This parameter was calculated by using the software Microactive V 1.00. The software calculates the volume accumulated according to an increase in N_2 adsorption by the sample calculated from the experimental PSD. This final value, the total cumulated pore volume is then multiplied by the density of liquid nitrogen as expressed in equation 3.3 [26]:

$$HK\ total\ Vp = V_{CUM}\, D \qquad \text{Eq.3.3}$$

Where *HK total Vp* is the total pore volume of the sample ($cm^3\ g^{-1}$), V_{CUM} is the total cumulative pore volume for points designated for HK calculations ($cm^3\ g^{-1}$) and D is the density conversion factor from the adsorptive properties dialog in ASAP 2020 (0.0015468 cm^3 liquid cm^{-3} STP).

3.4.2.2 Gurvich pore volume

For some materials obtained from literature, the Gurvich rule was applied in order to obtain the total pore volume of the sample. The Gurvich rule states that the pores are filled with a liquid adsorptive of bulk-like properties [27]. This assumption is also taken for the DR method, both of which are based on the Kelvin equation, and on some of the HK and Saito-Foley approaches.

3.4.2.3 Dubinin-Radushkevich pore volume

Dubinin and Radushkevich put forward an equation based on Polanyi's potential theory, which allows the micropore volume to be calculated from the adsorption isotherm. This potential theory considers the existence of a potential field in the surface of a solid in which the adsorbate molecules would "fall" from a point situated at a distance b_i to the surface. The layers would resemble that of the Earth's atmosphere, being more compressed the layers closer to the surface. All the points at a distance *b*

would have the same potential, creating equipotential layers that would delimitate spaces or volumes of adsorption [28].

All of Dubinin's theory is based on Polanyi's briefly described theory. This theory also leads to the assumption that the micropores' volume are filled with adsorbate in the liquid state, being this a physical adsorption process [28].

Dubinin and his collaborators studied the dependence of the porosity of several activated carbons with their grade of activation. They realized that, when considering a wide range of adsorbed quantities, the characteristic curves of different gases over one adsorbent were related. This led them to believe that by multiplying the potential of adsorption corresponding to a volume *V* of the space of adsorption *n* randomly chosen by a constant β, they would be able to get the potential of adsorption of any other adsorbate curve, which led them to the Dubinin-Radushkevich equation in 1935 [26, 28-30]. The characteristic curve of a system is established by plotting the logarithm of the amount adsorbed, *W*, versus $\log^2(1/x)$ (Equation 3.4) [21, 30]. When the basic DR equation is plotted in such logarithmic form, it can be written as:

$$\log(V) = \log(V_o) - \frac{B\,T^2}{\beta}\left[log\,\frac{P_o}{P}\right]^2 \qquad \text{Eq.3.4}$$

Where *V* is the volume adsorbed at equilibrium pressure (cm^3 STP g^{-1}), *V*o the micropore capacity (cm^3 STP g^{-1}), *B* is a constant, *T* the temperature of the analysis (K), *P*/*P*o the relative pressure (dimensionless) and β the affinity coefficient of analysis gas relative to *P*o gas (dimensionless).

Only the linear section of the plotted equation is used for the calculation of the micropore volume (from the intercept). Other parameters such as characteristic energy, equivalent surface area and pore size can also be estimated [21, 30]. The software Microactive V 1.00 was used for the calculation of the DR micropore pore volume.

3.4.3 Pore size distribution

Numerous PSD methodologies exist. From literature, no clear answer emerged about which methodology would be best to apply to MOFs, lacking general consensus. All

the adsorption graphs can be found in Supplementary Information C in case the reader wants to use a different methodology, which looks for consistency.

3.4.3.1 Barrett-Joyner-Halenda

The Barrett, Joyner and Halenda (BJH) is a methodology to calculate the pore size distribution based on a model that considers the adsorbent as a collection of cylindrical pores. BJH does all the calculations based in a desorption model, regardless of whether adsorption or desorption data have been used [26].

The model assumes that the pores are filled with condensed liquid nitrogen, where three zones can be observed (Figure 3.2): the core, the adsorbed layer and the walls of the cylindrical pore [26]. All the liquid nitrogen is assumed to evaporate from the core at the same point, this being related to a critical pressure defined by the Kelvin equation. The second zone, the adsorbed layer, is formed of adsorbed nitrogen that desorbs step by step with each pressure step. The thickness of the adsorbed layer and relative pressure is determined by the thickness equation. The last zone is the walls of the cylindrical pore, whose diameter is needed to determine the pore volume and area. However, the end area of the pore is not considered [26].

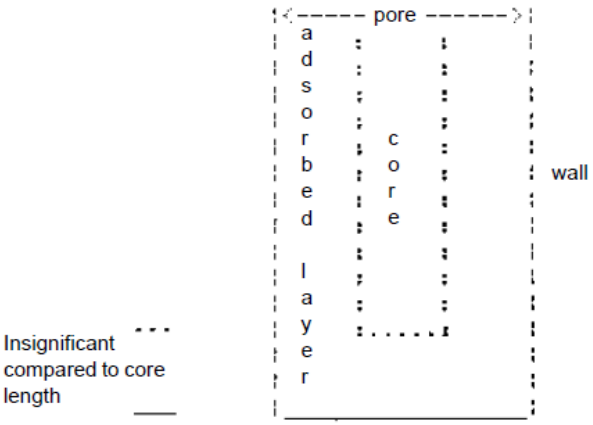

Figure 3.2. Cylindrical pore according to the BJH assumption. Reprinted from [26], with permission from Micromeritics. Copyright 2012.

Therefore, at a particular relative pressure, pores of a certain pore size will lose the condensed liquid adsorbate from the core (determined by the Kelvin equation). The adsorbed layer from these pores that has just lost the condensed liquid will still remain, and its thickness will decrease with decreases in pressure (calculated from decreases of pressure by using the thickness equation). In every desorption step, the condensed core

of pores of a certain pore size are lost, on top of the thickness of the adsorbed layer in bigger pores, which decreases [26, 31].

3.4.3.2 Density Functional Theory

The DFT (Density Functional Theory) method is a series of specific models that assume that the overall isotherm is a weighted average of a set of individual pore adsorption isotherms. By modelling individual pore geometry isotherms as well as their total pore volumes, a pore size distribution is possible to be obtained from the experimental adsorption isotherm [32]. The DFT models are created by classical approaches to adsorption as well as models based on modern statistical thermodynamics. Density functional theory is a practical alternative to molecular dynamics and Monte Carlo simulations, which are used as reference methods since their results are considered exact. These simulations can be used to determine the distribution of gas molecules in a system in equilibrium [26].

In molecular dynamics, position and speed of individual gas particles are calculated for short time intervals. The methodology accounts for the interaction forces between gas particles and a gas particle-simulated surface. By calculating the concentration of the particles both close and far from the surface, the amount of gas adsorbed in the surface can be calculated. Although the calculations involved are simple, the significant amount of calculations needed for a system of a few hundred particles require very fast computers [26].

With the Monte Carlo simulations, the equilibrium of a system is determined, starting with an assumption on where the gas particles are. Then, by a process of randomly moving particle per particle to a random distance in a random direction, the system is further “equilibrated” [26]. If the random move results in a configuration of lower total energy, the move is completed and another particle is moved. If the move results in a higher energy system, a probability of the event and a random number between 0 and 1 is generated. Only when the random number is smaller than the calculated probability, the move is accepted. Otherwise, another particle is selected to go through the same process. This process carries on until the system’s energy does not decrease anymore [26]. Monte Carlo simulations need less computational time than molecular dynamics,

giving the same results. However, neither of these simulations gives a practical way to calculate complete isotherms [26].

Density Functional Theory provides an accurate methodology to describe non-homogenous systems using fewer calculations. The modelled system consists of an open pore made of two parallel walls separated by a certain distance, immersed in the adsorptive at a determined temperature and pressure. The fluid responds to the wall, reaching an equilibrium distribution where the chemical potential of every point is that of the bulk fluid. The bulk fluid has a constant density and its chemical potential is determined by the system's pressure by using well-known equations. However, the density of the fluid near the walls is not constant. At equilibrium, the system has a minimum free energy, known as the grand potential energy (GPE). Calculating the particle density distribution that minimizes the GPE yields the equilibrium density profile. The problem must be solved by using iterative numerical methods and, as previously stated, is not as time-consuming as the other methodologies to calculate isotherm pressure points for a range of pore sizes.

The kernel that defines the pore geometry used for each material was the one that gave the best fitting with the experimental isotherm from the available library in the software Microactive V 1.00. To get the best results from DFT, a regularization value that would give the lowest roughness of distribution was chosen, balancing the increase of the isotherm fit (standard deviation of fit), while maintaining a high goodness of fit. This was easily done by choosing the closest regularization value available after both curves (Error of Fit and Roughness of Distribution) crossed each other, which can be graphically seen in Figure 3.3 for IRMOF-1:

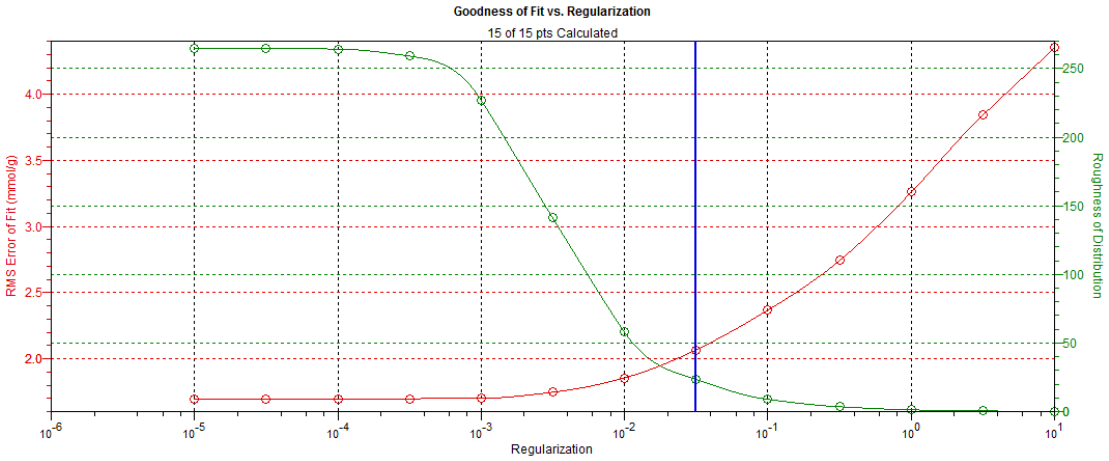

Figure 3.3. Graph indicating regularization values criteria. Regularization values (*X* axis in black), error of the fit values (red curve, left *Y* axis), roughness of distribution (green curve, right *Y* axis) and chosen regularization value (blue horizontal line).

3.4.4 High Temperature Pressure-1 calibration

The HTP-1 (High Temperature Pressure-1) allowed the measurement of hydrogen isotherms with materials at very high pressures that had not been tested before, meaning a correct calibration was of utmost importance. The HTP-1 can be calibrated with regard to dosing pressure, reactor volume and thermostat partition values. The dosing pressure calibration was only needed to be done once, before running all the experiments, ensuring that the volumes dosed were accurately measured. Doing this also calibrated the reactor volume. A detailed explanation and the results of the calibration can be found in Supplementary Information B.

3.5 Sorption model

As previously stated, hydrogen adsorption excess isotherms in solid-state porous materials can be experimentally obtained. However, the total amount stored in them, a quantity of more practical interest, cannot be measured from gas sorption tests. Its interest lies in the fact that a value of the total capacity, unlike excess uptake, takes into account all the hydrogen contained in the material, whether it is adsorbed or not. Adsorption thermodynamics are described by the spreading pressure and pressure tensor of the adsorptive, as well as the surface area of the material. Due to the complex geometry of porous materials, it is not possible to analyse the pressure tensor of the hydrogen [33]. Hence, a model needs to be used to predict the total hydrogen capacity of the materials.

The first coherent adsorption model was proposed by Langmuir in 1918. He introduced his theory of adsorption kinetic point of view in a flat surface. The assumptions of the Langmuir model are [34]:

- Homogeneity of the surface, meaning that the energy of adsorption is constant over all the adsorbent.
- Atoms or molecules are adsorbed at definite localised sites.
- Each site can only accommodate one molecule or atom, meaning that the adsorption is done in a monolayer.

Langmuir considered that a fraction of gas molecules are continuously striking the surface, condensing and held by the surface force until these adsorbed molecules evaporate again. His famous equation, the Langmuir equation, calculates the coverage of adsorbent molecules on a surface in terms of fractional loading θ_A, which depends on pressure at a determined temperature as seen in equation 3.5 [34]:

$$\theta_A = \frac{bP}{1+bP} \qquad \text{Eq.3.5}$$

Where *b* is the affinity constant or Langmuir constant, which relates to the strength of adsorption of the adsorbate to the surface of the adsorbent, which follows an Arrhenius relationship (equation 3.6), known as the Volmer equation [34]:

$$b = Ae^{\frac{Q}{RT}} \qquad \text{Eq.3.6}$$

Where *Q* is the heat of adsorption (kJ mol^{-1}), equal to the activation energy for desorption, *A* is the pre-exponential factor (MPa^{-1}) (related to the entropy and inversely proportional to the square root of the molecular weight), *R* is the molar gas constant (MPa cm^3 K^{-1} mol^{-1}) and *T* is the temperature (K).

A model was developed previously at the University of Bath in order to predict the total hydrogen capacity [35, 36]. The model assumes the absolute amount of hydrogen in the material to follow an IUPAC type I isotherm behaviour (monotonically increasing and getting to an asymptote at high pressures). The model expresses the amount of hydrogen in the pore by using the term fractional filling, θ, which can take values from 0 to 1. 0 Means that the pore is completely empty, while 1 would mean that the pore is completely filled. Research comparing pore filling equations by Bimbo *et al*. gave

justification for the use of the Tóth (which is derived from the Langmuir equation) as the most suitable equation for microporous systems [35, 37].

The Tóth has derived a model based on monolayer adsorption, considering the heterogeneity of the adsorbent where the energy of the sites is no longer equivalent (equation 3.7) [38]:

$$\theta = \frac{bP}{\left[1+(bP)^{c}\right]^{\frac{1}{c}}} \qquad \text{Eq.3.7}$$

In the Tóth equation, *b* is the affinity constant and c is the heterogeneity parameter. This model reduces to the Langmuir model for $c = 1$, which would refer to a homogeneous surface.

Due to the assumption of constant density that occupies a volume that increases according to a type I equation, the equations used to define the excess, absolute and total amount of hydrogen, being hydrogen within the particle (n_E, n_A and n_T respectively, shown in equations 3.8, 3.9 and 3.10) are [35, 36]:

$$n_E = (\rho_A - \rho_B)\theta_A V_P \qquad \text{Eq.3.8}$$

$$n_A = \rho_A \theta_A V_P \Leftrightarrow m_E + \rho_B \theta_A V_P \qquad \text{Eq.3.9}$$

$$n_T = \rho_A \theta_A V_P + \rho_B V_P (1-\theta_A) \Leftrightarrow m_E + \rho_B V_P \qquad \text{Eq.3.10}$$

Figure 3.5 shows a 77 K excess isotherm from a MOF (IRMOF-1), presenting the results obtained from modelling:

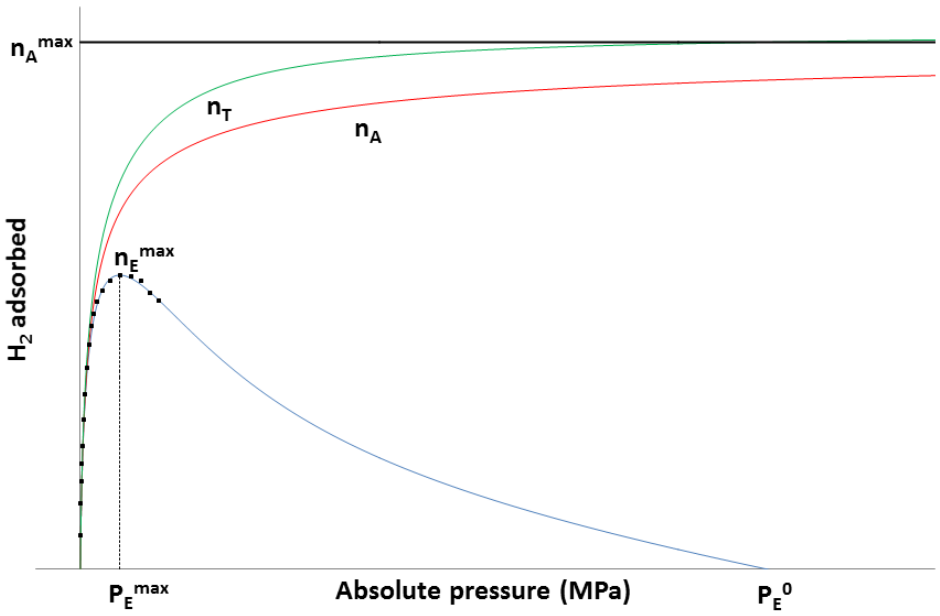

Figure 3.4. IRMOF-1 experimental points (black), excess isotherm (blue), absolute (red) and total (green) modelled isotherms.

Where the black square points are the experimental hydrogen excess points obtained from literature, n_E curve is the fitted excess, n_A is the absolute and n_T is the total hydrogen capacity, obtained from modelling the experimental data. n_E^{max} is the maximum excess uptake value, P_E^{max} is the pressure at which n_E^{max} is obtained, P_E^0 is the pressure at which the excess is 0 and n_A^{max} is the maximum hydrogen capacity of the material. n_A^{max} is obtained when the pore is completely filled (pore filling equal to 1), using equation 3.9 [35].

Excess refers to the total amount of the adsorbate minus the amount of adsorptive that would occupy the adsorbate at the system's temperature and pressure conditions. It is the additional amount of hydrogen contained in the system due to the existing interactions between the adsorbent and the adsorptive. Absolute refers to the amount of adsorbate in the pore and the total refers to the amount of adsorbate plus the amount of non-adsorbed adsorptive gas in the pore at system conditions.

Regarding other hydrogen models, Rodríguez-Reinoso's group proposes equations based on experimental measurements of sample packing density, sample skeletal density and experimental excess to calculate the gravimetric and volumetric total hydrogen capacity of a material [39]. This allowed them to avoid the unknown

parameter V_{ads}, known as the adsorbed phase volume, which is needed to calculate the absolute isotherm and therefore, the storage capacity of a material. The methodology can be applied with any adsorbent under any conditions.

Chahine's group uses a model adapted from Dubinin-Astakhov's to model hydrogen, nitrogen, and methane adsorption isotherms [40, 41]. The model assumes constant microporous adsorption volume, fitting it to experimental isotherms to describe the pore filling of subcritical gas in microporous adsorbents to estimate V_{ads} and therefore obtaining the material's absolute adsorption isotherm.

Dailly's research group at General Motors in the USA also uses a model based on Dubinin-Astakhov's to calculate the absolute, relying on the Dubinin-Astakhov's micropores filling mechanism [42]. However, these equations assume a subcritical adsorptive, meaning that the adsorptive would condense in the pores of the material. A problem arises when using Dubinin equations because of the use of *P*o, which is non-existent at the usual conditions when hydrogen is tested, *i.e.* supercritical conditions. Because of this, Dailly relies on approaches such as the one proposed by Amankwah and Schwarz [5]. The resultant model is fitted to experimental excess isotherms in order to obtain the Dubinin-Astakhov parameters to calculate the absolute hydrogen isotherms.

The model used, developed at the University of Bath was used, does not need to rely on estimates that assume a vapour pressure (like the Dubinin equations), which is inexistent for a supercritical gas. Also, it is based on the experimental excess amounts, being able to calculate the adsorbed density and a total the absolute uptake of the adsorbed gas.

3.5.1 Compressibility factors

In order to understand the relation between variables for hydrogen, a specific equation of state is used. Since hydrogen is not an ideal gas, the classical ideal gas law at high-pressures and/or low temperatures is not suitable for this purpose. For hydrogen, the Leachman's equation of state is the one that fits better and has been subject of improvements [44]. Leachman differentiates between *para*- and *ortho*hydrogen, the

two spin isomers of hydrogen. *Para*hydrogen is the prevalent form at low temperatures, while *ortho*hydrogen is more abundant at higher temperatures.

However, according to Bimbo *et al*., who developed the model, the high number of terms in the equation complicates integration and other different fitting tools [35]. Therefore, a simpler method to calculate the density of the hydrogen as a function of pressure and temperature was needed. In order to do this, data contained in the NIST Chemistry Webbook, which is based on the Leachman EOS, was fitted with a rational function (eq.3.11) to calculate the compressibility factor, *Z* (Figure 3.6). The compressibility factor is fitted using a 4 parameter rational function that depends on the pressure as shown in equation 3.11:

$$Z(P) = \frac{1 + A_1 P + A_2 P^2}{1 + A_3 P + A_4 P^2} \qquad \text{Eq.3.11}$$

By extracting the data from NIST, the obtained values of the four parameters (A1, A2, A3 and A4) for hydrogen at 77 K were:

A1: 0.06727 MPa^{-1} A2: 0.00421 MPa^{-2} A3: 0.10322 MPa^{-1}

A4: 2.90605E-4 MPa^{-2}

The hydrogen density value in the bulk (ρ_B) at those conditions is calculated as seen in equation 3.12:

$$\rho_B\,(P,T) = \frac{1}{Z}\frac{P}{RT} \qquad \text{Eq.3.12}$$

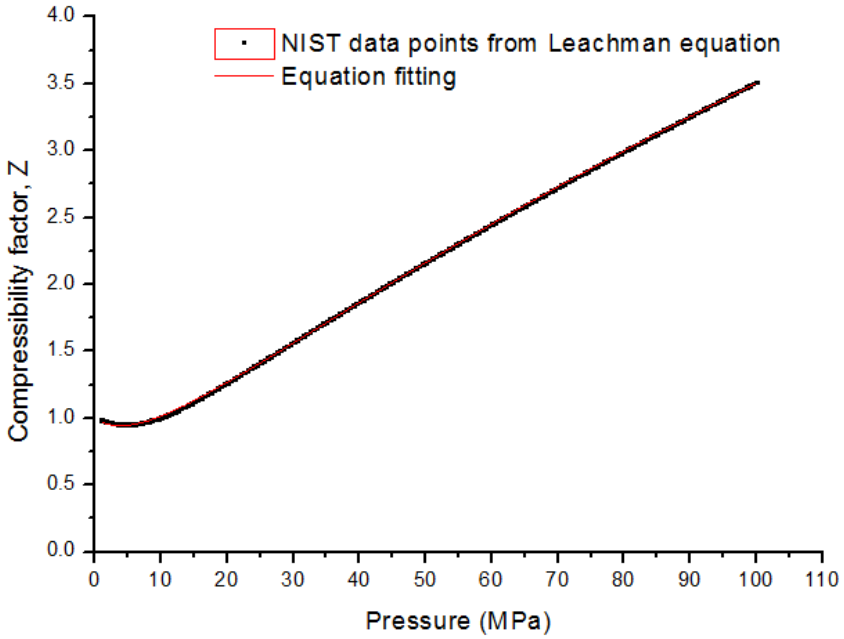

Figure 3.5. Plotted equation to get the parameters to calculate the compressibility factor values up to 100 MPa at 77 K.

3.6 Powder X-Ray Diffraction

X-rays are located in the electromagnetic spectrum, between UV and gamma radiation, having a range of wavelengths from 0.01 to 10 nm [45]. They are usually produced by the rapid deceleration of fast-moving electrons, converting their kinetic energy into a quantum of radiation [40]. X-rays diffraction technique is capable of measuring the space between planes of a material, that is, as a function of the atomic position [45, 46]. The intensity of the diffracted X-rays depend on the atomic species as well as on the atomic arrangement, following Bragg's law (Equation 3.13):

$$2d \sin \Theta = n\lambda \qquad \text{Eq.3.13}$$

where d is the interplanar spacing, Θ is the scattering angle, n is an integer and λ the wavelength of the incident wave [45, 46].

The incident waves can interfere either constructively (in phase) or destructively (phase difference π or out of phase), depending of the phase difference [45]. For each material, depending of its structure, a unique XRD fingerprint is obtained, which can be used to determine the correct synthesis of a material when compared to literature. The XRDs spectra are plotted as Intensity (a.u.) *vs.* 2Θ, being 2Θ the diffraction angle [45].

All the materials were tested and compared with literature and solvent free crystallographic data (CIF files) after being synthesized, showing the materials were synthesized correctly. The second successfully synthesized batches of ZIF-7, ZIF-9, ZIF-11 and ZIF-12 were sent to San Luis, Argentina because of a collaboration, shown in Chapter 8. IRMOF-1 powder XRD spectra is shown in Figure 3.6, being all of them, discussed and compared with literature in Supplementary Information D.

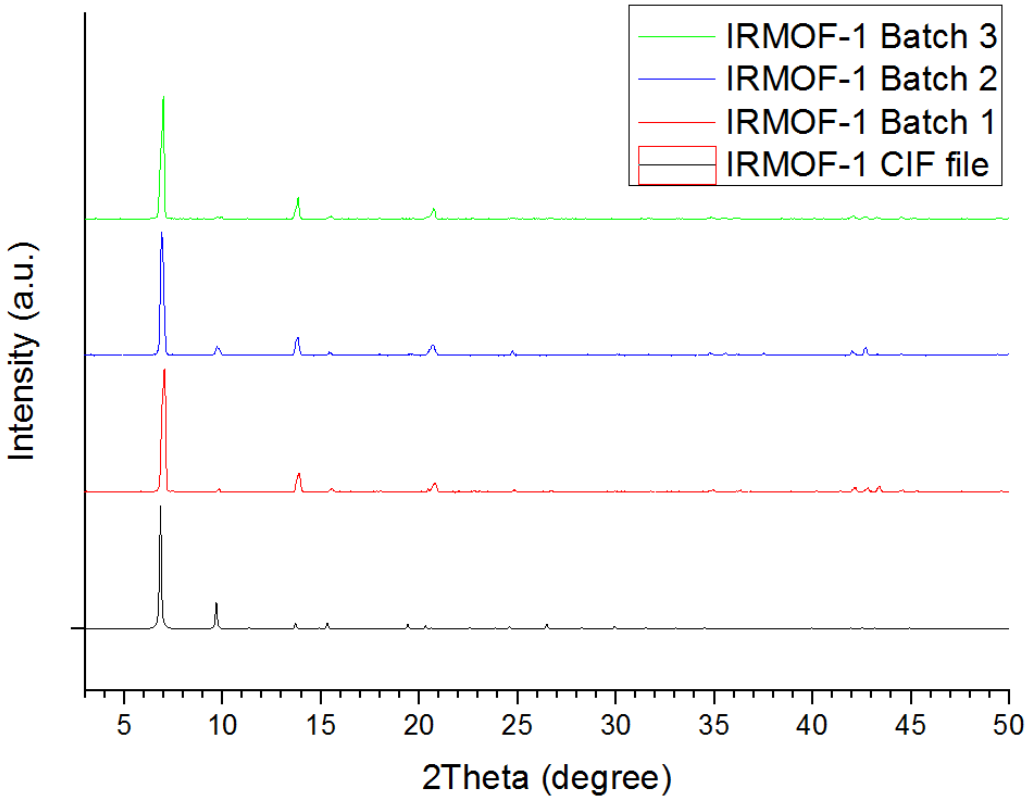

Figure 3.6. PXRD of IRMOF-1. PXRD from CIF file (black) and results from the three synthesized batches (red, blue and green).

Figure 3.6 presents the experimental IRMOF-1 spectra compared with the data from the CIF file, not fully matching in terms of peak intensity, which is also seen in literature [42]. The peak at 10 and 14 2θ are much closer that of literature data as with many of the smaller peaks. All this, together with the fact that the material obtained was also a colourless crystalline material corroborates the successful synthesis of IRMOF-1.

3.7 Thermogravimetric analysis

In this section, the TGA (thermogravimetrical analyser) results are presented. These tests show the thermal stability of the materials, using this data to determine the most suitable settings to degas each sample, avoiding its decomposition or collapse of the structure. In some cases they also serve as a further proof that the material has been synthesized successfully, together with the powder XRD data.

The degassing temperature of the materials was determined by the plateau region observed in the experiments for each material (where the % mass remains constant), indicating no decomposition or contaminants leaving the framework. Nitrogen was chosen as the carrier gas in order to emulate better the degassing conditions (vacuum) rather than air, which could have reacted with the sample. Measurements were done at a heating rate of 5 °C min^{-1}, as a compromise between speed and quality of results obtained, with samples usually tested between 20 and 600 °C. Buoyancy effects were corrected by subtracting results obtained from running tests with empty crucibles under the same settings. Temperatures were used to degas samples in different pieces of equipment (ASAP 2020, HTP-1 and AccuPyc 1330) for times between 6 and 8 h to ensure the materials were fully activated before being tested. Figure 3.7 shows the TGA results of IRMOF-1, being all the experiments and their results discussion in Supplementary Information E. Table 3.17 shows a summary of the degassing conditions chosen for each material based on the processed and analysed TGA results.

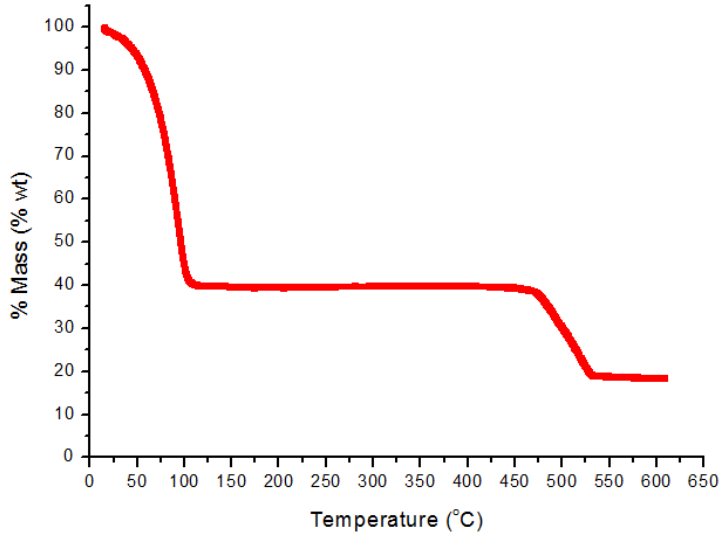

Figure 3.7. IRMOF-1 B1 TGA test from 20 to 600 °C, 5 °C min^{-1} under flowing nitrogen.

Figure 3.7 presents the TGA results of IRMOF-1, showing one step of weight loss of 60 % prior to the final thermal decomposition of the material at around 475 °C. The step of weight loss (20-100 °C) was mostly assigned to the loss of $CHCl_3$ from the solvent exchange, although it might also had other organics that were present in the lab. The lack of further steps of weight loss confirmed the non-existence of DEF in the pores because of the solvent exchange process. IRMOF-1 showed a stability plateau in the range of 100-475 °C, being the decomposition temperature the same as found in literature [52].

Table 3.17. Degassing conditions chosen for every material from TGA data analysis.

Material	**Degassing temperature (°C)**	**Material**	**Degassing temperature (°C)**
IRMOF-1	225	**MIL-101 (Cr)**	180
IRMOF-1 C60	140	**NH_2-MIL-101 (Cr)**	180
IRMOF-3	200 (test and literature) [48]	**UiO-66**	300
IRMOF-8	200 [49]	**UiO-67**	300
IRMOF-9	200	**TE3**	350
ZIF-7	200	**TE7_3**	350
ZIF-8	200	**TE7_20**	350
ZIF-9	225	**AX-21**	350
ZIF-11	250	**OLC-1750**	350
ZIF-12	300	**Silicalite ZSM-5**	200
CoNIm (RHO)	200 [12]	**HKUST-1**	250 (test and literature) [12]

3.8 Nitrogen sorption results

Table 3.18 summarizes all the characterization data obtained from nitrogen sorption experiments and literature. BET_1 (calculated following the BET ISO 9277, 2010 as explained in section 3.4.1.2) and pore volume values located in the first row for each were used in the correlations and discussions for each material, adding extra literature values in the following row/s for comparison. BET_2 values were calculated using the standard 5 point BET test (0.05-0.3 *P*/*P*o) so data could be easily compared with literature. Figures 3.8 and 3.9 show the experimental nitrogen isotherm of IRMOF-1 and its PSD from where the data was obtained. The rest of experimental isotherms can be found in Supplementary Information C.

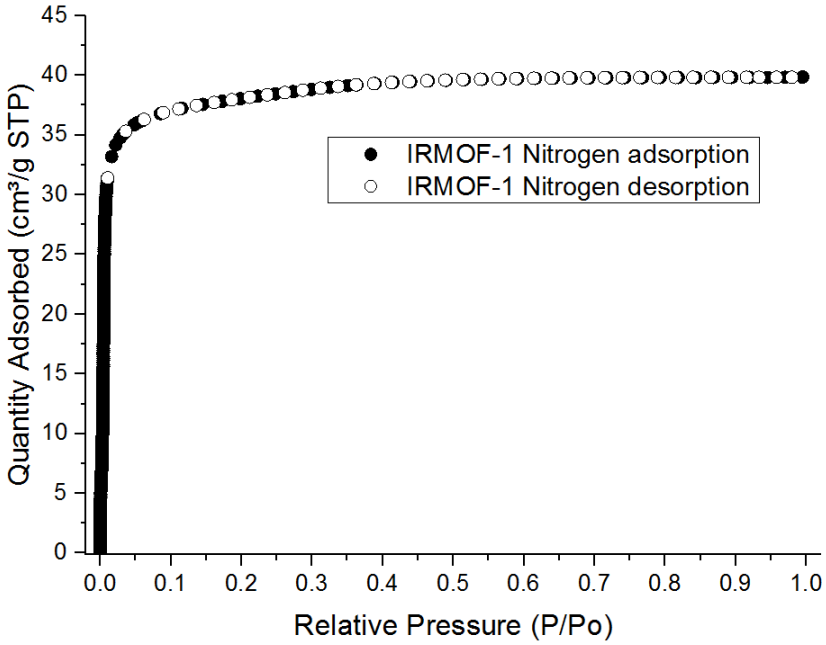

Figure 3.8. IRMOF-1 Nitrogen isotherm at 77 K.

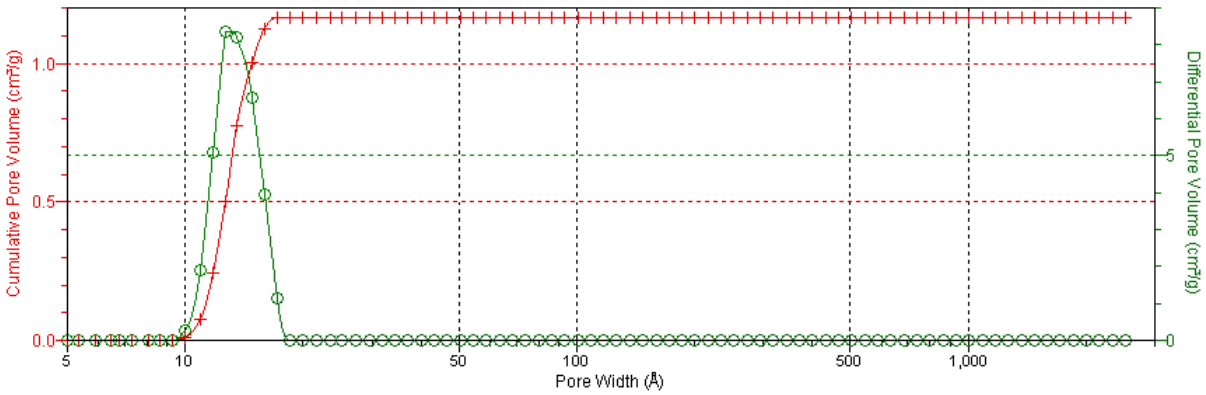

Figure 3.9. IRMOF-1 PSD using the Microactive software (DFT, N_2 slit).

Figure 3.8 shows the nitrogen amount adsorbed by IRMOF-1 at 77 K against its relative pressure, exhibiting a type I isotherm. This gives an indication of microporosity of the material, which can be seen in its PSD (DFT, N_2 slit) in Figure 3.9, indicating only one pore size of 13 Å or 1.3 nm.

Table 3.18. Summary of properties (BET, pore volume and pore diameter) for the different MOFs used.

MOF	BET_1 Surface area ($m^2 g^{-1}$)	Methodology /Reference	BET_2 Surface area ($m^2 g^{-1}$)	Methodology/ Reference	Pore Volume ($cm^3 g^{-1}$)	Methodology/ Reference	Pore Diameter (nm)	Methodology /Reference
IRMOF-1	3444 ± 16	From 4.8E-6 to 0.034 *P*/*P*o. N_2 at 77 K. R^2=0.9999	2703 ± 127	From 0.05 to 0.3 P/Po. N_2 at 77 K. R^2=0.9958	1.38 0.50	N_2 isotherm, total HK method at 0.99 *P*/*P*o N_2 isotherm, DR method	1.3	DFT, slit pore N_2. SDF: 1.85 E-2 mmol g^{-1}
	3534	From 0.02 to 0.1 *P*/*P*o. N_2 at 77 K [50]	-	-	1.13 1.186	N_2 isotherm, Gurvich method [42] MOFormics (software) [46]	1.21 and 1.50 1.215	X-Ray [52] X-Ray [47]
IRMOF-3	1728 ± 14	From 1.23E-5 to 0.046 *P*/*P*o. N_2 at 77 K. R2=0.9999	1234 ± 75	From 0.05 to 0.3 *P*/*P*o. N_2 at 77 K. R^2=0.9949	0.66 0.68	N_2 isotherm Total HK method at 0.99 *P*/*P*o N_2 isotherm, DR method	1.2	DFT, slit pore N_2. SDF: 0.72 mmol g^{-1}
	2163 and 2120	No ranges stated [53]	-	-			4	BJH [54]
IRMOF-6	2804	From 0.02 to 0.1 *P*/*P*o. N_2 at 77 K [50]	-	-	0.993 1.14	N_2 isotherm, Gurvich method [47] N_2 isotherm, DR method [52]	0.97 and 1.5	X-Ray [52]

	2476	BET, methodology not stated. N_2 at 77 K [52]						
IRMOF-8 (RT synthesis)	3285 ± 450	From 9.66-6 to 0.51 *P*/*P*o. N2 at 77 K. R^2=0.9771	4261 ± 249	From 0.05 to 0.3 *P*/*P*o. N_2 at 77 K. R^2=0.9953	2.26 0.85	N_2 isotherm, total HK method at 0.99 *P*/*P*o N_2 isotherm, DR method	1.6 1.6	DFT, slit pore N_2. SDF: 2.83 mmol g^{-1} DFT, cylinder Tarazona NLDFT. SDF: 1.88 mmol g^{-1}
	4461	From 0.05 to 0.08 *P*/*P*o. N_2 at 77 K. [10]	-	-	0.48 0.1911	N_2 isotherm, total pore volume [3] N_2 isotherm, t-plot [3]	1.71 1.1	Ar isotherm and NLDFT fitting [10] Solvothermal method. Ar isotherm and NLDFT fitting [10]
IRMOF-9	1444 ± 14	From 8.52E-7 to 0.049 *P*/*P*o. N_2 at 77 K. R^2=0.9998	1118 ± 54	-	0.59 0.72	N_2 isotherm, total HK method at 0.99 *P*/*P*o N_2 isotherm, DR method	1.2	DFT, slit pore N_2. SDF: 0.15 mmol g^{-1}
							1.45	Cerius2 (1.06 nm pore aperture) [9]

IRMOF-11	1984	From 0.02 to 0.1 *P*/*P*o. N_2 at 77 K [50]	-	-	0.830	N_2 isotherm, Gurvich method [47]	1.58	X-Ray [9]
IRMOF-20	4024	From 0.02 to 0.1 *P*/*P*o. N_2 at 77 K [50]	-	-	1.53	N_2 isotherm, DR method [47]	1.4 and 1.73	X-Ray [47]
	4593	From 0.02 to 0.35 *P*/*P*o. N_2 at 77 K [50]	3409	BET, methodology not stated. N_2 at 77 K [52]				
IRMOF-62	2420	[55]	-	-	0.91	N_2 isotherm, DR method [55]	0.52	Cerius2 [55]
	2550	[56]						
MOF-74	950	From 0.02 to 0.1 *P*/*P*o. N_2 at 77 K [4]	1072	From 0.02 to 0.35 *P*/*P*o. N_2 at 77 K [4]	0.327	N_2 isotherm, Gurvich method [10]	1.1	[47] X-Ray
MOF-177	4746	From 0.02 to 0.1 *P*/*P*o. N_2 at 77 K [50]	4730	From 0.03 to 0.07 *P*/*P*o. N_2 at 77 K [57]	2.65 1.75	N_2 isotherm, total HK method [53] N_2 isotherm, Gurvich method [47]	1.117 1.06	[47] X-Ray [59] N_2 isotherm
MOF-324	1600	[55]	-	-	0.59	N_2 isotherm, DR method [55]	0.76	[55] Cerius2
NH_2-MIL-101 (Al)	2543 ± 63	From 0.05 to 0.3 *P*/*P*o. N_2 at 77 K. R^2=0.9973	-	-	0.77	N_2 isotherm, DR method. Lab data	1.2 and 1.6	Lab data
	2100	From 0.05 to 0.15 *P*/*P*o. N_2 at 77 K [60]						

NH_2-MIL-101 (Cr)	1632 ± 33	From 1.1E-5 to 0.19 *P*/*P*o. N_2 at 77 K. R^2=0.9993	1515 ± 66	From 0.05 to 0.3 *P*/*P*o. N_2 at 77 K. R^2=0.9973	1.35 0.55	N_2 isotherm Total HK method at 0.99 *P*/*P*o N_2 isotherm, DR method	1.2 and 1.6 1.3, 1.5, 2.0 and 2.5	BJH. Experimental data DFT, slit pore N_2. SDF: 0.17 mmol g^{-1}
	2070	From 0.05 to 0.1 *P*/*P*o. N_2 at 77 K. [17]			2.26	N_2 isotherm, total pore volume at 0.99 *P*/*P*o [17]	1.54 and 1.99	[17] BJH
MIL-101 (Cr)	2555 ± 71	From 3.3E-6 to 0.25 *P*/*P*o. N_2 at 77 K. R^2=0.9988	2456 ± 117	From 0.05 to 0.3 *P*/*P*o. N_2 at 77 K. R^2=0.9967	1.78 0.81	N_2 isotherm, total HK method at 0.99 *P*/*P*o N_2 isotherm, DR method	1.2 and 1.6 1.3, 2.2 and 2.7	BJH. Experimental data DFT, slit pore N_2. SDF: 0.30 mmol g^{-1}
	2944	From 0.05 to 0.1 *P*/*P*o. N_2 at 77 K. [61]	2761	From 0.01 to 0.12 *P*/*P*o. N_2 at 77 K. [62]	2.57 1.51	N_2 isotherm, total pore volume at 0.99 *P*/*P*o [61] N_2 isotherm, Gurvich method at 0.95 *P*/*P*o [62]	1.6 and 2.1 0.7, 2.9 and 3.4 1.3 and 2.16	[61] BJH [62] Model data [63] DFT
ZIF-7	1676	Cerius2, single crystal X-ray [64]	1676	Cerius2, single crystal X-ray [64]	0.582	Cerius2, single crystal X-ray [64]	0.43 and 1.46	Cerius2, single crystal X-ray [64]
ZIF-8	1842 ± 68	From 1.13E-5 to 0.024 *P*/*P*o. N_2 at	1306 ± 63	From 0.05 to 0.3 *P*/*P*o. N_2 at 77 K. R2=0.9968	1.63 0.68	N_2 isotherm, total HK method at 0.99 *P*/*P*o	1.2	DFT, slit pore N_2. SDF: 0.78 mmol g^{-1}

		77 K. R^2=0.9979				N_2 isotherm, DR method		
	962	From 9E-3 to 8.4E-2 *P*/*P*o. N_2 at 77 K. R^2=0.9996 [11]			0.36	N_2 isotherm, micropore volume (method not stated) at *P*/*P*o 3.3E-2 [11]		
	1025	N_2 isotherm [65]	-	-	0.75 total 0.61 micro	N_2 isotherm, total pore volume [65] N_2 isotherm, microporous volume [65]	0.352 and 4.43	N_2 isotherm (methodology not stated) [65]
	1947	Cerius2, single crystal X-ray [64]	1947	Cerius2, single crystal X-ray [64]	0.663	Cerius2, single crystal X-ray [64]	11.6	Single crystal X-ray [64]
ZIF-9	1428	N_2 isotherm [66]	-	-	0.12	Single crystal X-ray. Software that evaluates volume accessible to He (using modified UFF parameters) [64, 67]	0.43	Single crystal X-ray [64-66]
ZIF-11	1676	Cerius2, single crystal X-ray [64]	1676	Cerius2, single crystal X-ray [64]	0.582	Cerius2, single crystal X-ray [64]	1.46	Single crystal X-ray [64]
					0.457	PLATON software [68]	1.49	PLATON software [68]
ZIF-12	926	From 2.5E-3 to 0.022 *P*/*P*o. N_2 at	727	From 0.05 to 0.3 *P*/*P*o. N_2	0.54	N_2 isotherm, Gurvich	0.66 and 1.4	HK for spherical pores

		77 K. R^2=0.9974		at 77 K. R^2=0.9957	0.39	method at 0.985 P/Po N_2 isotherm, DR method		
CoNIm (RHO)	1405 ± 40	From 6.62E-7 to 0.047 *P*/*P*o. N_2 at 77 K. R^2=0.9988	1015 ± 64	From 0.05 to 0.3 *P*/*P*o. N_2 at 77 K. R2=0.9946	0.53 0.63	N_2 isotherm Total HK method at 0.99 *P*/*P*o N_2 isotherm, DR method	1.2 and 1.5 1.2	DFT, cylinderpores in pillared clay. SDF: 0.44 mmol g^{-1} DFT, slit pore N_2. SDF: 0.48 mmol g^{-1}
	1858	BET. Range not stated. N_2 isotherm [12]	-	-	0.827	N_2 isotherm, micropore volume at *P*/*P*o = 0.1 [12]	2.23	X-ray single cristal [12]
UiO-66	823 ± 42	From 3.77E-7 to 0.032 *P*/*P*o. N_2 at 77 K. R^2=0.9963	870 ± 25	From 0.05 to 0.3 *P*/*P*o. N_2 at 77 K. R^2=0.9977	0.50 0.44	N_2 isotherm, total HK method at 0.99 *P*/*P*o N_2 isotherm, DR method	0.68 and 0.85 0.6 and 0.77	DFT, slit pore N_2. SDF: 0.24 mmol g^{-1} DFT, cylinder Tarazona NLDFT. SDF: 0.43 mmol g^{-1}
	969	From 0.05 to 0.25 *P*/*P*o. N_2 at 77 K [15]	-	-	0.52 0.43	N_2 isotherm. Total pore volume at *P*/*P*o = 0.97	0.75 and 1.2	DFT, cylinder Tarazona NLDFT.

						Micropore pore volume, T-plot (Harkins and Jura equation) [15]		
UiO-67	1351 ± 40	From 4.3E-7 to 0.035 *P*/*P*o. N_2 at 77 K. R^2=0.9965	1261 ± 62	From 0.05 to 0.3 *P*/*P*o. N_2 at 77 K. R^2=0.9966	0.78 0.67	N_2 isotherm Total HK method at 0.99 *P*/*P*o N_2 isotherm, DR method	1.1 0.62 and 1.0	DFT, slit pore N_2. SDF: 0.50 mmol g^{-1} DFT, cylinder Tarazona NLDFT. SDF: 0.65 mmol g^{-1}
	1877	From 0.05 to 0.25 *P*/*P*o. N_2 at 77 K [15]	-	-	0.95 0.85	N_2 isotherm, total pore volume at *P*/*P*o = 0.97 Micropore pore volume, T-plot (Harkins and Jura equation) [15]	1.2 and 1.6	DFT, cylinder Tarazona NLDFT.
HKUST-1	1343 ± 82	From 7.67E-7 to 0.013 *P*/*P*o. N_2 at 77 K. R^2=0.9949	1822 ± 4	From 0.05 to 0.3 *P*/*P*o. N_2 at 77 K. R^2=0.9999	0.71 0.67	N_2 isotherm, total HK method at 0.99 P/Po N_2 isotherm, DR method	0.46 and 0.85	DFT, slit pore N_2. SDF: 0.45 mmol g^{-1}
			1645	Methodology not stated [64]	0.833	N_2 isotherm, total pore volume [64]	0.57 and 1.1	DFT (desorption) [69]

	1507	BET, methodology not stated. N_2 at 77 K [47]			0.804	N_2 isotherm, DR method [69]		
TE3	1567 ± 21	From 1.2E-7 to 0.059 *P*/*P*o. N_2 at 77 K. R^2=0.9997	1258 ± 66	From 0.05 to 0.3 *P*/*P*o. N_2 at 77 K. R^2=0.9962	0.73 1.24	N_2 isotherm Total HK method at 0.99 *P*/*P*o N_2 isotherm, DR method	5.1, 8.1, 12 and 15	DFT, slit pore N_2. SDF: 0.10 mmol g^{-1}
TE7_20	1234 ± 7	From 2.13 E-6 to 0.049 *P*/*P*o. N_2 at 77 K. R^2=0.9999	1009 ± 45	From 0.05 to 0.3 *P*/*P*o. N_2 at 77 K. R^2=0.9972	0.52 1.33	N_2 isotherm Total HK method at 0.99 *P*/*P*o N_2 isotherm, DR method	5, 6.8, 12 and 15	DFT, slit pore N_2. SDF: 0.15 mmol g^{-1}
OLC-1750	320 ± 2	From 3.5E-6 to 0.33*P*/*P*o. N_2 at 77 K. R^2=0.9999	321 ± 1	From 0.05 to 0.3 *P*/*P*o. N_2 at 77 K. R^2=0.9999	0.13 1.29	N_2 isotherm Total HK method at 0.99 *P*/*P*o N_2 isotherm, DR method	11	DFT, slit pore N_2. SDF: 0.18 mmol g^{-1}
AX-21	2524 ± 47	From 1.13E-6 to 0.16 *P*/*P*o. N_2 at 77 K. R^2=0.9994	2555 ± 28	From 0.05 to 0.3 *P*/*P*o. N_2 at 77 K. R^2=0.9998	1.97 1.82	N_2 isotherm Total HK method at 0.99 *P*/*P*o N_2 isotherm, DR method	5, 6.8, 8.3, 12, 16 and 21	DFT, slit pore N_2. SDF: 0.15 mmol g^{-1}

3.9 HTP-1 density

Table 3.19 shows the pycnometry results obtained in the HTP-1 (Hiden Isochema, Warrington, UK) as part of the data needed to calculate the gravimetric uptake for each of the isotherms. These results can be used in future work together with the correlations to help predicting the properties of the theoretical material that would meet the DOE by, for example, including in the calculations for both the lowest and highest densities of the used materials (1.22 and 2.98 g cm^{-3} respectively) as an initial prediction range of the density of the predicted material (shown in Table 3.19). The error of the balance and HTP-1 when measuring the volume were ± 0.0001 g and ± 0.0004 cm^{-3} respectively. For the material with the highest error (lower measured mass and highest density), NH_2-MIL-101 (Cr), a value of ± 0.07167 g cm^{-3} was obtained, as seen in equation 3.13:

$$Error = \rho \cdot \left(\frac{m_E}{m} + \frac{V_E}{V} \right) = 2.98 \cdot \left(\frac{0.0001}{0.0500} + \frac{0.0004}{0.01677} \right) = 0.07167 \text{ g cm}^{-3} \qquad \text{Eq. 3.13}$$

Where m_E and V_E are the errors of the balance and HTP-1 and m and V the calculated mass and volume of NH_2-MIL-101 (Cr).

Table 3.19. Densities of the MOFs tested in the HTP-1 calculated by using helium pycnometry.

Material	**Density (g cm^{-3})**	**Material**	**Density (g cm^{-3})**
IRMOF-1	1.83	**ZIF-7**	1.40
IRMOF-3	1.70	**ZIF-8**	1.38
IRMOF-8	1.18	**ZIF-9**	1.33
IRMOF-9	1.51	**ZIF-11**	1.34
MIL-101 (Cr)	2.54	**ZIF-12**	1.22
NH_2-MIL-101 (Cr)	2.98	**ZIF-CoNIm**	1.67
NH_2-MIL-101 (Al)	1.22	**HKUST-1**	2.02

3.10 References:

1. Wang, Z.Q., K.K. Tanabe, and S.M. Cohen, *Tuning Hydrogen Sorption Properties of Metal-Organic Frameworks by Postsynthetic Covalent Modification.* Chemistry-a European Journal, 2010. 16(1): p. 212-217.
2. Ardelean, O., Blanita, G., Borodi, G., Mihet, M., Coros, M., Lupu, D., *On the enhancement of hydrogen uptake by IRMOF-8 composites with Pt/carbon catalyst.* International Journal of Hydrogen Energy, 2012. 37(9): p. 7378-7384.
3. Li, Y.W. and R.T. Yang, *Significantly enhanced hydrogen storage in metal-organic frameworks via spillover.* Journal of the American Chemical Society, 2006. 128(3): p. 726-727.
4. Wang, L.F., Stuckert, N. R., Chen, H., Yang, R. T., *Effects of Pt Particle Size on Hydrogen Storage on Pt-Doped Metal-Organic Framework IRMOF-8.* Journal of Physical Chemistry C, 2011. 115(11): p. 4793-4799.
5. He M., Y.J.F., Liu Q., Zhong Z. X., Wang H. T., *Toluene-assisted synthesis of RHO-type zeolitic imidazolate frameworks: synthesis and formation mechanism of ZIF-11 and ZIF-12.* Dalton Transactions, 2013. 42(47): p. 16608-16613.
6. Chavan S., V., J.G., Gianolio D., Zavorotynska O., Civalleri B., Jakobsen S., Nilsen M.H., Valenzano L., Lamberti C., Lillerud K.P., Bordiga S., *H2storage in isostructural UiO-67 and UiO-66 MOFs.* Physical Chemistry Chemical Physics, 2012. 14(5): p. 1614-1626.
7. Ferey G., M.-D.C., Serre C., Millange F., Dutour J., Surble S., Margiolaki, I., *A chromium terephthalate-based solid with unusually large pore volumes and surface area.* Science, 2005. 309(5743): p. 2040-2042.
8. Yaghi, O., Eddaoudi, M., Li, H., Kim, J., Rosi, N., *Isoreticular metal-organic frameworks, process for forming the same, and systematic design of pore size and functionality therein, with application for gas storage*. 2003, Google Patents.
9. Eddaoudi M., K.J., Rosi N., Vodak D., Wachter J., O'Keeffe M., Yaghi O.M., *Systematic design of pore size and functionality in isoreticular MOFs and their application in methane storage.* Science, 2002. 295(5554): p. 469-472.
10. Feldblyum, J.I., A.G. Wong-Foy, and A.J. Matzger, *Non-interpenetrated IRMOF-8: synthesis, activation, and gas sorption.* Chemical Communications, 2012. 48(79): p. 9828-9830.
11. Cravillon, J., Munzer, S., Lohmeier, S. J., Feldhoff, A., Huber, K., Wiebcke, M., *Rapid Room-Temperature Synthesis and Characterization of Nanocrystals of a Prototypical Zeolitic Imidazolate Framework.* Chemistry of Materials, 2009. 21(8): p. 1410-1412.
12. Biswal, B.P., T. Panda, and R. Banerjee, *Solution mediated phase transformation (RHO to SOD) in porous Co-imidazolate based zeolitic frameworks with high water stability.* Chemical Communications, 2012. 48(97): p. 11868-11870.
13. Cavka J.H., J.S., Olsbye U., Guillou N., Lamberti C., Bordiga S., Lillerud K.P., *A new zirconium inorganic building brick forming metal organic frameworks with exceptional stability.* Journal of the American Chemical Society, 2008. 130(42): p. 13850-13851.
14. Larabi, C. and E.A. Quadrelli, *Titration of Zr3(μ-OH) Hydroxy Groups at the Cornerstones of Bulk MOF UiO-67, [Zr6O4(OH)4(biphenyldicarboxylate)6], and Their Reaction with [AuMe(PMe3)]*. European Journal of Inorganic Chemistry, 2012. 2012(18): p. 3014-3022.
15. Chavan, S., Vitillo, J. G., Gianolio, D., Zavorotynska, O., Civalleri, B., Jakobsen, S., Nilsen, M. H., Valenzano, L., Lamberti, C., Lillerud, K. P., Bordiga, S., *H-2 storage in isostructural UiO-67 and UiO-66 MOFs.* Physical Chemistry Chemical Physics, 2012. 14(5): p. 1614-1626.
16. Wang, S., Bromberg, Lev, Schreuder-Gibson, Heidi, Hatton, T. Alan, *Organophophorous Ester Degradation by Chromium(III) Terephthalate Metal–Organic Framework (MIL-101) Chelated to N,N-Dimethylaminopyridine and Related Aminopyridines.* ACS Applied Materials & Interfaces, 2013. 5(4): p. 1269-1278.
17. Jiang, D.M., Keenan, L. L., Burrows, A. D., Edler, K. J., *Synthesis and post-synthetic modification of MIL-101(Cr)-NH2 via a tandem diazotisation process.* Chemical Communications, 2012. 48(99): p. 12053-12055.
18. Brunauer, S., P.H. Emmett, and E. Teller, *Adsorption of Gases in Multimolecular Layers.* Journal of the American Chemical Society, 1938. 60(2): p. 309-319.
19. Rouquerol, J., P. Llewellyn, and F. Rouquerol, *Is the BET equation applicable to microporous adsorbents?* Characterization of Porous Solids Vii - Proceedings of the 7th International Symposium on the Characterization of Porous Solids (Cops-Vii), Aix-En-Provence, France, 26-28 May 2005, 2006. 160: p. 49-56.

20. Horvath, G. and K. Kawazoe, *Method for the calculation of effective pore-size distribution in molecular-sieve carbon.* Journal of Chemical Engineering of Japan, 1983. 16(6): p. 470-475.
21. Dubinin, M.M., *The potential theory of adsorption of gases and vapors for adsorbents with energetically nonuniform surfaces.* Chemical Reviews, 1960 60(2): p. 235-241.
22. Marquardt, D.W., *An algorithm for least-squares estimation of nonlinear parameters.* Journal of the Society for Industrial and Applied Mathematics, 1963. 11(2): p. 431-441.
23. http://www.originlab.com/doc/. *Last checked 08/06/2015.*
24. *Determination of the specific surface area of solids by gas adsorption. BET method.* 2010.
25. Llewellyn, P.L., Rouquerol., J., Rodriguez-Reinoso, F., Seaton, *Is the BET equation applicable to microporous adsorbents?* . Elsevier, 2007. VII: p. 49-56.
26. *ASAP 2020 manual, Micromeritics.*
27. L., G., J. Phys. Chem. (URSS), 1915. 47, 805.
28. Martínez, J.M.M., *Adsorcion fisica de gases y vapores por carbones.* 1990.ISBN: 84-86809-33-9. Legal deposit: A-248-1990. University of Alicante.
29. Dubinin, M.M., *The potential theory of adsorption of gases and vapors for adsorbents with energetically nonuniform surfaces.* Chemical Reviews, 1960. 60(2): p. 235-241.
30. Nguyen, C. and D.D. Do, *The Dubinin–Radushkevich equation and the underlying microscopic adsorption description.* Carbon, 2001. 39(9): p. 1327-1336.
31. Barrett, E.P., L.G. Joyner, and P.P. Halenda, *The determination of pore volume and area distributions in porous substances .1. Computations from nitrogen isotherms.* Journal of the American Chemical Society, 1951. 73(1): p. 373-380.
32. Lastoskie, C., K.E. Gubbins, and N. Quirke, *Pore size distribution analysis of microporous carbons: a density functional theory approach.* The Journal of Physical Chemistry, 1993. 97(18): p. 4786-4796.
33. Myers, A.L. and P.A. Monson, *Adsorption in porous materials at high pressure: Theory and experiment.* Langmuir, 2002. 18(26): p. 10261-10273.
34. Do, D.D., *Adsorption Analysis: Equilibria and Kinetics.* Imperial College Press, 2008. 2: p. 13-24.
35. Bimbo, N., Ting, V.P., Hruzewicz-Kolodziejczyk, A., Mays, T.J., *Analysis of hydrogen storage in nanoporous materials for low carbon energy applications.* Faraday Discussions, 2011. 151(0): p. 59-74.
36. Sharpe, J.E., Bimbo, N., Ting, V. P., Burrows, A. D., Jiang, D. M., Mays, T. J., *Supercritical hydrogen adsorption in nanostructured solids with hydrogen density variation in pores.* Adsorption-Journal of the International Adsorption Society, 2013. 19(2-4): p. 643-652.
37. Bimbo N., S.J.E., Ting, V.P.,Noguera-Díaz, A., Mays, T.J., *Isosteric enthalpies for hydrogen adsorbed on nanoporous materials at high pressures.* Adsorption, 2013: p. 1-12.
38. Toth, J., *State equations of the solid-gas interface layers.* Acta Chimica Academiae Scientiarum Hungaricae, 1971. 69(3): p. 311-328.
39. Casco, M.E., et al., *High-Pressure Methane Storage in Porous Materials: Are Carbon Materials in the Pole Position?* Chemistry of Materials, 2015. 27(3): p. 959-964.
40. Dubinin, M.M. and V.A. Astakhov, *Development of ideas of volume filling of micropores during adsorption of gases and vapours by microporous adsorbents .1. Carbonaceous adsorbents.* Izvestiya Akademii Nauk Sssr-Seriya Khimicheskaya, 1971(1): p. 5-&.
41. Richard, M.A., P. Bénard, and R. Chahine, *Gas adsorption process in activated carbon over a wide temperature range above the critical point. Part 1: modified Dubinin-Astakhov model.* Adsorption, 2009. 15(1): p. 43-51.
42. Poirier, E. and A. Dailly, *Investigation of the Hydrogen State in IRMOF-1 from Measurements and Modeling of Adsorption Isotherms at High Gas Densities.* The Journal of Physical Chemistry C, 2008. 112(33): p. 13047-13052.
43. Amankwah, K.A.G. and J.A. Schwarz, *A modified approach for estimating pseudo-vapor pressures in the application of the Dubinin-Astakhov equation.* Carbon, 1995. 33(9): p. 1313-1319.
44. Leachman, J.W., Jacobsen, R. T., Penoncello, S. G., Lemmon, E. W., *Fundamental Equations of State for Parahydrogen, Normal Hydrogen, and Orthohydrogen.* Journal of Physical and Chemical Reference Data, 2009. 38(3).
45. George H. Stout, L.H.J., *X-Ray Structure Determination. A Practical Guide.* John Wiley & Sons.
46. Y. Waseda, K.S., E. Matsubara, *X-Ray Diffraction Crystallography.* Springer.
47. Millward, A.R. and O.M. Yaghi, *Metal-organic frameworks with exceptionally high capacity for storage of carbon dioxide at room temperature.* Journal of the American Chemical Society, 2005. 127(51): p. 17998-17999.
48. Servalli, M., M. Ranocchiari, and J.A. Van Bokhoven, *Fast and high yield post-synthetic modification of metal-organic frameworks by vapor diffusion.* Chemical Communications, 2012. 48(13): p. 1904-1906.

49. Nguyen, L.T.L., Nguyen, C. V., Dang, G. H., Le, K. K. A., Phan, N. T. S., *Towards applications of metal-organic frameworks in catalysis: Friedel-Crafts acylation reaction over IRMOF-8 as an efficient heterogeneous catalyst.* Journal of Molecular Catalysis a-Chemical, 2011. 349(1-2): p. 28-35.
50. Wong-Foy, A.G., A.J. Matzger, and O.M. Yaghi, *Exceptional H2 saturation uptake in microporous metal-organic frameworks.* Journal of the American Chemical Society, 2006. 128(11): p. 3494-3495.
51. First, E.L. and C.A. Floudas, *MOFomics: Computational pore characterization of metal-organic frameworks.* Microporous and Mesoporous Materials, 2013. 165: p. 32-39.
52. Rowsell, J.L.C. and O.M. Yaghi, *Effects of functionalization, catenation, and variation of the metal oxide and organic linking units on the low-pressure hydrogen adsorption properties of metal-organic frameworks.* Journal of the American Chemical Society, 2006. 128(4): p. 1304-1315.
53. Morris, W., Taylor, R. E., Dybowski, C., Yaghi, O. M., Garcia-Garibay, M. A., *Framework mobility in the metal-organic framework crystal IRMOF-3: Evidence for aromatic ring and amine rotation.* Journal of Molecular Structure, 2011. 1004(1-3): p. 94-101.
54. Yoo, Y. and H.K. Jeong, *Generation of covalently functionalized hierarchical IRMOF-3 by post-synthetic modification.* Chemical Engineering Journal, 2012. 181: p. 740-745.
55. Tranchemontagne, D.J., Park, K.S., Furukawa, H., Eckert, J., Knobler, C.B., Yaghi, O.M., *Hydrogen Storage in New Metal-Organic Frameworks.* Journal of Physical Chemistry C, 2012. 116(24): p. 13143-13151.
56. Peterson, G.W., et al., *Evaluation of MOF-74, MOF-177, and ZIF-8 for the removal of toxic industrial chemicals.* Chemical Biological Center. U.S. Army Research, Development and Engineering Command, 2008.
57. Furukawa, H., M.A. Miller, and O.M. Yaghi, *Independent verification of the saturation hydrogen uptake in MOF-177 and establishment of a benchmark for hydrogen adsorption in metal-organic frameworks.* Journal of Materials Chemistry, 2007. 17(30): p. 3197-3204.
58. Saha, D. and S. Deng. *Hydrogen adsorption properties and structural stability of metal-organic framework (MOF)-177*. in *AIChE Annual Meeting, Conference Proceedings*. 2008.
59. Li, Y. and R.T. Yang, *Gas adsorption and storage in metal-organic framework MOF-177.* Langmuir, 2007. 23(26): p. 12937-12944.
60. Serra-Crespo, P., Ramos-Fernandez, E. V., Gascon, J., Kapteijn, F., *Synthesis and Characterization of an Amino Functionalized MIL-101(Al): Separation and Catalytic Properties.* Chemistry of Materials, 2011. 23(10): p. 2565-2572.
61. Jiang, D.M., A.D. Burrows, and K.J. Edler, *Size-controlled synthesis of MIL-101(Cr) nanoparticles with enhanced selectivity for CO2 over N-2.* Crystengcomm, 2011. 13(23): p. 6916-6919.
62. Streppel, B. and M. Hirscher, *BET specific surface area and pore structure of MOFs determined by hydrogen adsorption at 20 K.* Physical Chemistry Chemical Physics, 2011. 13(8): p. 3220-3222.
63. Lin, K.S., Adhikari, A. K., Su, Y. H., Shu, C. W., Chan, H. Y., *Synthesis, characterization, and hydrogen storage study by hydrogen spillover of MIL-101 metal organic frameworks.* Adsorption-Journal of the International Adsorption Society, 2012. 18(5-6): p. 483-491.
64. Park K. S., N.Z., Cote A.P., Choi J.Y., Huang R.D., Uribe-Rom, F.J., Chae H.K., O'Keeffe M., Yaghi O.M., *Exceptional chemical and thermal stability of zeolitic imidazolate frameworks.* Proceedings of the National Academy of Sciences of the United States of America, 2006. 103(27): p. 10186-10191.
65. Zhang, Z.J., Xian, S. K., Xia, Q. B., Wang, H. H., Li, Z., Li, J., *Enhancement of CO2 Adsorption and CO2/N2 Selectivity on ZIF-8 via Postsynthetic Modification.* Aiche Journal, 2013. 59(6): p. 2195-2206.
66. Li, Q. and H. Kim, *Hydrogen production from NaBH4 hydrolysis via Co-ZIF-9 catalyst.* Fuel Processing Technology, 2012. 100: p. 43-48.
67. Battisti, A., S. Taioli, and G. Garberoglio, *Zeolitic imidazolate frameworks for separation of binary mixtures of CO2, CH4, N2 and H2: A computer simulation investigation.* Microporous and Mesoporous Materials, 2011. 143(1): p. 46-53.
68. Morris, W., He, N., Ray, K. G., Klonowski, P., Furukawa, H., Daniels, I. N., Houndonougbo, Y. A., Asta, M., Yaghi, O. M., Laird, B. B., *A Combined Experimental-Computational Study on the Effect of Topology on Carbon Dioxide Adsorption in Zeolitic Imidazolate Frameworks.* Journal of Physical Chemistry C, 2012. 116(45): p. 24084-24090.
69. Roy, A., Srivastava, AvanishK, S., Beer, S., Dilip, M., T.H., Gutch, P.K., Halve, A.K., *Degradation of sarin, DEClP and DECNP over Cu-BTC metal organic framework.* Journal of Porous Materials, 2013. 20(5): p. 1103-1109.

Chapter Four

Total Hydrogen Capacity Correlations

4 Total hydrogen capacity correlations

4.1 Introduction

In the past, relationships between adsorbent materials and their hydrogen adsorption were researched. Chahine and Bénard were the first that found a relationship between variables, known as the "Chahine rule" [1, 2]. Different microporous activated carbons were tested at 77 K at pressures up to 3.5 MPa, using the maximum uptake values from each isotherm (or close to the maximum value when they were limited by pressure). This obtained linear correlation predicted an increase of 1 wt % per 500 m^2 g^{-1} and a 1 wt % per 0.2 cm^3 g^{-1} of micropore volume.

Different types of microporous carbons, single-walled carbon nanotubes (SWCNTs), multi-walled carbon nanotubes (MWCNTs), polyhedral nanoparticles and activated carbons were tested at 77 K and RT by Panella *et al* [3]. The experimental data obtained were fitted to a Langmuir-type equation (type I isotherm), using the saturation value from each Langmuir fit (defined as "storage capacity"). The results also showed a scattered linear correlation between BET surface area and pore volume with storage capacity at both 77 K and RT. The work of Panella and colleagues concluded that the type of carbon used did not affect hydrogen adsorption, being high surface area and microporosity the desirable properties to obtain high hydrogen uptakes in nanoporous materials. Materials were tested up to 7 MPa, being degassed at 200 °C for only about 2 hours, showing also uncertainties in the experimental isotherms (few isotherm points as well as large error bars).

Gogotsi *et al* also researched possible relationships between hydrogen storage and intrinsic properties of carbide-derived carbons (CDCs) at pressures up to 6 MPa at 77 K [4]. The materials had tuned surface areas, pore volumes and pore sizes. Results showed a highly scattered correlation between hydrogen excess and surface area, pointing out that hydrogen capacity would vary linearly with surface area if the topology and size of the pores was negligible. Some of the tested materials outperformed the "Chahine rule", showing a greater proportion of pores with a diameter lower than 1.5 nm and/or 0.7 nm in their pore size distributions (PSDs). A graph of hydrogen excess per surface area was plotted for each material against their pore size, concluding that pores of 0.6–0.7 nm in diameter yield the highest hydrogen uptake at high pressures and 77 K, as well as indicating that pores larger than 1.5 nm

show little or no contribution. These results claimed the "Chahine rule" not to be universal, meaning that even a material with lower surface area can still achieve higher uptake if it has a larger amount of pores with a lower pore diameter [3, 4].

Thomas compared carbons, silicas, aluminas, metal-organic frameworks and polymer porous materials at cryogenic temperatures, observing scattered linear relations with surface area (in particular for surface areas higher than 1000 $m^2 g^{-1}$) and pore volume [5]. The correlations also indicated that materials with micropore pore volume values lower than 0.8 g cm^{-3} show an adsorbate density in their pores similar that of liquid hydrogen (70.8 kg m^{-3}). However, different methodologies for surface area (such as the BET and t-method) and pore volume needed to be used. Also, hydrogen isotherm data was very limited (0.1 MPa), making difficult the determination of the maximum hydrogen excess for each material. Yaghi and colleagues also found a linear relation between the maximum hydrogen uptake of several metal-organic frameworks at 77 K versus their Langmuir surface areas [6]. Some of these MOFs were used in this work due to the high pressure ranges in which they were measured. However, it was decided to use BET surface area rather than Langmuir because of the multilayer adsorption assumption, rather than the monolayer adsorption assumption that is made with the Langmuir methodology [6].

4.2 Maximum excess and total hydrogen capacity correlations

4.2.1 Hydrogen isotherm results and sorbate-induced gate-opening phenomena

The measured hydrogen excess isotherms are shown in Figures 4.1, 4.2, 4.3 and 4.4, grouped by topologies. Some of the isotherm data was obtained from literature (from Supplementary Information files or Engauge Digitizer V.4.1 (Engauge Digitizer, Sourceforge)) [6, 7]. NH_2-MIL-101 (Al) was synthesized and tested by Ibrahim Ahmet.

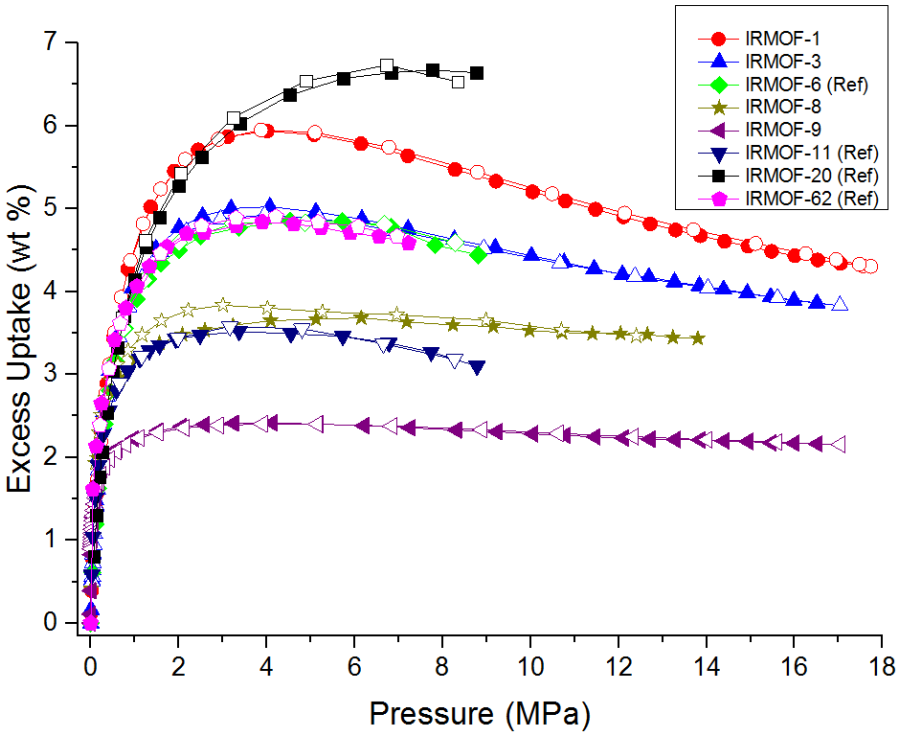

Figure 4.1. IRMOF family excess hydrogen isotherms measured at 77 K. Open symbols represent the desorption isotherms. Isotherm data of IRMOF-6, IRMOF-11, IRMOF-20 and IRMOF-62 was taken from literature [6, 7].

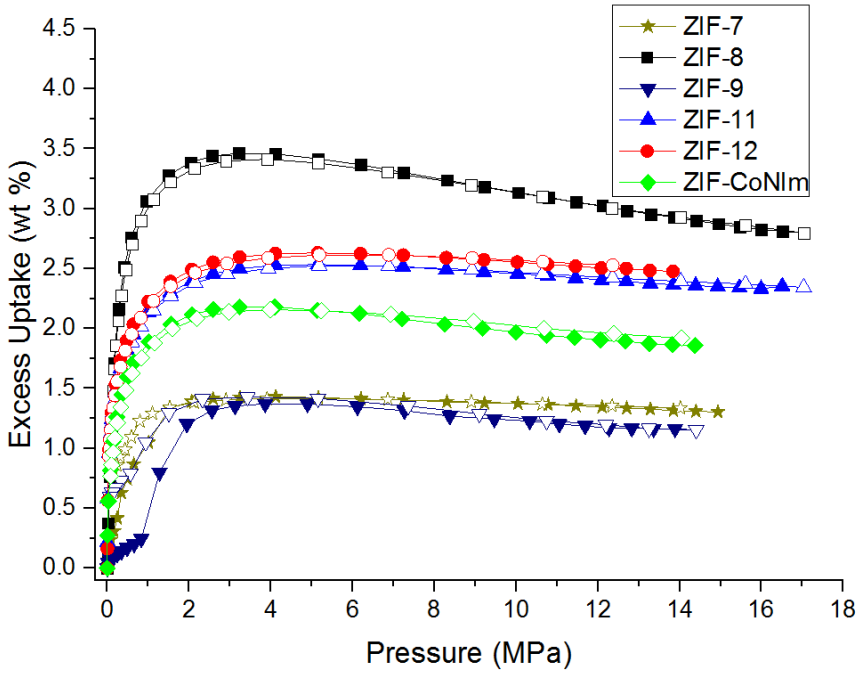

Figure 4.2. ZIF family excess hydrogen isotherms measured at 77 K. Open symbols represent the desorption isotherms.

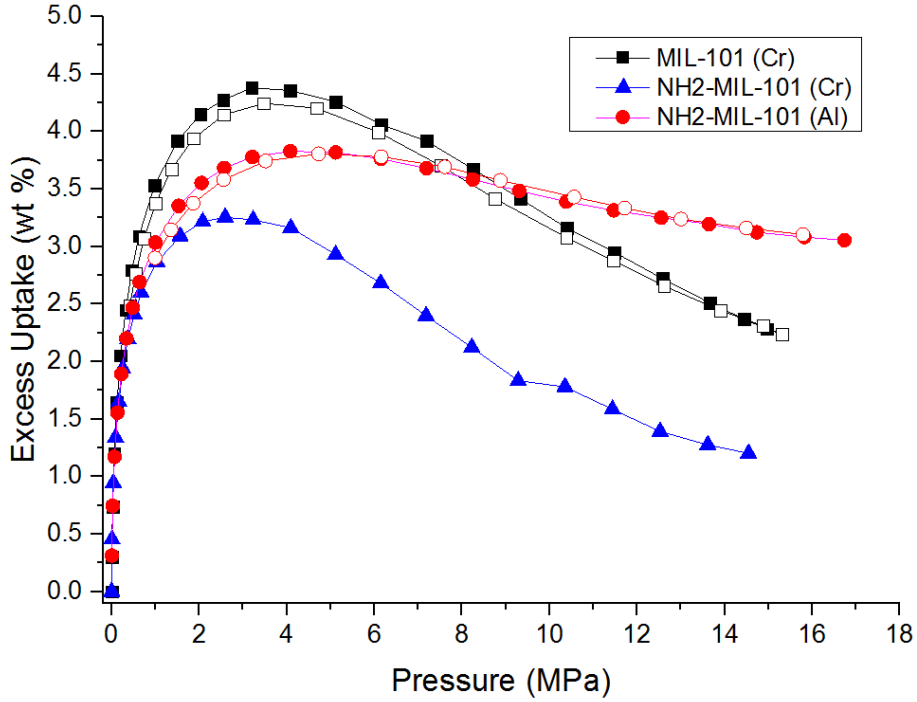

Figure 4.3. MIL family excess hydrogen isotherms measured at 77 K. Open symbols represent the desorption isotherms.

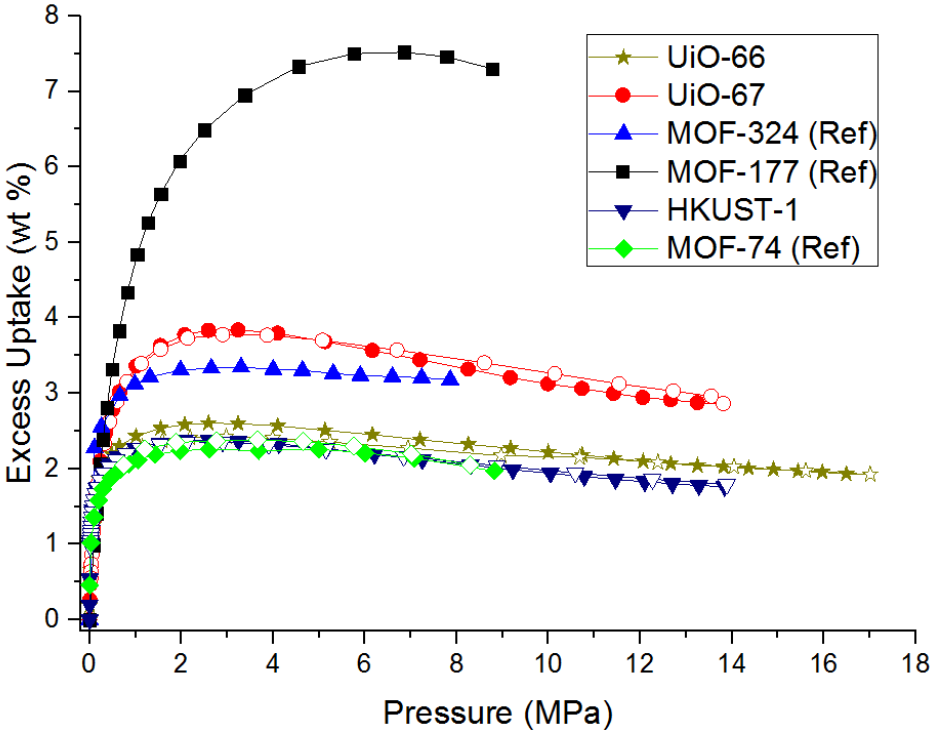

Figure 4.4. UiOs, MOFs and HKUST-1 excess hydrogen isotherms measured at 77 K. Open symbols represent the desorption isotherms. Isotherm data of MOF-324, MOF-177 and MOF-74 was taken from literature [6, 7].

The maximum excess uptake used in the correlations, together with its pressure for each material was taken from Figures 4.1, 4.2, 4.3 and 4.4 is presented in Table 4.1:

Table 4.1. Maximum H_2 excess uptake and its pressure for each of the materials at 77 K.

Material name	Pressure (MPa)	Maximum excess uptake (wt %)	Material name	Pressure (MPa)	Maximum excess uptake (wt %)
IRMOF-1	4.01	5.93	ZIF-7	4.12	1.43
IRMOF-3	4.07	5.02	ZIF-8	3.22	3.46
IRMOF-6	4.53	4.85	ZIF-9	3.86	1.37
IRMOF-8	6.15	3.68	ZIF-11	5.15	2.53
IRMOF-9	4.12	2.41	ZIF-12	5.15	2.63
IRMOF-11	3.37	3.52	ZIF-CoNIm	3.23	2.18
IRMOF-20	7.76	6.67	MIL-101 (Cr)	3.20	4.38
IRMOF-62	3.9	4.84	NH_2-MIL-101 (Cr)	2.59	3.25
MOF-74	4.99	2.26	NH_2-MIL-101 (Al)	4.08	3.82
MOF-177	6.85	7.52	UiO-66	2.59	2.60
MOF-324	3.30	3.34	UiO-67	3.23	3.84
HKUST-1	2.60	2.38			

Figure 4.2 shows all the ZIFs hydrogen excess isotherms. Two materials with an SOD topology, ZIF-7 and ZIF-9, showed unusual hydrogen isotherm shapes at low pressures. ZIF-7 has previously been reported as a flexible material that shows a sorbate-induced gate-opening phenomena, which involves narrow-to-large pore phase transitions [8-10]. This behaviour has been confirmed in CO_2 and C2-C4 alkane/alkaline adsorption isotherms [10, 11]. ZIF-7 and ZIF-9 only differentiate in the nature of the metal cluster they are made of, both showing abnormal isotherm shapes. This indicates that ZIF-9 also presents sorbate-induced gate-opening phenomena from the isotherm results at around 1 MPa and 77 K.

Also, the maximum hydrogen uptakes of both ZIF-7 and ZIF-9 are very similar in value, being 1.43 (at 4.12 MPa) and 1.37 (at 3.86 MPa) wt % respectively. These similitude in values have also been seen in their RHO homologues, ZIF-11 and ZIF-12, showing 2.53 and 2.63 wt % respectively (both at 5.15 MPa). These similar maximum excess results for both topologies

indicates that the nature of the metal used (Co or Zn) does not exert much influence on the hydrogen uptake of the material. Also, the difference in maximum excess uptake between the two forms is almost double in each case.

Figure 4.4 shows a 20 % less uptake in the UiO-67 excess isotherm when compared to literature, still showing the same shape, which has been attributed to sample variability [12]. The in-house synthesized batches present similar XRD patterns and lower BET surface areas from characterization data (N_2 isotherm data at 77 K), being this value 1347 ± 55 m^2 compared to 1877 m^2 obtained from literature (same BET range used, from 0.05 to 0.25 P/Po).

The characterization data from literature and experiments, including the BET ranges and employed methodologies can be found in Chapter 3.

4.3 Correlation analysis and discussion

IRMOF-8 was not used in the correlations due to large error bars in the BET surface area value, obtained from the N_2 PSD. The reason was due to the small amount of sample available, which was obtained from many attempted syntheses that produced very small amounts of material.

In Figure 4.5, the maximum hydrogen excess value of every material is plotted against their BET surface area divided by a thousand. Two linear fits were plotted, not fixing (red line) and fixing (black line) the fit at the origin (x, y = 0). In the graph it can be seen a scattered linear fitting where the maximum hydrogen uptake increases with increasing BET surface area, being the red fitting slightly better than the black one (equations and statistical goodness of fit are also shown in Figure 4.5). A larger degree of scattering exists at low BET ranges, which is believed to be due the different pore volume and PSDs of the materials. Also, IRMOF-3 and IRMOF-9 indicate very high uptakes when compared to their BET values. IRMOF-1 presents a higher uptake and bigger pore diameter (1.3 and 1.2 respectively), differentiating themselves in the linker, which is functionalized in the case of IRMOF-3. These results indicate that the amino group of the functionalized linker slightly reduces the pore size of the material as well as reducing the available area for adsorption, also increasing its weight. IRMOF-9 on the other hand, underperforms when compared to its surface area. This seems to be due to its interpenetrated structure, which adds extra weight and reduces the pore volume, lowering its hydrogen uptake when compared to other materials with the same topology. ZIF-12 shows

higher uptake than expected as well, probably due to the small size of its pores (0.66 and 1.4 nm pore diameter).

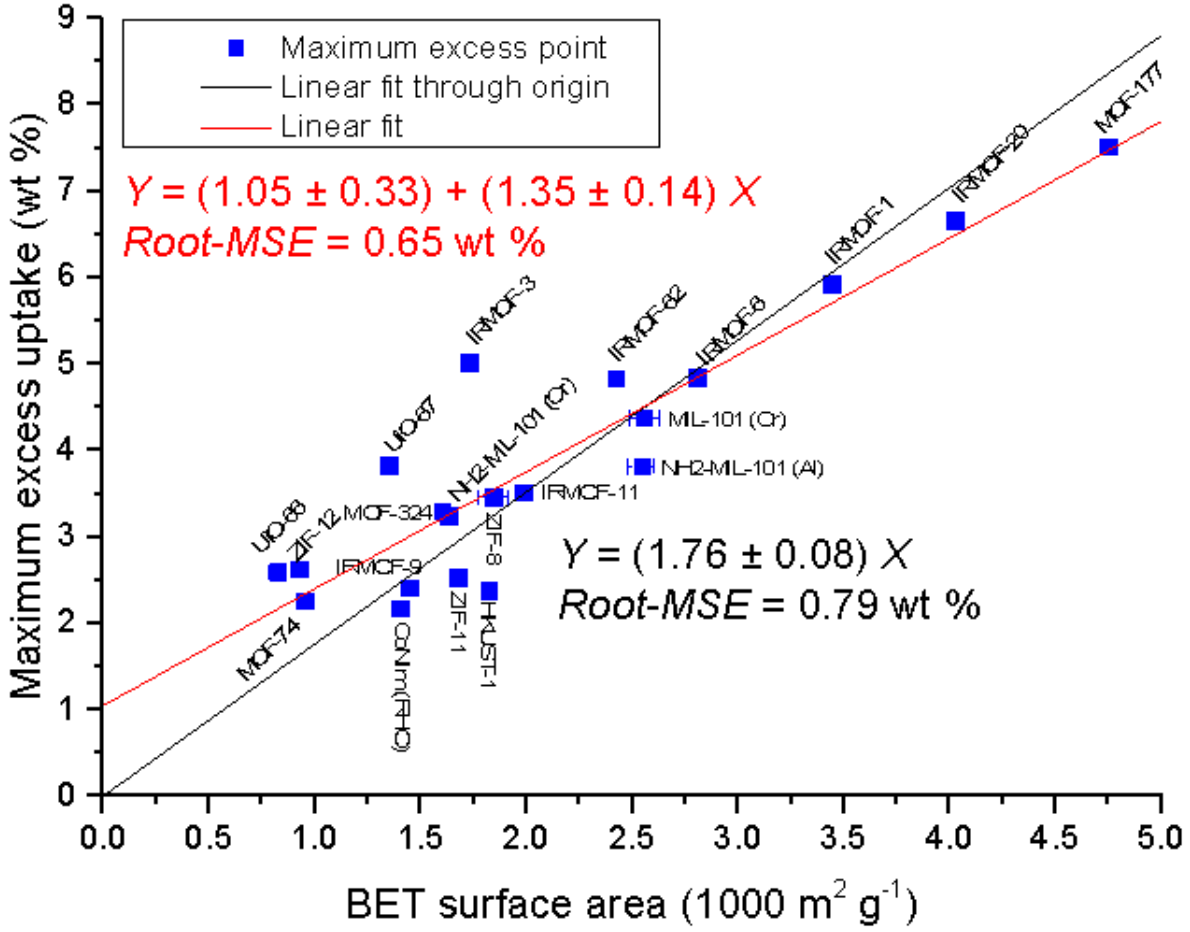

Figure 4.5. Maximum excess uptake of MOFs at 77 K vs BET surface area (N_2 at 77 K) per 1000 m^2 g^{-1}. Error bars represent the standard error obtained from the BET calculation. Errors from excess uptake measurements are within the size of the symbol. Upper equation (in red) corresponds to the fitting of the red line and the lower equation (in black) corresponds to the fitting of the black line.

In Figure 4.6, the micropore pore volume (DR methodology) from both in-house experiments and literature has been plotted against their maximum excess uptake. Figure 4.6 shows a highly scattered relation between variables with low correlation values (Root-MSEs of 1.2 and 1.1 wt % respectively), especially due to IRMOF-1 and IRMOF-3. An increase in the maximum uptake can be seen with increasing micropore volume, also found in the mentioned previous publications with activated carbons [1, 2, 5]. Also, the ideal pore size for maximal attraction of an adsorbate has been reported to be the same as its kinetic diameter, stating the influence of pore size for hydrogen adsorption [13]. The high scattering in Figure 4.6 is believed to be because the micropore volume values neglect the influence of pore sizes. The same applies to

their surface area relations (Figure 4.5), whose absolute values are higher, adding more dispersion to the micropore volumes relation in Figure 4.6. A similar reasoning explains the scattering in Figure 4.7, since the total pore volume is considered the same way, not taking into account any contribution from the micropores or the surface area of each material (Root-MSEs of 0.99 and 1.35 wt % respectively).

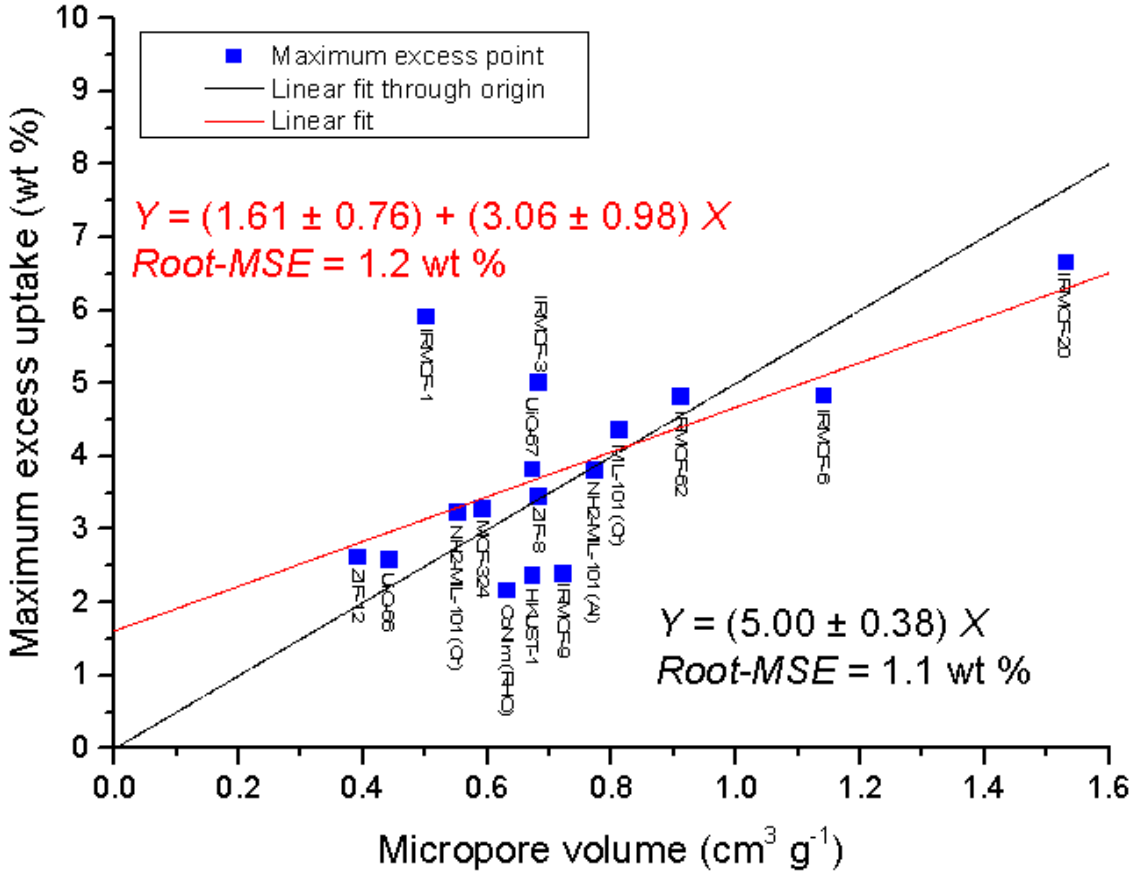

Figure 4.6. Maximum excess uptake of MOFs measured at 77 K versus their DR micropore pore volume. Errors from uptake measurements are within the size of the symbol. Upper equation (in red) corresponds to the fitting of the red line and the lower equation (in black) corresponds to the fitting of the black line.

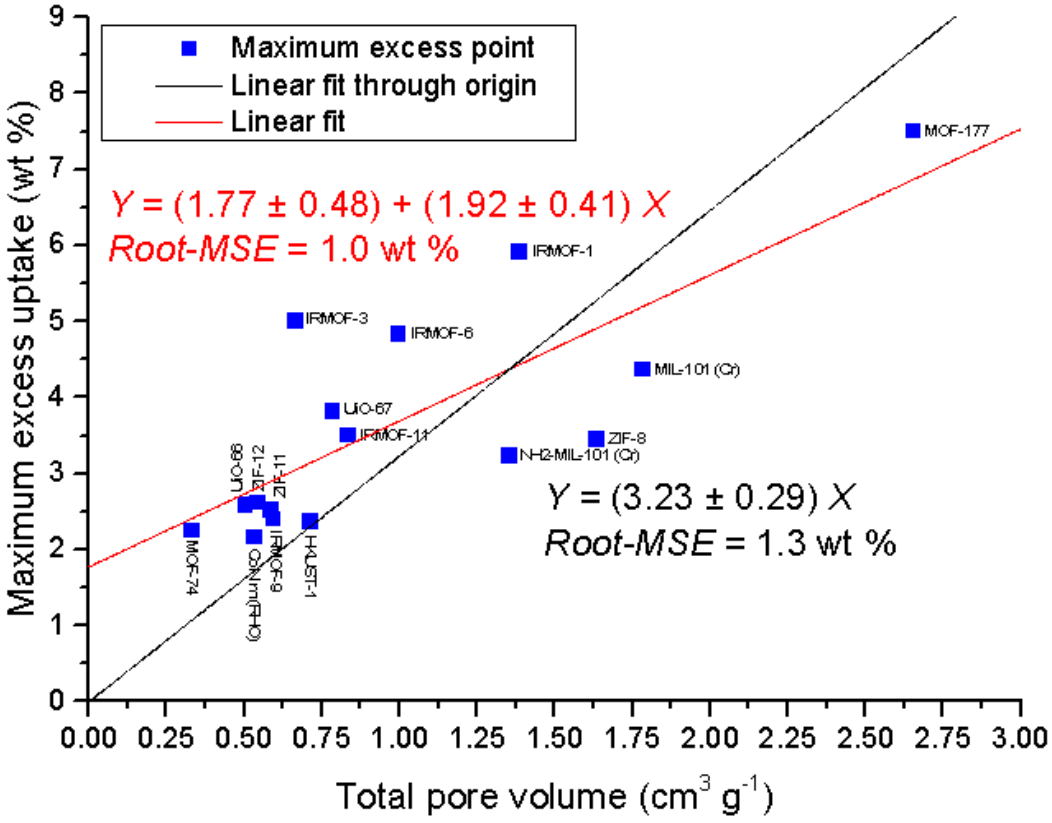

Figure 4.7. Maximum excess uptake of MOFs measured at 77 K versus their total pore volume (HK, Gurvich, Single crystal and Cerius2 methodologies from experiments and literature were used). Errors from uptake measurements are within the size of the symbol. Upper equation (in red) corresponds to the fitting of the red line and the lower equation (in black) corresponds to the fitting of the black line.

In Figure 4.8, the theoretical pore volumes obtained from the non-linear fitting of every fitted isotherm have been plotted against the in-house experimental pore volumes from nitrogen sorption and values from literature. In order to see the similitude in values between modelled pore volume and experimental and literature pore volumes, a straight line with equation $x = y$ has also been plotted. A general agreement can be seen (excluding MIL-101 (Cr), IRMOF-62 and MOF-74), particularly at low pore volume ranges (up to 0.75 $cm^3\ g^{-1}$).

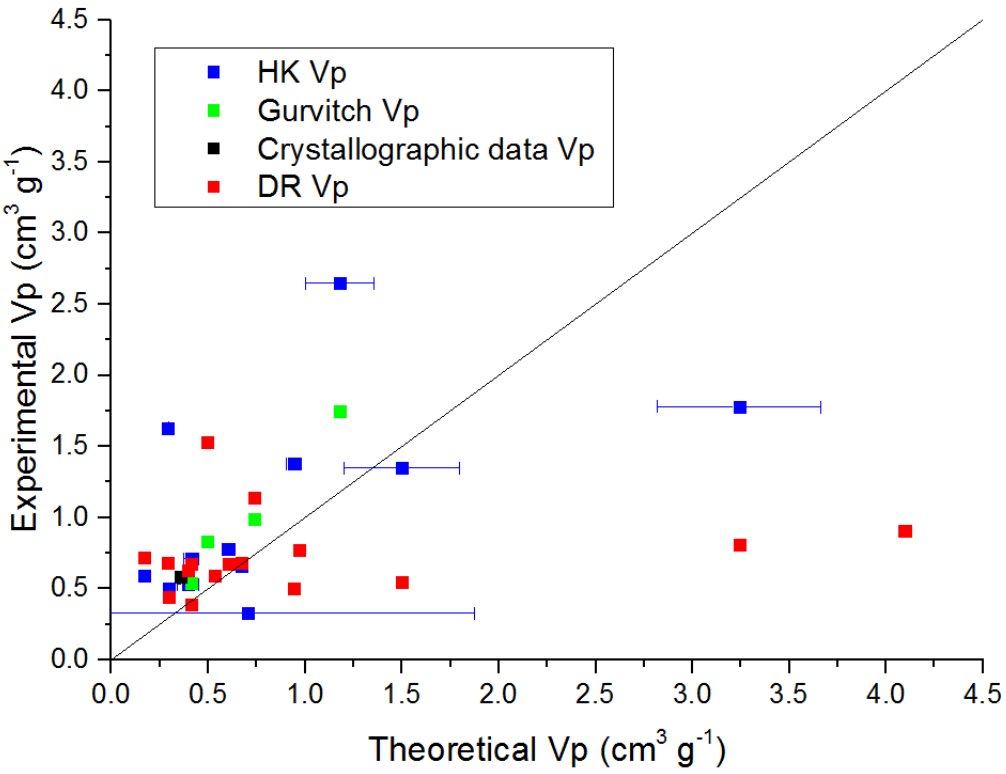

Figure 4.8. Theoretical pore volume obtained from non-linear fittings versus their experimental pore volumes. Error bars represent standard errors obtained from the fitting of the model.

Figure 4.9 shows the modelled total hydrogen capacities obtained from fitting the model (including error bars from adsorbate densities and pore volumes from fitting the model) against their BET surface area values divided by a thousand. Because of the high values obtained from the fit and/or error bars, MIL-101 (Cr), MOF-74 and IRMOF-62 (19.25 ± 2.65, 6.03 ± 12.04 and 29.18 ± 17.53 wt % respectively) have not been used in the correlations. ZIF-7 and ZIF-9 were not included either due to the inability to be fitted because of their unusual shapes at relatively low pressures. A table of the total hydrogen capacity values used for the correlations is in Supplementary Information F. A linear relationship between variables can be seen, with the total hydrogen capacity increasing with BET surface area, being the fitting slightly worse than that of the maximum hydrogen uptake correlation (Figure 4.5). The correlation also predicts several materials to perform better when compared with the excess uptake, like the MILs. This could be because higher pressure is needed for these materials to completely fill their pores due to their mesoporosity.

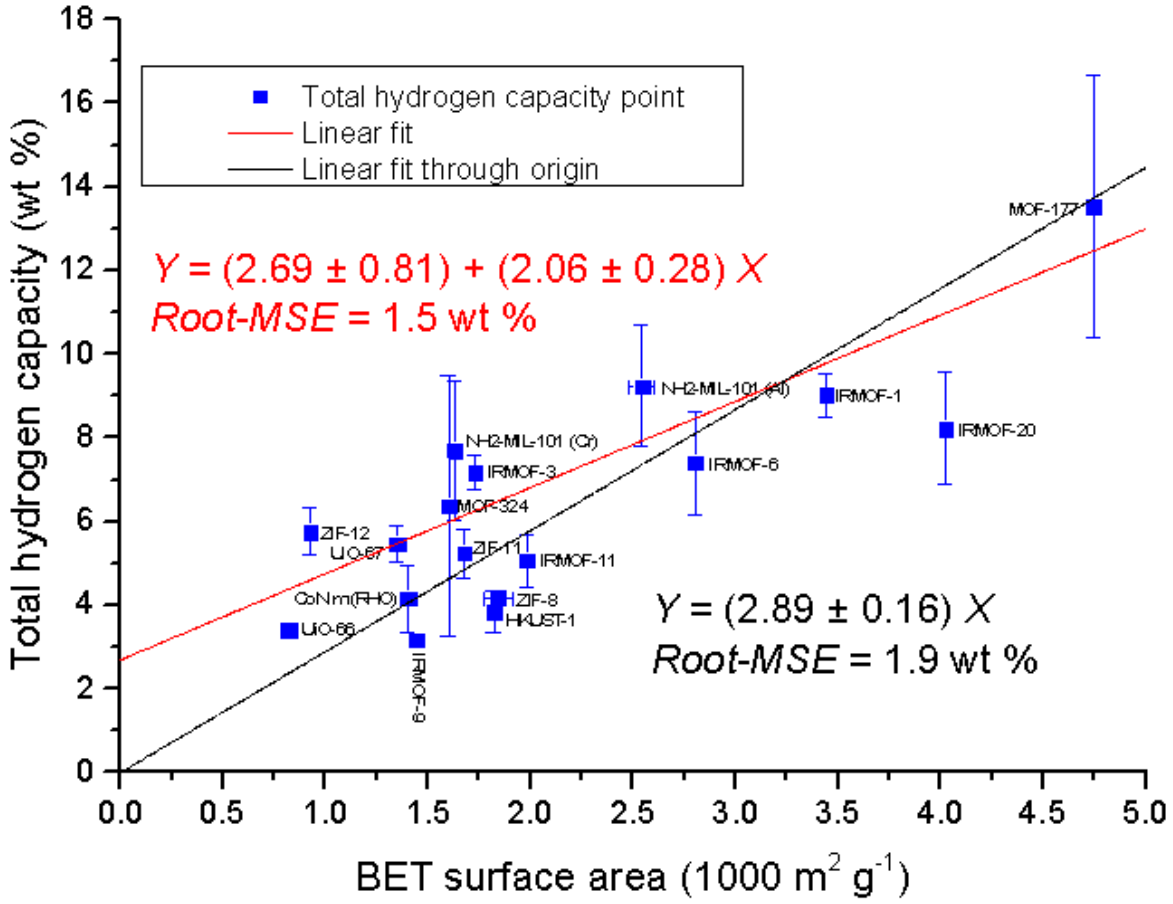

Figure 4.9. Total hydrogen capacity of MOFs versus their BET surface area (N_2 at 77 K) per 1000 m^2 g^{-1}. Error bars represent the standard error of the product of $\rho_A * Vp$ to calculate the total capacity. Upper equation (in red) corresponds to the fitting of the red line and the lower equation (in black) corresponds to the fitting of the black line.

Figure 4.10 correlates the experimental and literature pore volumes (HK, Gurvich, Single Crystal and Cerius2 methodologies) with the total hydrogen capacity of the MOFs. Every material apart from ZIF-8 shows a scattered linear relation (equations and Root-MSE values shown in Figure 4.10), showing on the other hand similar experimental BET surface area and micropore volume values when compared to literature [14]. When comparing to Figure 4.7, it can be seen that the red fit of the total hydrogen capacity correlation shows a slightly better fit (Root-MSE values 0.87 and 1.0 respectively). The reason behind this could be because the model considers all the pores of the material completely filled with adsorbed hydrogen. Although literature states that hydrogen is better stored in micropores, at high pressures, the amount of hydrogen adsorbed in the rest of the pores cannot be considered negligible.

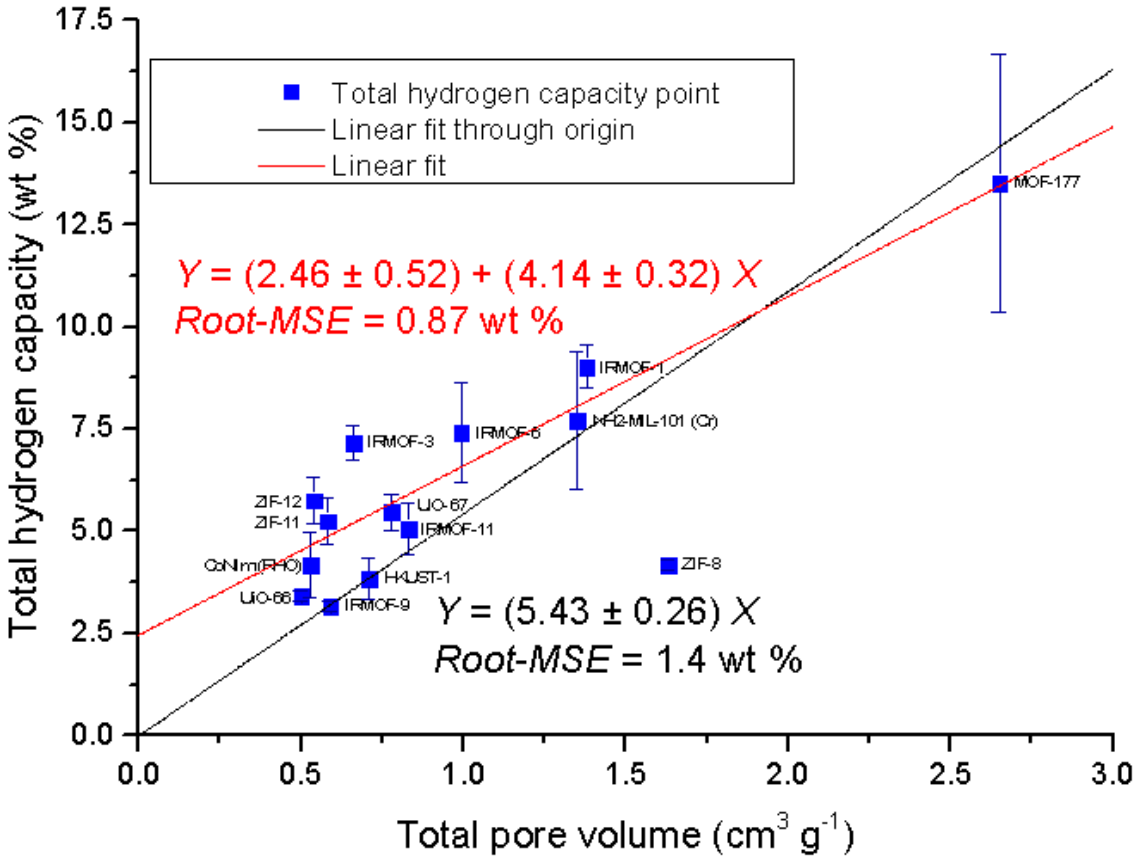

Figure 4.10. Modelled total hydrogen capacity versus total pore volume (from HK, Gurvich, single crystal and Cerius2 methodologies). Error bars represent the standard error of the product of $\rho_A * Vp$ to calculate the total capacity. Upper equation (in red) corresponds to the fitting of the red line and the lower equation (in black) corresponds to the fitting of the black line.

Micropore volume versus total hydrogen capacity did not show any correlation. As discussed in Figure 4.6, many factors exist that were not considered in the individual correlations, being this even more significant when the material's pores are assumed to be completely filled, giving the dismissed total pore volume even higher weighting. This could be due to different amounts of pore size ratios and micropore volumes for each material.

Figure 4.11 presents the predicted adsorbate density (ρ_A) obtained from non-linear model fittings. The plotted error bars represent the ρ_A uncertainties obtained from the fittings. The represented values are, overall, very high when compared with the density that of solid hydrogen (87 kg m^{-3} at 0 MPa and 4.4 K) [15]. Several pieces of work indicate the compressibility of solid H_2 (87 kg m^{-3} at 4 K and 0 MPa) [15, 16, 17]. A study with MOF-74 using neutron power diffraction and their measured isotherms shows that H_2 adsorbed on its surface at 77 K has a higher density that of solid H_2 at 4 K and 0 MPa. Results from different

materials indicate a reduction of the intermolecular distance of H_2 when adsorbed in materials with coordinatively unsaturated metal centers when compared to solid bulk hydrogen [18].

IRMOF-9 shows the highest value, which could be related to its interpenetrated structure. However, the fact of having an interpenetrated structure may increase the adsorbate density but reduce its pore volume, yielding a relatively low experimental uptake and total hydrogen capacity. IRMOF-20 presents the second highest adsorbate density, also presenting high surface area (4024 m^3 g^{-1}) [19] and pore volume, with microporous pores (1.4 and 1.73 nm) [19-21]. Most of the materials (IRMOF-1, IRMOF-3, IRMOF-6, ZIF-CoNIm, UiO-67, NH_2-MIL-101 (Al) and HKUST-1) show a hydrogen density around 80-90 kg m^{-3}. Since the predicted total hydrogen capacity is calculated as the product of the theoretical pore volume and the density of the adsorbate of the model fit ($Vp * \rho_A$), the result can come from either a high ρ_A or a high Vp value that the model could have given.

Therefore, the next section of this chapter will focus on the influence of the experimental hydrogen maximum pressure with the obtained theoretical pore volume results from the model fitting. Also, the effects on the predicted adsorbate densities obtained from the model when fixing experimental pore volumes from experimentation and literature will be shown.

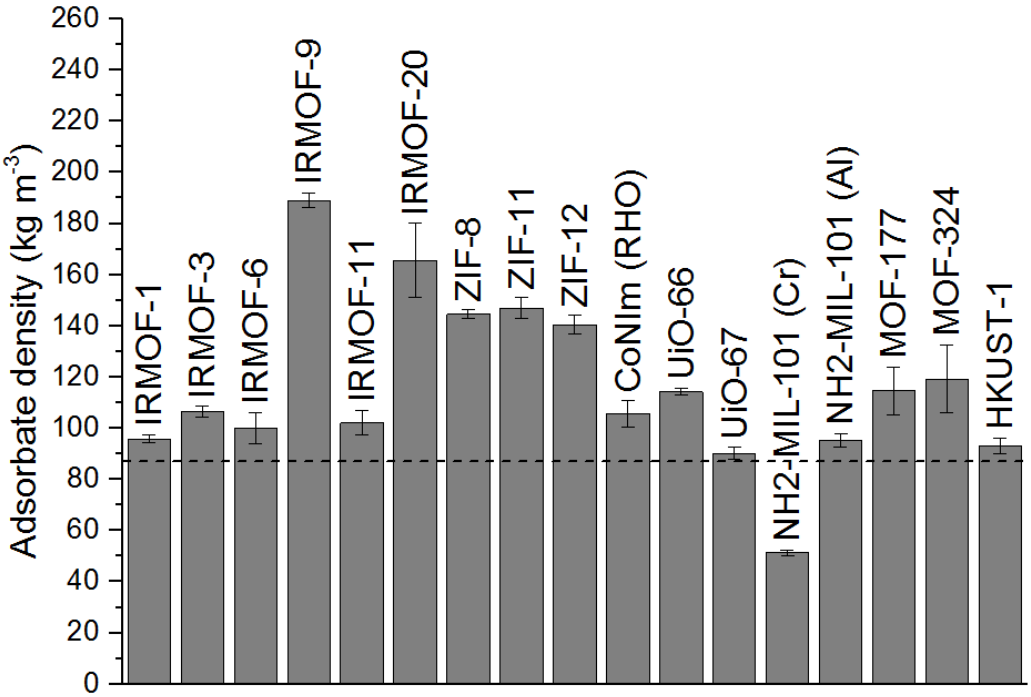

Figure 4.11. Predicted adsorbate density of the tested materials, including error bars from the model. Error bars represent the standard error of ρ_A obtained from the model fittings of the experimental hydrogen isotherms. Dashed line indicates the limiting density of solid hydrogen at 0 MPa (87 kg m^{-3}) [15].

4.4 Theoretical pore volume evaluation from model fittings

Further research of the effects of fixing the pore volume and the consequences of using different pressure ranges in the experimental hydrogen isotherms has been done. This study aims to show how well the model predicts the experimental pore volume of the materials and if its tendency with higher pressure ranges would tend to the experimental pore volume value/s. If this is the case, fixing the value of the experimental pore volume for each material would improve the robustness of the model and therefore, improve the prediction of the total hydrogen quantities for each material.

In order to do this, the whole of the excess isotherm taken from either literature or in-house experiments was fitted to the model without fixing the pore volume. After that, the modelled pore volume value and its error obtained from the fitting were plotted and the highest pressure data point from the excess isotherm, removed. The resultant isotherm with a lower maximum pressure than the previous was fitted and its new given modelling pore volume value, recorded. This process was followed until the fitting did not converge or gave very unreasonable modelling pore volume value for each available MOF.

Breathing materials ZIF-7 and ZIF-9 were not included in this study due to the inability to be fitted with the model because of their unusual initial shape. As previously mentioned, IRMOF-8 was not used in the correlations due to its high errors due to its low mass but it has been used in this study to compare its isotherm shape with other IRMOFs.

In each graph, the hydrogen adsorption isotherm at 77 K of each material was added as a guide for the reader. In Figure 4.12, all the results for the IRMOFs used in this work are shown:

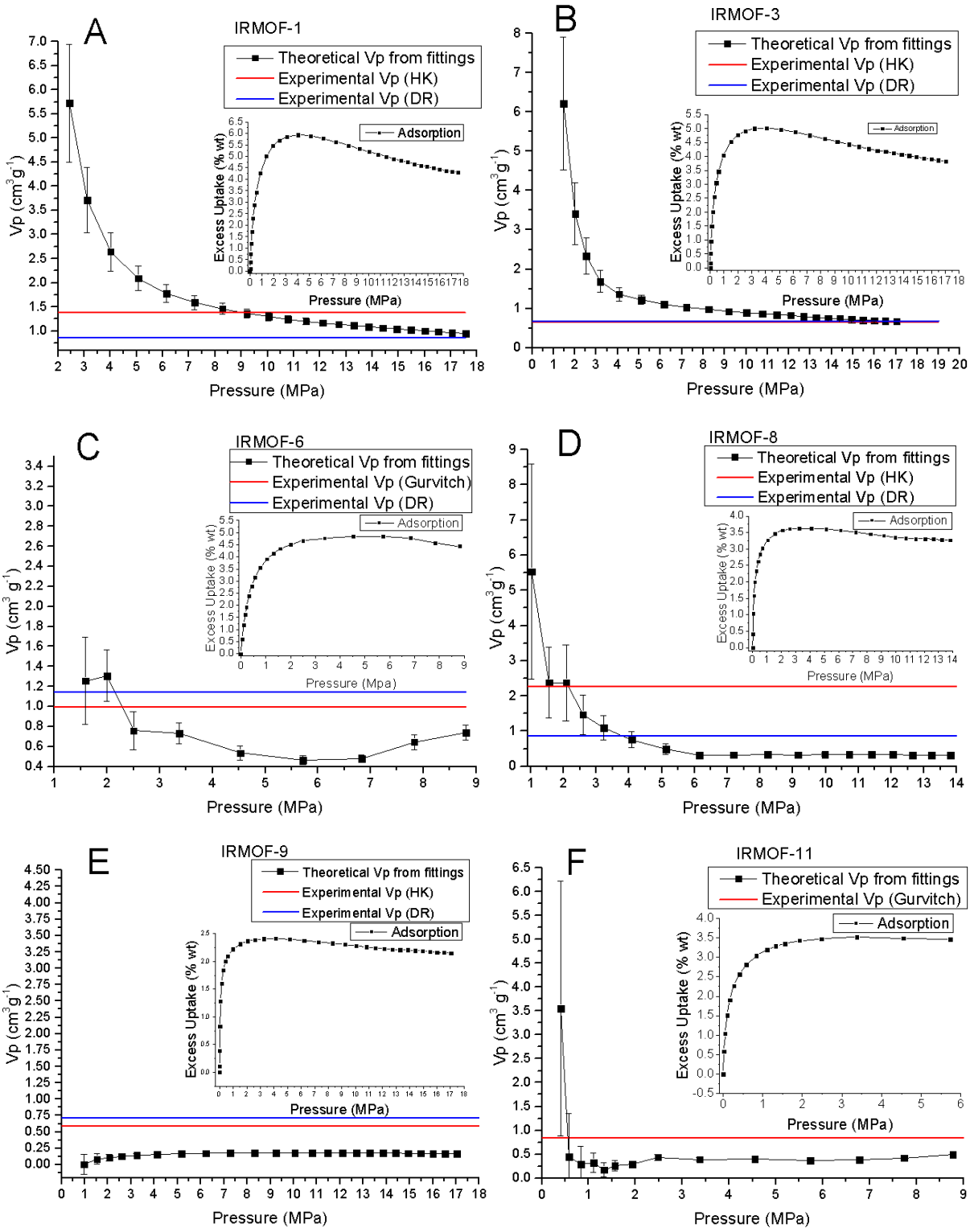
A
IRMOF-1
Theoretical Vp from fittings
Experimental Vp (HK)
Experimental Vp (DR)
Adsorption
Excess Uptake (% wt)
Pressure (MPa)
Vp (cm3 g-1)
B
IRMOF-3
Theoretical Vp from fittings
Experimental Vp (HK)
Experimental Vp (DR)
Adsorption
Excess Uptake (% wt)
Pressure (MPa)
Vp (cm3 g-1)
C
IRMOF-6
Theoretical Vp from fittings
Experimental Vp (Gurvitch)
Experimental Vp (DR)
Adsorption
Excess Uptake (% wt)
Pressure (Mpa)
Vp (cm3 g-1)
D
IRMOF-8
Theoretical Vp from fittings
Experimental Vp (HK)
Experimental Vp (DR)
Adsorption
Excess Uptake (% wt)
Pressure (MPa)
Vp (cm3 g-1)
E
IRMOF-9
Theoretical Vp from fittings
Experimental Vp (HK)
Experimental Vp (DR)
Adsorption
Excess Uptake (% wt)
Pressure (MPa)
Vp (cm3 g-1)
F
IRMOF-11
Theoretical Vp from fittings
Experimental Vp (Gurvitch)
Adsorption
Excess Uptake (% wt)
Pressure (MPa)
Vp (cm3 g-1)

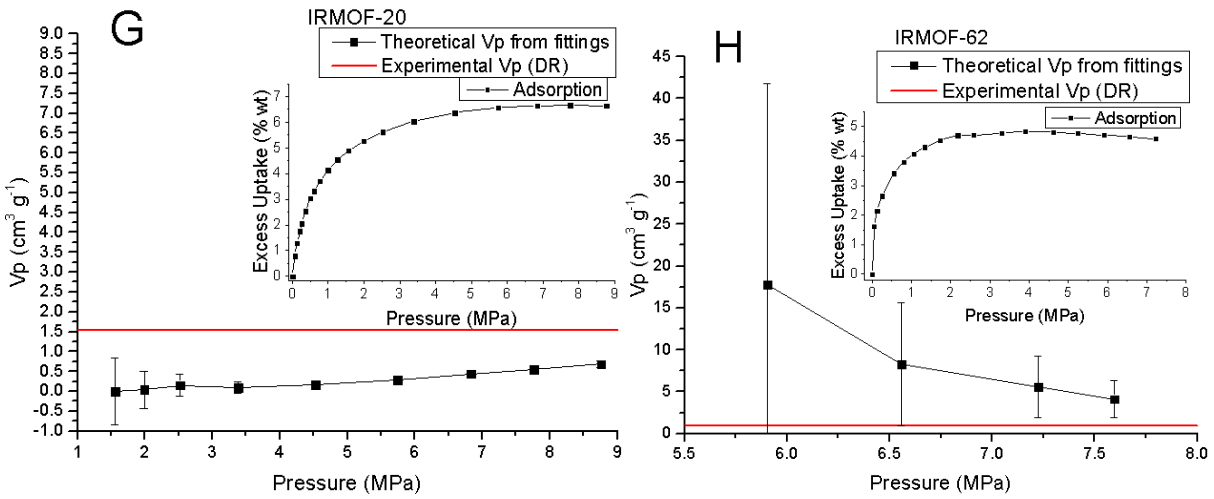

Figure 4.12. Modelled pore volume values obtained from fitting the model to hydrogen excess isotherm uptakes at different pressures of IRMOF-1 (A), IRMOF-3 (B), IRMOF-6 (C), IRMOF-8 (D), IRMOF-9 (E), IRMOF-11 (F), IRMOF-20 (G) and IRMOF-62 (H).

In Figure 4.12, a certain pattern can be seen in IRMOF-1, IRMOF-3, IRMOF-8 and IRMOF-11. For IRMOF-1 and IRMOF-3, the modelled pore volume values seem to asimptotically aproximate towards the micropore volume value (DR). However, IRMOF-8 and IRMOF-11 show a similar shape but passing over the experimental pore volume values. This indicates that if the isotherms of IRMOF-1 and IRMOF-3 were run at higher pressures, the modelled pore volume at those maximum pressures might have passed over the experimental pore volume values as well. Furthermore, IRMOF-6, IRMOF-9, IRMOF-20 and IRMOF-62 show different curves, being IRMOF-9 the only one that does not tend to towards its experimental pore volume values.

IRMOF-1 and IRMOF-3 are more similar both in shape and uptake (both maximum uptake and uptake in all points of the isotherm overall) than any of the other IRMOFs.

Figure 4.13 shows the results of the ZIFs used in the correlations:

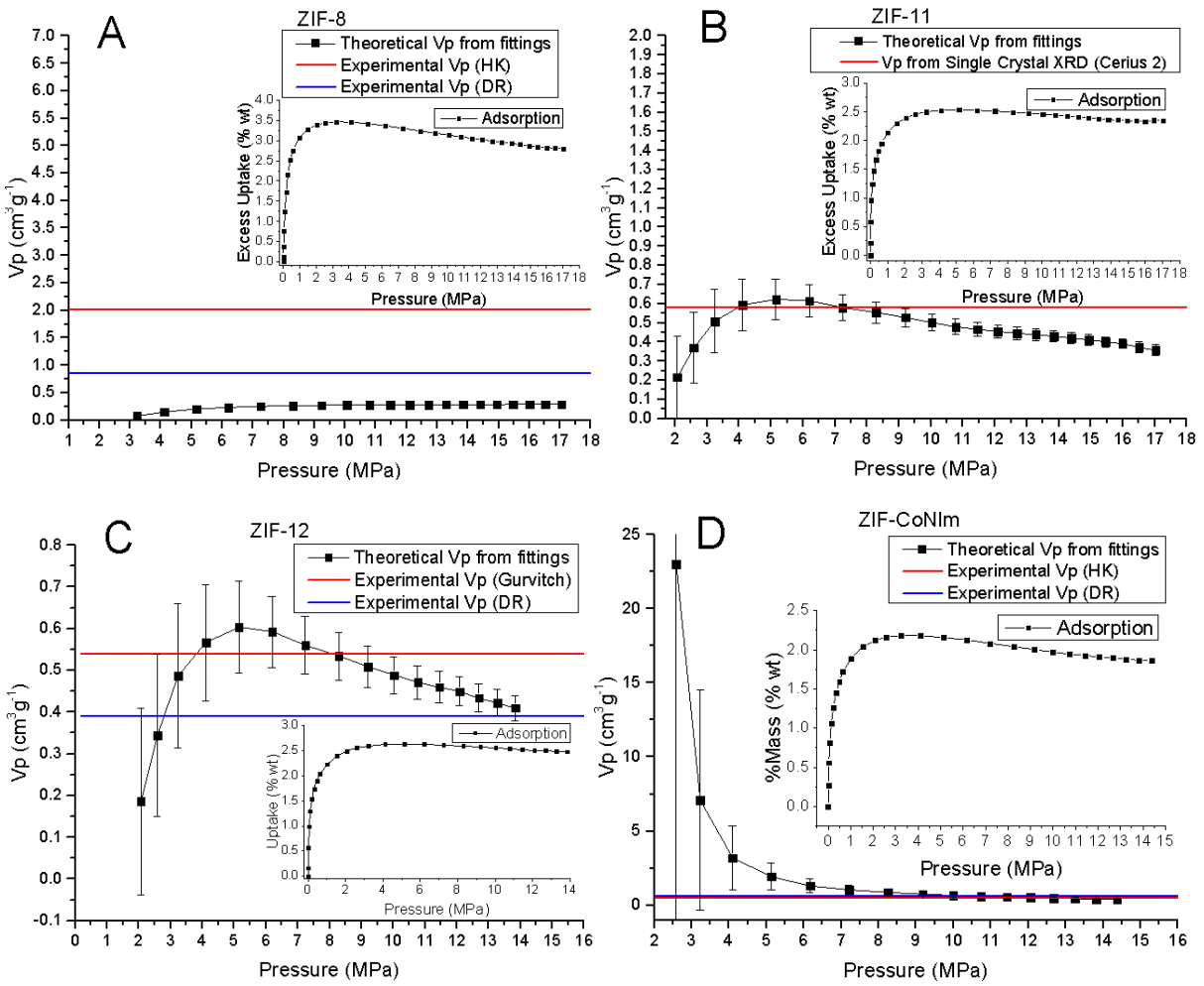

Figure 4.13. Theoretical pore volume values obtained from fitting the model to hydrogen excess isotherm uptakes at different pressures of ZIF-8 (A), ZIF-11 (B), ZIF-12 (C) and ZIF-CoNIm (D).

Figure 4.13 shows new patterns, seen in ZIF-11 and ZIF-12. The curves start at low pore volume values, raising until they get to a maximum and then diminising in value again. ZIF-12 values tend to get to the experimental micropore volume, not being the case for ZIF-11, whose pore volume value was calculated computationally with a different methodology. As with IRMOF-1 and IRMOF-3, ZIF-11 and ZIF-12 have an even closer similitude in both uptake and isotherm shape, giving almost the same modelled pore volume values.

ZIF-CoNIm shows the same shape that of most of the IRMOFs, being closer that of IRMOF-8 in values, despite of having a 1.5 wt % difference in maximum hydrogen uptake (at 3.23 and 6.14 MPa respectively). A similar discussion applies to ZIF-8 and IRMOF-9, having a difference of just over 1 wt %. In maximum hydrogen excess (at 3.22 and 4.13 MPa

respectively). This shows that the theoretical pore volume values are more dependant on the shape of the isotherm than their uptakes.

Figure 4.14 shows the results of the MILs used in the correlations:

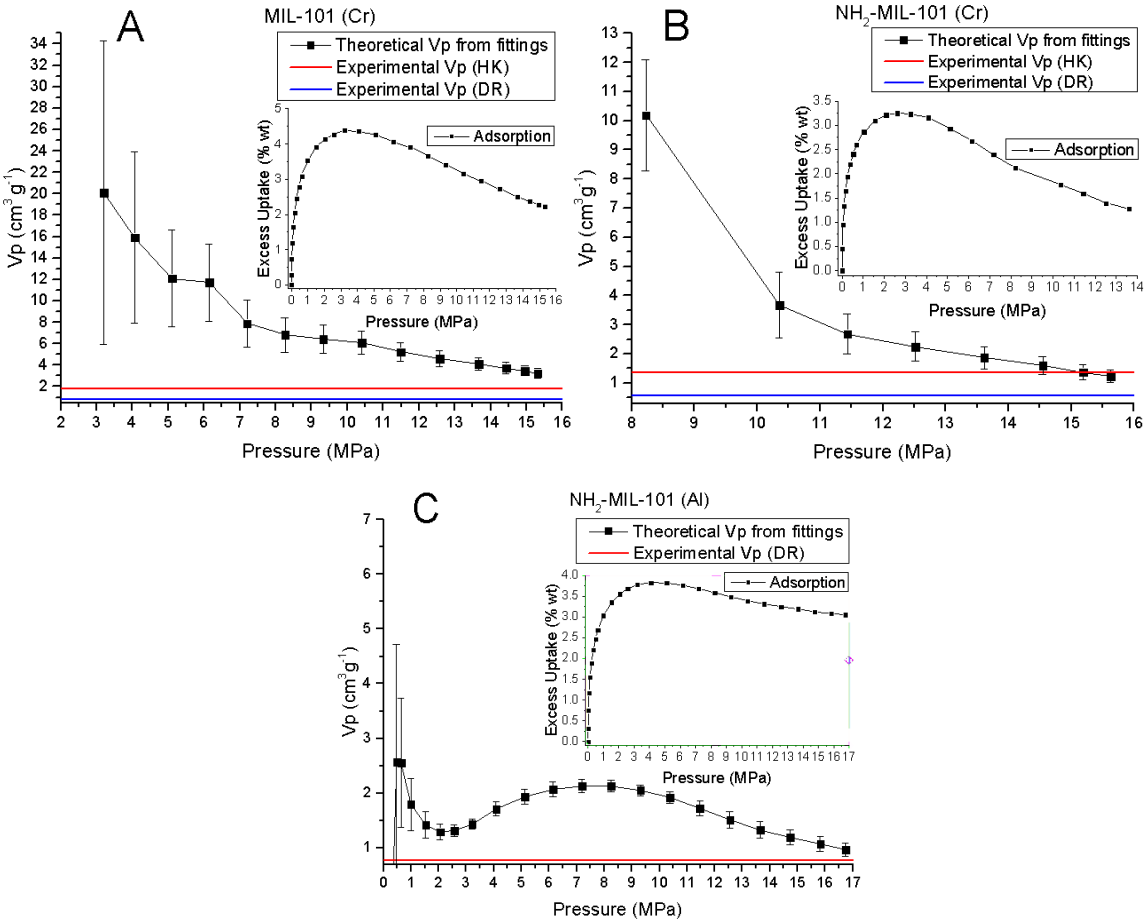

Figure 4.14. Theoretical pore volume values obtained from fitting the model to hydrogen excess isotherm uptakes at different pressures of MIL-101 (Cr) (A), NH_2-MIL-101 (Cr) (B) and NH_2-MIL-101 (Al) (C).

Figure 4.14 modelled pore volume curves show a tendency towards their micropore volume (DR), presenting NH_2-MIL-101 (Al) a variation in shape, with an increase in modelled pore volume from 2 to 8 MPa and a maximun before pore volume values drop again. Both MIL-101 (Cr) and NH_2-MIL-101 (Cr) show a very similar isotherm shape and similar pore volume tendencies as expected because of their similar isotherm shapes.

Figure 4.15 shows the results of the MOFs used in the correlations:

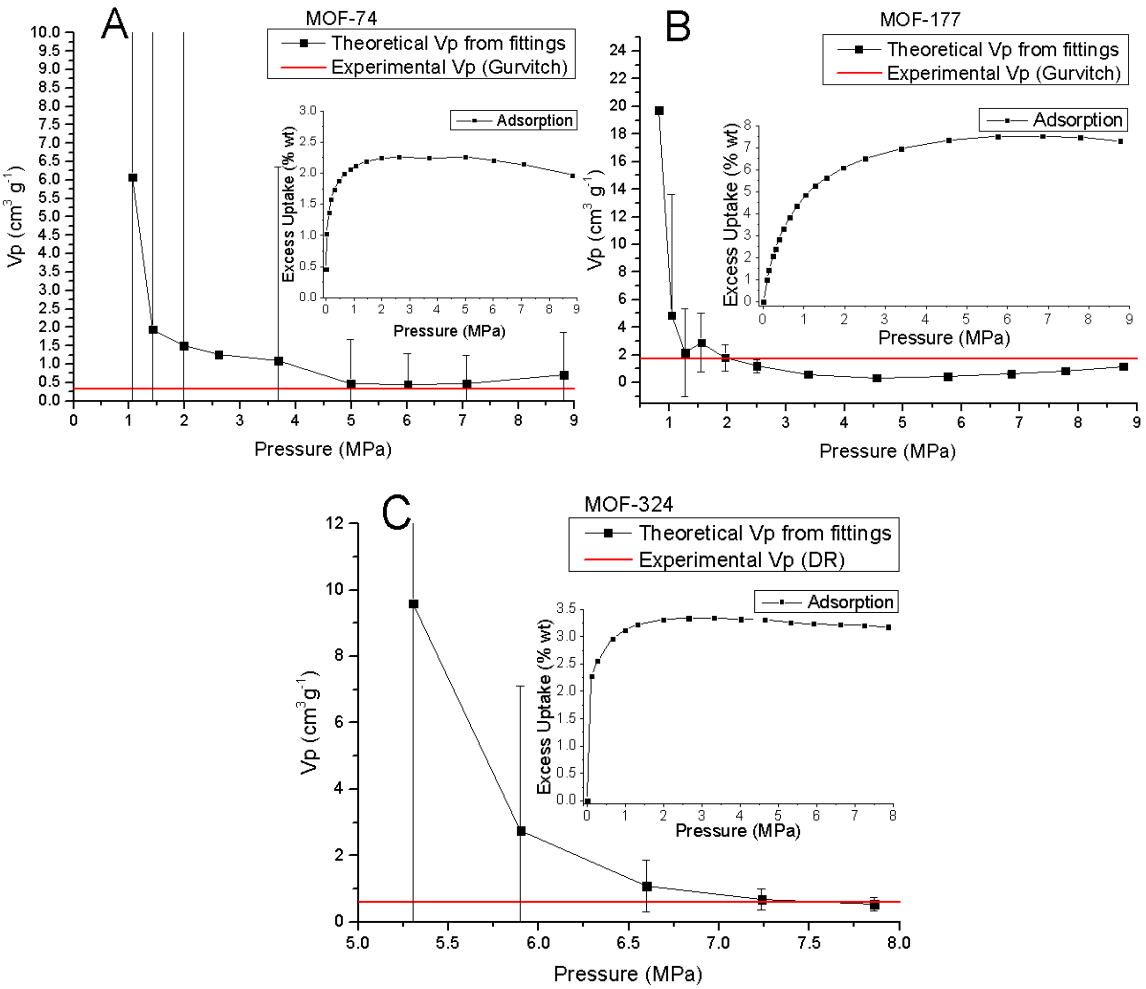

Figure 4.15. Modelled pore volume values obtained from fitting the model to hydrogen excess isotherm uptakes at different pressures of MOF-74 (A), MOF-177 (B) and MOF-324 (C).

Figure 4.15 shows similar modelled pore volume curve shapes, which have been seen before, especially in some IRMOFs. They all tend towards their experimental pore volumes but MOF-74, which starts deviating at its last pore volume value.

Figure 5.16 shows the results of the UiOs and HKUST-1 used in the correlations:

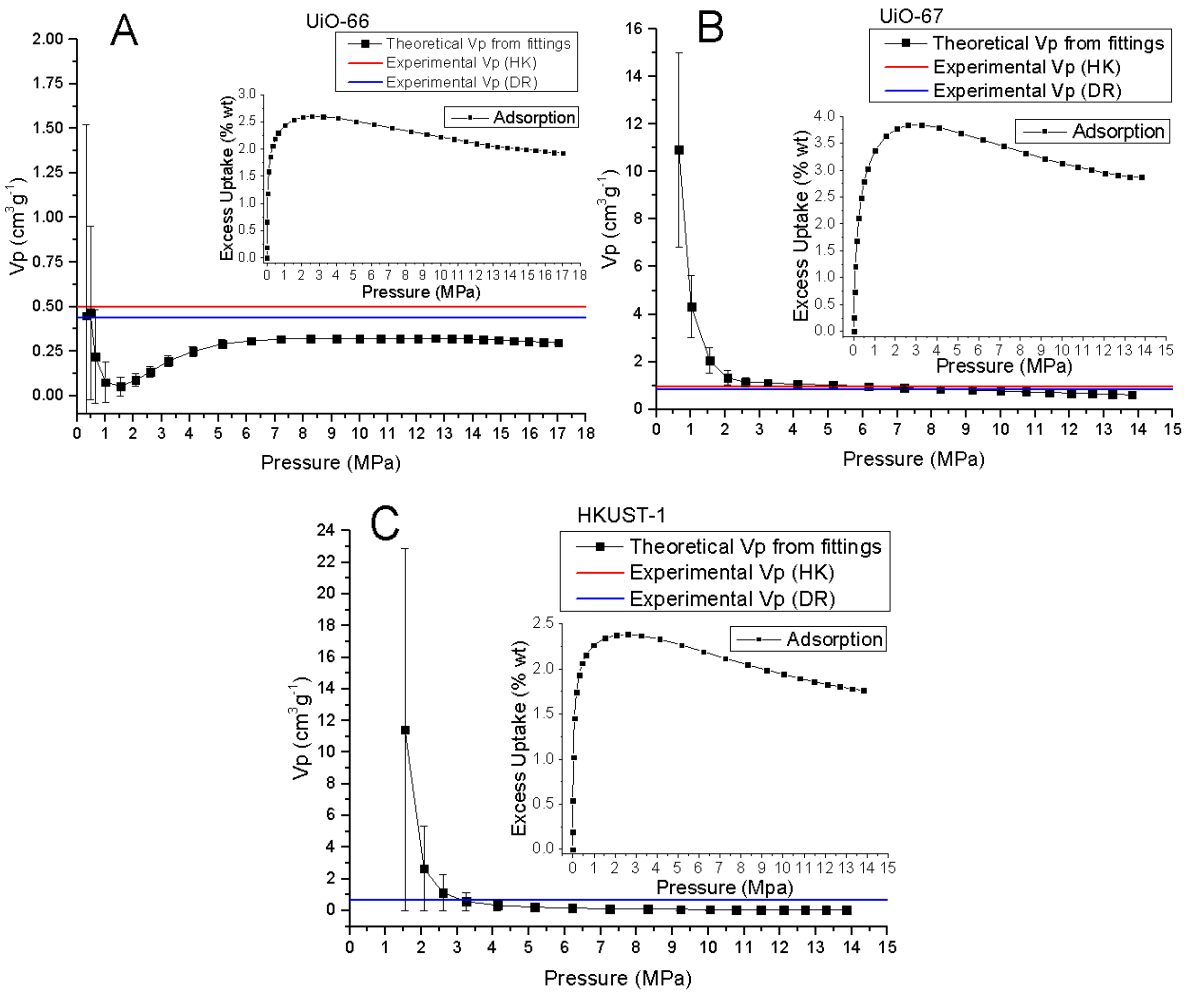

Figure 4.16. Modelled pore volume values obtained from fitting the model to hydrogen excess isotherm uptakes at different pressures of UiO-66 (A), UiO-67 (B) and HKUST-1 (C).

Figure 4.16 show patterns that have seen before in other materials, indicating no relationship between the modelled pore volume curve and topology or metal cluster nature. As a comparison, UiO-67 and HKUST-1 show the same sort of modelled pore volume pattern, having HKUST-1 a much lower uptake, different metal cluster (Cu *vs* Zr) and different topology.

4.5 Experimental pore volume fixing in model fittings

Model fittings not fixing the pore volume have been compared with model fittings in which the pore volume was fixed with experimental pore volume values from experiments or literature (HK, Gurvich, Cerius2 or DR). The same scale has been kept in the figures to show fitting differences. Table 4.2 shows the reduced Chi-squared values of each fitting as a statistical value that indicates goodness of fitting:

Table 4.2. Reduced Chi-squared values of hydrogen isotherm fittings at 77 K with different pore volumes.

Material	Reduced Chi-squared non fixed Vp fitting	Reduced Chi-squared HK*, Gurvich†, Cerius2 fixed Vp fixing	Reduced Chi-squared DR fixed Vp fitting
IRMOF-1	2.18E-3	6.79E-3*	2.30E-2
IRMOF-3	1.41E-3	1.36E-3*	4.92E-2
IRMOF-6	1.31E-3	1.85E-3†	2.53E-3
IRMOF-8	6.99E-4	2.42E-3*	1.81E-3
IRMOF-9	6.91E-5	4.64E-3*	4.09 E-3
IRMOF-11	6.93E-4	2.23E-3†	-
IRMOF-20	5.50E-4	-	1.83E-3
IRMOF-62	2.14E-3	-	5.30E-3
ZIF-8	1.62E-4	2.75E-2*	1.52E-2
ZIF-11	3.16E-4	6.05E-4	-
ZIF-12	1.86E-4	1.29E-3†	1.81E-4
ZIF-CoNIm	1.10E-3	1.19E-3*	1.37E-3
MIL-101 (Cr)	1.51E-3	3.72E-3*	3.35E-2
NH_2- MIL-101 (Cr)	8.69E-3	8.43E-3*	4.95E-2
NH_2- MIL-101 (Al)	2.13E-3	-	2.10E-3
UiO-66	2.13E-4	2.83E-3*	1.88E-3
UiO-67	1.68E-3	2.99E-3*	1.84E-3
MOF-74	1.67E-2	1.60E-2†	-
MOF-177	1.64E-3	4.17E-3†	-
MOF-324	6.73E-4	-	6.21E-4
HKUST-1	1.30E-3	2.07E-3*	1.97E-3

It can be seen that most of the non-fixed pore volume fittings show a lower reduced Chi-squared value, indicating slightly better fits (except IRMOF-3, NH_2- MIL-101 and (Cr) MOF-74 with HK and NH_2- MIL-101 (Al) and MOF-324 with DR). The fits have also been graphically represented to show how the model fits in each case.

In Figures 4.17, 4.18A and 4.18B, the model fittings with non-fixed, HK and Gurvich and DR pore volumes respectively for the IRMOF family can be seen:

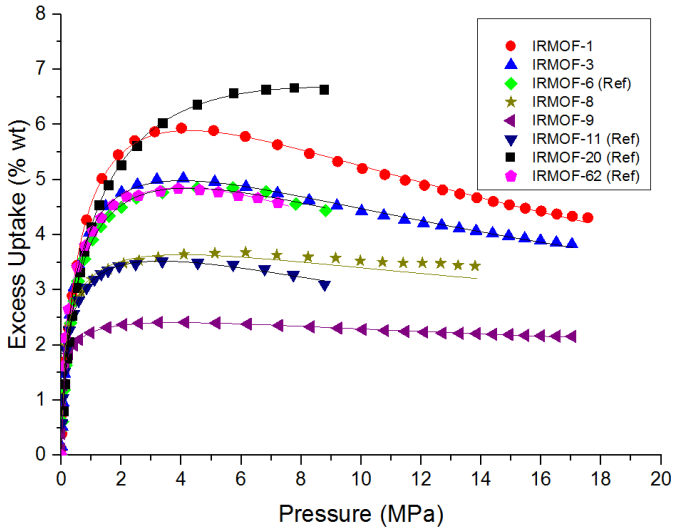

Figure 4.17. Excess hydrogen isotherms fitting for the IRMOF family of materials at 77 K (non-fixed pore volume).

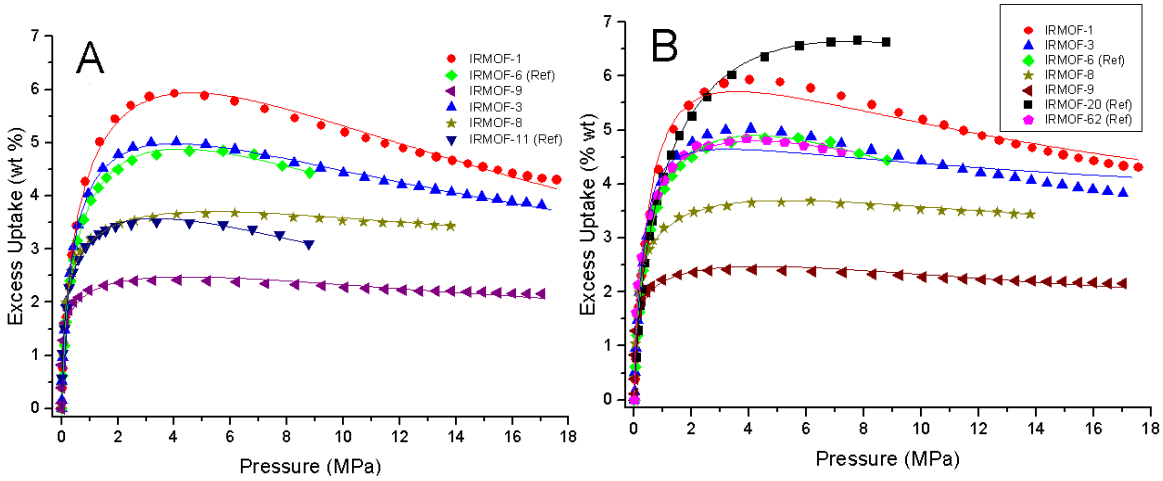

Figure 4.18. Excess hydrogen isotherms fitting for the IRMOF family of materials at 77 K. HK and Gurvich (A) and DR fixed pore volumes (B).

In Figures 4.17, 4.18A and 4.18B an improvement in the IRMOF-8 fitting is shown, although the fittings of IRMOF-1 in Figures 4.18A and 4.18B and IRMOF-3 in Figure 4.18B are shown not to be as good as the non-fixed pore volume ones.

In Figures 4.19, 4.20A and 4.20B, we can see the model fittings with non-fixed, HK, Gurvich and Cerius2 and DR pore volumes respectively for the ZIF family:

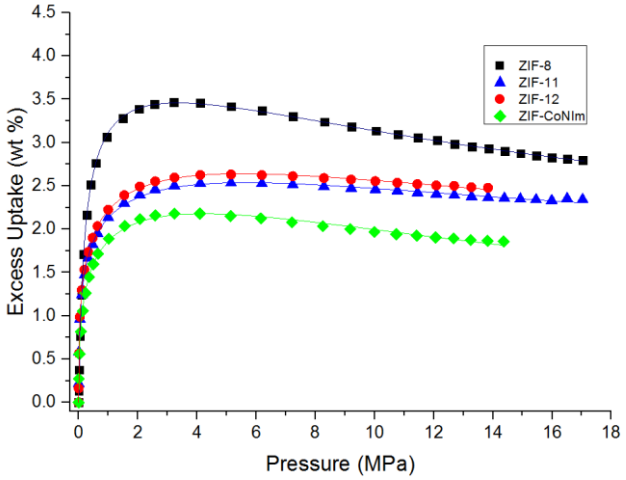

Figure 4.19. Excess hydrogen isotherms fitting for the ZIF family of materials at 77 K (non-fixed pore volume).

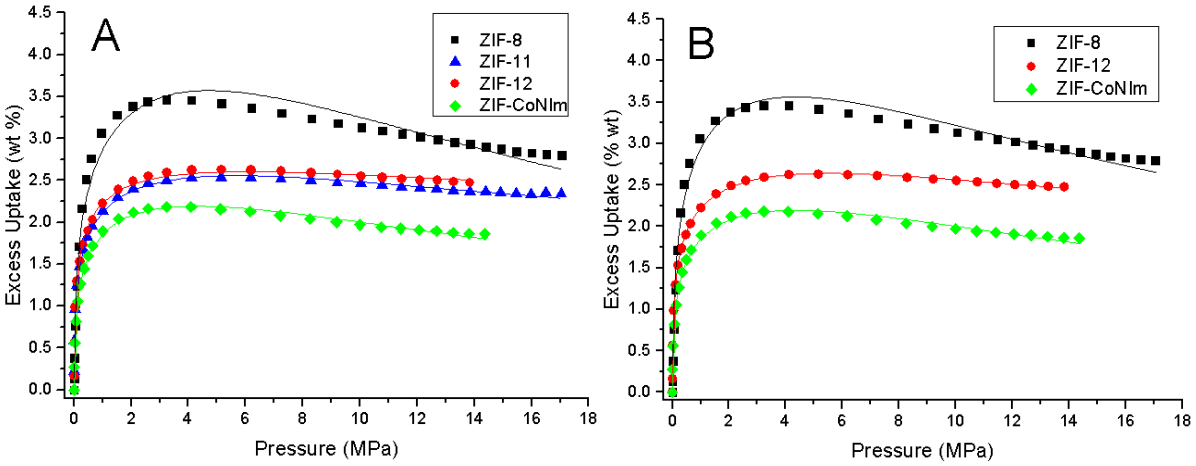

Figure 4.20. Excess hydrogen isotherms fitting for the IRMOF family of materials at 77 K. HK and Gurvich (A) and DR (B) fixed pore volumes.

In Figures 4.20A and 4.20B, fittings of ZIF-8 are shown, indicating a worse fit than the non-fixed pore volume fitting (Figure 4.19). The rest of the fittings show good fitting results in every case.

In Figures 4.21, 4.22A and 4.22B, we can see the model fittings with non-fixed, HK and DR pore volumes respectively for the MIL family:

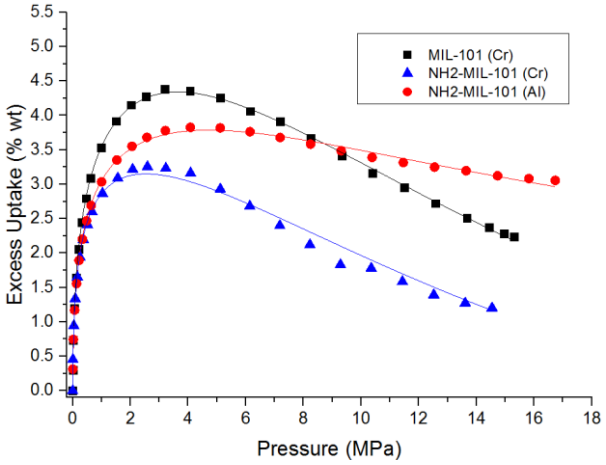

Figure 4.21. Excess hydrogen isotherms fitting for the MIL family of materials at 77 K (non-fixed pore volume).

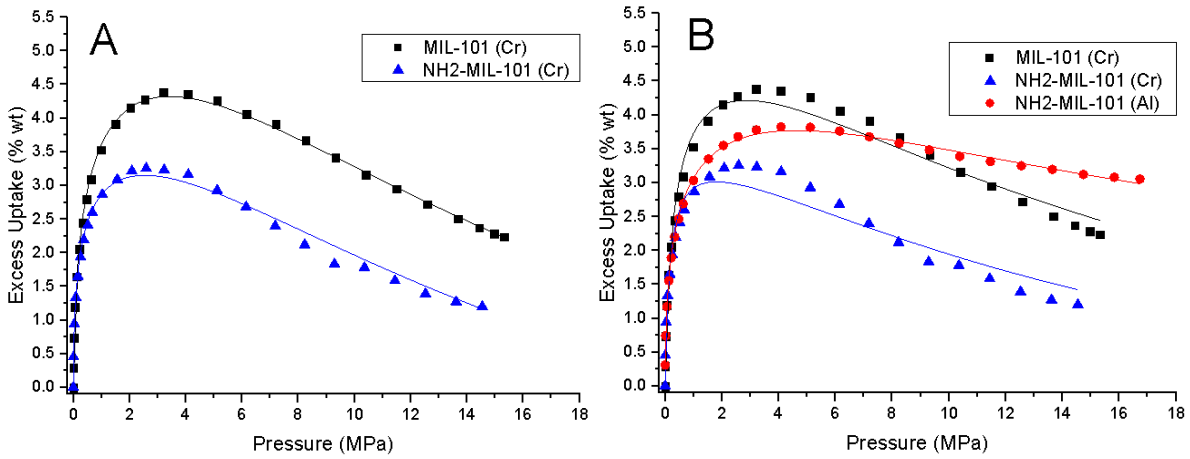

Figure 4.22A and 4.22B. Excess hydrogen isotherms fitting for the MIL family of materials at 77 K (HK and Gurvich and DR fixed pore volumes respectively).

In Figure 4.22B, the fittings of MIL-101 (Cr) and NH_2-MIL-101 (Cr) show to be worse than in the other cases (Figure 4.21A and 4.22A).

In Figures 4.23, 4.24A and 4.24B, we can see the model fittings with non-fixed, HK and DR pore volumes for the UiOs, MOFs and HKUST-1 respectively:

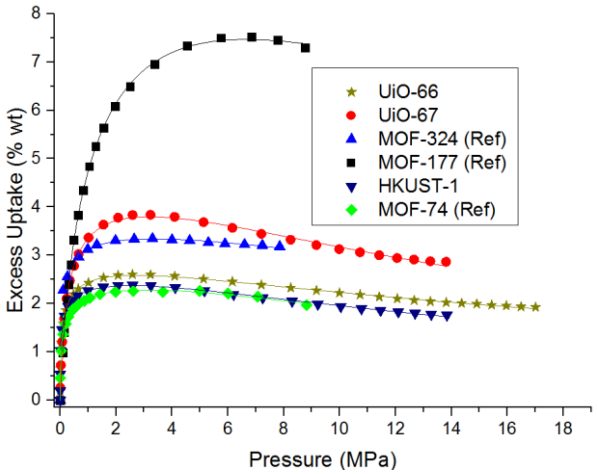

Figure 4.23. Excess hydrogen isotherms fitting for the UiOs, MOFs and HKUST-1 at 77 K (non-fixed pore volume).

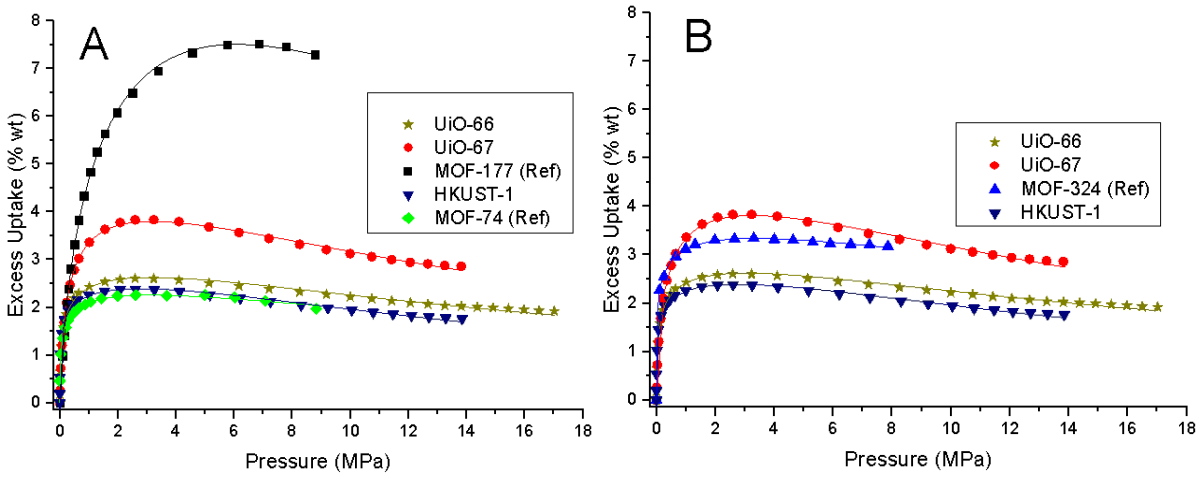

Figure 4.24 and 4.24B. Excess hydrogen isotherms fitting for the UiOs, MOFs and HKUST-1 at 77 K (HK and Gurvich and DR fixed pore volumes respectively).

Model fittings shown in Figures 4.23, 4.24A and 4.24B show good agreement with the experimental data in all cases.

Many of the analysed model fittings obtained from fixing experimental pore volume values also show good fitting of the experimental isotherms, being corroborated by low reduced Chi-squared values shown in Table 4.2. The adsorbate densities of those fittings that showed a good agreement with the experimental hydrogen isotherm results have been compared against the values obtained from non-fixed that were previously shown in Figure 4.11 (Figure 4.25).

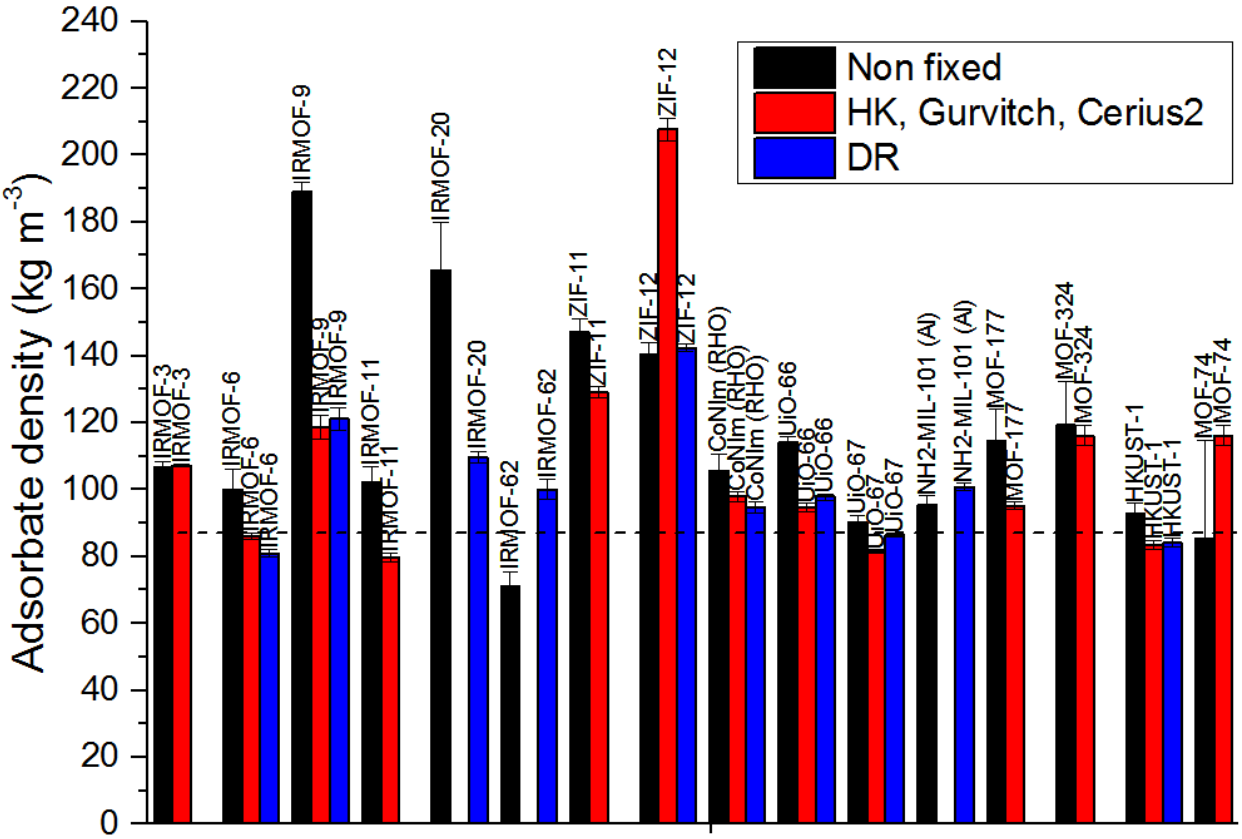

Figure 4.25. Predicted adsorbate density of MOFs with different pore volumes (non-fixed, HK, Gurvich and DR), including error bars from the model. Error bars come from the standard error of ρ_A when fitting the hydrogen isotherms to the model. Dashed line indicates the limiting density of solid hydrogen at 0 MPa (87 kg m^{-3}) [15].

As shown in Figure 4.25, adsorbate density values are lower overall when experimental pore volumes are used in the model, being closer to the solid density of solid hydrogen. However, MOF-74 and ZIF-12 densities from DR pore volumes are predicted to be much higher. This made their total hydrogen capacity values to be lower (from 5.75 ± 0.57 to 5.18 ± 0.08 and from 6.05 ± 12.04 to 6.85 ± 0.18 respectively), which seem more logical taking into account their low uptake seen in their experimental hydrogen excess isotherms at 77 K. Also, IRMOF-62 shows more realistic values (from 29.18 ± 17.53 to 9.29 ± 0.26).

4.6 Discussion and conclusions

ZIF-7 and ZIF-9 show unusual hydrogen excess isotherms at low pressures. ZIF-7 (SOD) has been reported to have a sorbate-induced gate-opening mechanism, indicating the same feature on ZIF-9 (SOD). This indicates relationships between flexibility and the SOD topology, although ZIF-8 (SOD) did not show any unusual feature. Also, the uptakes of ZIF-7 and ZIF-9 are very similar as well as the uptakes of their RHO homologues ZIF-11 and ZIF-12, indicating

little relationship between the nature of the metal cluster (Zn or Co) and their hydrogen uptake. Furthermore, an uptake relationship has been seen between the SOD and RHO topologies for these materials, indicating that the RHO topology might be a better topology for hydrogen adsorption than the SOD.

Correlations with the modelled total hydrogen capacity have also shown linear although scattered relations with surface area and total pore volume, showing the latter a slightly lower Root-MSE value (for the non-fixed linear fit, red line). This fact is believed to be because the model considers all the materials' pores fully filled of adsorbate, taking into consideration the total pore volume when the material is fully filled. No pore size relations were found, probably because of the mix of pore sizes with different ratios in many of the chosen materials.

The maximum excess uptake correlations fitted through the origin (black line, one parameter) were compared with the "Chahine rule", showing many similarities. The BET surface area correlations (1.76 ± 0.08 wt % per 1000 $m^2\ g^{-1}$) proved to be very similar to the "Chahine rule" (2 wt % per 1000 $m^2\ g^{-1}$). Same similitudes were found for the micropore volume correlations (5.00 ± 0.37 wt % per $cm^3\ g^{-1}$ of micropore volume compared to 5 wt % per $cm^3\ g^{-1}$ of micropore volume from the "Chahine rule"). Nevertheless, the two parameter linear fittings (red line) gave lower Root-MSE values, suggesting that the "Chahine rule" overestimates the predicted maximum hydrogen uptake quantities.

From the total hydrogen capacity correlations, equations for BET surface area ($(2.69 \pm 0.81) + (2.06 \pm 0.28)\ X$ total wt % per 1000 $m^2\ g^{-1}$) and for total pore volume ($(2.46 \pm 0.52) + (4.14 \pm 0.32)\ X$ total wt % per $cm^3\ g^{-1}$) were obtained. However, the model indicated very high hydrogen adsorbate densities within the pores of most of the materials when compared to solid hydrogen (87 kg m^{-3} at 0 MPa and 4.4 K) [15].

The methodology applied in section 4.4 allowed checking the change of the modelled pore volume value obtained with the fitting at different maximum hydrogen pressures, tending to more unreasonable values as the maximum pressure of the isotherm becomes lower. A general tendency exists for the modelled pore volumes of the materials to decrease in value with higher pressures. In many cases, the modelled pore volume values get closer to the experimental pore volume of the material, surpassing these in some other cases.

The same curve shapes can be identified in materials with different uptakes, metal cluster and topologies in IRMOF-1, IRMOF-3, IRMOF-7, ZIF-CoNIm, UiO-67 and HKUST-1. Other materials have a similar curve shape to the previously mentioned (IRMOF-6, IRMOF-11, MOF-177 and UiO-66), differentiated in the value of the modelled pore volume at low pressures, which was very low and tended to go up as the maximum used pressure increased. This indicates the existence of different patterns that seem to heavily depend on the shape of the isotherms.

Overall, the higher the maximum pressure of the experimental isotherm was, the closer the modelled pore volume value from the model fitting was to the experimental value. However, the results proved not to be as trivial and clear as initially observed on the three MILs, not showing a direct increase of the robustness of the model by fitting the experimental pore volume for each material. Therefore, since most of the modelled pore volume values obtained at high pressures were somehow close to the experimental ones, although not following a general rule, the experimental pore volume values were used in the model fittings.

In section 4.5, some fittings showed inconsistencies, not fitting well to the experimental isotherms when fixing them with their experimental pore volume/s. The adsorbate density was obtained from each other of the fittings, being them compared with the adsorbate densities obtained from the non-fixed Vp fittings. These new fitting resulted in lower densities overall, also showing more reasonable total hydrogen capacities in some cases.

4.7 References

1. Channing, A. and P. Justin, *Storage Materials Based on Hydrogen Physisorption*, in *Hydrogen Storage Technology*. 2012, Taylor & Francis. p. 213-238.
2. Chahine, R. and T.K. Bose, *Characterization and optimization of adsorbents for hydrogen storage.* Hydrogen Energy Progress Xi, Vols 1-3, 1996: p. 1259-1263.
3. Panella, B., M. Hirscher, and S. Roth, *Hydrogen adsorption in different carbon nanostructures.* Carbon, 2005. 43(10): p. 2209-2214.
4. Gogotsi Y., P.C., Osswald S., Simmons J.M., Yidirim T. , Laudisio G., Fischer J.E. , *Importance of pore size in high-pressure hydrogen storage by porous carbons.* International Journal of Hydrogen Energy, 2009. 34(15): p. 6314-6319.
5. Thomas, K.M., *Hydrogen adsorption and storage on porous materials.* Catalysis Today, 2007. 120(3-4): p. 389-398.
6. Wong-Foy, A.G., A.J. Matzger, and O.M. Yaghi, *Exceptional H-2 saturation uptake in microporous metal-organic frameworks.* Journal of the American Chemical Society, 2006. 128(11): p. 3494-3495.
7. Tranchemontagne, D.J., Park, K.S., Furukawa, H., Eckert, J., Knobler, C.B., Yaghi, O.M., *Hydrogen Storage in New Metal-Organic Frameworks.* Journal of Physical Chemistry C, 2012. 116(24): p. 13143-13151.
8. Aguado, S., Bergeret, , Titus, M.P., Moizan, V., Nieto-Draghi, C., Bats, N., Farrusseng, D., *Guest-induced gate-opening of a zeolite imidazolate framework.* New Journal of Chemistry, 2011. 35(3): p. 546-550.
9. Ryder, M.R., Civalleri, Bartolomeo, B., Thomas D., Henke, S., Rudić, S., Cinque, G., Fernandez-Alonso, F., Tan, J.C., *Identifying the Role of Terahertz Vibrations in Metal-Organic Frameworks: From Gate-Opening Phenomenon to Shear-Driven Structural Destabilization.* Physical Review Letters, 2014. 113(21): p. 215502.
10. Pera-Titus, M., *Intrinsic Flexibility of the Zeolitic Imidazolate Framework ZIF-7 Unveiled by CO2 Adsorption and Hg Intrusion.* ChemPhysChem, 2014. 15(8): p. 1581-1586.
11. van den Bergh, J., Gucuyener, C., Pidko, E. A.,Hensen, E. J. M., Gascon, J., Kapteijn, F., *Understanding the Anomalous Alkane Selectivity of ZIF-7 in the Separation of Light Alkane/Alkene Mixtures.* Chemistry-a European Journal, 2011. 17(32): p. 8832-8840.
12. Chavan, S., Vitillo, J. G., Gianolio, D., Zavorotynska, O., Civalleri, B., Jakobsen, S., Nilsen, M. H., Valenzano, L., Lamberti, C., Lillerud, K. P., Bordiga, S., *H-2 storage in isostructural UiO-67 and UiO-66 MOFs.* Physical Chemistry Chemical Physics, 2012. 14(5): p. 1614-1626.
13. Rowsell, J.L.C. and O.M. Yaghi, *Strategies for Hydrogen Storage in Metal–Organic Frameworks.* Angewandte Chemie International Edition, 2005. 44(30): p. 4670-4679.
14. Zhang, Z.J., Xian, S. K., Xia, Q. B., Wang, H. H., Li, Z., Li, J., *Enhancement of CO2 Adsorption and CO2/N2 Selectivity on ZIF-8 via Postsynthetic Modification.* Aiche Journal, 2013. 59(6): p. 2195-2206.
15. Silvera, I.F., *The solid molecular hydrogens in the condensed phase: Fundamentals and static properties.* Reviews of Modern Physics, 1980. 52(2): p. 393-452.
16. Goodwin and Prydz (1972), J Res National Bureau of Standards – A, 76A, 2, 81-101
17. Johnston *et al*. J Am Chem Soc (1954) 76, 1482
18. Liu, Y., et al., Increasing the density of adsorbed hydrogen with coordinatively unsaturated metal centers in metal-organic frameworks. Langmuir, 2008. 24(9): p. 4772-4777.
19. Wong-Foy, A.G., A.J. Matzger, and O.M. Yaghi, *Exceptional H2 saturation uptake in microporous metal-organic frameworks.* Journal of the American Chemical Society, 2006. 128(11): p. 3494-3495.
20. Millward, A.R. and O.M. Yaghi, *Metal-organic frameworks with exceptionally high capacity for storage of carbon dioxide at room temperature.* Journal of the American Chemical Society, 2005. 127(51): p. 17998-17999.
21. Rowsell, J.L.C. and O.M. Yaghi, *Effects of functionalization, catenation, and variation of the metal oxide and organic linking units on the low-pressure hydrogen adsorption properties of metal-organic frameworks.* Journal of the American Chemical Society, 2006. 128(4): p. 1304-1315.

Chapter Five

Characterisation of adsorbed hydrogen density

5 Characterisation of adsorbed hydrogen density

5.1 Introduction

Researching changes in the density of the adsorbed hydrogen in the pores or the vicinity of nanoporous materials is of utmost importance for a further understanding of hydrogen adsorption. This would mean that in some parts of the pore of the material, a much more dense layer than originally thought might exist, being needed to be able to account for this effect (observed with TOSCA) in order to predict in a more accurate way how hydrogen is adsorbed in the pores and which properties favour this state. Also, modelling this phenomenon helps understanding what really happens in the pore, getting towards a better theoretical ability to predict the behaviour of future materials and, therefore, target better hydrogen storage materials. The work presented in this Chapter is a follow up of research previously started at ISIS, being part of a publication as stated in Chapter 1 [1].

Predictions of adsorbed hydrogen density and pressure inside the pore of IRMOF-1 (MOF-5) as a function of the distance from the pore wall points at low temperatures (ranging between around 40 K and 77 K) show that the pressure inside the pores is high enough to increase hydrogen's density [2-5]. This increase in density is referred as a phase change from gaseous hydrogen to a pseudo-condensed hydrogen state. These predicted densities, higher than bulk solid hydrogen, are attributed to the increased force field in the pores of the MOF [2-5].

As previously stated, solid dihydrogen can be detected by INS (Inelastic Neutron Scattering) tests. When a vessel containing hydrogen equilibrated at 13 K is measured, a sharp intense centred peak at 118 cm^{-1} (14.62 meV) can be observed. At higher temperatures there is a strong and broad shoulder (with some weak overlying features at 37.19 meV). Both peaks can be observed in Figure 5.1:

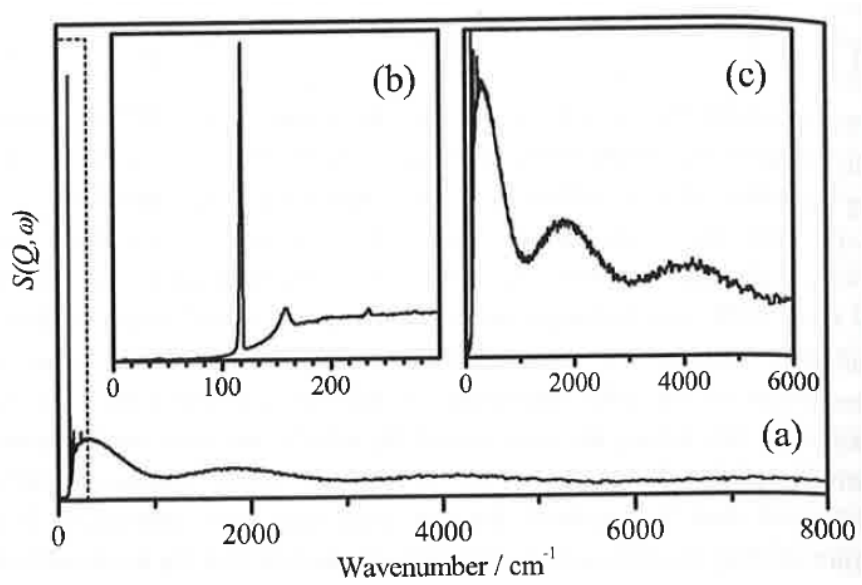

Figure 5.1. INS spectrum of solid dihydrogen at 13 K at different wavenumber ranges. Reprinted from [6], with permission from World Scientific. Copyright 2005.

In the solid and liquid state, dihydrogen has many unusual features that makes it different from other molecular solids and liquids. The most pronounced characteristic is that even when in solid-state, the free rotor that describes the rotational motion of an isolated molecule is almost unperturbed by interactions between the neighbouring dihydrogen molecules. Dihydrogen molecules with their centres of mass localised at lattice positions rotate freely even at the lowest temperatures. This behaviour occurs due to the weak hydrogen intermolecular interactions (the nearest neighbour distances are at around 3.8 Å) and the small moment of inertia of the dihydrogen molecule [6, 7].

5.2 Background

Neutrons are generated in a neutron source. There are two different types of neutron sources: reactor and spallation. Research nuclear reactors use thermal neutrons to induce fission in a critical mass of ^{235}U to produce high energy fast neutrons as shown in Equation 5.1 [6]:

$$n_{thermal} + {}^{235}_{92}U \rightarrow 2.5\, n_{fast+fission\ products} + 180\ MeV \qquad \text{Eq. 5.1}$$

From the 2.5 neutrons produced in every fission, only one neutron is able to leave the core to be used experimentally. About 0.5 neutrons are lost to adsorption and the other one is needed to continue the nuclear reaction. Due to the natural low prevalence of ^{235}U (0.7 % in abundance

in all uranium), natural uranium needs to be enriched. This can lead to concerns regarding nuclear weapon proliferation [6].

Research core reactors are immersed in the middle of a large tank of water that acts as a coolant and moderator. The latest and most advanced research reactor is the 20 MW FRM-II reactor, located in Munich, Germany, whereas the most powerful one with 57 MW of power is the Institut Laue Langevin in Grenoble, France [6].

Spallation sources on the other side, consist of a heavy metal target that is bombarded with pulses of high-energy protons from a powerful accelerator. When protons hit the nuclei in the target, an internuclear cascade is triggered, exciting individual nuclei into a higher energetic state. Some trigger more reactions, while others leave the target. Approximately 15 neutrons are produced per high-energy proton delivered to the target [6]. In Figure 5.2 a diagrammatic representation of the spallation process is shown:

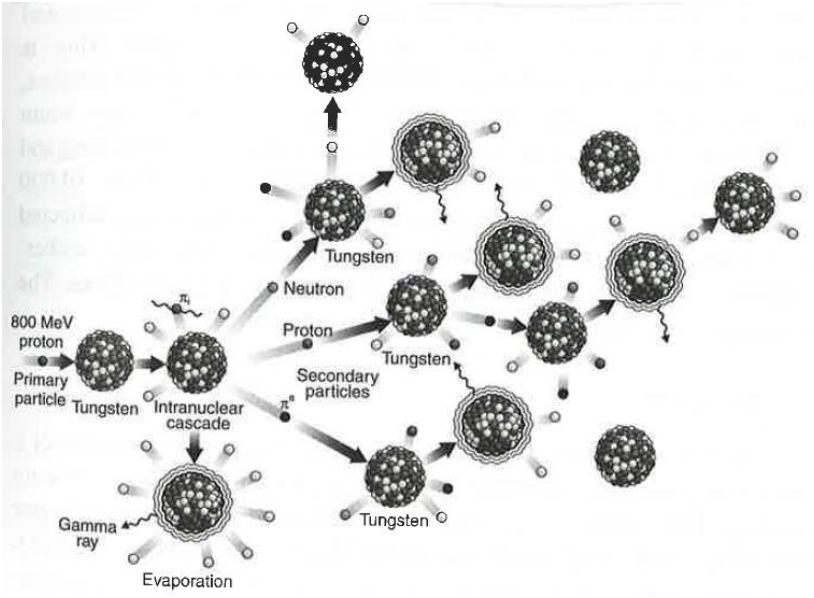

Figure 5.2. Diagrammatic representation of the spallation process. Reprinted from [6], with permission from World Scientific. Copyright 2005.

This process results in a very intense neutron pulse and a modest heat production when compared to a nuclear reactor. The biggest spallation source is the SNS in Oak Ridge, Tennessee, United States. The second biggest, where the experiments took place, is the ISIS neutron source, which is at the Rutherford Appleton Laboratory, Oxfordshire, UK. The instrument used for the INS experiments was TOSCA [6].

At ISIS, the proton beam production begins with H_2 gas together with hot caesium vapour and a caesium-coated cathode to generate H^- ions. The H^- ions are held by an electric field and placed in a radio frequency quadropole accelerator. The accelerator injects the ions into a linear accelerator (also known as LINAC), accelerating the ions to 37 % the speed of light. After this, the ion beam is passed through a 0.3 μm thick aluminium foil, removing both electrons from each ion, leaving only the protons. The proton beam is then injected for approximately 130 cycles of the synchrotron, until it accumulates 4.2×10^{13} protons. These are later on accelerated to 84 % of the speed of light and thrown in pulses of 100 ns long separated 230 ns. These pulses hit the ISIS target, made of thin tungsten plates, where the neutrons are produced and sent to all the different devices [6].

Inelastic scattering is a fundamental scattering process in which the kinetic energy of an incident particle is not conserved (in contrast to elastic scattering). In an INS experiment, it is observed how the strength of neutron scattering varies with the energy transfer and momentum transfer. The momentum is the quantity of movement of a particle (defined as the product of the mass and speed of the particle). Part of this momentum is transferred from the neutron to the atoms of the sample, making them vibrate while the energy of the incident neutron is lost or increased. The intensities obtained from INS tests can be directly related to the atomic displacements of the scattering atom. Unlike photons, neutrons are able to penetrate deeply, passing through walls of vessels (generally aluminium or steel), where the sample is located. Therefore, INS results are weighted to the measurement of bulk properties. By the same token, INS results of a sample plus its container can be straightforwardly manipulated, *e.g* the background subtraction of the signal pertaining to the vessel where the sample is confined [6].

INS spectra are sensitive to hydrogen atom vibrations. The neutron incoherent scattering cross section of hydrogen is uniquely high, making its signal around ten times more visible than any other atom. Also, the measured INS intensities are proportional to the concentration of the elements in the sample, making INS a useful technique to measure hydrogen and its interaction with the sample [6]. Furthermore, INS spectrometers presents a wide measuring range (from 16 to 4000 cm^{-1}). It can measure below 400 cm^{-1}, a region experimentally more difficult for infrared and Raman spectroscopies. This is especially important since the peak that indicates

the presence of solid-like hydrogen (found at 14.7 meV or 118.5 cm^{-1}) is of paramount importance for studying hydrogen interactions [6].

Although detailed understanding of a molecular structure is best achieved by the use of diffraction techniques, many systems of interest and importance to the chemical and materials science communities do not appear as single crystals (such as activated carbons). Neutron vibrational spectroscopy is just another variant with the ability to calculate the spectral band positions and intensities, even for non-crystalline materials [6]. For INS tests, carbons were chosen to study fundamental interactions of hydrogen with materials as carbon materials are simpler model compounds while the hydrogen capacity studies were done solely on MOFs due to their high uptakes. Also, previous INS experiments with TE7, an activated carbon, showed the 14.7 meV solid-like hydrogen peak at 77 K.

As mentioned in Chapter 4, Gogotsi *et al.* investigated a large number of carbide-derived carbons that possessed controlled pore size distributions and surface areas in order to determine the optimum pore size for hydrogen storage [8]. According to the results obtained, it was found that pores larger than 1.5 nm in diameter have little contribution to hydrogen storage and that materials containing pore sizes between 0.6 and 0.7 nm in diameter provide the largest hydrogen uptake per unit of area at high pressures and 77 K. Therefore, the best hydrogen storage materials will have high microporosity being most of these between 0.6 and 0.7 nm in diameter [8, 9]. Also, high surface area and high micropore volume have shown to have a positive effect on hydrogen storage [8, 9]. In Figure 5.3, a plot presenting the excess capacity normalized per surface area of each material versus pore size experimentally shows which pore ranges are best for hydrogen storage.

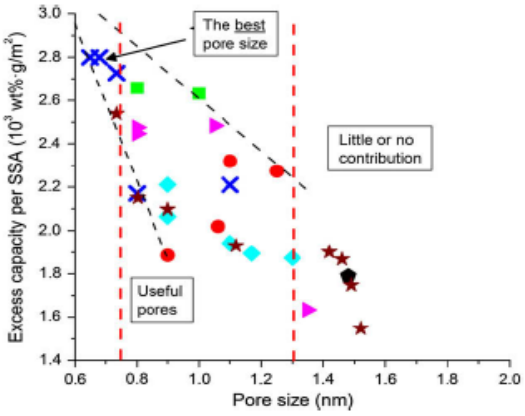

Figure 5.3. Excess capacity normalized to surface areas *vs.* average pore size for several tested carbide-derived carbons. Reprinted from [8]. Copyright 2009, with permission from Elsevier.

5.3 Inelastic Neutron Scattering model validation

5.3.1 Introduction

Two BeCu sample cells were tested at 77 K with hydrogen during this experiment using a high pressure rig in TOSCA, located in the Rutherford Appleton Laboratory, Oxfordshire, United Kingdom. Both cells were tested in a range between 0 and 359 bar. One sample contained a mix of TE7_20 carbon beads, degassed 23 h at 350 °C, and deuterated octadecane, a material used to fill the intergranular space between the beads while the other cell tested was empty. Both cells where previously leak tested at high pressures with He in order to make sure no leaking occurred during the measurements.

Octadecane was previously tested at the University of Bath, showing inability to trap hydrogen. Therefore, octadecane is assumed to entirely fill the interstitial space and, at the same time, allow hydrogen to pass through, being only able to be adsorbed in the TE7_20 carbon beads.

5.3.2 Results and discussion

From the normalised empty cell results seen in Figure 5.4, the relationship between the integrated intensity (in the inelastic region since all hydrogen is in gaseous state in the empty cell) and hydrogen density was drawn. In order to achieve this, the density value at every pressure was obtained from the NIST website. Afterwards, a linear fitting between intensity and density was performed, obtaining equation 5.2 (R^2 = 0.998), where X is the integrated intensity from the inelastic region (meV) and Y is the hydrogen density (mol m^{-3}), whose results can be seen in Table 5.1:

$$Y = 170.28\,X + 191.71 \qquad \text{Eq.5.2}$$

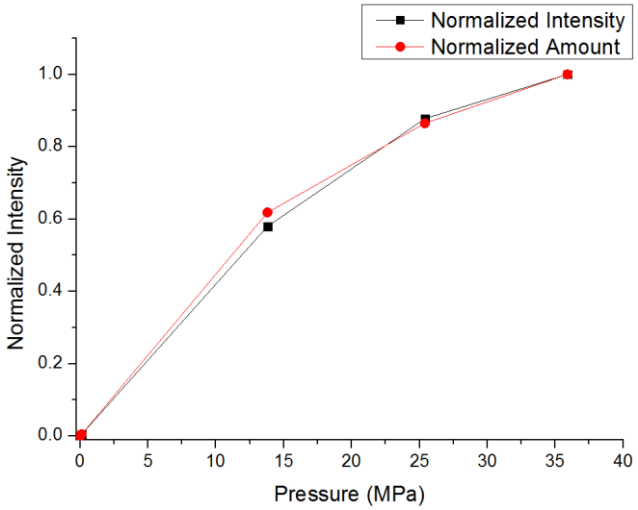

Figure 5.4. Normalized intensity (2 to 500 meV) and normalized amount (density) vs pressure of the empty can.

Table 5.1. INS intensity from the empty can (TOSCA) and NIST density data.

Empty can	**Pressure (MPa)**	**Integrated intensity from inelastic region (2 to 500 meV)**	**NIST density (mol m^{-3})**
Inelastic region (2 to 500 meV)	0	33.81	0
	0.102	34.70	156.45
	13.8	142.97	19845
	25.4	198.93	27767
	35.9	221.97	32096

In Figure 5.5 and Figure 5.6, the raw data from INS in the elastic (-2 to 2 meV) and inelastic regions (2 to 500 meV) are respectively shown:

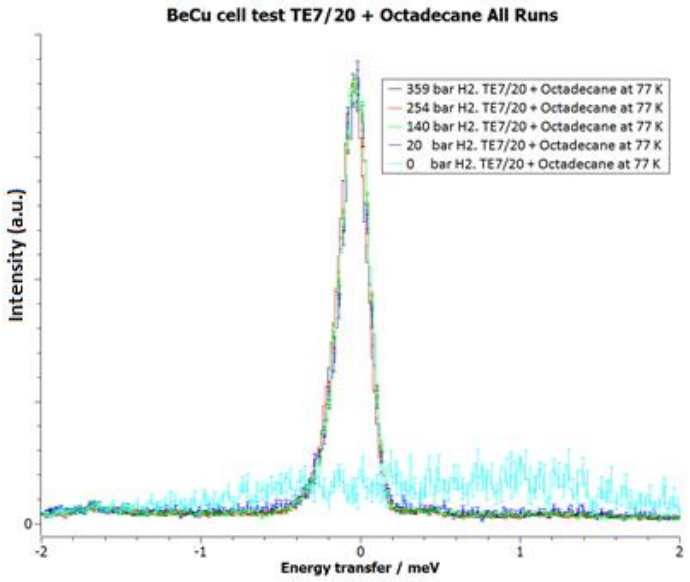

Figure 5.5. TE7_20 + Octadecane intensity vs Energy transfer (meV) in the elastic region (-2 to 2 meV) from TOSCA at 0 (teal), 20 (blue), 140 (green), 254 (red) and 359 (black) bar and 77 K.

Figure 5.5 presents the area in the elastic region from the can with TE7_20 + Octadecane, showing a negligible noise at 0 bar, increasing at 20 bar, showing a very similar area for the rest of tested pressures (140, 254 and 359 bar). This indicates that the amount of hydrogen adsorbed by the TE7_20, or absolute, remains the same with increasing pressure, as later shown in Figure 5.8 compared with the model results.

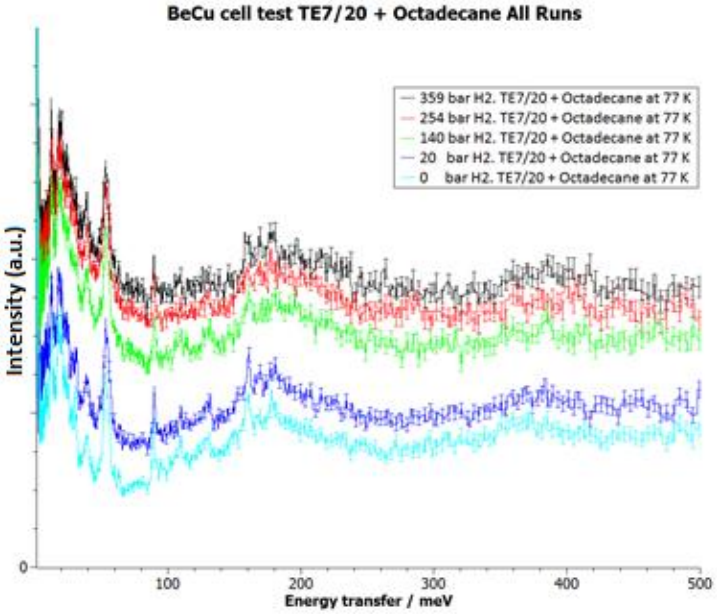

Figure 5.6. TE7_20 + Octadecane intensity vs Energy transfer (meV) in the inelastic region (2 to 500 meV) from TOSCA at 0 (teal), 20 (blue), 140 (green), 254 (red) and 359 (black) bar and 77 K.

Figure 5.6 presents the inelastic region from the can with TE7_20 + Octadecane. Data at 0 bar shows the background signal (of the can, TE7_20 and octadecane), increasing the overall signal level with increasing pressure. This is due an increase of the hydrogen density of the gaseous hydrogen contained in the can.

Equation 5.2 was later used to determine the gaseous hydrogen density in the cell with the TE7_20 and deuterated octadecane. This was done by using the equation and integrated intensity values from the inelastic region, whose results from graphs and calculations are gathered in Table 5.2:

Table 5.2. INS intensity from the can with TE7_20 + octadecane (TOSCA) and NIST density data.

TE7_20 + Octadecane can	**Pressure (MPa)**	**Integrated intensity from elastic region (-2 to 2 meV)**	**Integrated intensity from inelastic region (2 to 500 meV)**	**NIST density (mol m^{-3})**
Inelastic region (2 to 500 meV)	0	0	0	0
	2.7	8.60	21.72	3890
	14	8.84	70.29	12162
	25.4	8.75	92.27	15905
	35.9	8.61	106.70	18362

TE7_20 was tested with hydrogen up to 14 MPa at 77 K (Figure 5.7). This data was modelled in order to obtain the absolute amount of hydrogen in the sample and compare it with the normalised intensity obtained from the elastic region from Table 5.2, seen in Figure 5.8:

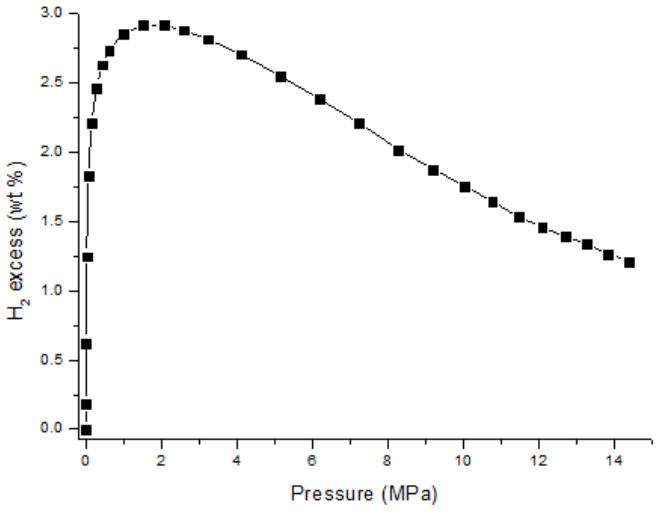

Figure 5.7. TE7_20 experimental hydrogen excess isotherm at 77 K.

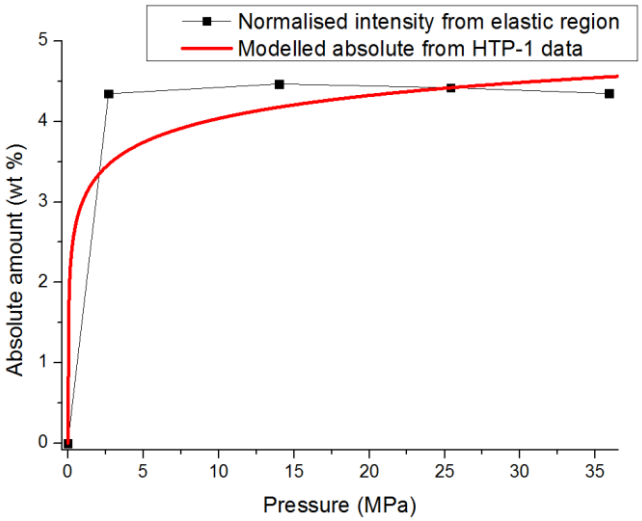

Figure 5.8. Modelled absolute adsorption data from the HTP-1 and normalised INS scattering intensity values from the elastic area (2 to -2 meV).

From Figure 5.8, it can be seen that the INS data gives an almost constant intensity in the elastic region for most of the tested pressure points (the deviation from the last two could have been produced because of less exposure time to the beam due to time constrains), suggesting that the amount of dense hydrogen in the sample gets to a maximum and remains constant from 2 MPa, where the maximum uptake is obtained (Figure 5.7). The experimental data do not correlate with the model at lower pressures, getting to very similar values at the higher tested pressures (Figure 5.8).

From this calculated intensity from the elastic area (that relates to the densified hydrogen in the pores), added to the gaseous amount of hydrogen obtained from the inelastic region, the total amount of hydrogen in the material is calculated. This total amount is compared with the modelled total amount of hydrogen (fitting results from data shown in Figure 5.7) in Figure 5.9:

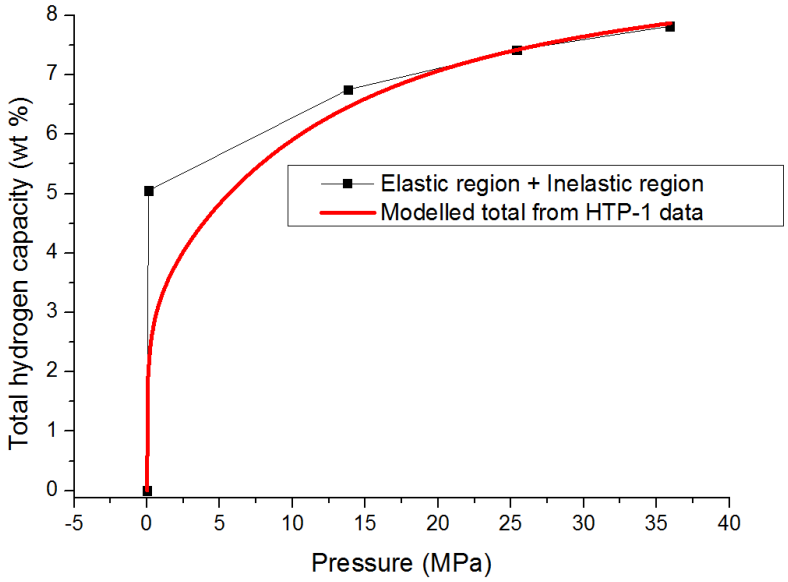

Figure 5.9. TOSCA total hydrogen normalized amount (in arbitrary units) vs modelled total adsorption data from the HTP-1.

From Figure 5.9, a similar result is obtained, showing large differences at low pressures and very similar data values at high pressures, showing that the model adapts well to the experimental TOSCA data at high pressures. However, neither the modelled isotherm nor the TOSCA data show a plateau at high pressures as it was expected. This result is likely to be due to the increase of gaseous hydrogen in the sample. In Figure 5.6, an increased signal in the inelastic region is observed from 254 to 359 bar, meaning that more gaseous bulk hydrogen has been incorporated in the pores of the sample (and not adsorbed). Since the absolute amount, remains constant and the gaseous hydrogen increases, it is assumed that the pores of the TE7_20 are partially filled with dense hydrogen being the rest non-adsorbed gaseous hydrogen. This non-adsorbed hydrogen inside the pores equals the bulk density and increases as the bulk pressure increases.

It was found that, despite the existence of the densified hydrogen peaks in the elastic region, the 14.7 meV peak that ratifies the existence of solid-like hydrogen is absent in the raw data. This fact states uncertainty regarding the existence of solid-like hydrogen in the TE7_20 carbon beads with octadecane. There might be interactions between the deuterated octadecane and the activated carbon that could block the signal or do not allow hydrogen to interact with the TE7_20 as strongly as if it was not present.

5.4 Evidence of Solid-like Hydrogen in Activated Carbons

5.4.1 Introduction

This second set of experiments was conducted on 4 different activated carbons: TE3 carbon beads, TE7_20 carbon beads (MAST Carbon International, Basingstoke, UK), AX-21 and carbon onion OLC-1750 (INM, Leibniz Institut Saarbrücken, Germany). All the materials were tested at 0 and 1 bar to an equivalent of 12 h per test. The aim was to find more materials that showed the 14.7 meV solid-like hydrogen peak signal by using different types of carbons and determine which intrinsic properties (especially pore size) may contribute to the appearance of this phenomena.

5.4.2 Results and discussion

All the materials were degassed according to the settings specified in Chapter 3 for 18 h before they were sent in ASAP 2020 tubes to the Rutherford Appleton Laboratory, Oxfordshire. At ISIS, all the samples were loaded inside stainless steel cells in order to be tested in TOSCA using a glovebox. Before the samples were tested, they were degassed again at 200 °C overnight under vacuum. The TGA information data of the materials can be found in Supplementary Information E.

Hydrogen isotherms at 77 K and characterization by nitrogen adsorption were done in order to measure their hydrogen excess and determine their intrinsic properties. Figure 5.10 shows the adsorption isotherms of the 4 materials up to 1 bar and at high pressures for the 3 materials with the highest uptake, all measured at 77 K. From this results, it can be seen that AX-21 is the one with the highest hydrogen uptake, followed by the TE3 carbon beads (a more microporous version of TE7_20), TE7_20 and OLC-1750.

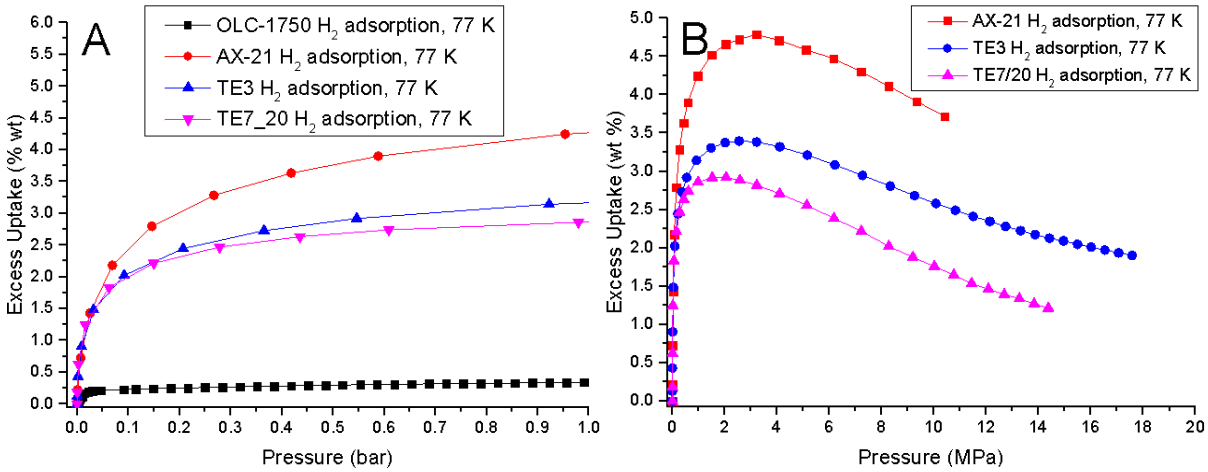

Figure 5.10. 77 K hydrogen excess isotherms of OLC-1750, AX-21, TE3 and TE7_20 up to 1 bar (A) and high pressure hydrogen uptake of AX-21, TE3 and TE7_20 (B).

In the Figures 5.11 to 5.14, the raw data obtained from the test of the 4 materials at both 0 and 1 bar of pressure are shown. Background intensities (data at 0 bar) measure the signal from the stainless steel can and each activated carbon, being these different due to their different carbon natures. The differences observed between 0 and 1 bar measurements are due to the hydrogen present in the cell with the materials:

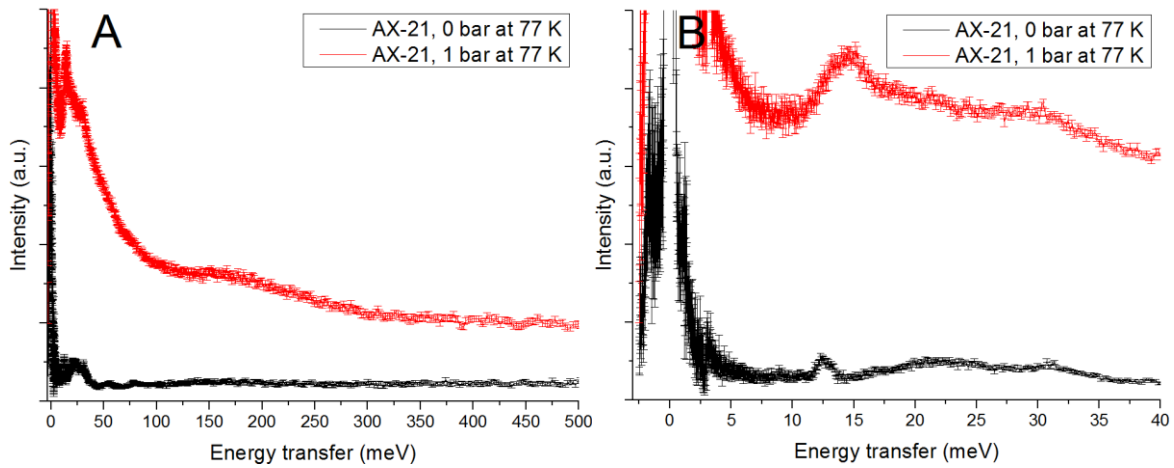

Figure 5.11. AX-21 raw plots at 1 bar and 0 bar. Inelastic region (0 to 500 meV for A and 0 to 40 meV for B).

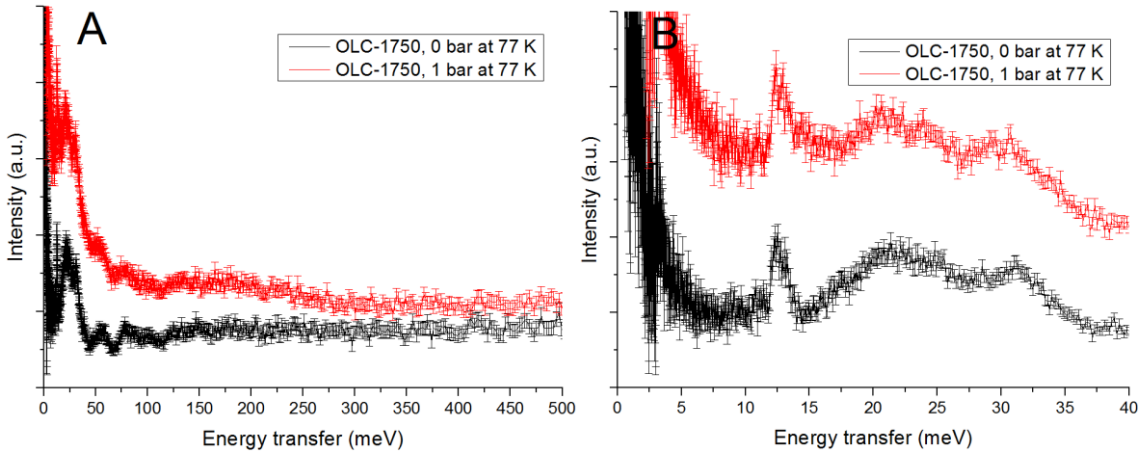

Figure 5.12. OLC-1750 raw plots at 1 bar and 0 bar. Inelastic region (0 to 500 meV for A and 0 to 40 meV for B).

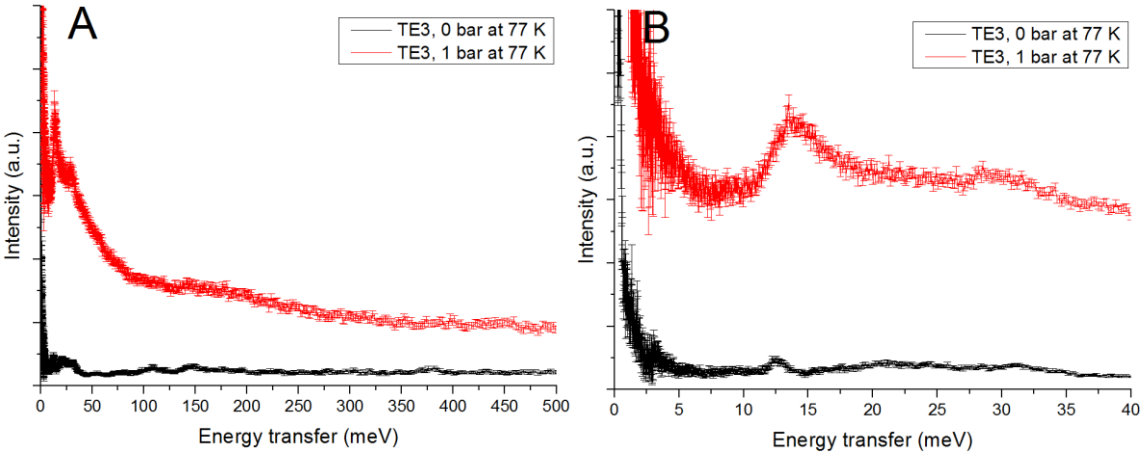

Figure 5.13. TE3 raw plots at 1 bar and 0 bar. Inelastic region (0 to 500 meV for A and 0 to 40 meV for B).

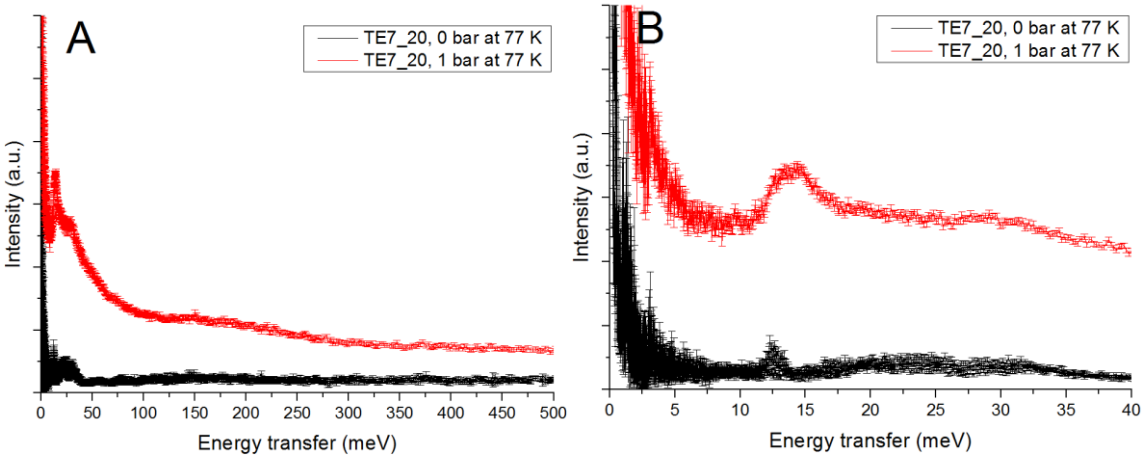

Figure 5.14. TE7_20 raw plots at 1 bar and 0 bar. Inelastic region (0 to 500 meV for A and 0 to 40 meV for B).

Since the main feature is the peak at 14.7 meV, it was decided for each material to subtract the 0 bar from the 1 bar data, obtaining the change in INS resulted from the interaction of hydrogen for each material. After that, the area below the 14.7 meV peak was calculated for each material. A Gaussian curve with centre in 14.7 meV ranged from 10 to 20 meV was fit for each dataset. The fitting graphs can be seen in Figure 5.15, being a summary of the fittings and the materials characterization gathered in Table 5.3 that can also be found in Chapter 3:

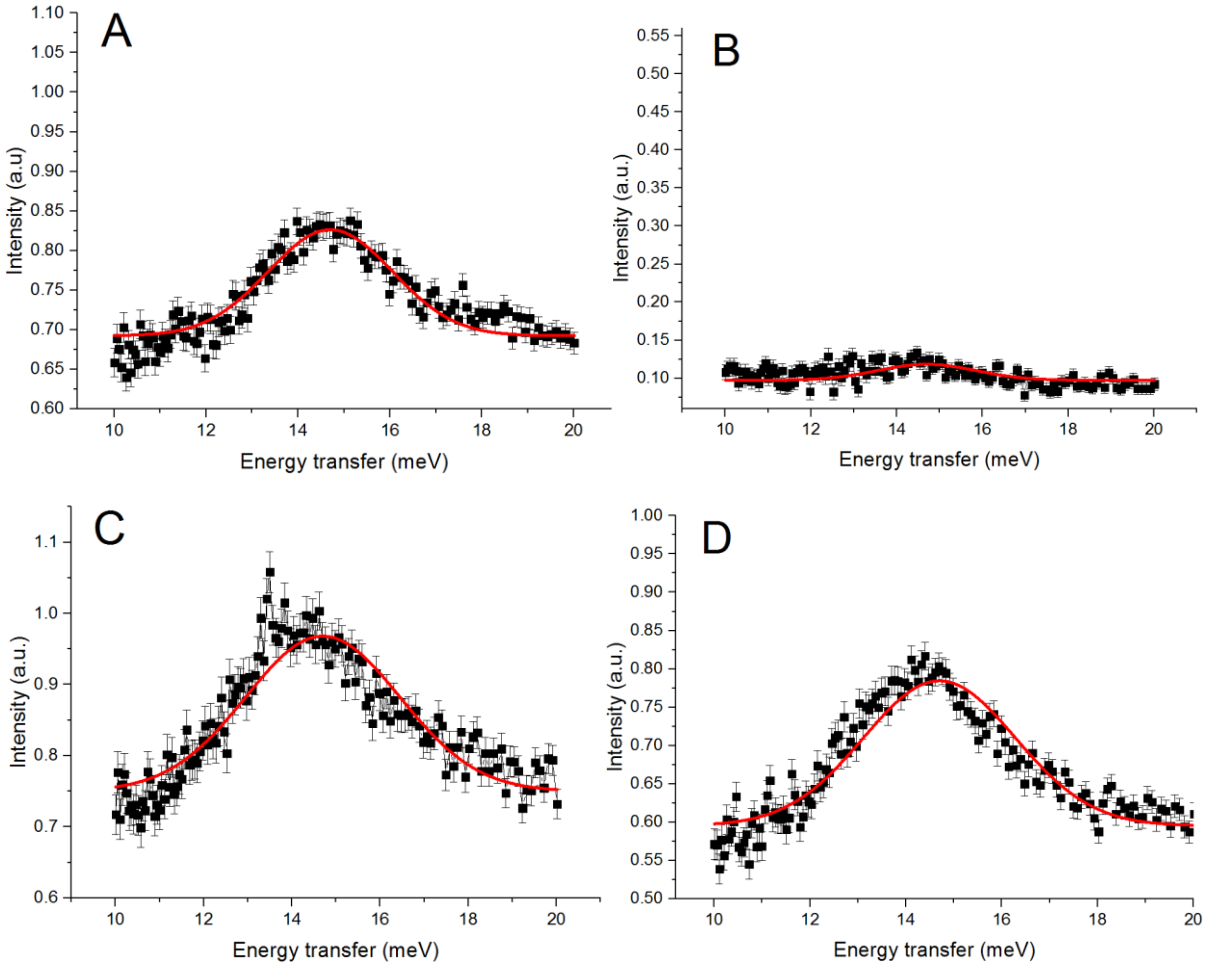

Figure 5.15. 14.7 meV Gaussian peak fit with center in 14.7 meV ranged between 10 and 20 meV for AX-21 (A), OLC-1750 (B), TE3 (C) and TE7_20 (D).

Table 5.3. 14.7 meV Gaussian peak fit results and nitrogen characterization results of AX-21, OLC-1750, TE3 and TE7_20. Error bars represent the standard error when calculating the area below the curve and the BET calculations.

Material:	14.7 meV area peak (Gauss):	BET ($m^2\ g^{-1}$)	Total pore volume (HK) ($cm^3\ g^{-1}$)	Micropore volume (DR) ($cm^3\ g^{-1}$)	Pore diameter (DFT, N_2) (Å)
AX-21	0.4533 ± 0.0243	2524 ± 47	1.82	1.97	5, 6.8, 8.3, 12, 16 and 21
OLC-1750	0.0605 ± 0.0109	320 ± 2	1.29	0.13	11
TE3	0.9561 ± 0.0742	1567 ± 21	1.24	0.73	5.1, 8.1, 12 and 15
TE7_20	0.7510 ± 0.0436	1234 ± 7	1.33	0.52	5, 6.8, 12 and 15

From the fitting results it can be observed that all but the OLC-1750 present the 14.7 meV peak. The highest area value corresponds to TE3, the material with the second highest uptake. This difference in intensity of more than two times than AX-21 seems to be related to TE3's narrower PSD, having more or denser solid-like hydrogen in the pores. By applying the model, fixing different pore volume values, the following adsorbate densities were obtained (Table 5.4):

Table 5.4. Adsorbate densities obtained by using different pore volume values when fitting the model to the experimental data. Error bars represent the standard error of ρ_A obtained from the model fittings of the experimental hydrogen isotherms.

Material:	Vp from model ($cm^3\ g^{-1}$)	ρ ± error (non-fitted Vp) ($kg\ m^{-3}$)	ρ ± error (DR) ($kg\ m^{-3}$)
TE3	0.75	77.89 ± 0.61	78.39 ± 0.25
AX-21	1.16	77.86 ± 1.53	69.04 ± 1.00
TE7_20	0.83	58.38 ± 0.22	67.14 ± 0.78

The predicted adsorbate density values obtained from the fitting (DR) also indicate a denser adsorbate density for TE3 compared to AX-21, indicating a more efficient storage. However, AX-21 shows a higher hydrogen uptake due to its greater pore volume and surface area, being the pore volume 2.7 times higher that of TE3. Same reasoning applies between TE7_20 and AX-21.

When comparing TE3 and TE7_20, TE3's peak area is 27 % higher while showing very similar PSDs. This difference can be accounted for the higher microporosity of TE3 compared to TE7_20, being this value around 40 % higher (Table 5.3), which also explains the higher hydrogen uptake seen on Figure 5.10. PSD results also show TE3 to have higher micropore volume at lower widths (5 Å) compared to TE7_20. PSD results are shown in Figure 5.16:

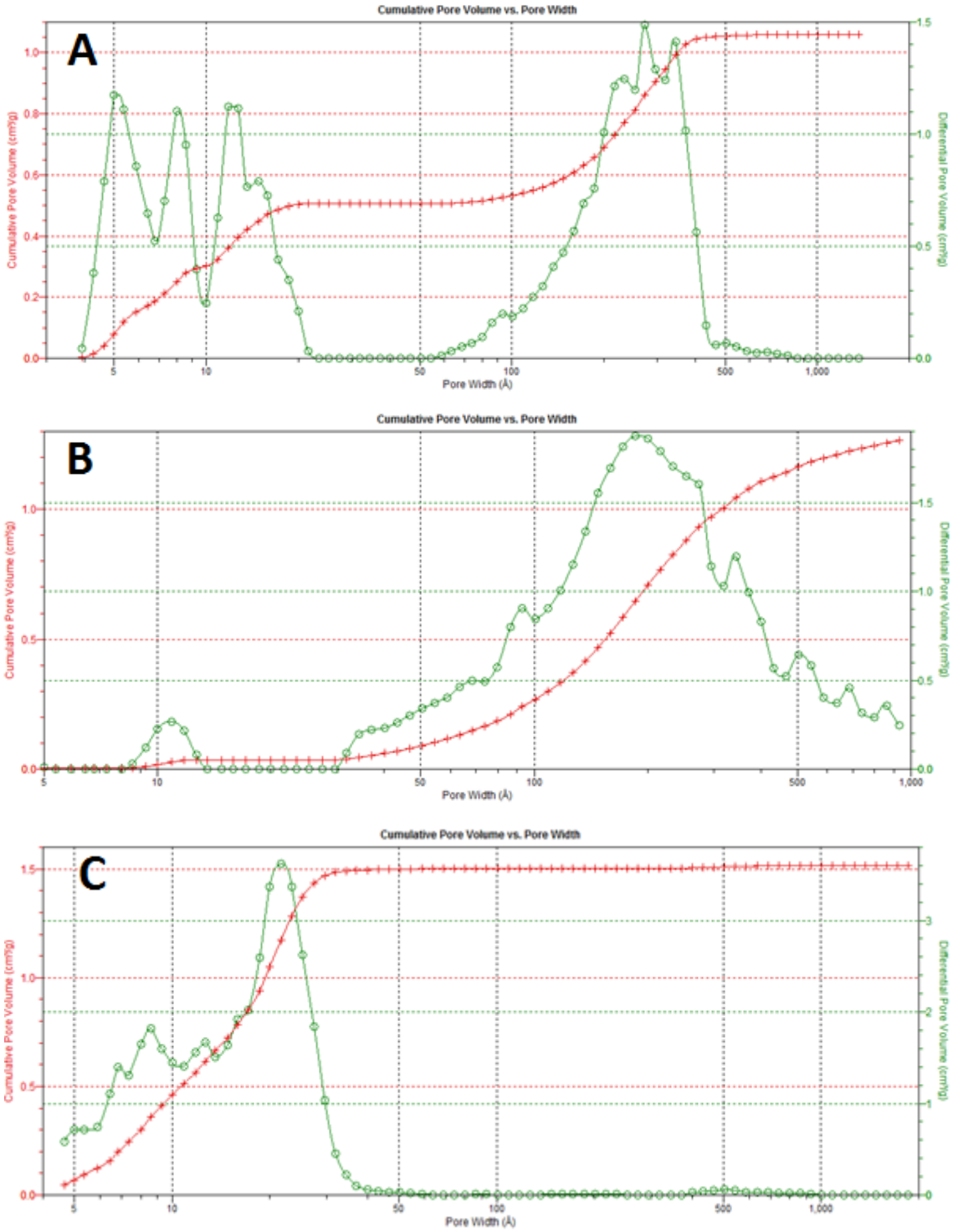

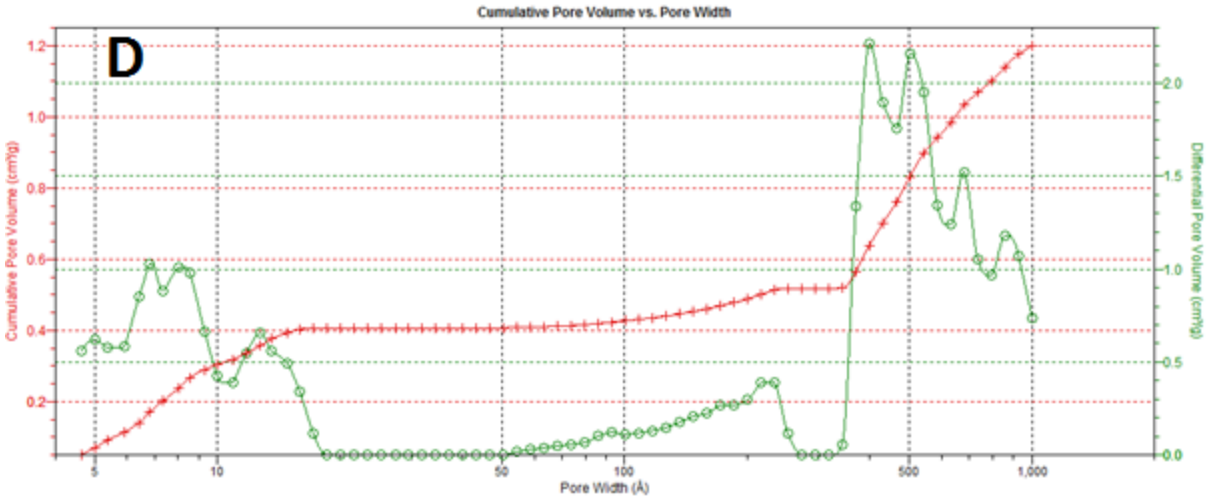

Figure 5.16. TE3 (A), OLC-1750 (B), AX-21 (C) and TE7_20 (D) nitrogen DFT pore size distributions.

Peak intensity was correlated against all intrinsic properties (total pore volume, micropore volume, BET and pore size), only showing a relationship with pore size, which can be seen in Figure 5.17:

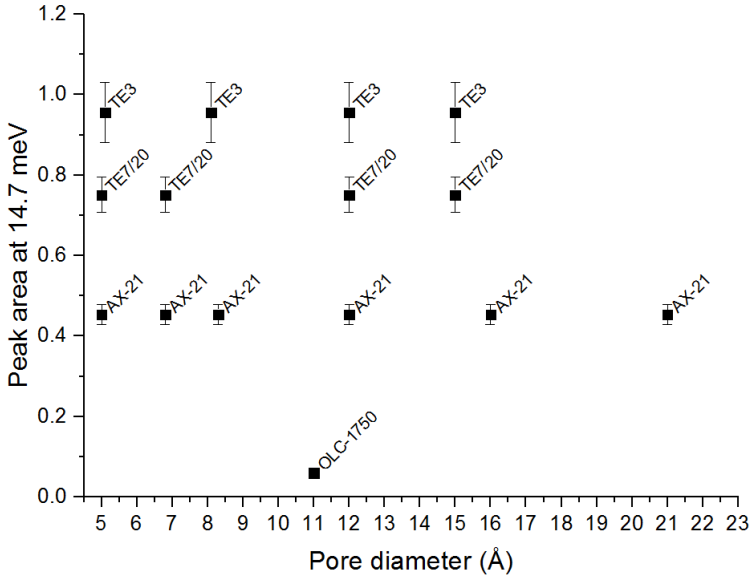

Figure 5.17. Fitted intensity area from the 14.7 meV peak vs PSD calculated from nitrogen adsorption (DFT). Error bars represent the standard error when calculating the area below the curve of the 14.7 meV.

As previously stated, OLC-1750, with a pore size of 11 Å, did not show any 14.7 meV peak, meaning that the pores of TE3, TE7_20 and AX-21 with sizes above 11 Å will have a lower hydrogen adsorption compared to the smaller ones. From the previous comparison between TE3 and TE7_20, it can be seen that the intensity of the 14.7 meV peak is favoured by a higher microporous volume and a higher amount of lower pore sizes (5 Å). However, this data does

not clearly show the solid-like contribution of each pore smaller than 11 Å due to the various different pore sizes observed in TE3, TE7_20 and AX-21.

5.5 Conclusions

The absence of the 14.7 meV peak in the first study using octadecane and TE7_20, created uncertainties regarding the existence of solid-like hydrogen in the material's pores as well as the results obtained. This lead to several possible reasons such as the blocking of the signal by the octadecane. Other possibility is that, although octadecane lets hydrogen to pass through, it might have affected the adsorption of hydrogen by the activated carbon. This might be because the octadecane covers the pores and/or the walls of the pores, not allowing hydrogen to bind as strongly as without octadecane.

The results of the second study confirmed the existence of solid-like hydrogen within the pores of some of the tested microporous activated carbons and their relationship with their smaller pore sizes [1]. This conclusion helps towards a wider understanding of hydrogen storage by using nanoporous materials, further backing up the model used to model the excess used in the correlations in Chapter 4. OLC-1750, a material with pores of 11 Å in diameter and above, shows no 14.7 meV peak, being probably to be too large and therefore having weaker van der Waals forces for adsorbing hydrogen in solid-like state at 77 K.

The model agreed with the experimental results, showing that TE3 has the highest peak area and predicted adsorbate density among the four materials. These observations indicated the existence of a pore range for the formation of solid-like hydrogen in the pore, being this between 5 and 11 Å. From this data and previous experiments, it can be predicted that there will be solid-like hydrogen if a material has pores within 5 and 7 Å. Since TE3 showed a higher 14.7 meV peak area compared to TE7_20, having a very similar PSD, it indicates that a higher microporous volume enhances the amount of solid-like hydrogen in the material. TE3 showed more 5 Å pores than TE7_20, indicating that these pores can hold denser solid-like hydrogen, although more research needs to be conducted. This conclusion is not far from Gogotsi *et al*., which concluded that 7 Å is the optimum pore size for hydrogen storage [8].

5.6 References:

1. Ting, V.P., Ramirez-Cuesta A.J., Bimbo N., Sharpe, J.E., Noguera-Diaz A., Presser V., Rudic S., Mays, T.J., *Direct Evidence for Solid-like Hydrogen in Microporous Carbon at Supercritical Temperatures.* ACS Nano, 9 (8), pp 8249–8254.
2. Bae, Y.S. and R.Q. Snurr, *Molecular simulations of very high pressure hydrogen storage using metal-organic frameworks.* Microporous and Mesoporous Materials, 2010. 135(1-3): p. 178-186.
3. Dundar E., Zacharia R., Chahine R., Benard P., *Modified potential theory for modeling supercritical gas adsorption.* International Journal of Hydrogen Energy, 2012. 37(11): p. 9137-9147.
4. *Dundar E., Zacharia R., Chahine R., Benard P., Performance comparison of adsorption isotherm models for supercritical hydrogen sorption on MOFs (vol 363, pg 74, 2014).* Fluid Phase Equilibria, 2014. 367: p. 204-204.
5. N. C. Gallego, L.L.H., D. Saha, C.I. Contescu, Y.B. Melnichenko, *Hydrogen Confinement in Carbon Nanopores: Extreme Densification at Ambient Temperature.* Journal of the American Chemical Society, 2011. 133(35): p. 13794-13797.
6. Mitchell P.C.H., P.S.F., Ramirez-Cuesta A.J., Tomkinson J. , *Vibrational Spectroscopy with Neutrons.* 2005, World Scientific.
7. Silvera, I.F., *The solid molecular hydrogens in the condensed phase: Fundamentals and static properties.* Rev. Mod. Phys., 1980. 52: p. 393-452.
8. Gogotsi Y., P.C., Osswald S., Simmons J.M., Yidirim T. , Laudisio G., Fischer J.E. , *Importance of pore size in high-pressure hydrogen storage by porous carbons.* International Journal of Hydrogen Energy, 2009. 34(15): p. 6314-6319.
9. Panella, B., M. Hirscher, and S. Roth, *Hydrogen adsorption in different carbon nanostructures.* Carbon, 2005. 43(10): p. 2209-2214.

Chapter Six

Impregnation studies. Pore size modification

6 Impregnation studies. Pore size modification

6.1 Background

Increasing the enthalpy of adsorption of materials would increase their hydrogen capacities. It has been calculated that an energy interaction of about 20 kJ mol^{-1} would give a high adsorption capacity in MOFs at ambient temperatures [1, 2].

To improve the enthalpy of adsorption of these materials, several ideas such as the use of shorter linkers, investigation of new topologies, catenation, increasing the number of open metal sites, using lighter metals as metal ions or clusters, the use of functionalised linkers and impregnation have been proposed [1].

Catenation consists in growing two or more frameworks with MOF topologies that allow this. This catenation can take the form of interpenetration (obtaining a maximum displacement from each other framework) or interweaving (minimal displacement, having many close contacts and forming an infinite periodic chain mail). Interpenetration is preferred over interweaving since it decreases the pore size without blocking adsorptive sites, whereas interweaving does block them, providing an increase in the stability of the structure by effectively thickening the framework walls [1-3].

Another possibility is to create open metal sites in the framework. Several MOFs have been seen with metal clusters that have additional terminal ligands bound to them. These are solvent molecules that can be released by simple heating. In the best cases, these terminal ligands are removed without affecting the framework structure, leaving an open metal site exposed to the void region. MOF-11 and HKUST-1 are examples of materials that allow open metal sites while still showing stability [1, 2].

Also, using lighter metals as metal ions or clusters could reduce the framework density and therefore, increase their gravimetric uptake. Light cations such as Li^{+}, Na^{+}, $Mg^{2+,}$ and Al^{3+} could be used [1, 2]. Furthermore, their organic linkers could be functionalised as well, increasing their affinity for hydrogen, and therefore, their heat of adsorption.

Hydrogen correlations presented in Chapter 4 have shown that a high surface area and/or high pore volume in nanoporous materials contribute towards increasing their hydrogen capacities. Also, the size of the pores of the materials, as pointed out in Chapters 4 and 5 affects hydrogen sorption as well. The ideal pore size for maximum attraction of adsorbate to the MOF is considered to be the same as the adsorbate's van der Waals diameter [1]. Ideal materials should be tuned this way as well as being formed of light elements and having thin walls [1].

The optimum design of MOFs for hydrogen storage has been elusive, many of them have been found not to effectively store the gas due to the large spacing between their walls or links. As an example, IRMOF-1 pore size is 15 Å, far from the 2.89 Å kinetic diameter of hydrogen (shown in Figure 6.1), leading to an unused volume at the centre of the pores that would detract from the volumetric packing density [1, 2, 4].

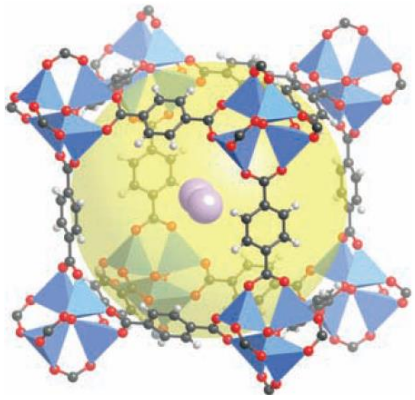

Figure 6.1. IRMOF-1 (MOF-5). The pore (yellow sphere, 15.2 Å) is much larger than the size of a hydrogen molecule (lilac, shown with atomic van der Waals radii of 1.2 Å), which has a kinetic diameter of 2.89 Å. Framework atoms C: black, H: white, O: red, Zn: blue tetrahedra. Reprinted from [5], with permission from John Wiley and Sons.

One way of tuning the pore size of a material is impregnation. This technique consists in inserting another adsorbate surface inside the large pores of a MOF. As an example, C_{60} can be included in a MOF to reduce the free diameter of the pores, providing additional adsorptive sites and reduce the effective pore size [1, 2]. Theoretical calculations using the Lennard-Jones potential function and a variety of Monte Carlo techniques indicated that MOF-177 impregnated with C_{60} fullerenes would have a high hydrogen adsorption enthalpy (11 kJ mol^{-1}) with a small decrease as a function of the hydrogen filling, not diminishing this value with hydrogen loading [6]. Fullerenes are considered as attractive materials for hydrogen storage, being able to store up to 58 hydrogen atoms internally, equivalent to an excess uptake of 7.5 wt %. "Decoration" of fullerene external surfaces with transition metals result in higher

adsorption performance. Therefore, it is desirable to design MOFs made of transition metals that have high hydrogen uptakes, containing fullerenes in the pores of their structures [6]. Because of this, a system formed of a MOF and C_{60} carbon fullerenes inside its framework was designed in order to optimise pore size.

6.2 Results and discussion

IRMOF-1 was impregnated with fullerene C_{60} (purchased from Sigma Aldrich) with the intention of increasing the adsorption of hydrogen. As previously defined, impregnation consists of inserting another adsorbate surface inside the large pores of a MOF. This would reduce the free diameter of the pores, providing additional adsorptive sites [1, 2].

Synthesis protocols and XRD spectra and characterization results of both IRMOF-1 and IRMOF-1 C_{60} have been previously described in Chapter 3 and Supporting Information D, E and F. Because of its relevance in this study, the powder XRD spectra of both species are presented again in Figure 6.2:

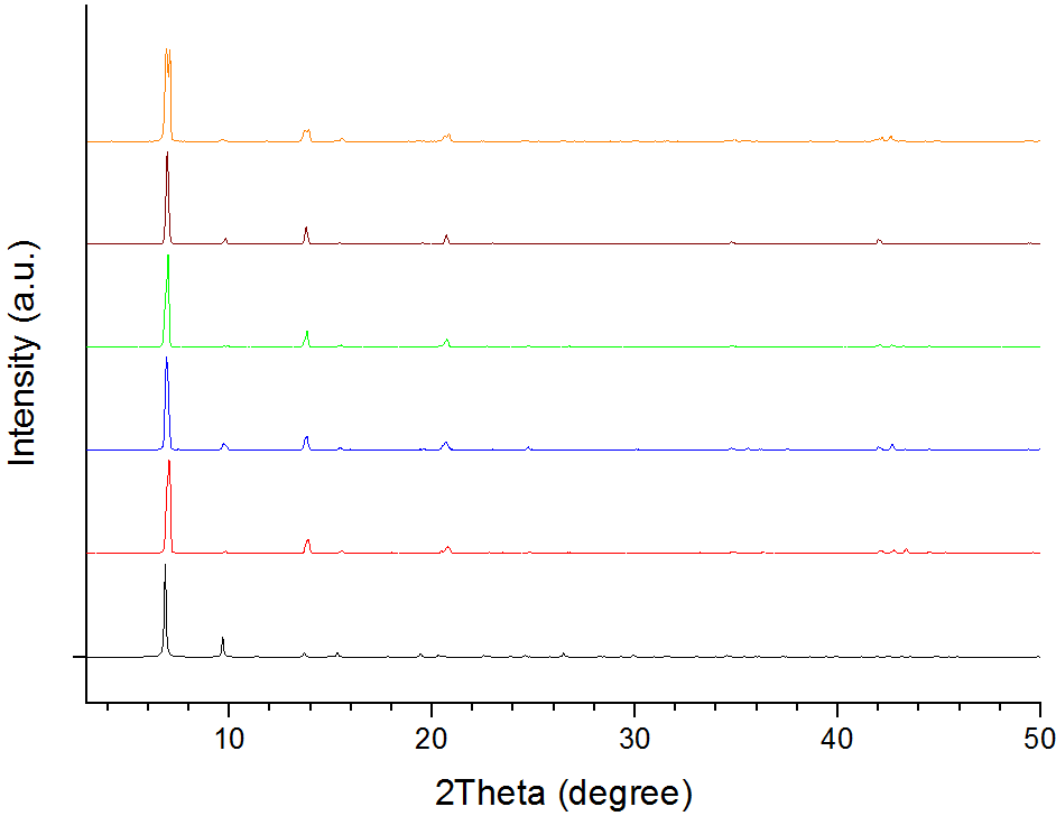

Figure 6.2. PXRD of IRMOF-1. PXRD from CIF file (black), IRMOF-1 (red, blue and green) and IRMOF-1 C_{60} batches (brown and orange).

According to literature, the fullerene C_{60} has 0.8 nm in diameter, whereas different values have been found for IRMOF-1, shown in Table 6.1 [7]:

Table 6.1. Pore and window diameter of IRMOF-1.

Material	Pore diameter (nm)	Window diameter (nm)
IRMOF-1	1.1 and 1.5 [8]	0.75, 1.12 [8]
IRMOF-1	1.21 and 1.5 [9]	
IRMOF-1	1.52 [1]	
IRMOF-1	1.3 (DFT N_2, experimental)	

Therefore, it seems physically feasible to impregnate C_{60} in IRMOF-1. To achieve this, dichlorobenzene was added to the original synthesis in order to dissolve the C_{60}, using a modified synthesis from Yaghi's *et al* patent [10]. Two batches of IRMOF-1 C_{60} and three of IRMOF-1 were synthesized. The C_{60} batches showed a dark colour compared to the colourless IRMOF-1 crystals, indicating the presence of C_{60}.

Materials were characterized with N_2 and tested with H_2 being the results showed in Table 6.2 (compared with literature) and Figure 6.3 [8, 11]. The BET values obtained show very close values to one of the literature publications [11].

Table 6.2. IRMOF-1 C_{60} and IRMOF-1 surface area results from nitrogen adsorption and comparison with literature. Errors represent standard error values from the BET method.

Material	Surface area (m^2 g^{-1})	BET range (P/Po)	R^2
IRMOF-1 C_{60}	3371 ± 22	9.6 E-3 to 0.034	0.9999
IRMOF-1	3444 ± 16	4.8 E-6 to 0.034	0.9999
IRMOF-1	3534 [11]	0.02 to 0.1	
IRMOF-1	630-2900 [8]		

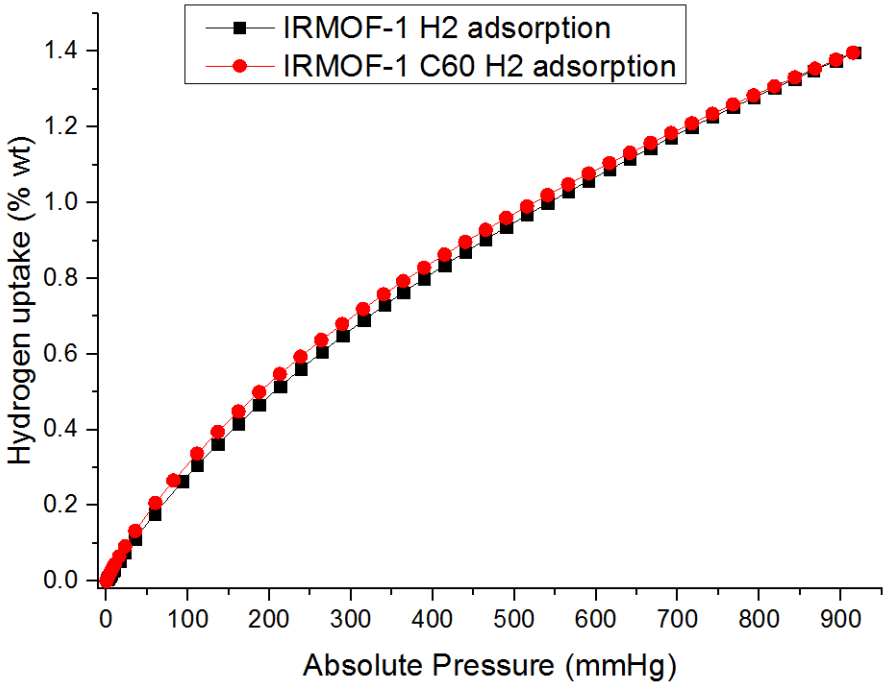

Figure 6.3. Hydrogen excess isotherms of IRMOF-1 and IRMOF-1 C_{60} up to 900 mmHg (1.2 bar) and 77 K.

IRMOF-1 C_{60} shows a smaller surface area compared to IRMOF-1. Although the incorporation of C_{60} intends to increase the adsorption surface, nitrogen, due a higher kinetic diameter might not have been able to enter some pores where C_{60} was present because of steric constrains. In Figure 6.3, hydrogen uptake results barely show differences in uptake at the maximum pressure tested between IRMOF-1 and IRMOF-1 C_{60}. A minimal boost between 50 and 750 mmHg can be observed.

Raman spectroscopy tests were also done to get an insight on their structure. Raman spectroscopy is a technique that allows the observation of vibrational, rotational, and other low-frequency modes in a system. In Raman spectroscopy, the interest lies in how much the scattered light differs from the incident light, with the plotted spectrum the difference between the two, the Raman shift (*X* axis) in cm^{-1} versus the intensity (*Y* axis). From it, information such as composition of the material, stress, crystal symmetry and crystal quality can be drawn [12].

The crystals of the samples were contained in glass vials full of $CHCl_3$ while being tested in the Raman micro-spectrometer. This setup provided sample-protection since they are both moisture and air sensitive. $CHCl_3$ also acted as a coolant, reducing the heating of the samples

because of their exposure to the beam. UV Raman spectra were obtained at 325nm excitation on dry samples.

Green (532 nm) and UV light (325 nm) lasers were used at 5 % of the total intensity. For each test, 5 accumulative runs of 25 seconds each were performed. Only the green light results are shown because the 532 nm showed small interactions with the glass, being the results not conclusive. According to the calibration data, a Renishaw attenuation of 5 % for 325 nm and 532 nm was equivalent to 119 and 5430 microwatts respectively at the objective. Figure 6.4 shows the obtained results:

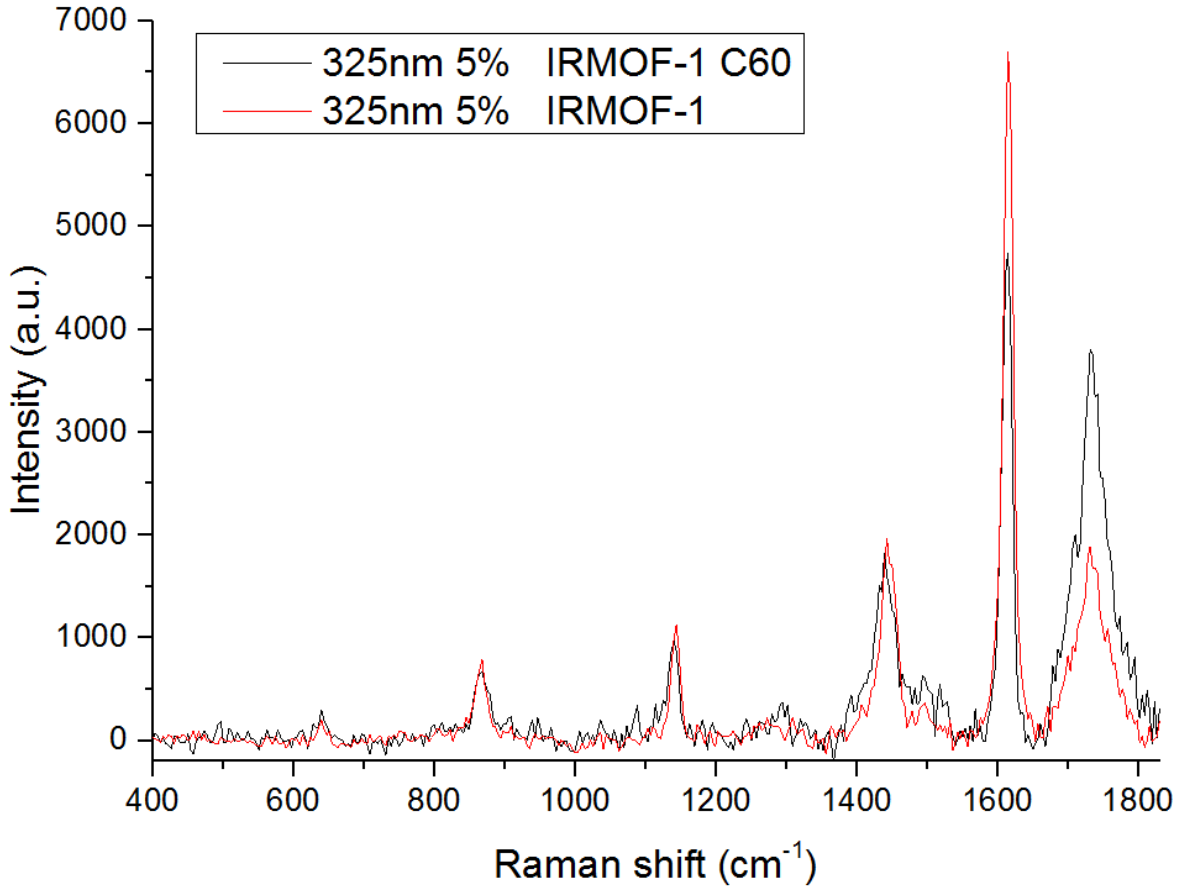

Figure 6.4. IRMOF-1 C_{60} and IRMOF-1 Raman spectra tested with green light (325 nm).

Data was truncated up to 1800 cm^{-1}, leaving the range where relevant peaks were found. WIRE 4.1 software (Renishaw, Gloucester, UK) was used for data processing and fitting. In order to correct the background of both Raman tests, a level 9 polynomial order function was used.

IRMOF-1 C_{60} showed an increased luminescence before removing the background, further indicating the colour difference of the samples, because of the presence of C_{60}. As it can be

seen in Figure 6.4, the peaks obtained from IRMOF-1 C_{60} are broader, which indicates a higher disorder or variation in the bonds of the impregnated framework compared to IRMOF-1, pointing out the possibility of C_{60} being in the structure or between MOF grains. In order to see more accurately the peak shifts and differences between both frameworks, a Gaussian curve fit was applied. By doing trial and error it was found that a curve fit using a smooth window of 7 and a fitting to a polynomial of third order in the software settings gave the best results. In tables 6.3 and 6.4 the fitting results for both tests are shown:

Table 6.3. IRMOF-1 C_{60} Raman fitting results.

IRMOF-1 C_{60}						
Peak fit number	**Centre**	**Width**	**Height**	**Area**	**Quality factor (Height/Area)**	**Fitting ChiSq**
1	867	24	667	25167	0.026	203
2	639	19	221	5187	0.042	
3	1140	19	919	27637	0.033	
4	1441	42	1557	101804	0.015	
5	1613	18	4388	82473	0.053	
6	1738	47	3620	268606	0.013	

Table 6.4. IRMOF-1 Raman fitting results.

IRMOF-1						
Peak fit number	**Centre**	**Width**	**Height**	**Area**	**Quality factor (Height/Area)**	**Fitting ChiSq**
1	865	22	712	24203	0.029	24
2	640	14	152	2340	0.065	
3	1143	16	1047	21335	0.049	
4	1445	26	1889	76401	0.024	
5	1615	18	6300	137638	0.046	
6	1734	58	1620	148513	0.011	

From the fitting results in tables 6.3 and 6.4 and Figure 6.4, it can be seen that IRMOF-1 C_{60} peaks are broader than the IRMOF-1 ones. This indicates a higher disorder in the IRMOF-1 C_{60} due to the presence of C_{60}. Also, IRMOF-1 shows a higher crystallinity because of the

higher peak quality factor (Height/Area) values except for the last peak fit curve. It can also be seen that some peaks of the IRMOF-1 C_{60} experience a shift compared to the IRMOF-1 version. These shifted peaks may be either red or blue shifted. A red shifted peak indicates that the peak is found at a higher frequency or lower energy while a blue shifted peak means the opposite [13]. The values of the centres of the peaks remain almost unchanged for the second peak. Two red shifts (peaks 1 and 6 of 1.82 and 3.76 cm^{-1} difference) and three blue shifts (peaks 3, 4 and 5 with a difference of 3.76, 4.4 and 1.95 cm^{-1} respectively).

A red shift occurs due an expansion of the unit cell of the material [13]. This expansion could have happened due to heating, expanding the material, leading to a change in the lattice [13]. However, this effect is considered to be minimised since the crystals were immersed in $CHCl_3$ while being tested. A second reason for this phenomenon is the strain in the organic ligands of the framework. This could happen if C_{60} is located inside the framework, stretching the ligands in which the C_{60} was caged. The blue shifts are due to the change of quality factor and condensation, growing some of the crystals around the C_{60} and therefore disrupting the crystal growth. In literature, Raman measurements of therepthalic acid and literature IRMOF-1 compared to experimental IRMOF-1 can be found in Tables 6.5 and 6.6 [14]:

Table 6.5. Terephthalic acid and terephthalic acid disodium salt Raman peaks, 512 nm [14].

Terephthalic acid (512 nm) (cm^{-1})		**Terephthalic acid disodium salt (512 nm) (cm^{-1})**	
1650	C=O stretching	**1598**	Carboxylate group stretching (in and out of phase)
1614	Vibrational fingerprints benzene (in-plane)	**1425**	
1445		**1133**	Probably deformation involving carboxylate group with C-C stretching
1285	C-O stretching	**863**	Out of plane C-H deformation mode
1176	Vibrational fingerprints benzene (in-plane)	**838**	
1120		**820**	
827	Vibrational fingerprints benzene (out-of-plane)	**690**	
798		**640**	
627			

Table 6.6. IRMOF-1 Raman literature and experimental peaks at 512, 442 and 325 nm [14].

IRMOF-1 (512 nm) (cm^{-1}) [14]	IRMOF-1 (442 nm) (cm^{-1}) [14]	IRMOF-1 (325 nm) (cm^{-1}) [14]	Experimental IRMOF-1 (325 nm) (cm^{-1})
630	632	578	639.821
810	810		865.564
860	863	1155	1142.71
1430	1434		1445.12
1610	1612		1615.3
			1734.19

When comparing the experimental data with the literature, it can be seen that the quality of the data is much higher at 325 nm [14]. Peak number 3 (1142 cm^{-1}) is very close from the one at 1155 cm^{-1}, also at 325 nm. However, the closest one experimentally obtained from 578 cm^{-1} is 639.8 cm^{-1} [14]. When comparing with the other two spectra, the peaks at 630, 1430 and 1610 cm^{-1} are very close from the experimental ones (639, 1442 and 1615). However, experimental data shows very sharp and intense extra peaks at 1142 and 1734 cm^{-1}, not appearing in literature. Likewise, experimental data does not show any peak at 810 cm^{-1}, seen in literature.

When comparing XRD spectra, IRMOF-1 C_{60} Batch 1 shows shifts compared to the IRMOF-1 version. Furthermore, IRMOF-1 C_{60} Batch 2 shows clear extra peaks at around 7, 14 and 21 2θ (Figure 6.5), indicating the possible presence of twined growth, a split population of both IRMOF-1 and IRMOF-1 C_{60} or a reduction in intensity because of the presence of C_{60} that adsorbs X-ray radiation, showing a double peak in the IRMOF-1 C_{60} XRD pattern. To rule out the possibility of C_{60} adsorbing part of the X-rays creating a double peak pattern, the amplitudes of those peaks were compared (Table 6.7). It was observed an amplitude of 0.10 and 0.11 2θ, higher for the area around 7 and 14 2θ, having the area around 21 2θ the same amplitude. This indicates the existence of two different signals slightly shifted, indicating the very probable presence of a split population of impregnated and non-impregnated IRMOF-1. Since the impregnated material showed a higher absolute intensity (I), a value of around 0.01 normalized intensity (NI) was used to determine the start and end of every peak for both materials:

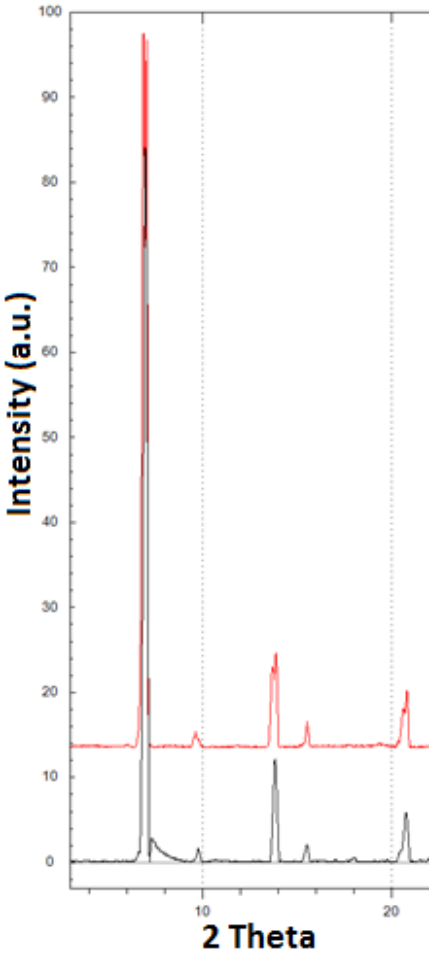

Figure 6.5. PXRD zoom for comparison of B1 IRMOF-1 (black) and B2 IRMOF-1 C_{60} (red). It can be seen in the C_{60} version the existence of extra peaks at 7, 14 and 21 2θ. An artifact was created after the peak at 7 2θ due to background correction in the IRMOF-1 XRD.

Table 6.7. XRD peak width measurements of B1 IRMOF-1 and B2 IRMOF-1 C_{60} (2θ, intensity and normalized intensity).

Material	Peak	Start of the peak			End of the peak			Peak width (2θ)
		2θ	I (a.u)	NI (a.u)	2θ	I (a.u)	NI (a.u)	
IRMOF-1	Around 7	6.62	43.58	0.012	7.28	38.05	0.010	0.66
IRMOF-1 C_{60}		6.52	110.08	0.009	7.28	148.64	0.012	0.76
IRMOF-1	Around 14	13.66	47.28	0.013	14.04	32.51	0.009	0.38
IRMOF-1 C_{60}		13.53	131.75	0.011	14.02	127.32	0.010	0.49
IRMOF-1	Around 21	20.38	36.34	0.010	20.94	39.79	0.011	0.56
IRMOF-1 C_{60}		20.38	117.99	0.010	20.94	128.67	0.011	0.56

6.3 Conclusions

A system formed of a MOF (IRMOF-1) and C_{60} was successfully synthesized by using a modified synthesis method of IRMOF-1. The difference in colour, Raman results (shifts and peak quality factor changes) and observed wider double peaks in XRD spectra showed the existence of C_{60} in the framework. Nitrogen adsorption tests showed a slight reduction in the surface area of the new material when compared to IRMOF-1, probably due to steric constrains. Hydrogen adsorption tests presented a very small boost in hydrogen adsorption at very low pressures, barely showing enhanced hydrogen adsorption from the pore size optimization studies.

The approach used to measure the materials in the Raman yielded clearer data results than the observed literature [14]. It also ensured diminishing of red shifts due to heating and prevented the materials from decomposing or gaining water from the environment. Raman results showed a higher disorder in the impregnated version and a slight expansion of the unit cell observed from the red shifted peaks. XRD results showed the probable existence of both populations because of the incomplete impregnation of all the crystals of the framework, indicated by some regions with double peaks, wider that of IRMOF-1 XRD.

The difference in pore size between C_{60} and IRMOF-1's pore window is 0.32 nm [8], while the difference between C_{60} and IRMOFs-1's pore diameter ranges is between 0.72 and 0.30 nm, depending on the methodology used [1, 8, 9]. The window and pore diameter results from literature come from crystallographic data, which do not take into account the van der Waals diameter of the atoms, which would make these differences even smaller. This could have led to the impossibility of the framework to grow around C_{60} or C_{60} to diffuse into the pore. Other possibility could be that the C_{60} was able to get into the pore, not existing enough space for hydrogen to adsorb inside the remaining free pore space of the framework.

6.4 References

1. Rowsell, J.L.C. and O.M. Yaghi, *Strategies for Hydrogen Storage in Metal–Organic Frameworks.* Angewandte Chemie International Edition, 2005. 44(30): p. 4670-4679.
2. Durbin, D.J. and C. Malardier-Jugroot, *Review of hydrogen storage techniques for on board vehicle applications.* International Journal of Hydrogen Energy, 2013. 38(34): p. 14595-14617.
3. Chen, B.L., Eddaoudi, M., Hyde, S. T., O'Keeffe, M., Yaghi, O. M., *Interwoven metal-organic framework on a periodic minimal surface with extra-large pores.* Science, 2001. 291(5506): p. 1021-1023.
4. Breck, D.W., *Zeolite Molecular Sieves.* Wiley, New York, 1974.
5. Hansen J., R.R., Sato M., Lo K., *Global surface temperature change.* Reviews of Geophysics, 2010. 48(4): p. n/a-n/a.
6. Thornton, A.W., Nairn, Kate M., Hill, James M., Hill, Anita J., Hill, Matthew R., *Metal−Organic Frameworks Impregnated with Magnesium-Decorated Fullerenes for Methane and Hydrogen Storage.* Journal of the American Chemical Society, 2009. 131(30): p. 10662-10669.
7. Goel, A., J.B. Howard, and J.B. Vander Sande, *Size analysis of single fullerene molecules by electron microscopy.* Carbon, 2004. 42(10): p. 1907-1915.
8. Korotcenkov, G., *Handbook of Gas Sensor Materials: Properties, Advantages and Shortcomings for Applications* Springer, 2013. Volume 2: New Trends and Technologies: p. 166.
9. Rowsell, J.L.C. and O.M. Yaghi, *Effects of functionalization, catenation, and variation of the metal oxide and organic linking units on the low-pressure hydrogen adsorption properties of metal-organic frameworks.* Journal of the American Chemical Society, 2006. 128(4): p. 1304-1315.
10. Yaghi, O., Eddaoudi, M., Li, H., Kim, J., Rosi, N., *Isoreticular metal-organic frameworks, process for forming the same, and systematic design of pore size and functionality therein, with application for gas storage*. 2003, Google Patents.
11. Wong-Foy, A.G., A.J. Matzger, and O.M. Yaghi, *Exceptional H2 saturation uptake in microporous metal-organic frameworks.* Journal of the American Chemical Society, 2006. 128(11): p. 3494-3495.
12. *Raman Renishaw DM 2500M manual.*
13. M. Cardona, R.M., *Light Scattering in Solids IX. Novel Materials and Techniques.* Springer, 2007. 108.
14. Bordiga, S., Lamberti, C., Ricchiardi, G., Regli, L., Bonino, F., Damin, A., Lillerud, K. P., Bjorgen, M., Zecchina, A., *Electronic and vibrational properties of a MOF-5 metal-organic framework: ZnO quantum dot behaviour.* Chemical Communications, 2004(20): p. 2300-2301.

Chapter Seven

Adsorption of CO_2, N_2 and Ar in ZIFs and Structural Flexibility upon Adsorption

7 Adsorption of CO_2, N_2 and Ar in ZIFs and Structural Flexibility upon Adsorption

7.1 Introduction

As previously stated in Chapter 1, an increase in population, overall wealth and therefore energy consumption has ended up in a rise in CO_2 emissions. This is due our dependence and primary use of fossil fuels as an energy source, contributing to anthropogenic global warming. Because of this difficult and long process of decarbonisation, substituting fossil fuel usage with renewable energies, CO_2 capture would also help reduce anthropogenic global warming, also improving air quality.

This Chapter is divided in two parts. In the first part, ZIF-7, ZIF-9, ZIF-11 and ZIF-12 have been tested with different gases (N_2, Ar and CO_2) to check for flexibility features on ZIFs. In the second part of the chapter, the possibility of creating mixed materials for enhanced CO_2 adsorption between ZIFs and zeolite 13X beads, another material with great potential for CO_2 adsorption, is explored [1]. The previously mentioned ZIFs were used for this study due to their availability, easy synthesis, yield, high thermal stability and relatively low cost compared to other MOFs. ZIF-7 and ZIF-9 have been reported as excellent candidates for CO_2 adsorption at high pressures and other ZIFs such as ZIF-70, ZIF-78 and ZIF-82 have already reported very high CO_2 uptakes at low pressures and complete retention of CO_2 while letting CH_4, CO, and N_2 through the pores of the framework in breakthrough experiments [2-5]. These mixed materials could be used in CO_2 capturing systems to reduce its increasing concentration in the atmosphere, using the ZIFs selectivity to try to block water from getting adsorbed by the zeolite while letting other gases pass through. Another use could be to put the mixed material in filters to purify gas streams. A filtering system was already developed and installed in the laboratory, filled with zeolite 13X beads and an activated carbon. This is connected to a hydrogen cylinder with the intention of further purifying hydrogen before being used in experiments, improving the measurements on that device and having the possibility to be used in different pieces of equipment.

The characterization experiments were carried out in collaboration with Karim Sapag and Jhonny Villarroel (Universidad Nacional de San Luis, Department of Physics, San Luis,

Argentina). The CO_2 breakthrough experiments were carried out in collaboration with Semali Perera and Olivier Camus (Department of Chemical Engineering, University of Bath, Bath, United Kingdom).

7.2 Materials and synthesis

ZIF 7, ZIF-9, ZIF-11 and ZIF-12 were synthesized in the presence of 13X zeolite beads. The commercial 13X zeolite beads were purchased from Zeochem AG, Switzerland. A list of the chemicals used together with their purity and supplier can be found in Supplementary Information A.

All ZIFs were synthesized using a scaled up procedure to ensure enough sample was obtained [6]. Syntheses were done in 150 mL Fisher glass containers with 20 g of zeolite 13X beads. Initially, 27.2 g of ethanol or 19.2 g of methanol (for ZIF-12) were added, increasing the temperature of the vessel due to the adsorption of ethanol/methanol by the beads. Once it cooled down, 0.4800 g of bIm (benzimidazole) and 0.24 g of ammonia hydroxide (28–30% aqueous solution) were added. In case of ZIF-11 and ZIF-12, 12.8 and 18.4 g of toluene were respectively added afterwards. Finally, 0.4400 g of zinc acetate dihydrate or 0.5000 g of cobalt acetate dihydrate (zinc for ZIF-7 and ZIF-11 and cobalt for ZIF-9 and ZIF-12) were added to the mix, stirring the solution for 3 h at RT. The measured quantities were as seen in Table 7.1:

Table 7.1. Measured quantities for ZIF-7, ZIF-9, ZIF-11 and ZIF-12 (X4) + 20 g of zeolite 13X beads.

Materials:	**bIm (g)**	**Ethanol (g)**	**Methanol (g)**	**Toluene (g)**	**Ammonia hydroxide (g)**	**Zinc acetate dihydrate (g)**	**Cobalt acetate tetrahydrate (g)**
ZIF-7 (X4)	0.4805	27.2	-	-	0.24	0.4400	-
ZIF-9 (X4)	0.4801	27.2	-	-	0.24	-	0.5000
ZIF-11 (X4)	0.4800	27.2	-	12.8	0.24	0.4403	-
ZIF-12 (X4)	0.4801	-	19.2	18.4	0.24	-	0.5000

The reactions yielded a white or purple powder (synthesized material) as well as a brown liquid (coming from the binder). The flasks were decanted, putting all the solution in centrifuge beakers. The suspensions were centrifuged at 6000 RPMs for 10 minutes, decanting the solutions and replacing it with fresh ethanol (methanol for ZIF-12). After this, the entire content of the tubes was poured back in the Fisher glass container, repeating this process a total of 3 times for each synthesis. Finally, more ethanol/methanol was added to the container, allowing 48 h for solvent exchanging before the liquid was dried at RT and then heated up at 120 °C in a vacuum oven. Figure 7.1 shows the mixed zeolite 13X beads with ZIF-9 and ZIF-11 respectively:

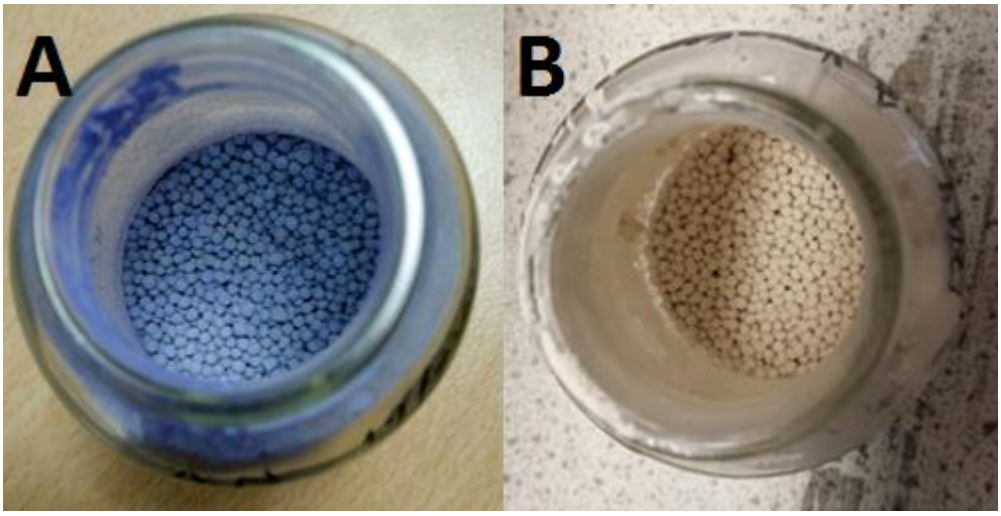

Figure 7.1. Zeolite 13X beads with ZIF-9 (A) and ZIF-11 (B) mixed material.

7.3 Results and discussion

7.3.1 Mixed material characterization results

Non-attached ZIF powder from the ZIF reactions in presence of zeolite 13X beads was tested in the X-ray diffractometer as well as pure zeolite 13X powder. The powder XRD results can be seen in Figure 7.2:

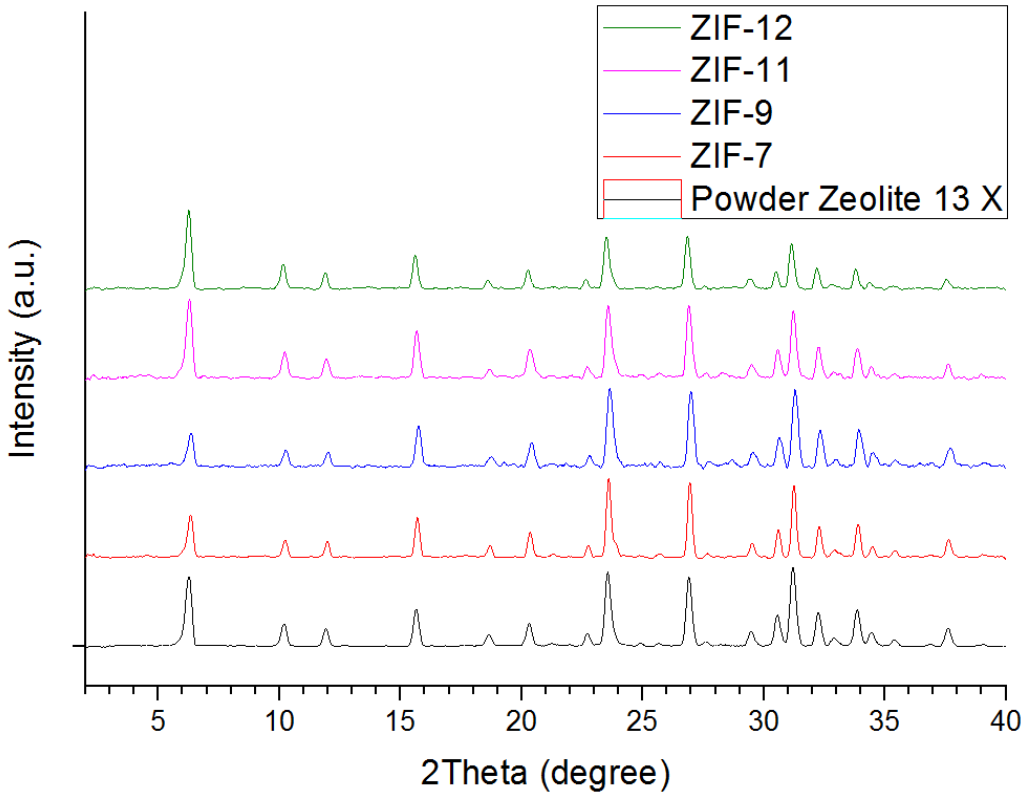

Figure 7.2. Powder XRD patterns of ZIFs reacted in presence of zeolite 13X. Powder zeolite 13X (black), ZIF-7 (red), ZIF-9 (blue), ZIF-11 (pink) and ZIF-12 (green).

Figure 7.2 clearly shows that all the XRD spectra belongs to zeolite 13X, being unable to see the diffraction patterns of any of the ZIFs. This means that the zeolite does not stay completely bound. Some of the zeolite that formed part of the beads got mixed with the synthesized ZIF, being unable to quantify the amount of ZIF that is in the mix that covers the zeolite 13X beads. The apparition of a coloured solid (white for ZIF-7 and ZIF-11 and purple for ZIF-9 and ZIF-12) during the syntheses was the only confirmation of the ZIFs synthesis.

Zeolite 13X beads were also tested in the TGA to check its thermal stability and determine the degassing temperature of the mixed materials. Figure 7.3 shows the TGA results of zeolite 13X:

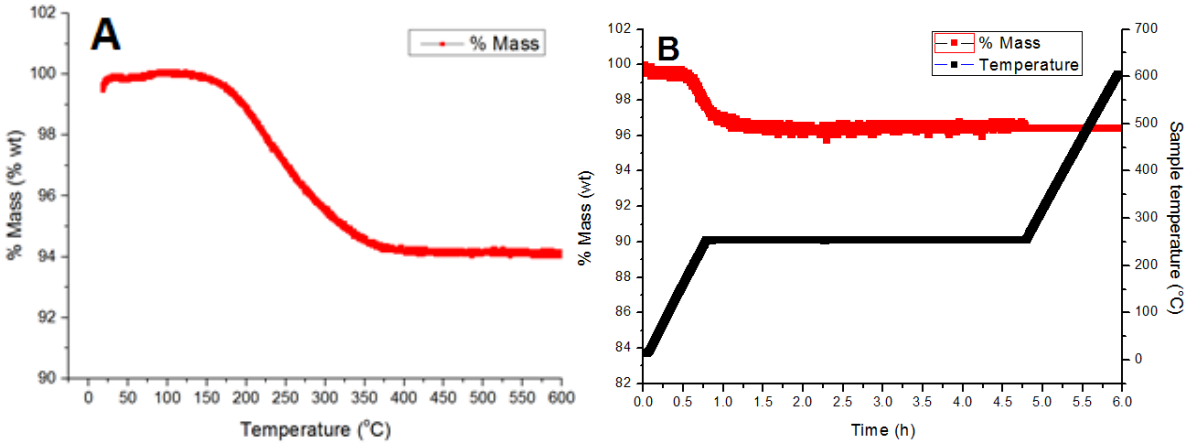

Figure 7.3. Zeolite 13X TGA test from 20 to 600 °C, 5 °C min^{-1} under nitrogen (A) and zeolite 13X TGA from 20 to 250 °C, holding at 250 (for 4 h) and then from 250 to 600 °C, 5 °C min^{-1} under nitrogen (B).

Figure 7.3A shows one step of weight loss of 6 %, not showing thermal decomposition of the zeolite at temperatures up to 600 °C. The small step of weight loss (20-375 °C) is assigned to the loss of water and possible organics present in the lab. Since the test was done at 5 °C min^{-1} and water did not immediately leave the beads, zeolite 13X showed a stability plateau in the range of 375-600 °C. Figure 7.3B shows another TGA test where the temperature was first held at 250 °C for 4 h, which eventually showed no mass change, indicating that 250 °C was enough to degas the ZIF-zeolite mixed materials.

7.3.2 ZIF gas adsorption results

As previously stated in Chapter 3, ZIF-7, ZIF-9, ZIF-11 and ZIF-12 scaled up batches were synthesized and sent to San Luis, Argentina (over 500 mg). These were the second successfully synthesized batch for each material. Their XRD patterns and thermal stability tests can be found in the Supplementary Information files D and E. Figures 7.4 to 7.7 show ZIF-7, ZIF-9, ZIF-11 and ZIF-12 isotherms with N_2, Ar (at 77 K) and CO_2 (at 273 K) respectively.

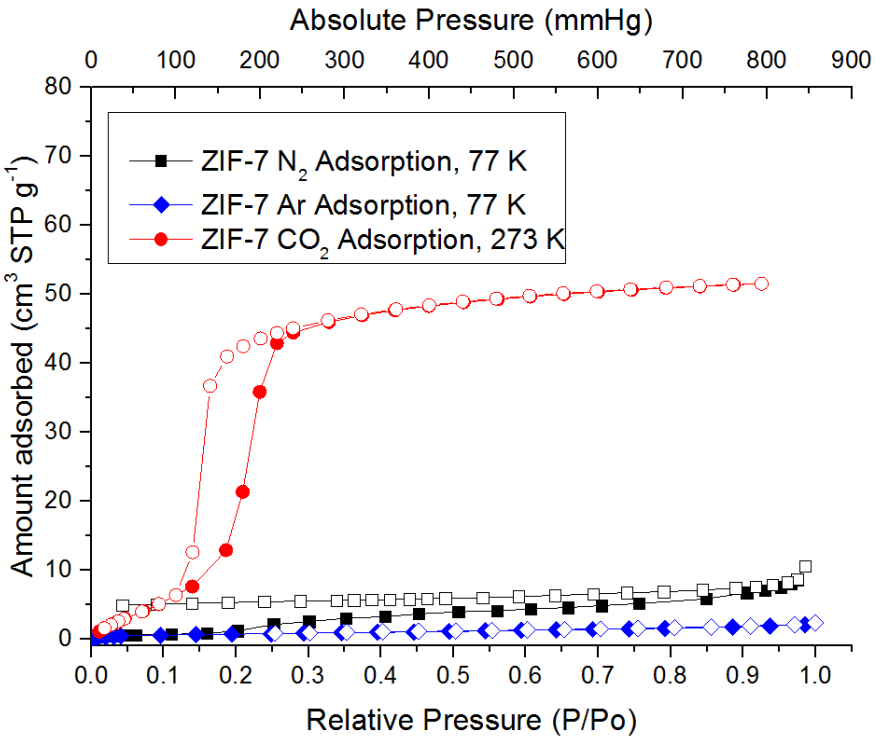

Figure 7.4. ZIF-7 isotherms, tested with N_2 and Ar at 77 K and with CO_2 at 273 K. Relative pressure refers to N_2 and Ar while the Absolute pressure axis refers to the CO_2 isotherm. Open symbols indicate desorption isotherms.

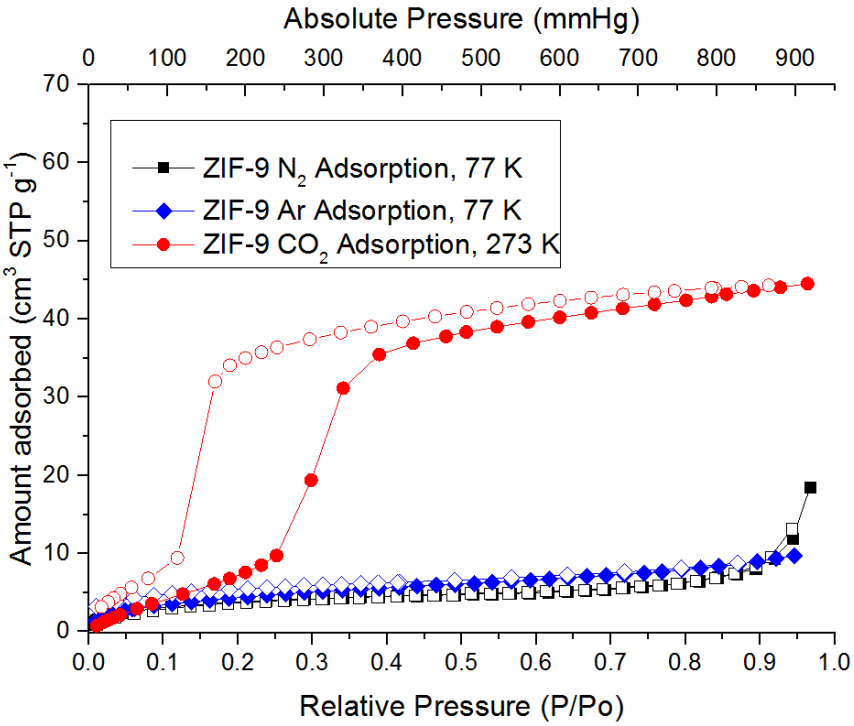

Figure 7.5. ZIF-9 isotherms, tested with N_2 and Ar at 77 K and with CO_2 at 273 K. Relative pressure refers to N_2 and Ar while the Absolute pressure axis refers to the CO_2 isotherm. Open symbols indicate desorption isotherms.

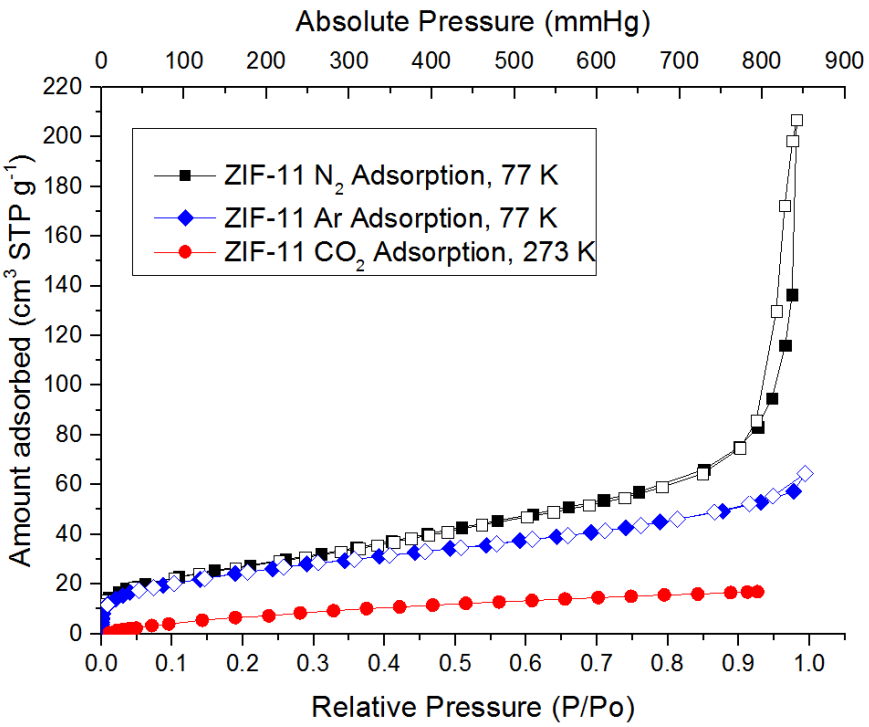

Figure 7.6. ZIF-11 isotherms, tested with N_2 and Ar at 77 K and with CO_2 at 273 K. Relative pressure refers to N_2 and Ar while the Absolute pressure axis refers to the CO_2 isotherm. Open symbols indicate desorption isotherms.

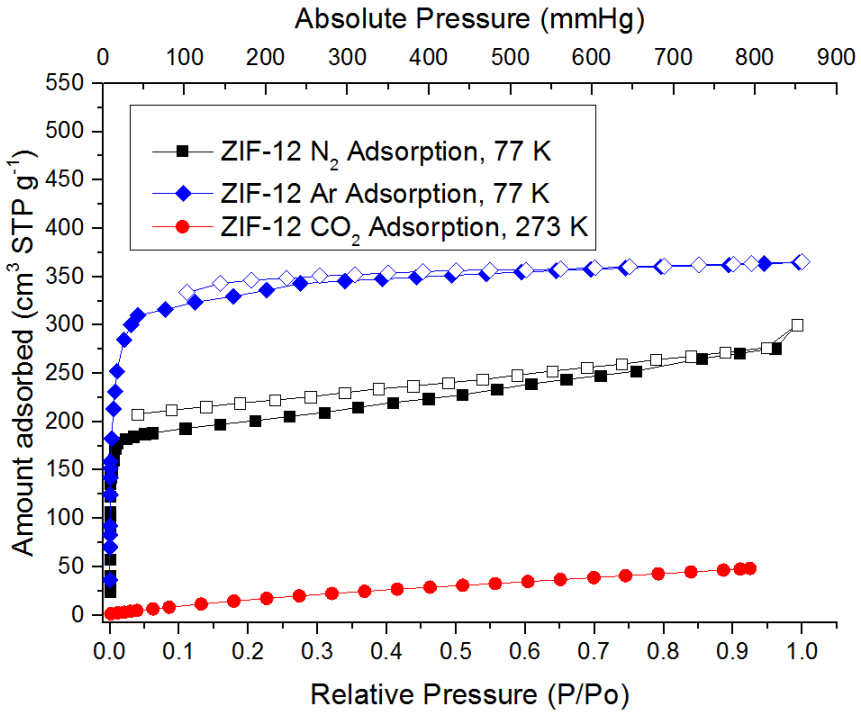

Figure 7.7. ZIF-12 isotherms, tested with N_2 and Ar at 77 K and with CO_2 at 273 K. Relative pressure refers to N_2 and Ar while the Absolute pressure axis refers to the CO_2 isotherm. Open symbols indicate desorption isotherms.

ZIF-7 shows the highest CO_2 adsorption of all, exhibiting 51.50 cm^3 STP g^{-1} at 793 mmHg, followed by 48.30 cm^3 STP g^{-1} by ZIF-12 and 43.96 cm^3 STP g^{-1} by ZIF-7 at the same pressure. ZIF-7 shows a sharp increase in CO_2 adsorption between 100 and 200 mmHg, while ZIF-12 and ZIF-11 adsorption isotherms rise progressively. This difference in shape and steepness at the highest pressure tested may indicate that although they present very similar CO_2 uptakes, ZIF-12 might present higher adsorption than ZIF-7 and ZIF-9 at higher pressures as they seem to start getting closer to plateau at the maximum pressure shown. From all the tested ZIFs, it was found in literature that ZIF-7 shows a complex behaviour regarding the adsorption of CO_2 due to the existence of different forms due to its flexibility, giving a value of 3.5 KJ mol^{-1} at 298 K [7]. Both ZIF-7 and ZIF-9 present hysteresis in the desorption curve, indicating sorbate-induced gate-opening phenomena, observed in literature and high pressure hydrogen isotherm in Chapter 5, involving a narrow-to-large pore phase transition [8-11]. ZIF-7 and ZIF-9 show barely any N_2 or Ar adsorption, having these molecules a higher kinetic diameter (3.64 and 3.4 Å respectively) than the pore windows of ZIF-7 and ZIF-9 (2.9 Å), being the materials flexible enough to allow CO_2 into the framework (3.3 Å kinetic diameter) indicating that the gases only adsorb to the surface, not being able to enter the pores of the framework [6, 12-14].

ZIF-11 and ZIF-12, although identical according to literature, exhibit different N_2, Ar and CO_2 adsorption isotherms, both different in shape and amounts adsorbed (Figures 7.6 and 7.7). This fact also indicates signs of flexibility in both materials since according to literature they possess a 3.0 Å pore window aperture, lower than the kinetic diameters of all the tested gases, although no hysteresis has been found on the experimental desorption isotherms [6, 15]. ZIF-11 has been reported as a H_2 sieve because of its pore windows, stating the exclusion of bigger molecules like N_2 by using *ab initio* based Grand Canonical Monte Carlo Simulations [6, 14].

Nevertheless, their experimental hydrogen uptakes at high pressure are very similar as shown in Chapter 4, hydrogen having a smaller kinetic diameter than their pore windows, not indicating any sign of flexibility in those tests for ZIF-11 and ZIF-12. A maximum hydrogen uptake of 3.17 wt % for ZIF-11 has been reported, being its experimental maximum 2.53 wt % at 5.15 MPa according to Chapter 4 results [6, 15]. ZIF-12 presents type I isotherms for the adsorption of both N_2 and Ar, presenting higher adsorption that of ZIF-11. These values are 300.38 and 206.72 cm^3 STP g^{-1} for N_2 and 365.31 and 64.46 cm^3 STP g^{-1} for Ar at 0.99 P/Po. ZIF-11 on the other hand presents type II isotherms for the adsorption of both N_2 and Ar.

This indicates that the four ZIFs present flexibility features, being higher for the RHO topologies since a difference of 0.1 Å in pore window allow the RHO forms to adsorb N_2 and Ar, which have 0.34 and 0.1 Å higher kinetic diameter that of CO_2 [13, 14]. The reason of this higher flexibility is thought to be due the RHO topology, which is formed of 4, 6 and 8 membered rings while the SOD is form only by 4 and 6 membered rings, presenting two more benzimidazolate linkers to further open the pore windows of the framework.

7.3.3 CO_2 breakthrough experiments

In industrial applications with gas or liquid mixtures, packed beds made of single pellets are used to adsorb one or various components from its flow. Usually this beds are stationary, switching to a second bed when the first one gets saturated (in order to regenerate it) [16]. At the inlet of the bed, the adsorptive concentration is C_0, getting in contact with the adsorbent, which starts getting saturated towards equilibrium. In between the inlet and outlet, there is an existing mass transfer zone where the adsorptive is being adsorbed (Figure 7.8.a) [16]. This zone where the gas is being adsorbed by the adsorbent progresses with time. It comes to a time when the adsorbent of the column has been completely saturated and the adsorptive gets to the exit of the column. The time when this happens is defined as the breakthrough time, t_b. After this time, the breakthrough curve appears (Figure 7.8.b) [16]:

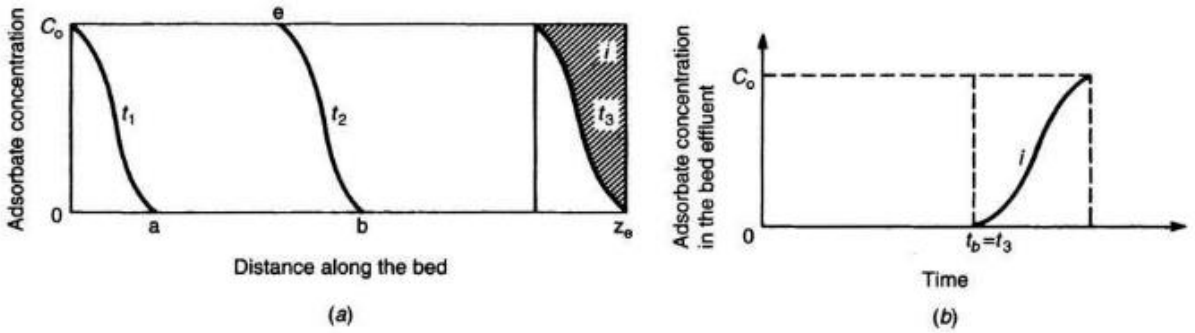

Figure 7.8. Distribution of adsorbate concentration in the fluid phase through a bed. (a) Development and progression of an adsorption wave along a bed at three different times, t_i. (b) Breakthrough time, t_b and breakthrough curve (i). C_0 is the initial concentration of the adsorptive at the inlet and z_e the total length of the packed bed column [16].

7.3.3.1 Equipment and materials

In order to do the CO_2 adsorption flow-breakthrough experiments, an apparatus whose schematic is shown in Figure 7.9 was used. It consisted of a feed gas flow system, an adsorption column and an effluent gas analytical system. The tested adsorbents were degassed at different temperatures for at least 20 hours before the adsorption experiments. The dynamic adsorption experiments were carried out by starting with 250 mL min^{-1} of 4000 ppmv carbon dioxide gas at 2 bar at 20 °C.

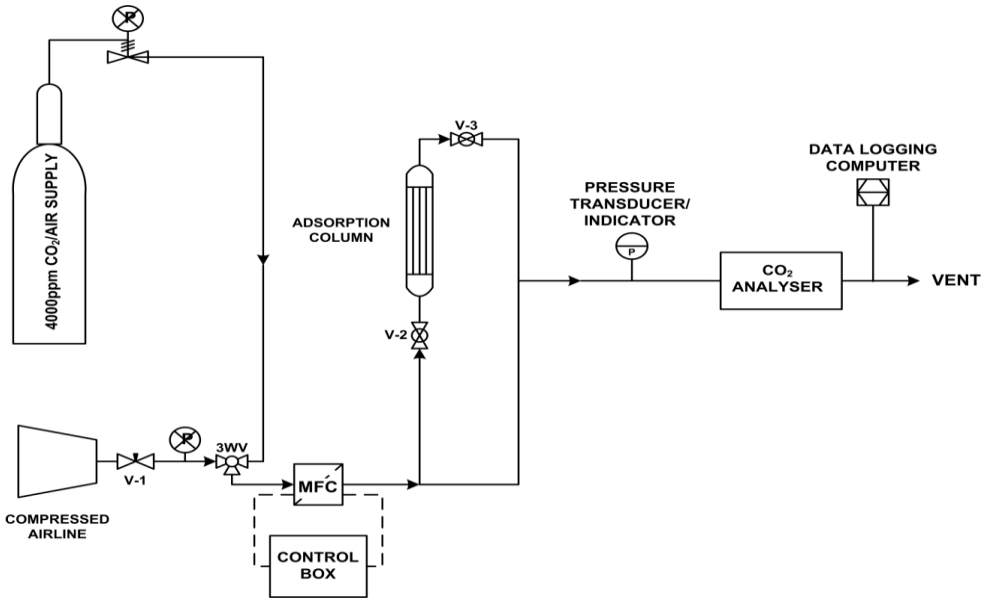

Figure 7.9. Schematic diagram of adsorption flow-breakthrough apparatus.

Experimental adsorption breakthrough curves obtained from the different tests were analysed to evaluate the adsorption performance of the reference material, zeolite 13X beads, and zeolite 13X mixed with the different ZIFs. All the mixed materials were degassed overnight in an oven at 250 °C except ZIF-12 mixed material, which was degassed at 300 °C because ZIF-12 TGA results showed the plateau region at 275 °C (Supplementary Information E). A constant amount of sample (17 g) was tested every time in the flow-breakthrough apparatus.

From these results, the breakthrough time, t_b, (h) was obtained. The breakthrough time is defined as the time taken for the adsorbent bed to be completely saturated with the adsorbate gas (CO_2) [10]. However, in this experiment, the time when the column has been completely saturated with CO_2 and its concentration has risen to 350 ppm of CO_2 has been used, defined as t_{b350}. Figure 7.10 and the summarising Table 7.4 show the results obtained:

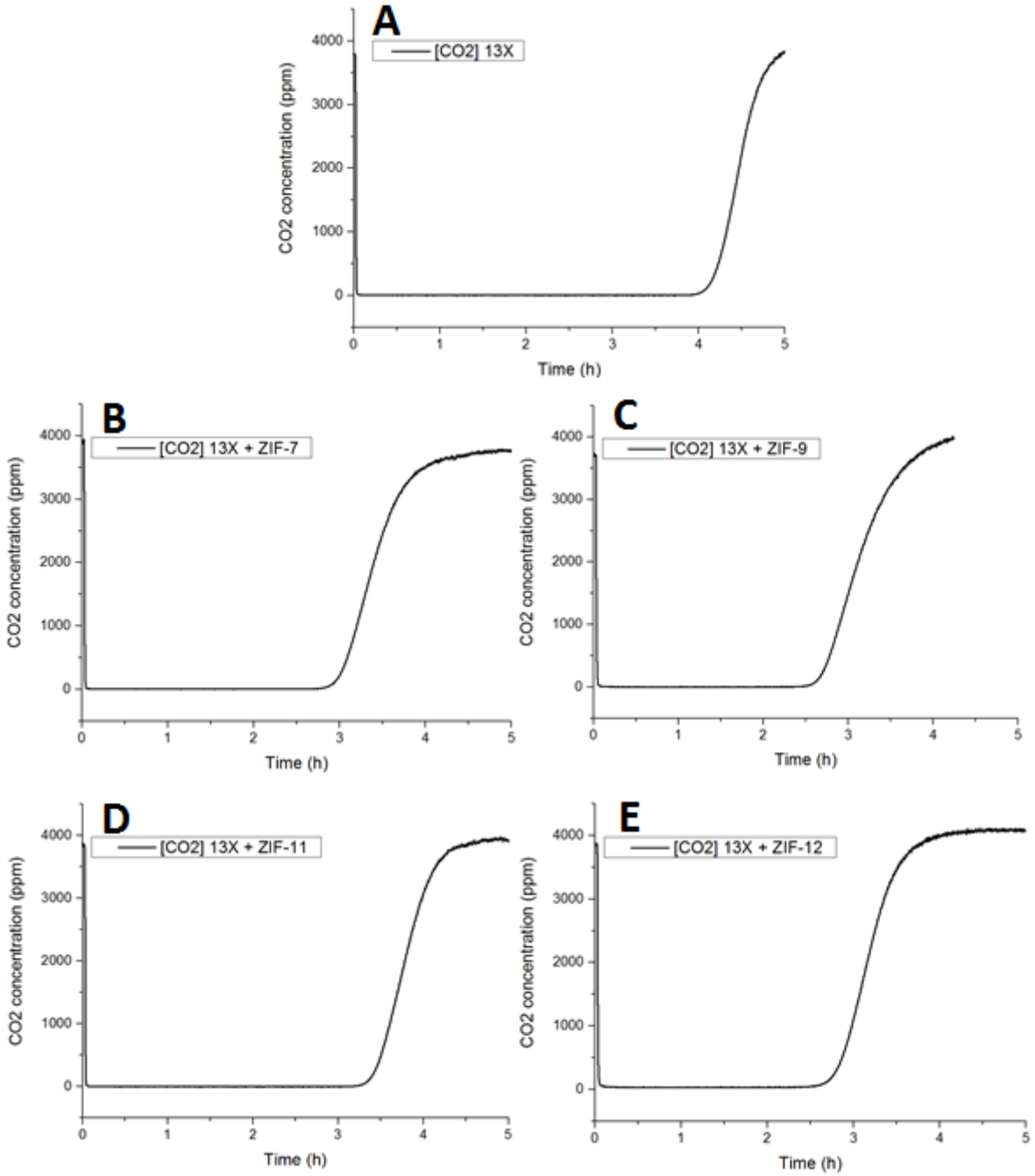

Figure 7.10. Zeolite 13X (A), zeolite 13X + ZIF-7 (B), zeolite 13X + ZIF-9 (C), zeolite 13X + ZIF-11 (D) and zeolite 13X + ZIF-11 (E) breakthrough experiments.

Table 7.2. CO_2 Breakthrough times for zeolite 13X beads alone and zeolite-ZIF mixed materials.

Material:	t_{b350} (h)
Zeolite 13X	4.17
Zeolite 13X + ZIF-7	3
Zeolite 13X + ZIF-9	2.71
Zeolite 13X + ZIF-11	3.44
Zeolite 13X + ZIF-12	2.79

From the results obtained, it can be seen that the breakthrough time of zeolite 13X alone is higher that of any of the zeolite 13X mixed materials, being 39, 53, 21 and 49 % higher than the mixed materials in ascending numerical order.

Initial observations indicate that the mixed zeolite with ZIF-11 shows the second highest performance. The CO_2 concentration during the experiment was 4000 ppm, at 2 bar. The partial pressure of CO_2 in the column was 6 mmHg as seen in equation 8.1:

$$P_{CO2} = \frac{4000\ ppm\ CO_2}{1000000\ ppm\ total} * 2\ bar * \frac{750.06\ mm\ Hg}{1\ bar} = 6\ mmHg\ CO_2 \qquad \text{Eq 8.1}$$

From the adsorption isotherms (Figures 7.4 to 7.7), ZIF-7 was expected to show the highest breakthrough time, followed by ZIF-9, ZIF-12 and ZIF-11. This was thought because ZIF-7 and ZIF-9 exhibited a higher CO_2 adsorption and are unable to adsorb N_2 as ZIF-11 and ZIF-12. However, the isotherms have been measured at a slight different temperature and adsorption kinetics are not taken into account since they present equilibrium adsorption. Regardless of this, very similar results for ZIF-7 and ZIF-9 were expected, as for ZIF-11 and ZIF-12.

This disparity in results can be explained by the fact of not being able to quantify the amount of tested ZIF and zeolite 13X at the start of the breakthrough experiment as explained in the discussion of Figure 7.2. Therefore, different amounts of zeolite 13X must have been in the column for each mixed material, being the ZIF-11 mixed material the one that had more. As seen in Figure 7.11, CO_2 adsorption of zeolite 13X beads and powder is much higher that of the ZIFs at low pressures:

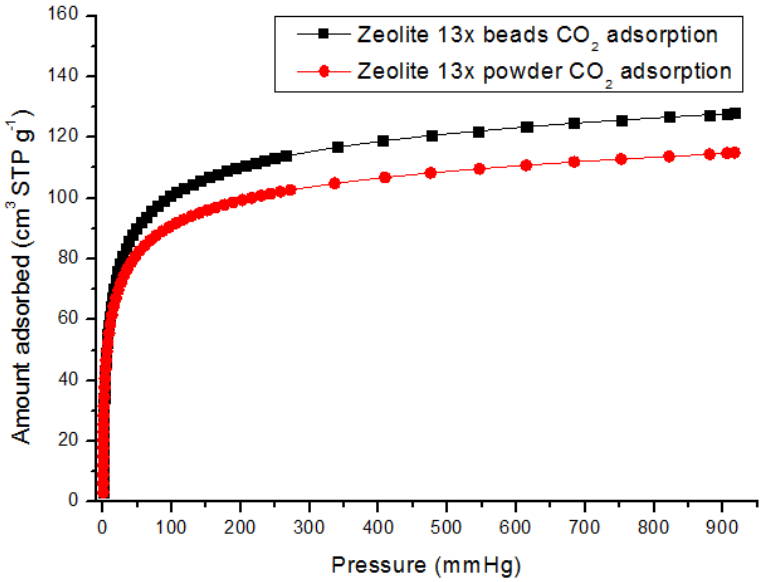

Figure 7.11. CO_2 isotherms at 273 K on zeolite 13X beads and powder.

Figure 7.11 also shows that, despite the zeolite 13X beads contain between a 20 and a 15 % of binder, their CO_2 adsorption is higher that of the pure powder. Ageing of the pure powder or better quality of the zeolite 13X beads have been seen as the most plausible reasons. The density of the beads was also tested in an AccuPyc 1330, obtaining a value of 1.19 ± 0.01 cm^3 g^{-1}. Two samples were degassed overnight at 350 °C, doing repeatability runs (10 purges and 10 runs) at 26.7, 27.1, 25.3 and 25.6 °C respectively. The average of the four results with the lowest standard error from each 10 runs were used.

7.4 Conclusions

ZIF-7, ZIF-9, ZIF-11 and ZIF-12 were tested with N_2, Ar and CO_2. ZIF-7 and ZIF-9 only showed CO_2 adsorption isotherms with hysteresis, corroborating sorbate-induced gate-opening phenomena [7-10]. ZIF-11 and ZIF-12 showed adsorption with the three gases, also indicating flexibility of ZIF-11 and ZIF-12 (RHO topology), with ZIF-11 considered a H_2 sieve [6, 14]. This flexibility, not previously reported is even higher that of ZIF-7 and ZIF-9 (SOD topology). Adsorption of N_2 and Ar, with kinetic diameters of 3.62 and 3.40 Å (0.34 and 0.1 Å higher than CO_2), having pore windows only 0.1 Å bigger than ZIF-7 and ZIF-9 [6, 12-14]. The reason of this increased flexibility is thought to be due the differences of the RHO topology compared to the SOD, which is formed of 4, 6 and 8 membered rings, while the SOD form only by 4 and 6 membered rings, presenting two more benzimidazolate linkers that allow further flexibility of the pore windows of the framework.

Some of the zeolite 13X got mixed with the ZIF in every synthesis reaction, only been able to see the powder XRD pattern of the zeolite, not allowing individual gravimetric quantification of the zeolite and the ZIFs and therefore increasing the uncertainty of the breakthrough results.

The mix of ZIF and zeolite 13X successfully covered the beads, opening the possibility to use ZIFs in new mixed materials with higher CO_2 adsorption. Although they have been pointed out as excellent materials for CO_2 adsorption and storage, different results were shown at low pressures [1]. Zeolite 13X alone proved to be the material with the highest breakthrough time. This is thought to be the case due to different amounts of Zeolite 13X in the mixed materials due to different loss of zeolite during the synthesis, which has the highest potential of all for CO_2 adsorption at low pressures.

The thermal stability, density and CO_2 adsorption capacity at low pressures and 273 K of this batch of zeolite 13X beads used for CO_2 breakthrough were first determined at the University of Bath, showing unexpected higher adsorption than the zeolite 13X powder. Ageing of the pure powder or better quality of the zeolite 13X beads have been seen as the most plausible reasons. This new data about the materials could help in the future for system design purposes.

7.5 References

1. Cavenati, S., C.A. Grande, and A.E. Rodrigues, *Adsorption Equilibrium of Methane, Carbon Dioxide, and Nitrogen on Zeolite 13X at High Pressures.* Journal of Chemical & Engineering Data, 2004. 49(4): p. 1095-1101.
2. Phan A., D.C.J., Uribe-Romo F.J., Knobler C.B., O'Keeffe M., Yaghi O.M., *Synthesis, Structure, and Carbon Dioxide Capture Properties of Zeolitic Imidazolate Frameworks.* Accounts of Chemical Research, 2010. 43(1): p. 58-67.
3. Banerjee, R., Furukawa, H., Britt, D., Knobler, C., O'Keeffe, M., Yaghi, O.M., *Control of Pore Size and Functionality in Isoreticular Zeolitic Imidazolate Frameworks and their Carbon Dioxide Selective Capture Properties.* Journal of the American Chemical Society, 2009. 131(11): p. 3875-3877.
4. Banerjee R., P.A., Wang B., Knobler C., Furukawa H., O'Keeffe M., Yaghi O. M., *High-Throughput Synthesis of Zeolitic Imidazolate Frameworks and Application to CO2 Capture.* Science, 2008. 319(5865): p. 939-943.
5. Zhao, P., Bennett, T.D., Casati, N.P.M., Lampronti, G.I., Moggach, S. A., Redfern, S.A.T., *Pressure-induced oversaturation and phase transition in zeolitic imidazolate frameworks with remarkable mechanical stability.* Dalton Transactions, 2015. 44(10): p. 4498-4503.
6. He M., Y.J.F., Liu Q., Zhong Z. X., Wang H. T., *Toluene-assisted synthesis of RHO-type zeolitic imidazolate frameworks: synthesis and formation mechanism of ZIF-11 and ZIF-12.* Dalton Transactions, 2013. 42(47): p. 16608-16613.
7. Du, Y., et al., *New High- and Low-Temperature Phase Changes of ZIF-7: Elucidation and Prediction of the Thermodynamics of Transitions.* Journal of the American Chemical Society, 2015. 137(42): p. 13603-13611.
8. Aguado, S., Bergeret, , Titus, M.P., Moizan, V., Nieto-Draghi, C., Bats, N., Farrusseng, D., *Guest-induced gate-opening of a zeolite imidazolate framework.* New Journal of Chemistry, 2011. 35(3): p. 546-550.
9. Ryder, M.R., Civalleri, Bartolomeo, B., Thomas D., Henke, S., Rudić, S., Cinque, G., Fernandez-Alonso, F., Tan, J.C., *Identifying the Role of Terahertz Vibrations in Metal-Organic Frameworks: From Gate-Opening Phenomenon to Shear-Driven Structural Destabilization.* Physical Review Letters, 2014. 113(21): p. 215502.
10. Pera-Titus, M., *Intrinsic Flexibility of the Zeolitic Imidazolate Framework ZIF-7 Unveiled by CO2 Adsorption and Hg Intrusion.* ChemPhysChem, 2014. 15(8): p. 1581-1586.
11. al., R.S.C.e., *Separation of carbon dioxide from nitrogen utilizing zeolitic imidazolate framework materials .United States Patent Application 20090214407. Code A1. Figure 18.* http://appft.uspto.gov/netacgi/nph-Parser?Sect1=PTO2&Sect2=HITOFF&u=%2Fnetahtml%2FPTO%2Fsearch-adv.html&r=1&f=G&l=50&d=PG01&p=1&S1=20090214407&OS=20090214407&RS=20090214407 *Last accessed 23/06/15.* 2009.
12. Park K. S., N.Z., Cote A.P., Choi J.Y., Huang R.D., Uribe-Rom, F.J., Chae H.K., O'Keeffe M., Yaghi O.M., *Exceptional chemical and thermal stability of zeolitic imidazolate frameworks.* Proceedings of the National Academy of Sciences of the United States of America, 2006. 103(27): p. 10186-10191.
13. Duan, J.G., Higuchi, M., Krishna, R., Kiyonaga, T., Tsutsumi, Y., Sato, Y., Kubota, Y., Takata, M., Kitagawa, S., *High CO2/N-2/O-2/CO separation in a chemically robust porous coordination polymer with low binding energy.* Chemical Science, 2014. 5(2): p. 660-666.
14. Faiz Mohammad, D.P., *Specialty polymers : materials and applications.* New Delhi : I.K. International Pub. House, 2007: p. 51.
15. Han, S.S., S.-H. Choi, and W.A. Goddard, *Zeolitic Imidazolate Frameworks as H2 Adsorbents: Ab Initio Based Grand Canonical Monte Carlo Simulation.* The Journal of Physical Chemistry C, 2010. 114(27): p. 12039-12047.
16. Richardson, J.M.C.J.F., *Chemical Engineering. Particle Technology & Separation Processes.* 1991 (Fourth edition). 2: p. 1008-1010.

Chapter Eight

Concluding Remarks

8 Concluding remarks

8.1 Conclusions

The main aim of this thesis was to investigate relationships between intrinsic properties of nanoporous materials and their maximum hydrogen uptake and total hydrogen capacities for hydrogen storage for sustainable applications. These are the conclusions that can be drawn from this work:

1) The adsorbent materials were tested with hydrogen at higher pressure ranges than presented in literature with some of them never tested before for hydrogen adsorption. During the course of the experiments, ZIF-9 was found to exhibit flexibility, an interesting feature that has been receiving a lot of attention. Also, relationships between two ZIF topologies for hydrogen adsorption were found, not relying on the nature of the metal. All these findings are related to the objectives I and II set in the aims and objectives of the thesis in Chapter 2.

2) Data gathered from characterization experiments, modelling of hydrogen experimental isotherms on synthesized materials and data obtained from literature allowed the creation of the correlations of their intrinsic properties against their total hydrogen uptake and total hydrogen capacities, which is directly related to the objective II set in the aims and objectives of the thesis in Chapter 2.

3) The obtained correlations together with their densities allow the prediction of the properties (BET surface area and pore volume) of a MOF that would meet the DOE targets given the system properties (mass and volume) as well as the density, filling fraction and packing of the material, which is directly related to the objective II set in Chapter 2 (2.8 Aim and objectives of the thesis).

4) The model was used to predict the adsorbate densities within the pore of the tested materials, which contributed to the prediction of the total hydrogen capacity of every material. However, the model indicated very high hydrogen adsorbate densities within the pores of most of the materials when compared to solid hydrogen. A methodology was developed in order to obtain tendencies of the modelled pore volume values

obtained from the model fitting. This indicated that the theoretical pore volume would not approach the experimental ones with experimental hydrogen excess at higher pressures in many cases. Also, model fittings using experimental pore volumes were done, showing high goodness of fit in many cases and lowering the adsorbate densities of the materials to closer densities that of solid hydrogen in most of the cases, indicating more realistic adsorbate densities. All these findings are related to the objective III set in the aims and objectives of the thesis in Chapter 2.

5) INS tests with different activated carbons backed up the existence of solid-like hydrogen in different activated carbon materials with very small microporous pores. This has been proved by the appearance of the 14.7 meV peak when tested with hydrogen at low pressures and 77 K. Results indicated the presence of the signal in materials with microporous pores ranged between 5 and 6.8 Å, not being shown in a material whose lowest pore size was 11 Å. From this data and previous experiments, it can be predicted the presence of solid-like hydrogen in materials with pores within 5 and 7 Å, narrowing down the optimum pore size range for hydrogen storage in nanoporous materials, which is directly related to the objective IV set in Chapter 2 (2.8 Aim and objectives of the thesis).

6) IRMOF-1 C_{60} was successfully synthesized by using the modified synthesis method of IRMOF-1 to further research on pore size optimisation. A change in colour, XRD and Raman tests indicate the presence of C_{60} in the structure and possible changes in the unit cell, giving the XRD wider peaks compared to the non-impregnated version. However, only a negligible boost in hydrogen adsorption at very low pressures was shown, which is directly related to the objective V set in the aims and objectives of the thesis in Chapter 2.

7) The ZIF and zeolite 13X mixed material combination was proven to be feasible, opening the possibility of using ZIFs that showed high CO_2 capabilities to create new mixed materials for CO_2 adsorption. However, part of the zeolite 13X beads got detached from the beads, mixing with the ZIFs, not allowing individual gravimetric quantification of the zeolite or ZIFs in the mixed materials. Zeolite 13X beads thermal stability, CO_2 isotherm at 273 K and low pressure and density has been first tested,

giving additional information for CO_2 adsorption systems, showing higher capacity than the powder zeolite 13X. This research is directly related to the objective VI set in the aims and objectives of the thesis in Chapter 2.

8) ZIF-11 and ZIF-12 also showed flexibility features shown in Chapter 8 when further characterizing them because of observation of flexibility in ZIF-9. Adsorption isotherms with N_2, Ar and CO_2 were done to further explore this. The materials show different adsorption amounts and different isotherm shapes for Ar and N_2, molecules whose kinetic diameter is bigger that of the ZIFs pore window aperture (3.0 Å). All these findings are directly related to the objective I set in the aims and objectives of the thesis in Chapter 2.

8.2 Suggested future work

The work presented in this thesis showed the interests and importance of modelling hydrogen adsorption in nanoporous materials. During the course of this work some ideas derived from conclusions of this work or as a result of working in this area are suggested as future work:

1) The methodology used in this thesis assumes a constant pore volume and some of the models that try to expand the use of the model to flexible materials such as ZIF-7 or ZIF-9 did not yield satisfactory results. Other new models to fit the experimental isotherms of these materials would be interesting for the development of the model for flexible materials.

2) The methodology used assumes constant adsorbate density within the pores of the materials. Trying to develop the model to diminish the predicted adsorbate density as the adsorbed hydrogen is further away from the walls of the pore would make the model more realistic. Also, the model could probably be further improved by considering the surface area of the material, as the strongest correlation found was between surface area and the maximum excess uptake of the tested materials. Also, considering more than a unique pore volume in the model to include different contributions from both micropore and meso/macropore volumes would allow a better prediction of the total hydrogen capacity of modelled nanoporous material datasets.

3) INS results and conclusions pointed out that nanoporous materials with micropore volumes ranged between 5 and 6.8 Å will show the solid-like hydrogen peak at 14.7 meV and that materials with pore sizes of 11 Å or higher will not show it [1]. Testing activated carbons whose lowest pore sizes are 8, 9 or 10 Å would give a pore size range where the solid-like hydrogen phenomena occurs. This would give the range of pore sizes for optimum hydrogen storage for the design of future materials. Also, when that range is found, testing materials with the highest micropore size within the found range and different pore shapes would give hints about the most adequate pore shapes and topologies for hydrogen storage.

4) The correlations include several different MOF topologies and metals as well as a wide range of surface areas and pore volumes. However, the correlation could be further strengthen to give better property predictions by adding data from more materials, especially if they exhibit different topologies, very high hydrogen uptakes, surface areas and/or pore volumes.

5) Impregnation results on IRMOF-1 for pore size optimization barely show any improvement in hydrogen uptake. Modifying the synthesis to try to increase the amount of C_{60} in the framework or trying different crystalline materials like MOF-177, studied in literature, could show improvements in hydrogen uptake.

6) Zeolite 13X beads have shown the highest CO_2 uptakes at very low (4000 ppm, 2 bar) and low pressures (up to 950 mmHg), showing the best breakthrough time when used alone. However, CO_2 uptakes of ZIF-7, ZIF-12 and especially of ZIF-70, ZIF-78 and ZIF-82 are also high at low pressures, indicating high potential at higher pressures as well as complete retention of CO_2 while letting CH_4, CO, and N_2 through the pores of the framework in breakthrough experiments [2-4]. Testing these ZIFs up to 20 bar might show higher CO_2 uptakes than zeolite 13X beads, making interesting the creation of mixed ZIF-zeolite 13X beads to improve the hydrogen purification system connected to the IGA or other hydrogen testing devices in lab 1.04.

Supplementary Information (Supplied in electronic format)

Supplementary Information A

List of used chemicals together with their purity and supplier for material syntheses.

Supplementary Information B

ASAP 2020 and HTP-1 accuracy and calibration tests.

Supplementary Information C

Experimental N_2 characterization sorption results at cryogenic temperatures.

Supplementary Information D

Experimental XRD spectra of the synthesized materials, discussed and compared to the CIF files from The Cambridge Crystallographic Data Centre.

Supplementary Information E

Experimental TGA results of most of the synthesized materials, discussed and, in some cases, compared with literature.

Supplementary Information F

Table with the total hydrogen capacity values used for the correlations.

8.3 References

1. Ting, V.P., Ramirez-Cuesta A.J., Bimbo N., Sharpe, J.E., Noguera-Diaz A., Presser V., Rudic S., Mays, T.J., *Direct Evidence for Solid-like Hydrogen in Microporous Carbon at Supercritical Temperatures.* ACS Nano, 9 (8), pp 8249–8254.
2. Phan A., D.C.J., Uribe-Romo F.J., Knobler C.B., O'Keeffe M., Yaghi O.M., *Synthesis, Structure, and Carbon Dioxide Capture Properties of Zeolitic Imidazolate Frameworks.* Accounts of Chemical Research, 2010. 43(1): p. 58-67.
3. Banerjee, R., Furukawa, H., Britt, D., Knobler, C., O'Keeffe, M., Yaghi, O.M., *Control of Pore Size and Functionality in Isoreticular Zeolitic Imidazolate Frameworks and their Carbon Dioxide Selective Capture Properties.* Journal of the American Chemical Society, 2009. 131(11): p. 3875-3877.
4. Banerjee R., P.A., Wang B., Knobler C., Furukawa H., O'Keeffe M., Yaghi O. M., *High-throughput synthesis of zeolitic imidazolate frameworks and application to CO2 capture.* Science, 2008. 319(5865): p. 939-943.

Supplementary information A

List of used chemicals together with their purity and supplier for material syntheses

The list of the used chemicals together with their purity and supplier name is shown here:

-Zinc nitrate hexahydrate, reagent grade (98 %) from Sigma Aldrich.
-Zinc acetate dihydrate (97+ %) from Alfa Aesar.
-Cobalt (II) nitrate hexahydrate, ACS (98.0-102 %) from Alfa Aesar.
-Cobalt (II) acetate tetrahydrate (98 %) from Alfa Aesar.
-Chromium (III) nitrate nonahydrate (99 %) from Sigma Aldrich.
- Zirconium tetrachloride anhydrous (98 %) from Acros Organics.
-2-Aminoterephthalic acid (99 %) from Sigma Aldrich.
-Terephthalic acid (98 %) from Sigma Aldrich.
-2,6-Naphtalene dicarboxylic acid (99 %) from Sigma Aldrich.
-4,4'-biphenyldicarboxilic acid (BPDC) (97 %) from Sigma Aldrich.
-Benzimidazole (99 %) from Alfa Aesar.
-2-Methylbenzimidazole (97 %) from Alfa Aesar.
-2-Nitrobenzimidazole (98 %) from Acros Organics.
-Fullerene-C60 (99 %) from Sigma Aldrich.
-Ammonium hydroxide, ACS (28.0-30.0 %) from Alfa Aesar.
-Ethanol, absolute from Fischer Scientific.
-Ethanol (95 % v/v) from Fisher Scientific.
-Methanol (>99.9) from Sigma Aldrich.
-Methanol purum (> 99.0 %) from Fluka analytical.
-N,N-Diethylformamide (99 %) (DEF) from Acros Organics.
-N,N-Diethylformamide (99 %) (DEF) from Alfa Aesar.
-N,N-Dimethylformamide (DMF), analytical reagent grade, from Fischer Scientific.
-Toluene, ACS (99.5 %) from Alfa Aesar.

Supplementary information B

ASAP 2020 and HTP-1 accuracy and calibration tests.

B.1 ASAP 2020 reference material tests

Material details and settings:

Lot: A-501-50. PIN: 004/16821/00

-Location: laboratory 1.04, 9W, Chemical Engineering Department, University of Bath

-Device used: ASAP 2020

Test settings:

-Sample was degassed at 90 °C during 1 h while evacuating and 4 h under vacuum at 350 °C during 4 h (10 °C min-1).

- Sample mass range: 0.2-0.3 g

-Volumetric method used. 5 Point BET surface area (from 0.05 to 0.3 P/Po).

-Nitrogen was used for the determination: BOC N2, 99.998 % purity.

Table B.1 shows the results obtained and their comparison with the supplier's results (Micromeritics):

Table B.1. Silica-alumina reference tests results and comparison with the supplier's.

	BET (m^2 g^{-1})	Total pore volume (0.990 to 0.998 P/Po) (cm^3 g^{-1})	Single point specific surface area (m^2 g^{-1})	Average pore diameter (Å)
Supplier's values	213 ± 13	0.6 ± 0.08 (at 0.995 P/Po)	208 ± 6	114 ± 15
Test 1 (18/02/13)	208 ± 2	0.62 (at 0.998 P/Po)	204.9	119
Test 2 (03/04/14)	212 ± 1	0.63 (at 0.998 P/Po)	208.9	118
Test 3 (15/10/14)	211 ± 1	0.61 (at 0.996 P/Po)	207.6	115
Test 4 (09/06/15)	210 ± 2	0.61 (at 0.998 P/Po)	206.52	119

The results obtained from the ASAP 2020 during the duration of the PhD showed outstanding closeness with the supplier's results except for the total pore volume value. Despite of the settings, the device always measured above 0.995 P/Po. However, the values obtained between the tests were very close. From this it can be concluded that the ASAP 2020 was correctly calibrated during the period where all the materials were tested/characterized.

B.2 High Temperature Pressure-1calibration

The HTP-1 (High Temperature Pressure-1) allowed the measurement of hydrogen isotherms with materials at very high pressures that had not been tested before, meaning a correct calibration was of utmost importance. The HTP-1 can be calibrated with regard to dosing pressure, reactor volume and thermostat partition values. The dosing pressure calibration was only needed to be done at the beginning of the course of the experiments, ensuring that the volumes dosed are accurately measured. Doing this also calibrated the reactor volume.

The reactor volume calibration ensures a fixed volume for the reactor. If the reactor is properly calibrated, a pycnometry test on an empty reactor should yield a value very close to zero. As an example, the value when the immersion reactor was last calibrated (October 2014) was 0.0011 ± 0.0001 cc. The thermostat partition values affect differently each pressure point at a given temperature, also depending on the used gas. Ideally, when running a hydrogen isotherm with an empty reactor, there should be a straight line, measuring 0 μmol (uptake) along all the pressure points (on an uptake vs pressure graph). However, this cannot be achieved in practice, and a ± 50 μmols from zero at any pressure according to the device manufacturer company is considered acceptable.

The thermostat partition value was changed after calibration tests on January 2013, October, 2014 and again on November, 2014. This last calibration was done in order to increase the liquid nitrogen level of the system to allow longer analysis, which was required for some materials due to their low kinetics. The blank isotherm results at high pressures after reactor calibration and changes in the thermostat partition are shown in Figure B.1:

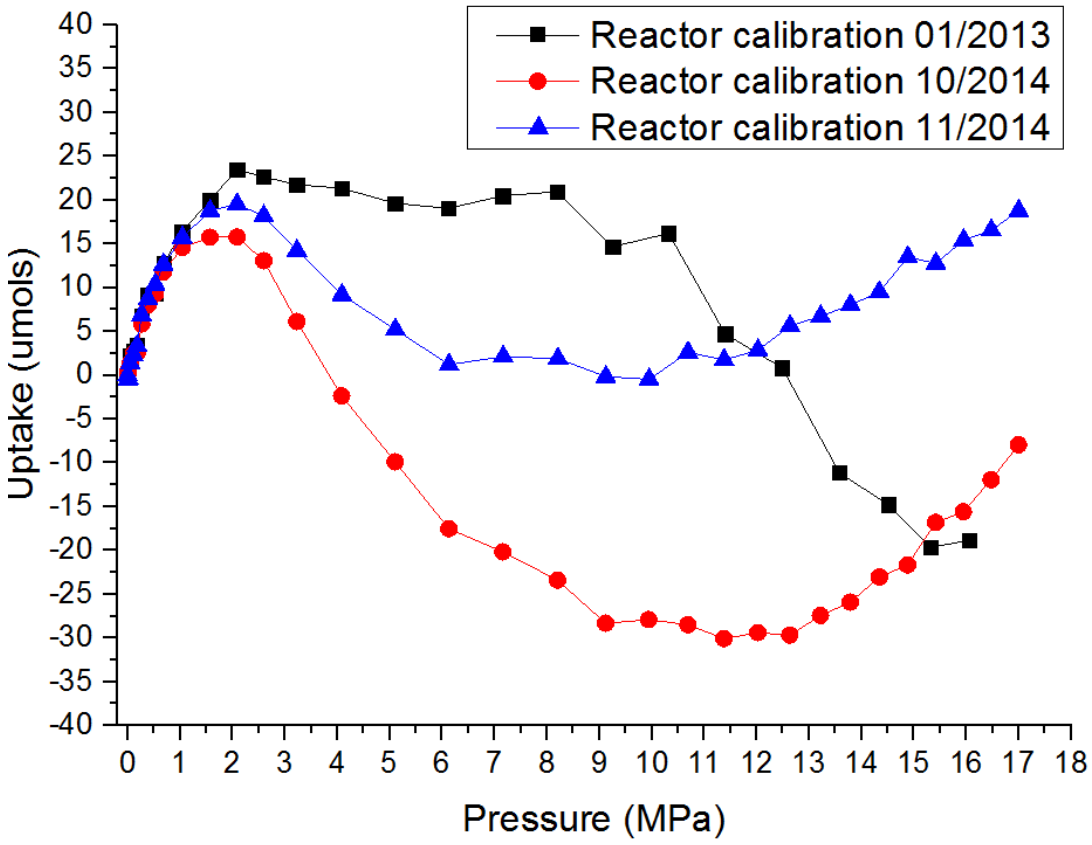

Figure B.1. Hydrogen blank isotherms measured 77 K used to calibrate the immersion reactor.

As it can be seen, the values are within ± 50 μmols, indicating that the system was fully calibrated when the materials were tested.

Supplementary information C

Experimental N_2 characterization sorption results at cryogenic temperatures.

IRMOF-1

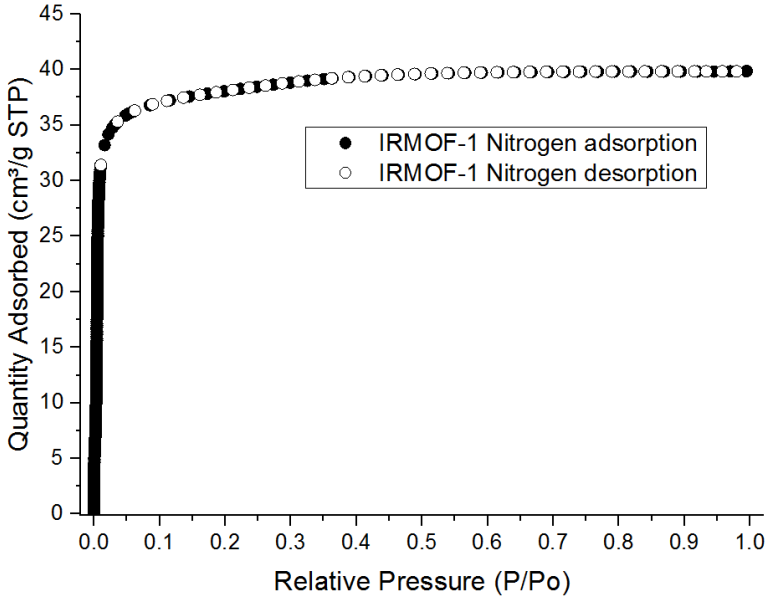

Figure C.1. IRMOF-1 Nitrogen isotherm at 77 K.

IRMOF-3

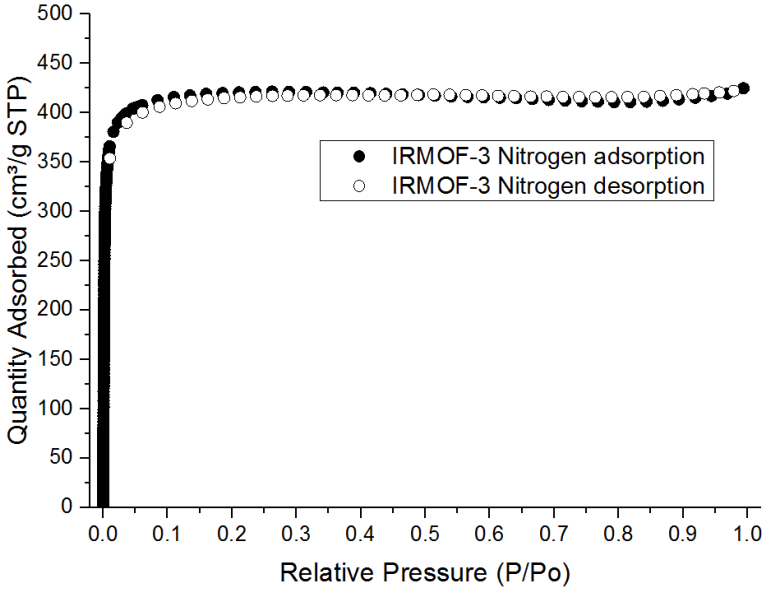

Figure C.2. IRMOF-3 Nitrogen isotherm at 77 K.

IRMOF-8

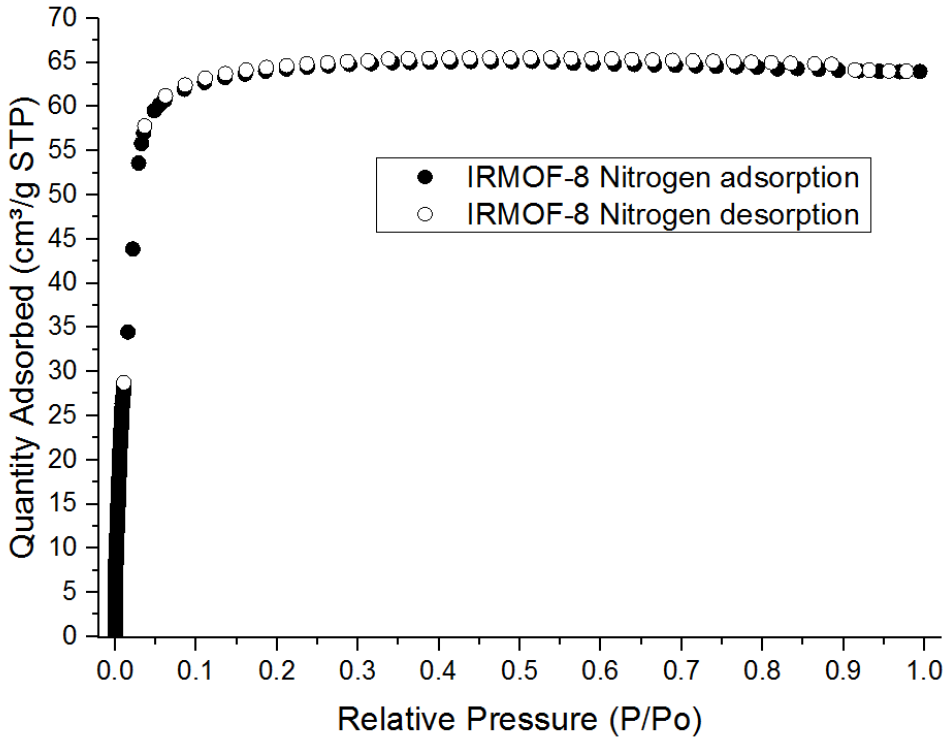

Figure C.3. IRMOF-8 Nitrogen isotherm at 77 K.

IRMOF-9

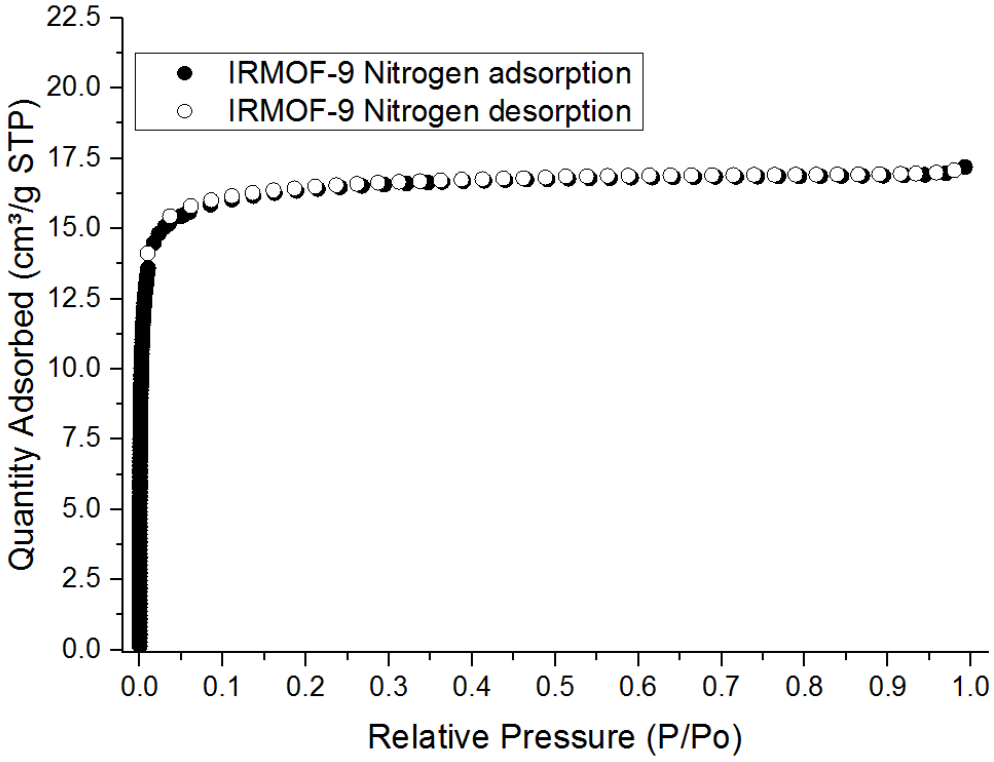

Figure C.4. IRMOF-9 Nitrogen isotherm at 77 K.

ZIF-8

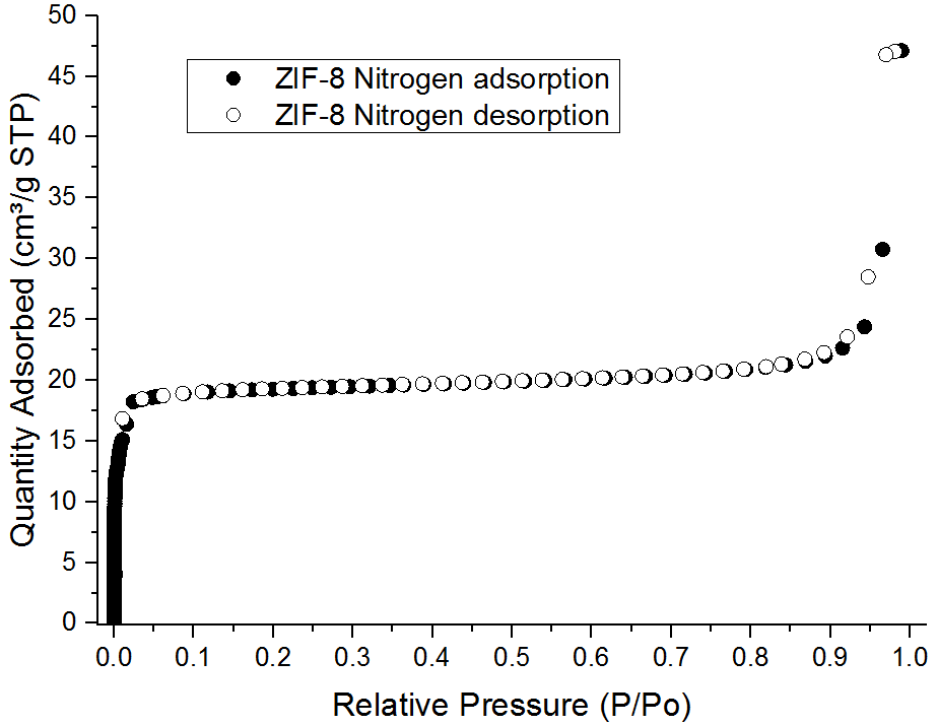

Figure C. 5. ZIF-8 Nitrogen isotherm at 77 K.

ZIF-12

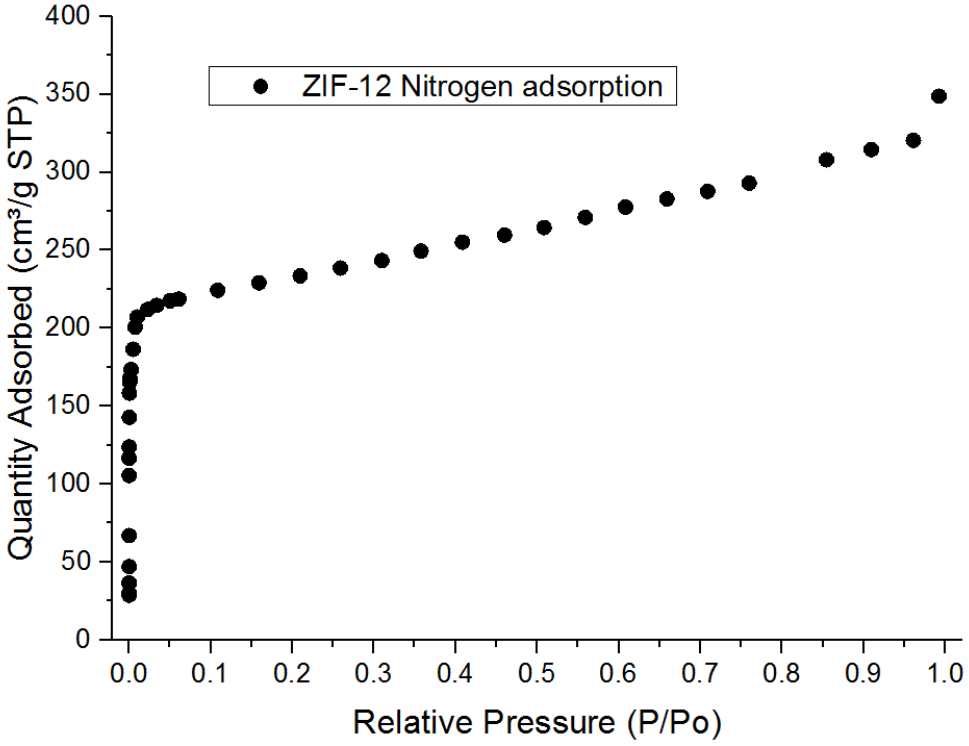

Figure C.6. ZIF-12 Nitrogen isotherm at 77 K.

CoNIm (RHO)

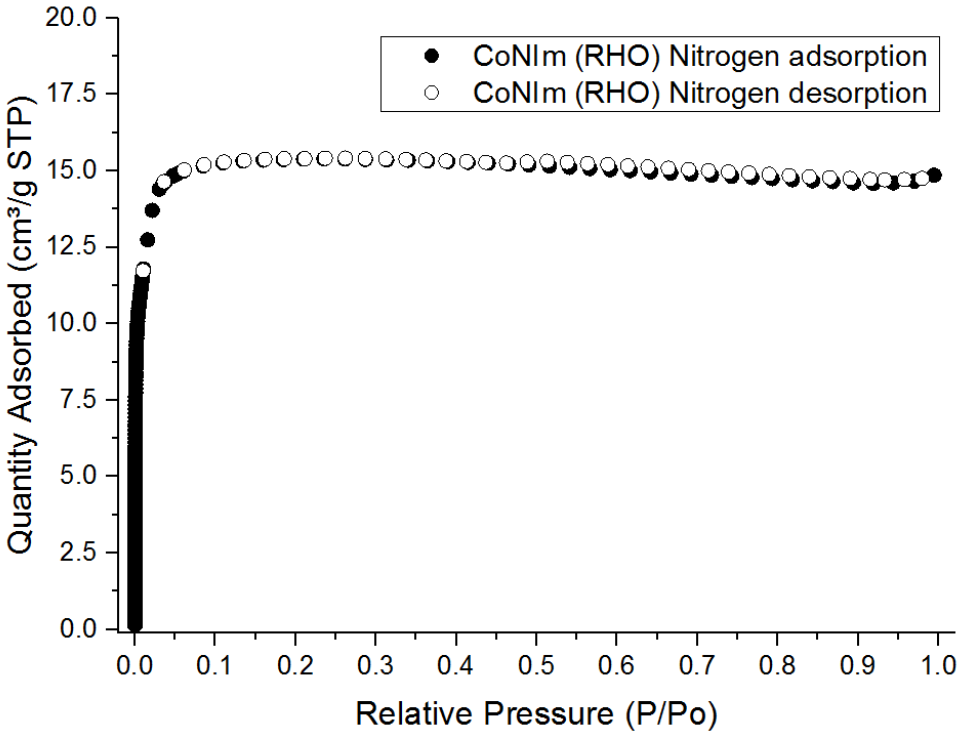

Figure C.7. CoNIm (RHO) Nitrogen isotherm at 77 K.

MIL-101 (Cr)

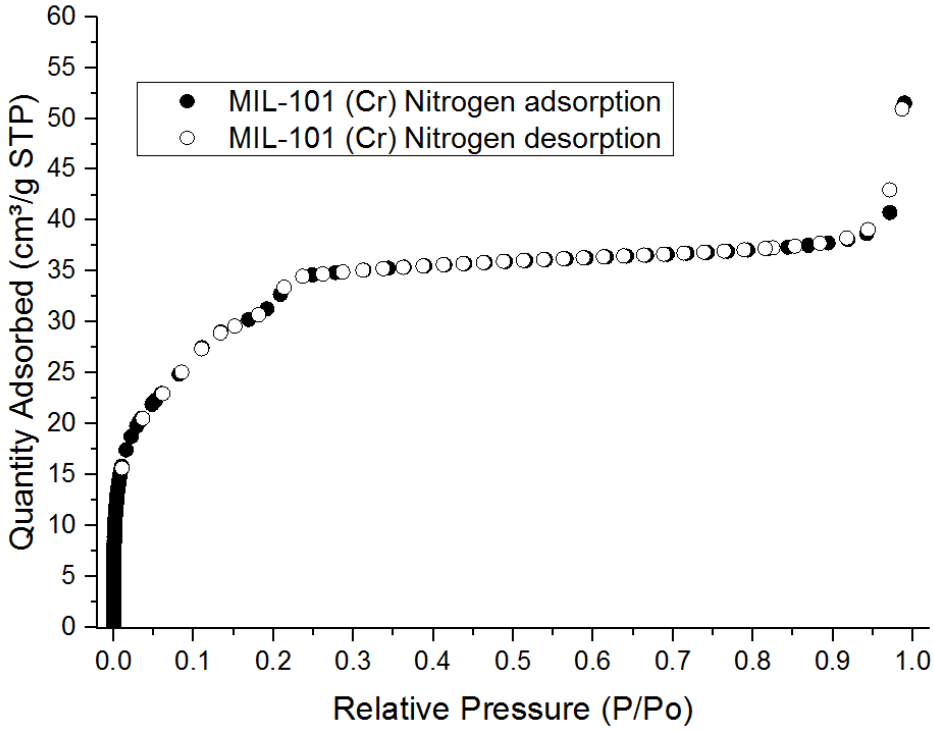

Figure C.8. MIL-101 (Cr) Nitrogen isotherm at 77 K.

NH_2-MIL-101 (Cr)

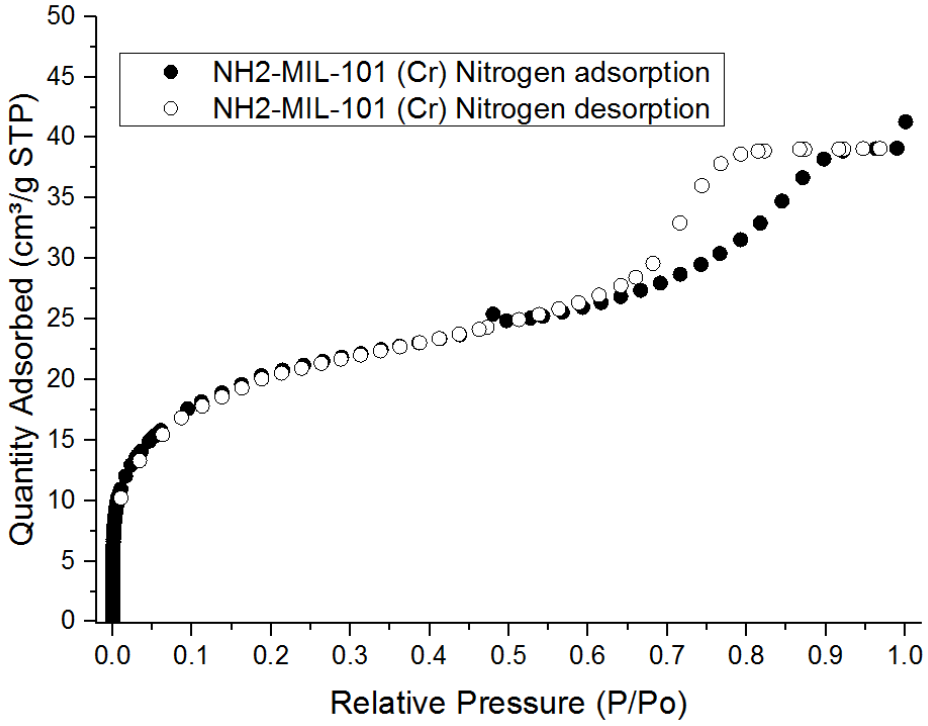

Figure C.9. NH_2-MIL-101 (Cr) Nitrogen isotherm at 77 K.

NH_2-MIL-101 (Al) (Ibrahim's Ahmet data)

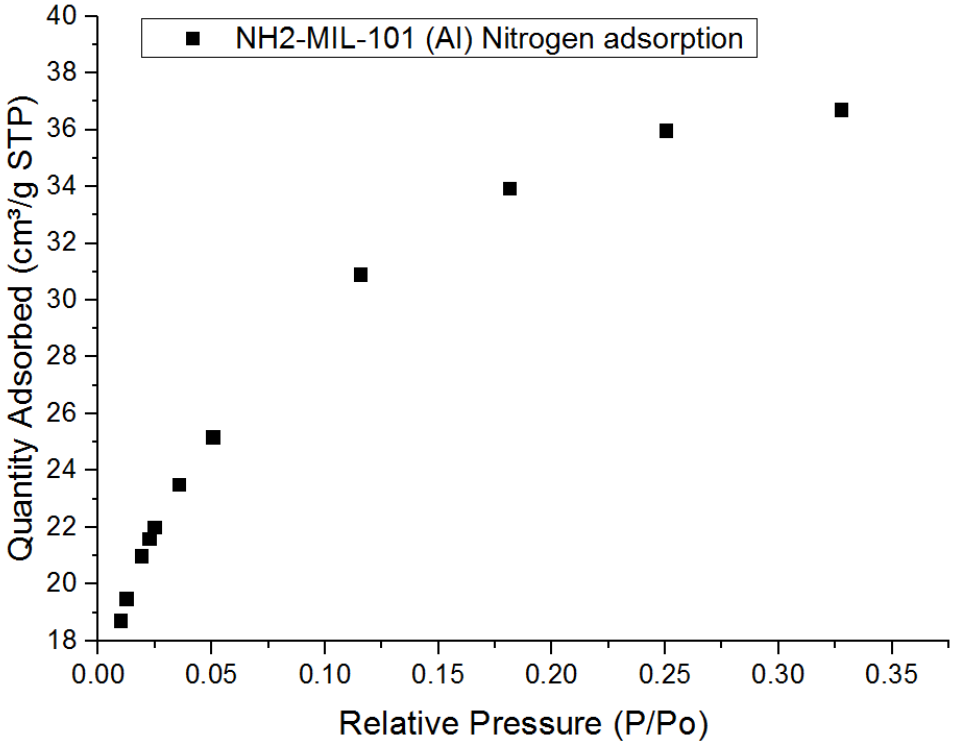

Figure C.10. NH_2-MIL-101 (Al) Nitrogen isotherm at 77 K from Ibrahim's Ahmet.

UiO-66

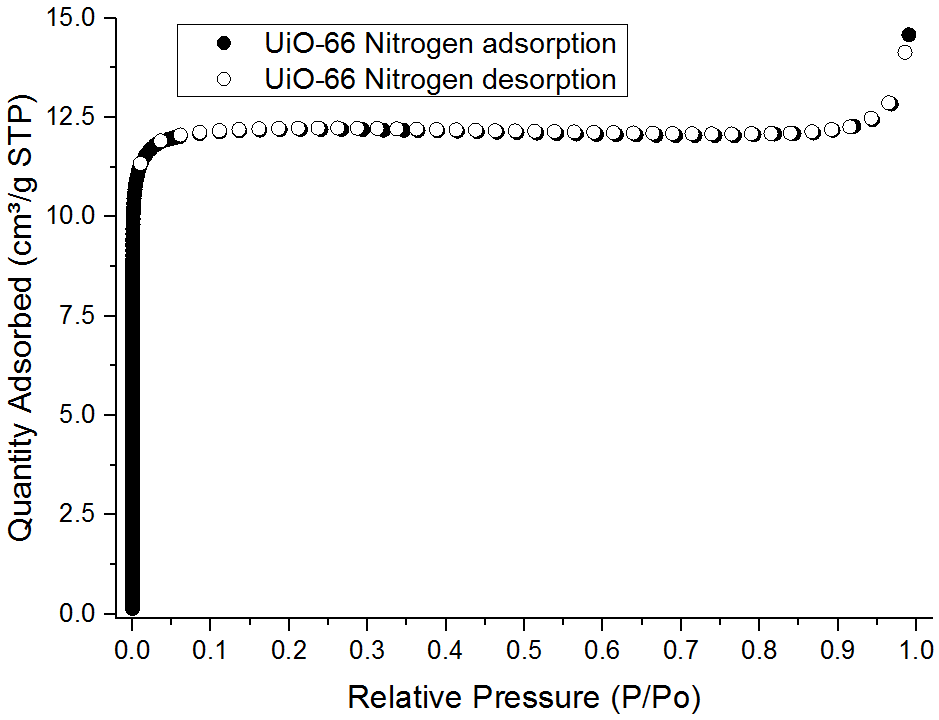

Figure C.11. UiO-66 Nitrogen isotherm at 77 K.

UiO-67

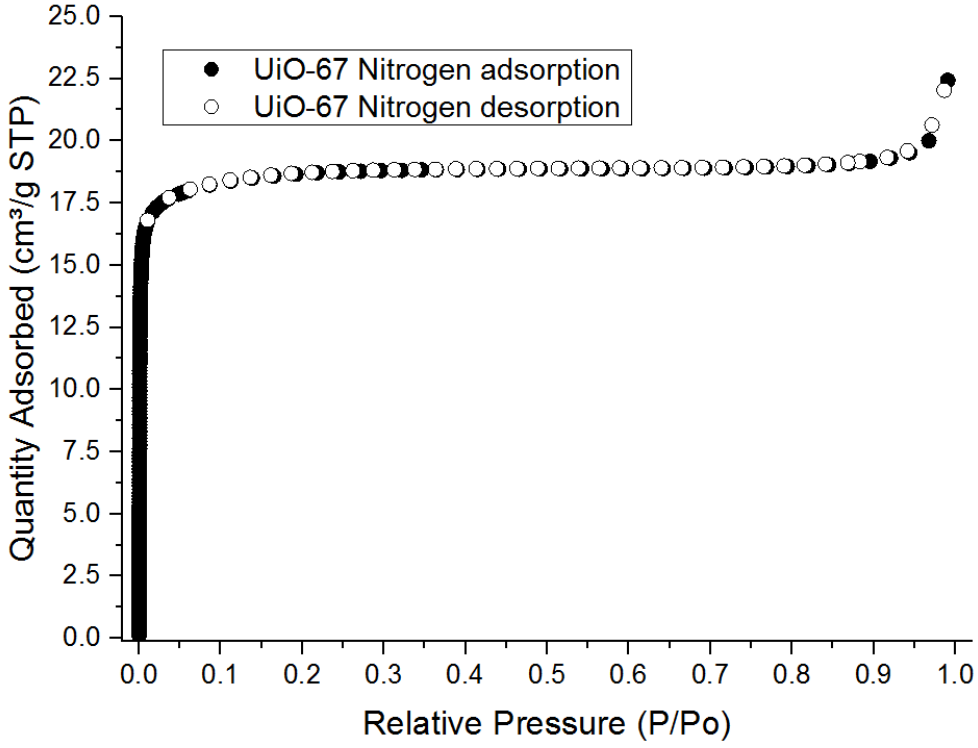

Figure C.12. UiO-66 Nitrogen isotherm at 77 K.

HKUST-1

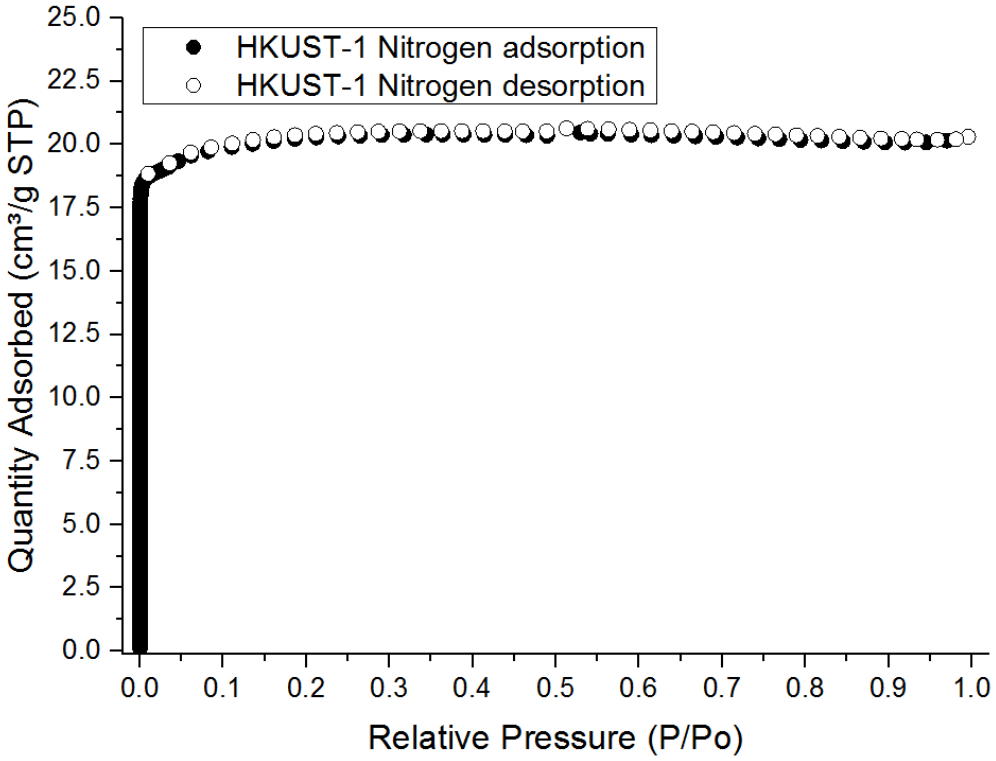

Figure C.13. HKUST-1 Nitrogen isotherm at 77 K.

Supplementary information D

Experimental XRD spectra of the synthesized materials

IRMOF-1

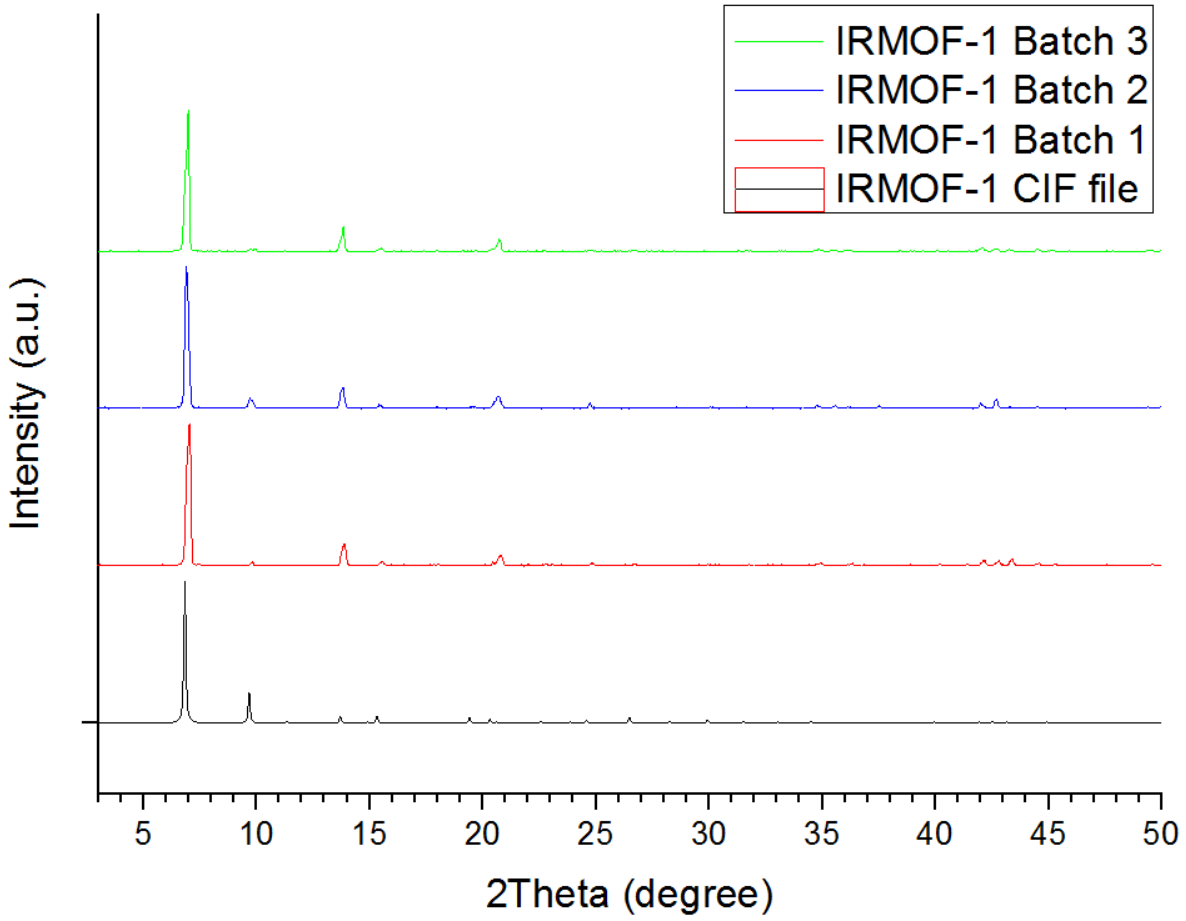

Figure D.1. PXRD of IRMOF-1. PXRD from CIF file (black) and results from three synthesized batches (red, blue and green).

Figure D.1, presents the experimental IRMOF-1 spectra compared with the data from the CIF file, not fully matching in terms of peak intensity, which is also seen in literature [1]. The peak at 10 and 14 2θ are much closer that of literature data as with many of the smaller peaks. All this, together with the fact that the material obtained was also a colourless crystalline material corroborates the successful synthesis of IRMOF-1.

IRMOF-1 C60

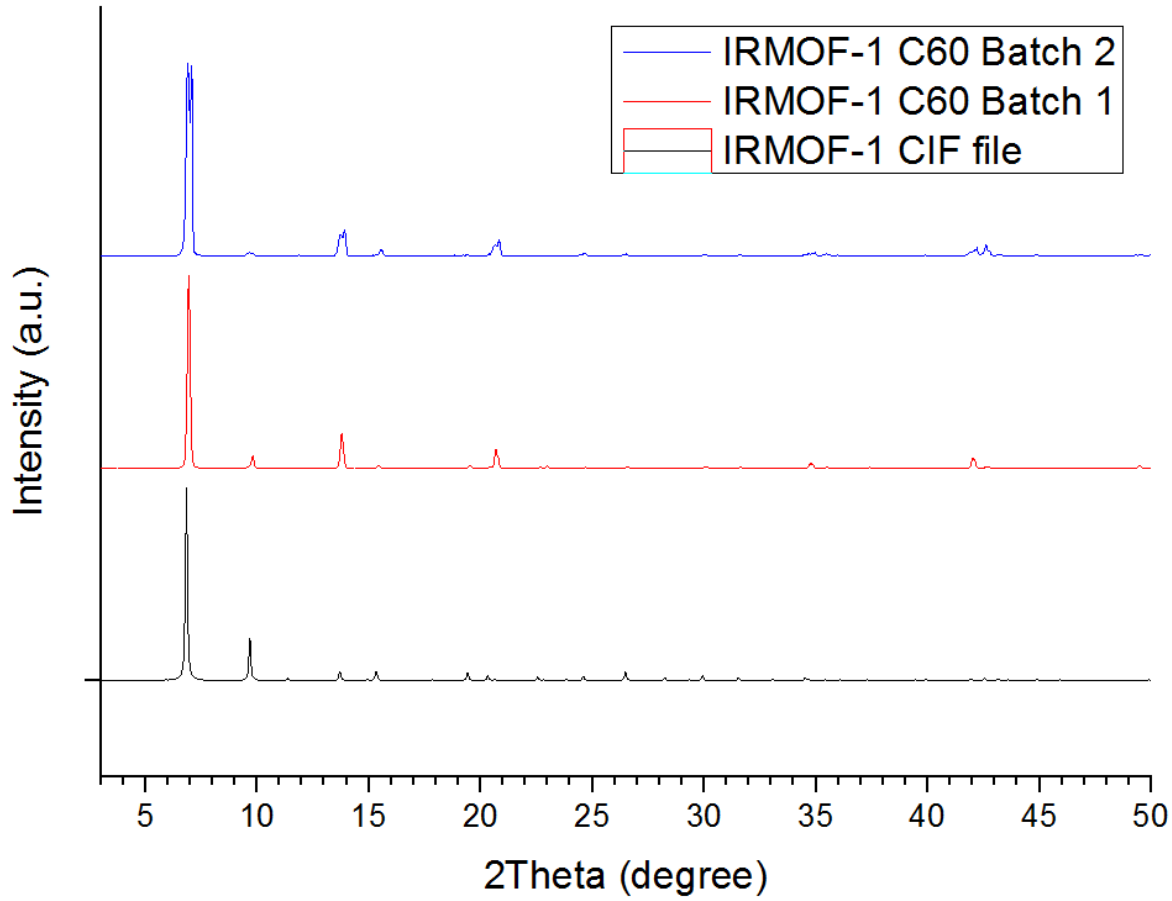

Figure D.2. PXRD of IRMOF-1 C_{60}. PXRD from CIF file (black) and results from the two synthesized batches (red and blue).

The experimental XRD results of IRMOF-1 C_{60} in Figure D.2 show very similar results that of the experimental IRMOF-1 spectra from Figure D.1. Also, the colour of the crystals is brown-orange compared with the colourless crystals from IRMOF-1, showing that C_{60} is present.

IRMOF-3

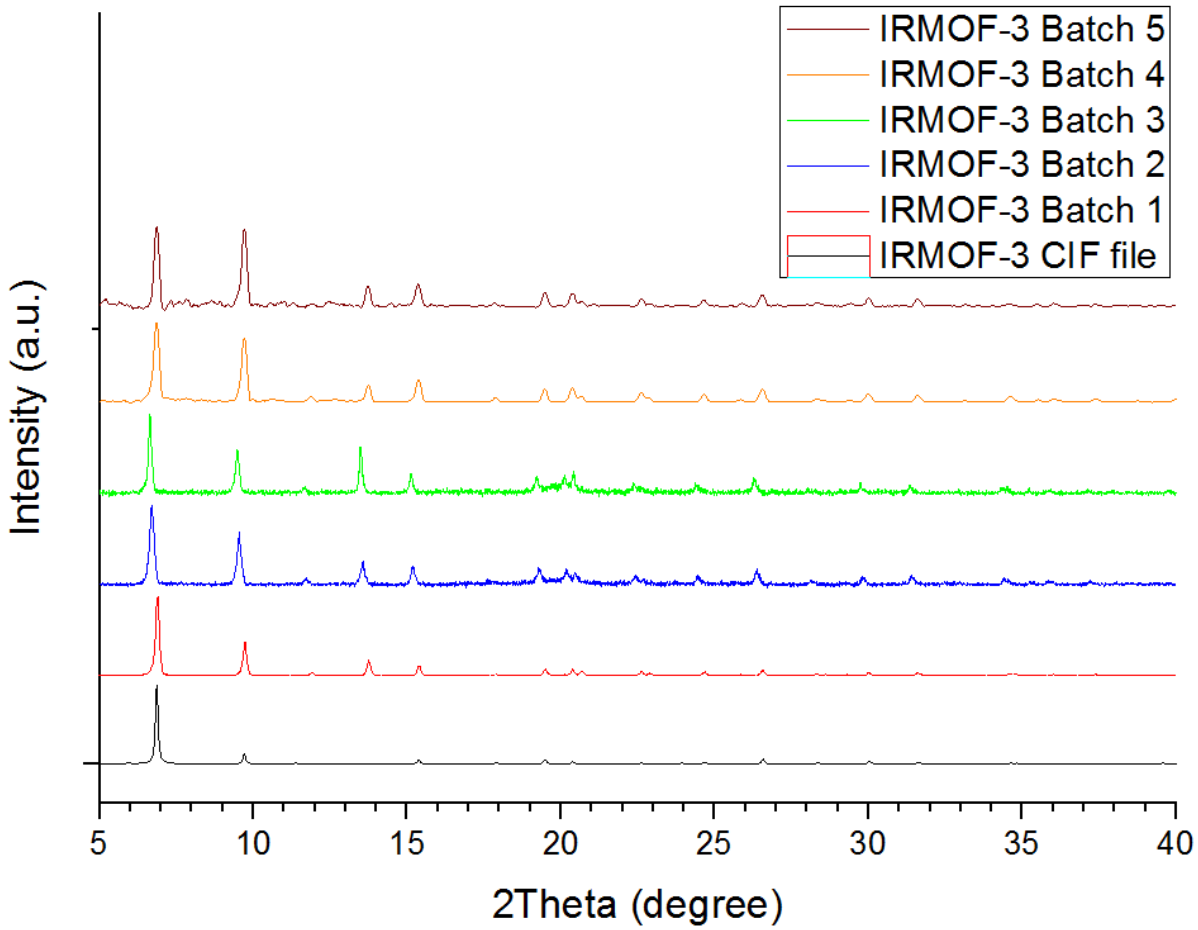

Figure D.3. PXRD of IRMOF-3. PXRD from CIF file (black) and results from the five synthesized batches (red, blue, green, orange and brown).

The IRMOF-3 PXRD from the tests in Figure D.3 show a very close match with the CIF, aside from the fact that the intensity of the peak observed around 10 2θ is higher, which is believed to be due the solvent they were immersed in while they were tested (DMF). However, when compared with literature data, it is also shown a very close intensity ratio with the two highest peaks of the PXRD as in Figure D.3, indicating the correct synthesis of IRMOF-3 [2].

IRMOF-8

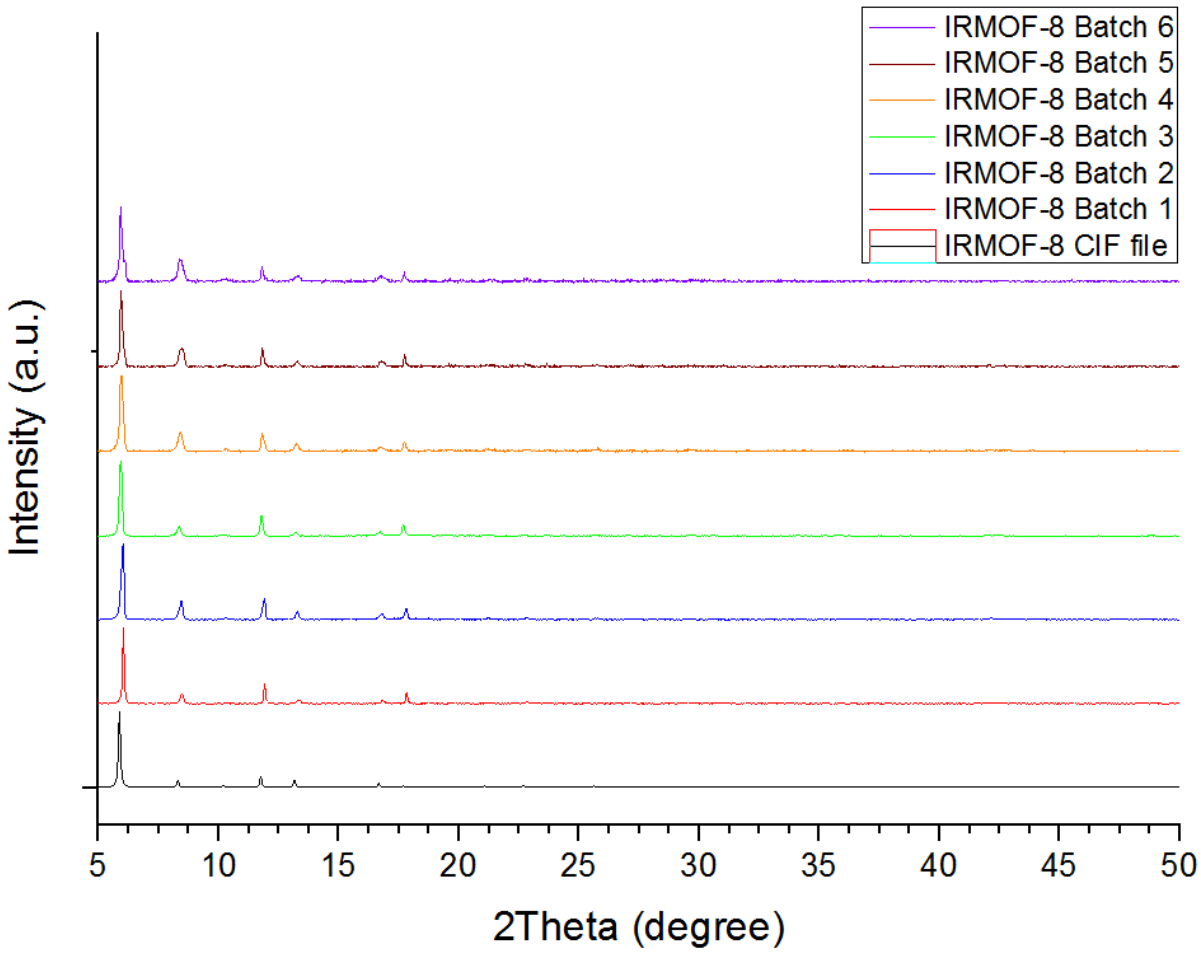

Figure D.4. PXRD of IRMOF-8. PXRD from CIF file (black) and results from the six synthesized batches (red, blue, green, orange, brown and purple).

From the results of the synthesized IRMOF-8 batches in Figure D.4, it can be seen that all the major peaks are in place (6, 9, 11.5, 12.5, 17 and 18 2θ), showing a higher peak ratio at around 18 2θ when compared with the CIF file. When further compared to experimental literature values, the peak ratio looks closer that of the CIF file, indicating the correct synthesis of the 6 IRMOF-8 batches [3].

IRMOF-9

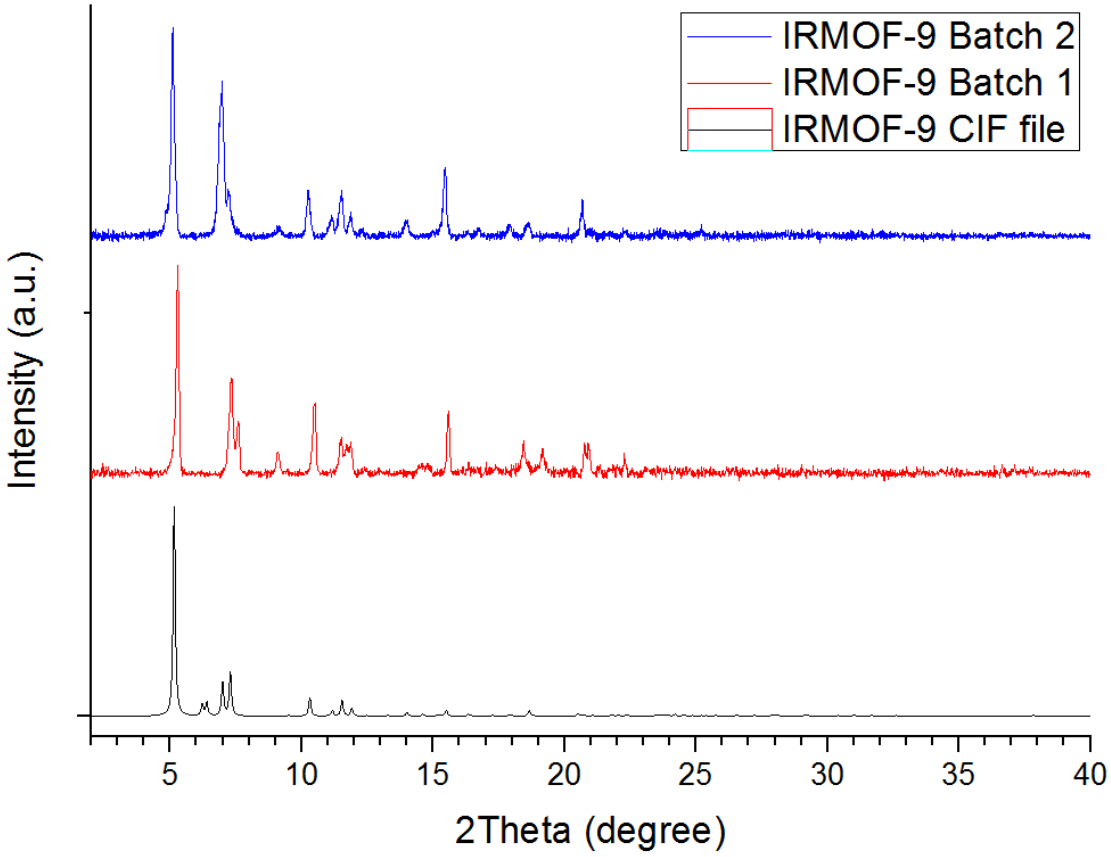

Figure D.5. PXRD of IRMOF-9. PXRD from CIF file (black) and results from the two synthesized batches (red and blue).

IRMOF-9 experimental batches shown in Figure D.5 might indicate the presence of the material that was intended to be synthesized in the first place, IRMOF-10. Batches show a higher peak ratio for the smaller peaks than the one from the CIF file, which are related to guests present in the pores (DMF). The authors of the IRMOF patent were unable to obtain single crystals of IRMOF-10 of sufficient quality, so a simulated pattern had to be created based on the IRMOF-12 coordinates, indicating the difficulty of its synthesis [4].

ZIF-7

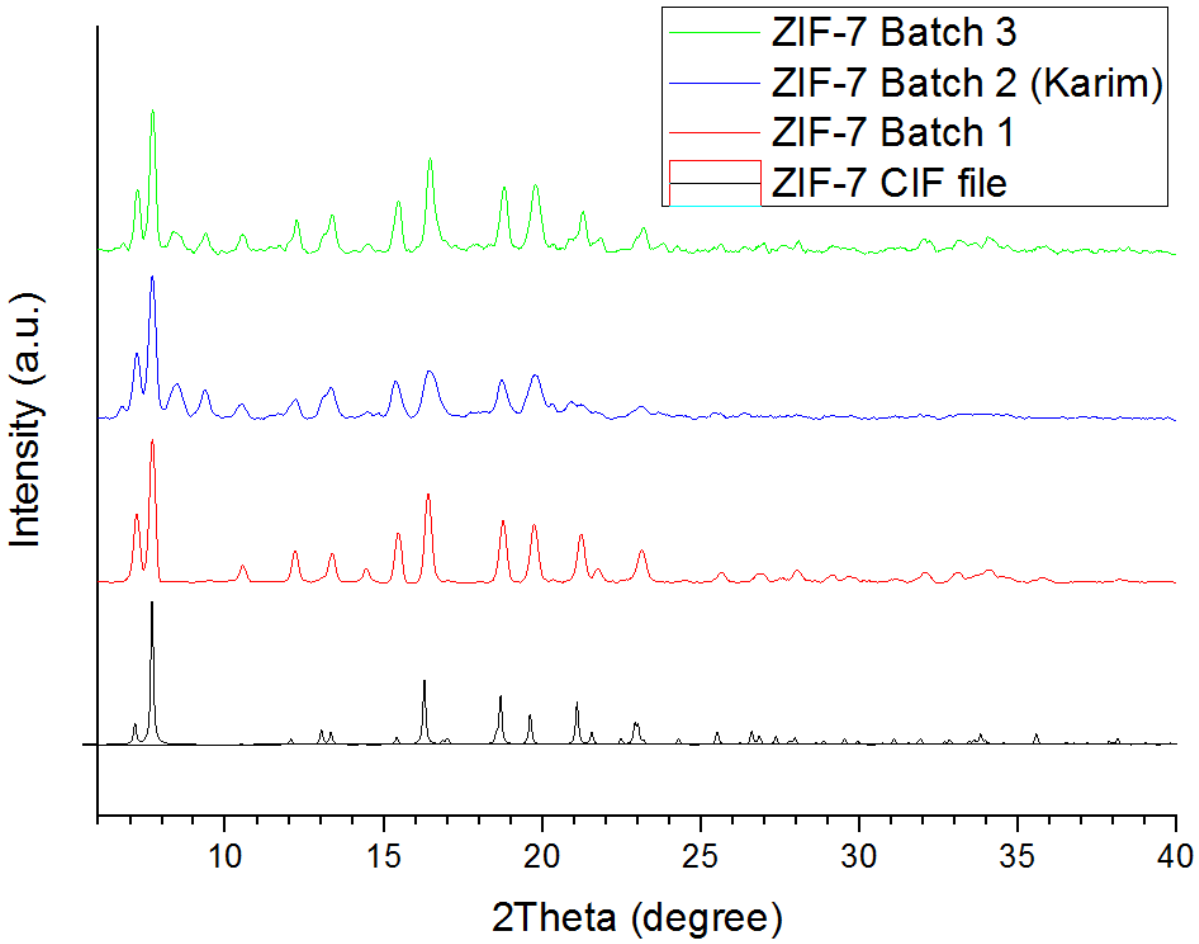

Figure D.6. PXRD of ZIF-7. PXRD from CIF file (black) and results from the three synthesized batches (red, blue and green).

As it can be seen in Figure D.6, the experimental batches of ZIF-7 (but the red one) show additional peaks at 7, 9 and 11 2θ when compared with the CIF file. When the first batch was made, it was decided to fully evacuate the framework before testing, rather than testing them when in ethanol (blue and green batches). The lack of peaks in the last batch proves that the additional peaks found in the two first batches were due to ethanol in the pores. The results from the evacuated batch (red) shows the exact same pattern as the experimental PXRDs from literature, were the synthesis methodology was found, including the peak at 10 2θ which cannot be really seen in the CIF file [5]. Data was shown to the authors and a synthesis expert from the University of Bath, agreeing with the successful synthesis of ZIF-7.

ZIF-8

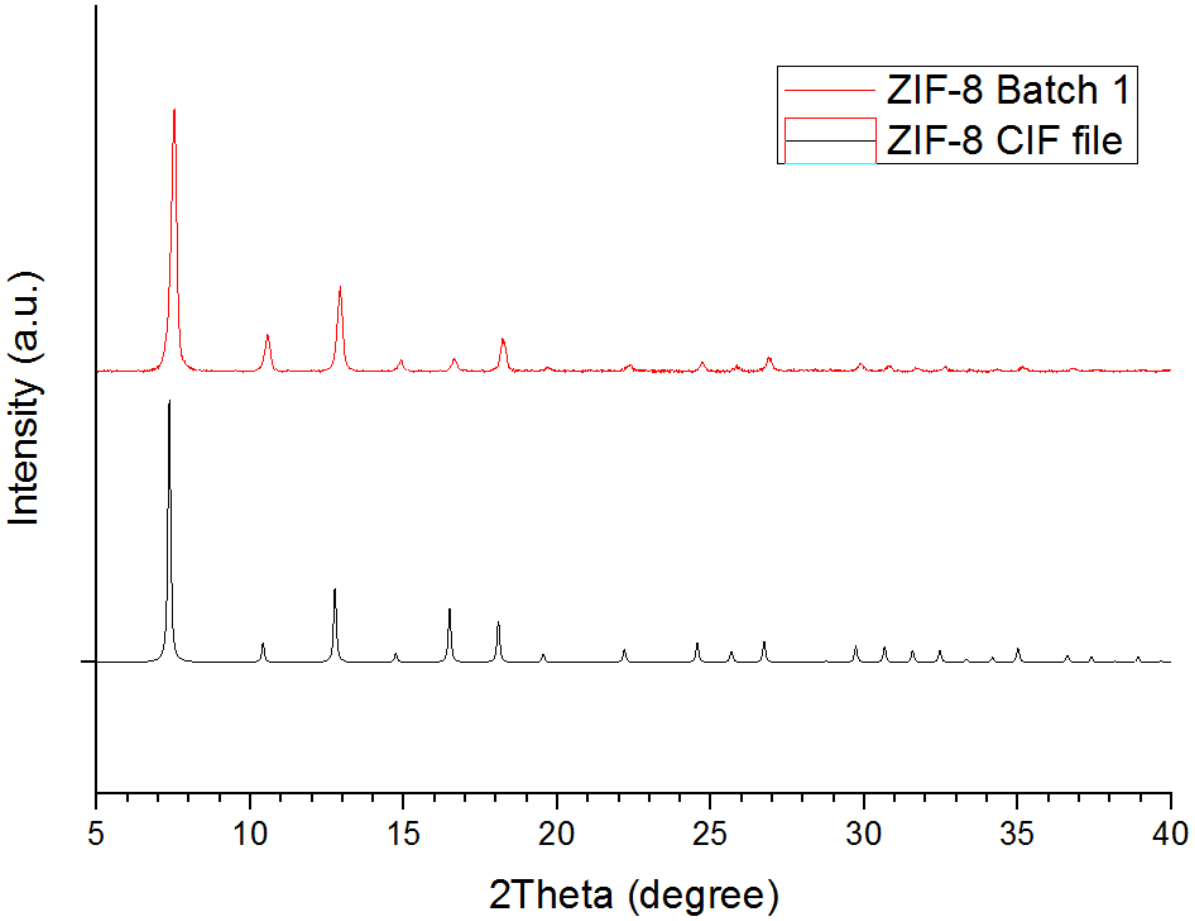

Figure D.7. PXRD of ZIF-8. PXRD from CIF file (black) and results from the synthesized batch (red).

Figure D.7 shows that the experimental PXRD of ZIF-8 looks almost the same as the one from the CIF file. The peaks at 11 and 17 2θ show a lower intensity than the theoretical PXRD but exactly the same when compared with experimental PXRD from literature were the synthesis methodology was taken, proving its correct synthesis [6].

ZIF-9

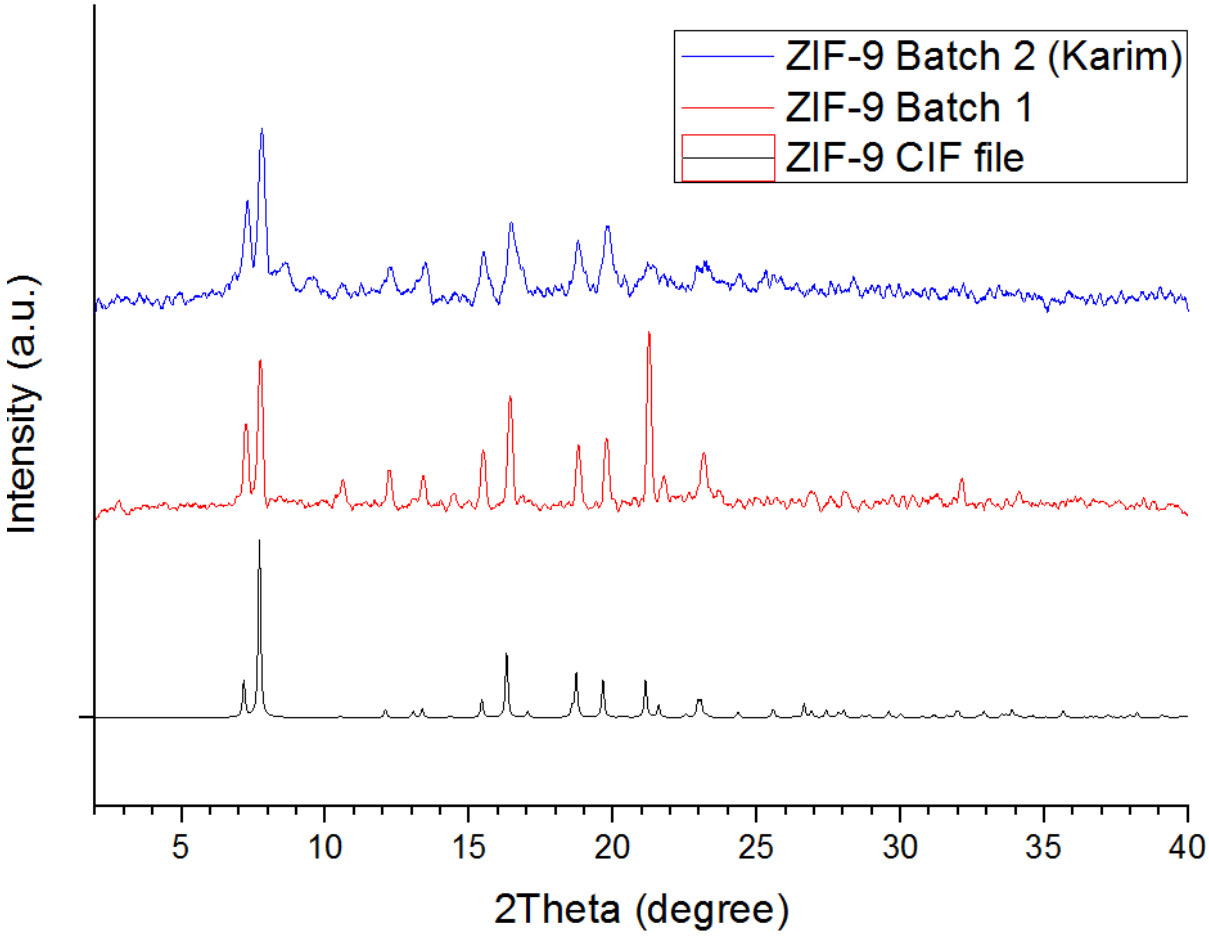

Figure D.8. PXRD of ZIF-9. PXRD from CIF file (black) and results from the two synthesized batch (red and blue).

Figure D.8 presents the experimental batches of ZIF-9, showing all the major peaks when compared with the CIF file. However, when comparing with literature, obtained XRD patterns are shown to have more noise [7]. After discussing with the authors and an expert from the University of Bath, it was determined to be a minor structural change because the initial solvent where the sample was evaporated using a vacuum oven at room temperature whereas the authors left it evaporate at room temperature and pressure.

ZIF-11

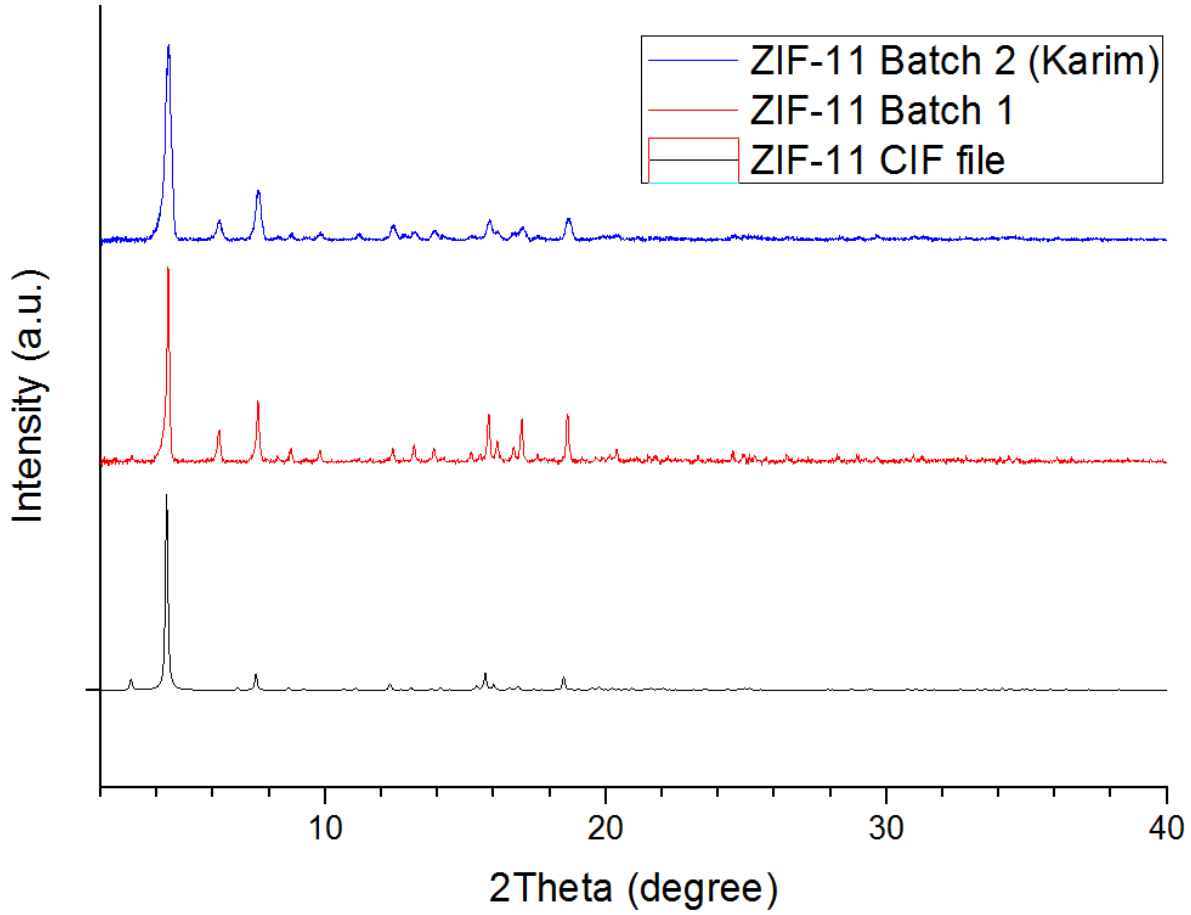

Figure D.9. PXRD of ZIF-11. PXRD from CIF file (black) and results from the two synthesized batches (red and blue).

The experimental patterns of ZIF-11 (Figure D.9) look similar that of the CIF file. The whole spectra, including the peak at 3 2θ, which is barely present, looks like literature data (washed three times as the synthesized materials before being tested) [5]. A small difference exists in peak intensity in the peak at 7.5 2θ, which is likely to be caused by the ethanol in the pores or because of a slight structural change due to drying speed of the material (vacuum at room temperature vs room temperature and pressure). Data was presented to authors and expert, agreeing the correct synthesis of the material.

ZIF-12

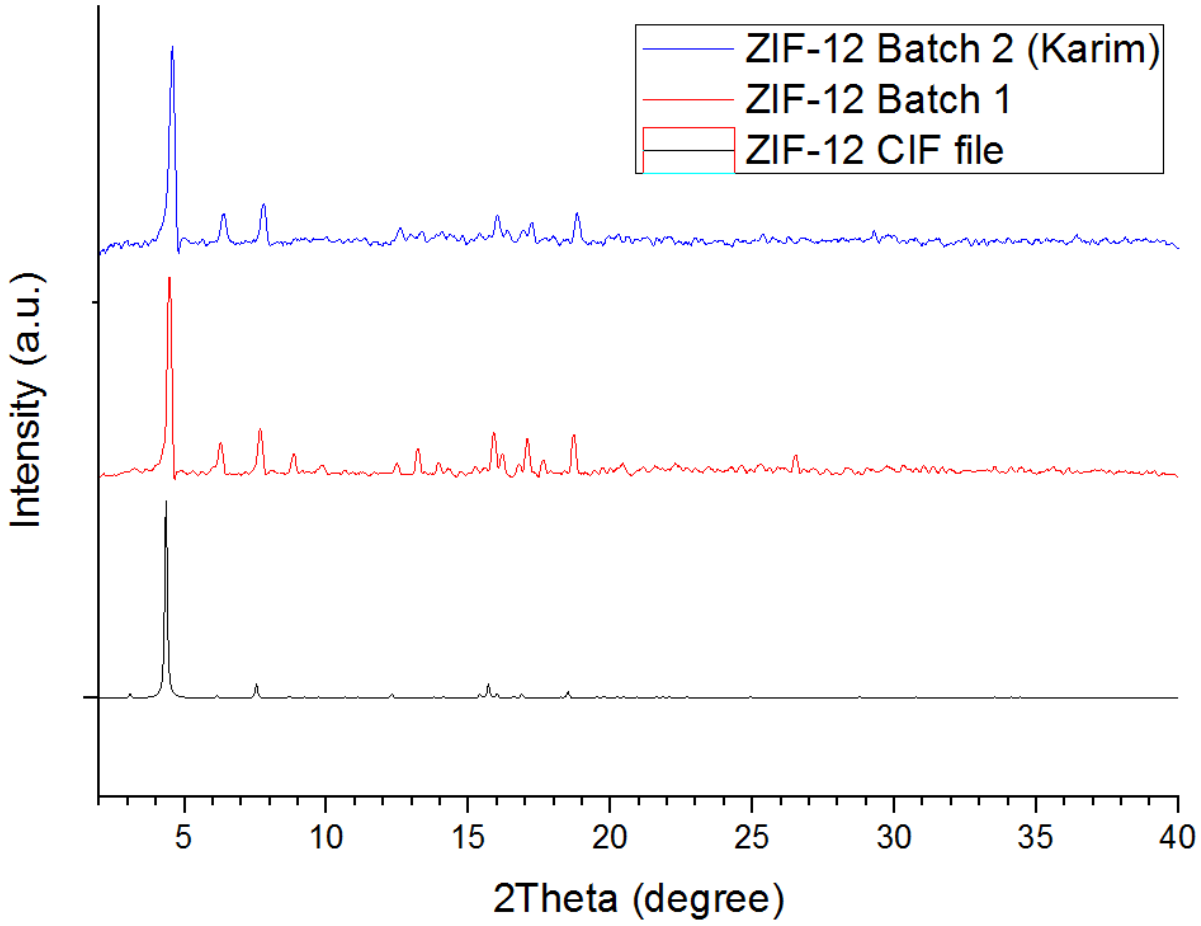

Figure D.10. PXRD of ZIF-12. PXRD from CIF file (black) and results from the two synthesized batches (red and blue).

ZIF-12 experimental batches seen in Figure D.10 also show resemblance with the CIF file, being these almost the same when compared with experimental spectra found in literature, indicating the correct synthesis of the material [5].

CoNIm (RHO)

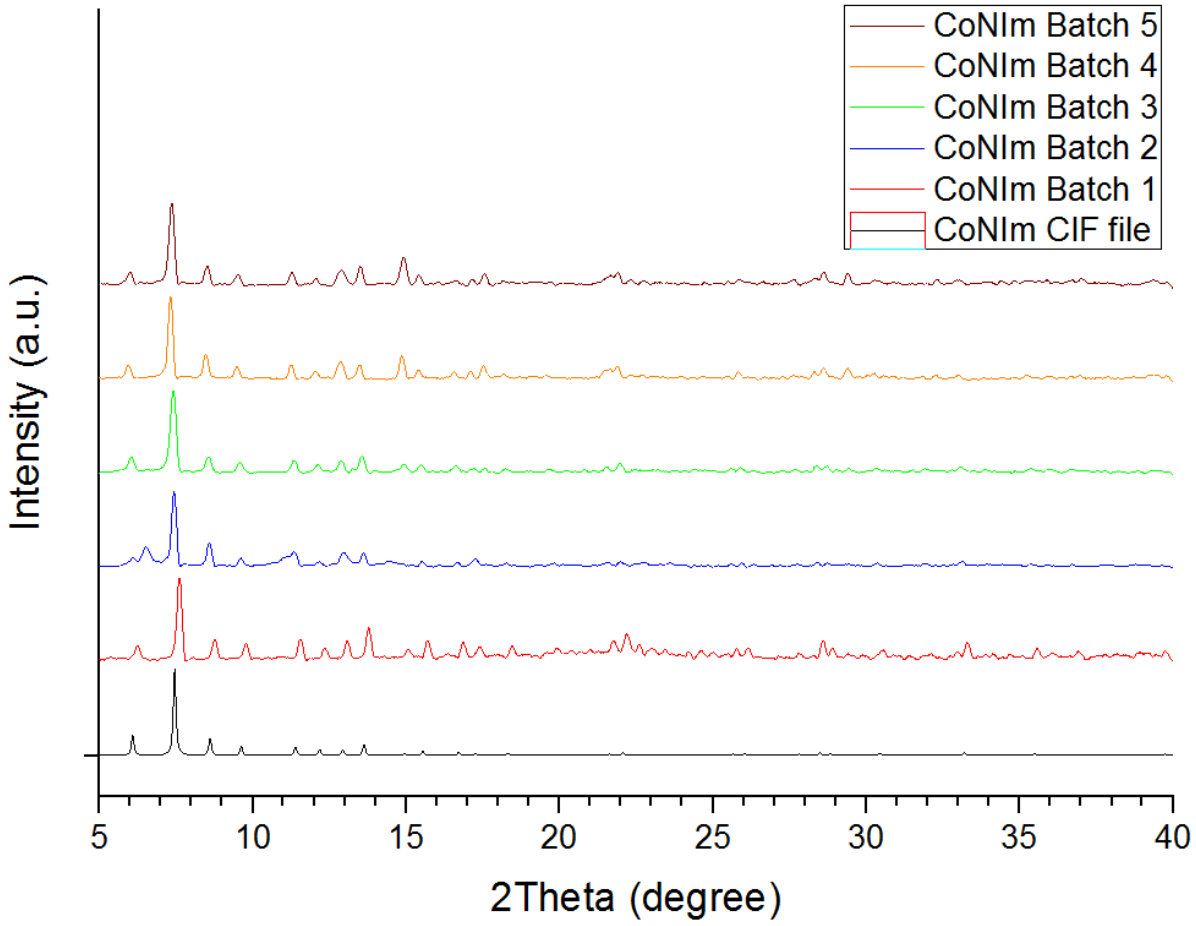

Figure D.11. XRD patterns of CoNIm (RHO). CIF file (black) and experimental evacuated batches (in red, blue, green, yellow and brown).

Figure D.11 exhibits the synthesized batches of CoNIm (RHO), which resemble the experimental batches from the author and the CIF file, being a slight shift of the peak at 7.5 2θ in the first batch [8]. The batches were solvent exchanged with a mix of methanol and acetone and heated up under vacuum at 200 °C before been tested, as indicated by the author [8].

MIL-101 (Cr)

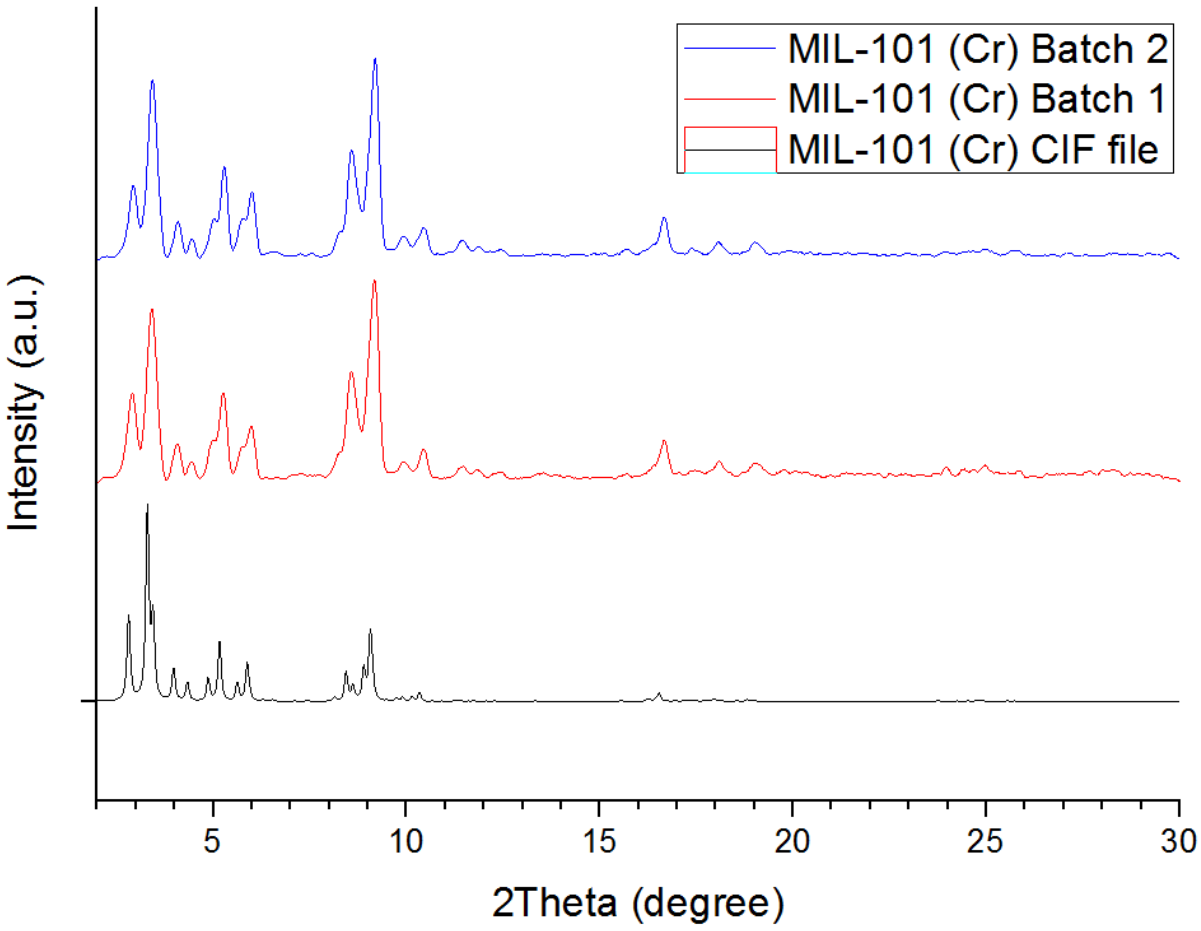

Figure D.12. XRD patterns of MIL-101 (Cr). CIF file (black) and experimental batches 1 and 2 (red and blue).

Figure D.12 shows the experimental MIL-101 (Cr) XRD spectra, which perfectly matches the CIF file apart from the shoulder at around 3.5 2θ, probably because of lack of resolution. When compared to literature (which used both microwave and autoclave methods), the profiles also match.

NH_2-MIL-101 (Cr)

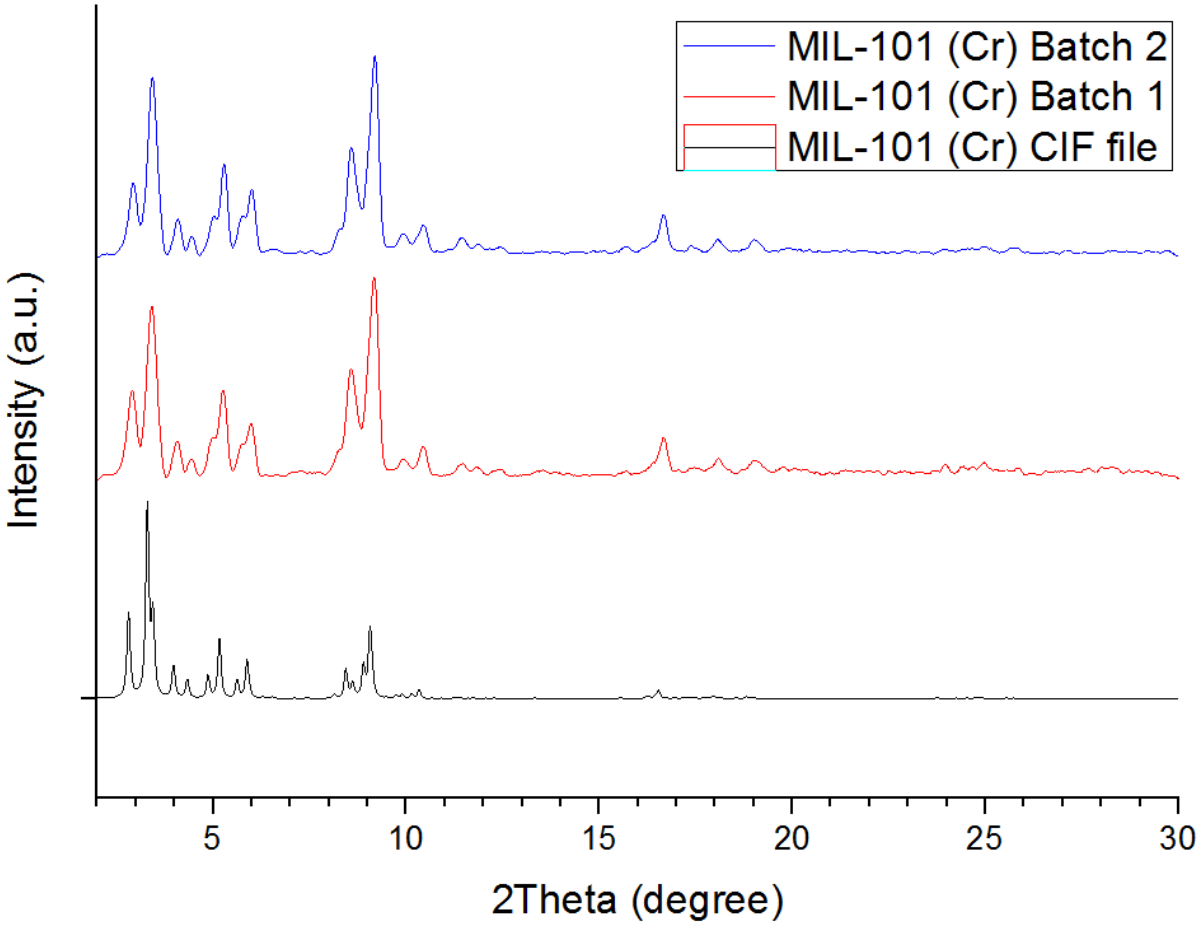

Figure D.13. XRD patterns of NH_2-MIL-101 (Cr). CIF file of MIL-101 (Cr) (black) and experimental NH_2-MIL-101 (Cr) batches 1 and 2 (red and blue).

Figure D.13 shows the experimental NH_2-MIL-101 (Cr) patters as well as MIL-101 (Cr) CIF file, as no CIF file was found for NH_2-MIL-101 (Cr) in the crystallography database. Given that NH_2-MIL-101 (Cr) and MIL-101 (Cr) have the same framework and the X-ray scattering will be dominated by the metal centres, the powder patterns will be virtually identical, especially given that the amino groups will be disordered. The same approach has been seen in literature [9]. As it can be seen, the experimental batches match perfectly, being the intensity ratio for the peak situated at 9 2θ, higher that of the peak at 2 2θ.

UiO-66

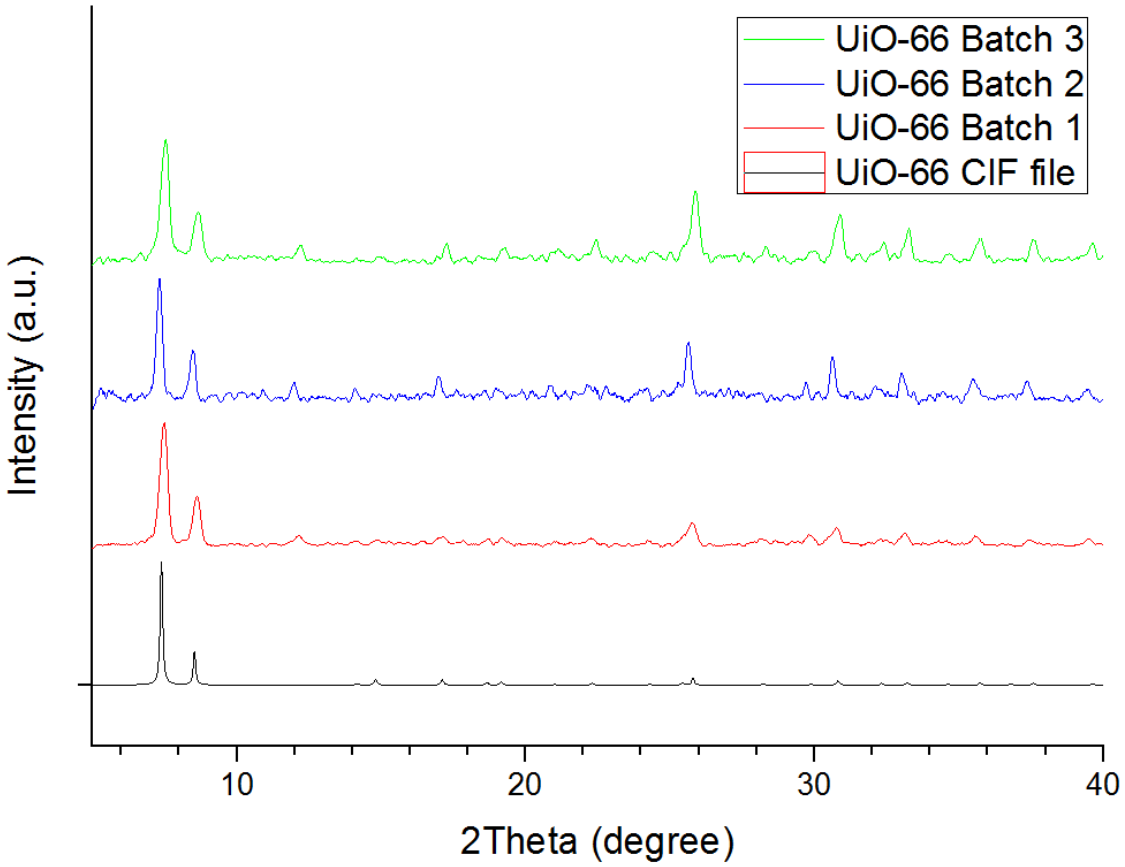

Figure D.14. XRD patterns of UiO-66. CIF file (black) and experimental batches (red, blue and green).

As it can be seen in Figure D.14, all the main peaks match of the experimental UiO-66 batches match with those of the CIF file. However, an unusual peak at 12 2θ was found that was not found in the theoretical structure in literature [10]. Initially, it was thought it could be due to particle size, particle orientation or an impurity from the $ZrCl_4$ used. However, one of the batches was tested under Ar (blue), showing that the peak is just caused because of the presence of water in the pores as it can be seen in Figure D.14:

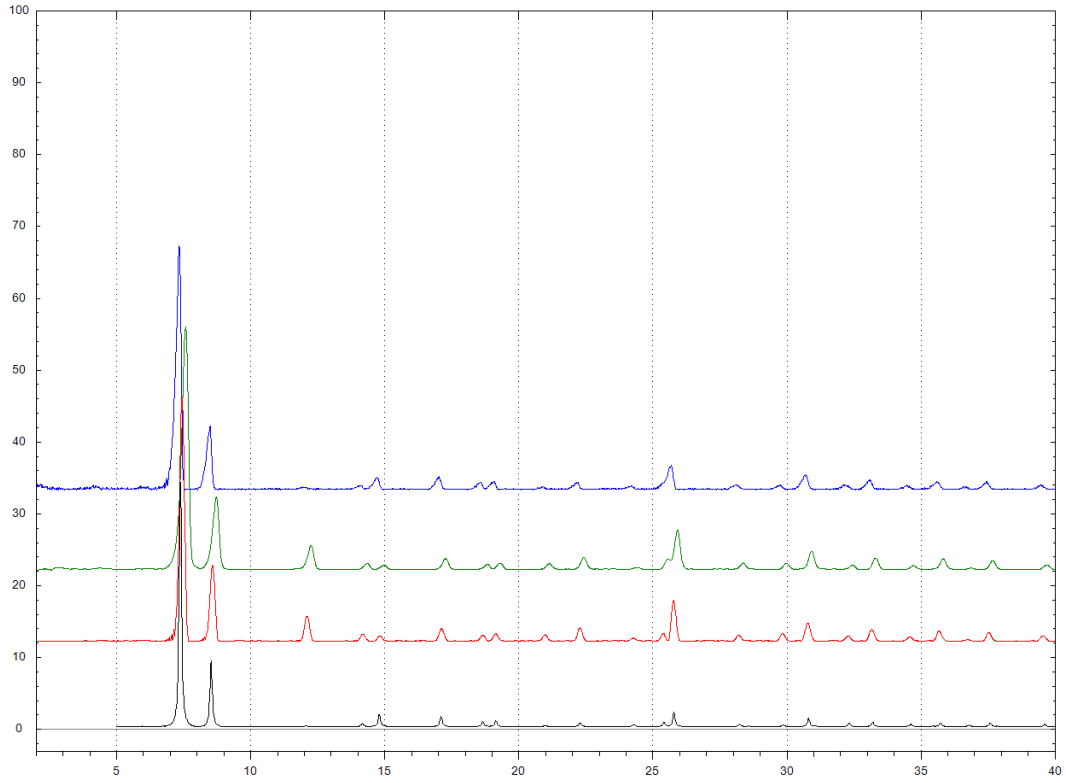

Figure D.15. XRD patterns of UiO-66. CIF file (black), batches following the hydrothermal bomb methodology (red and green) evacuated at 175 and 300 °C respectively and commercial batch tested under Ar (blue).

UiO-67

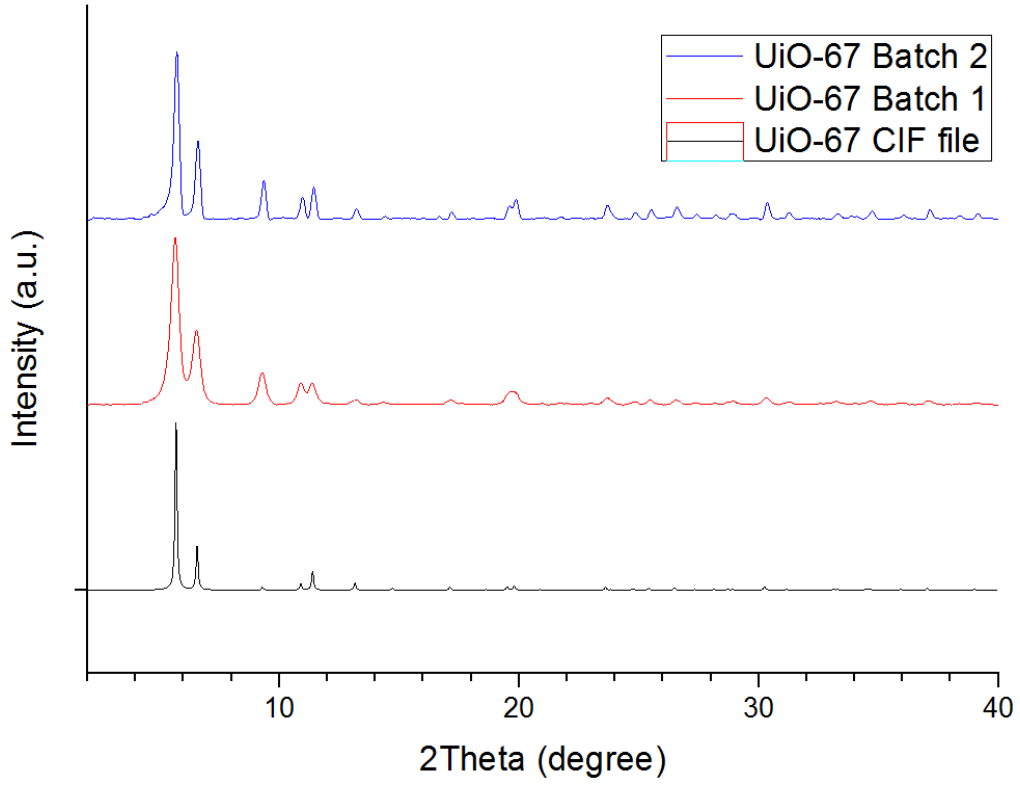

Figure D.16. XRD patterns of UiO-67. CIF file (black), and experimental batches (red and blue).

Figure D.16 shows the experimental spectra of UiO-67 batches, which match with the CIF file, apart from the higher intensity of peak at around 9 2θ, which is believed to be a peak due to water in the structure as it was shown in Figures D.13 and D.14 with UiO-66. When comparing the synthesized batches with literature used as reference, the batches also show good agreement [10].

HKUST-1

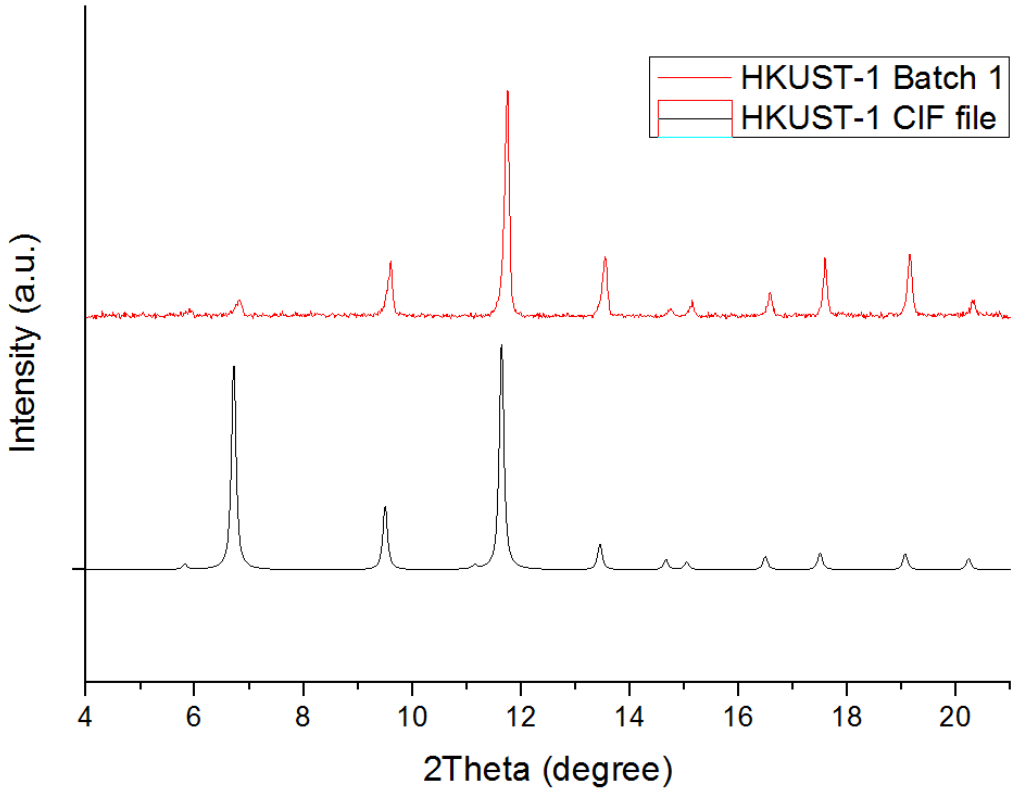

Figure D.17. XRD patterns of HKUST-1. CIF file (black), commercial sample (red).

Figure D.17 compares the commercial HKUST-1 sample results against the CIF file, showing a perfect match with the pattern obtained from the CIF file. However, the intensity of the peak at around 7.5 2θ is extremely low, which has also been seen in experimental patterns found in literature [11].

References

1. Millward, D.R. and O.M. Yaghi, *Metal-organic frameworks with exceptionally high capacity for storage of carbon dioxide at room temperature.* Journal of the American Chemical Society, 2005. 127(51): p. 17998-17999.
2. Wang, Z.Q., K.K. Tanabe, and S.M. Cohen, *Tuning Hydrogen Sorption Properties of Metal-Organic Frameworks by Postsynthetic Covalent Modification.* Chemistry-a European Journal, 2010. 16(1): p. 212-217.
3. Ardelean, O., Blanita, G., Borodi, G., Mihet, M., Coros, M., Lupu, D., *On the enhancement of hydrogen uptake by IRMOF-8 composites with Pt/carbon catalyst.* International Journal of Hydrogen Energy, 2012. 37(9): p. 7378-7384.
4. Yaghi, O., Eddaoudi, M., Li, H., Kim, J., Rosi, N., *Isoreticular metal-organic frameworks, process for forming the same, and systematic design of pore size and functionality therein, with application for gas storage*. 2003, Google Patents.
5. He M., Y.J.F., Liu Q., Zhong Z. X., Wang H. T., *Toluene-assisted synthesis of RHO-type zeolitic imidazolate frameworks: synthesis and formation mechanism of ZIF-11 and ZIF-12.* Dalton Transactions, 2013. 42(47): p. 16608-16613.
6. Mu, L., et al., *A novel method to improve the gas storage capacity of ZIF-8.* Journal of Materials Chemistry, 2012. 22(24): p. 12246-12252.
7. Li, Q. and H. Kim, *Hydrogen production from NaBH4 hydrolysis via Co-ZIF-9 catalyst.* Fuel Processing Technology, 2012. 100: p. 43-48.
8. Biswal, B.P., T. Panda, and R. Banerjee, *Solution mediated phase transformation (RHO to SOD) in porous Co-imidazolate based zeolitic frameworks with high water stability.* Chemical Communications, 2012. 48(97): p. 11868-11870.
9. Jiang, D.M., Keenan, L. L., Burrows, D. D., Edler, K. J., *Synthesis and post-synthetic modification of MIL-101(Cr)-NH2 via a tandem diazotisation process.* Chemical Communications, 2012. 48(99): p. 12053-12055.
10. Chavan, S., Vitillo, J. G., Gianolio, D., Zavorotynska, O., Civalleri, B., Jakobsen, S., Nilsen, M. H., Valenzano, L., Lamberti, C., Lillerud, K. P., Bordiga, S., *H-2 storage in isostructural UiO-67 and UiO-66 MOFs.* Physical Chemistry Chemical Physics, 2012. 14(5): p. 1614-1626.
11. Yan, X.L., et al., *Extremely enhanced CO2 uptake by HKUST-1 metal-organic framework via a simple chemical treatment.* Microporous and Mesoporous Materials, 2014. 183: p. 69-73.

Supplementary information E

Experimental TGA results

IRMOF-1

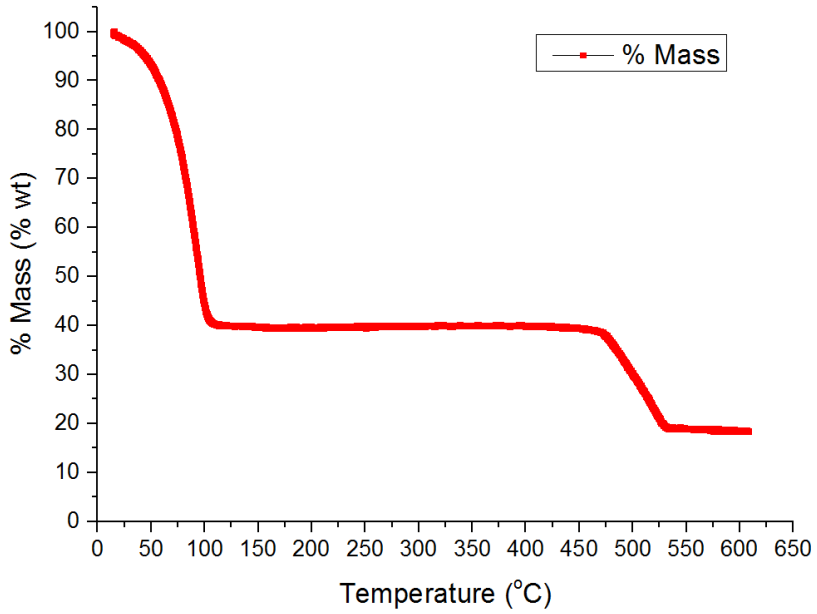

Figure E.1. IRMOF-1 B1 TGA test from 20 to 600 °C, 5 °C min^{-1} under nitrogen.

Figure E.1 presents the TGA results of IRMOF-1, showing one step of weight loss of 60 % prior to the final thermal decomposition of the material at around 475 °C. The step of weight loss (20-100 °C) was assigned to the loss of $CHCl_3$ from the solvent exchange, although it might also had other organics that were present in the lab. The lack of further steps of weight loss confirmed the non-existence of DEF in the pores because of the solvent exchange process. IRMOF-1 showed a stability plateau in the range of 100-475 °C, being the decomposition temperature the same as found in literature [1].

IRMOF-1 C60

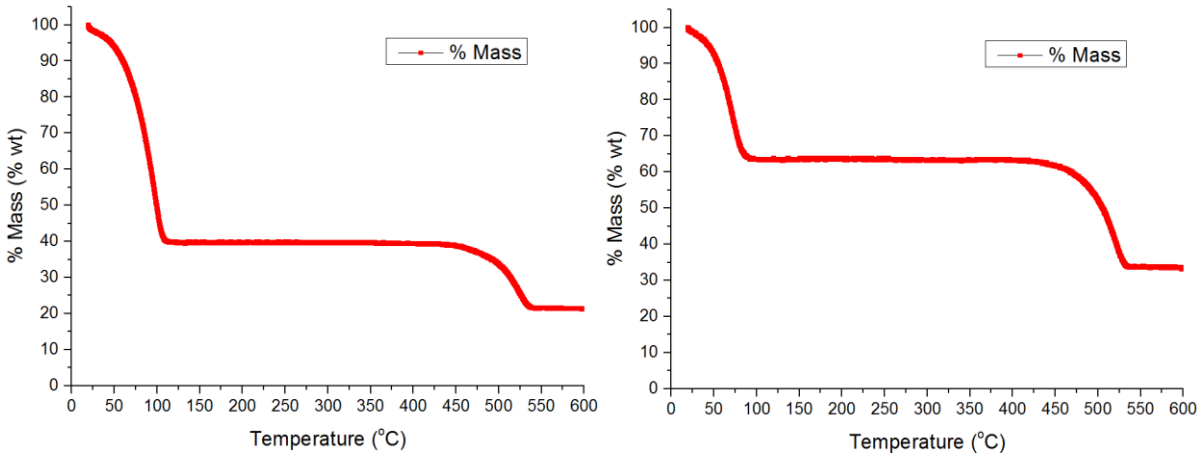

Figure E.2A and E.2B. IRMOF-1 C_{60} Batches 1 and 2. TGA tests from 20 to 600 °C, 5 °C min^{-1} under nitrogen.

Figure E.2A and E.2B show one step of weight loss of 60 and 35 % respectively prior to the final thermal decomposition of IRMOF-1 C_{60} at around 450 °C. The steps of weight loss for both batches (20-100 °C) were mostly assigned to the loss of different amounts of $CHCl_3$ from the solvent exchange, although they might also contained other organics that were present in the lab. The lack of further steps of weight loss confirmed the non-existence of DEF in the because of the solvent exchange process. Both batches showed a stability plateau in the range of 100-450 °C.

IRMOF-3

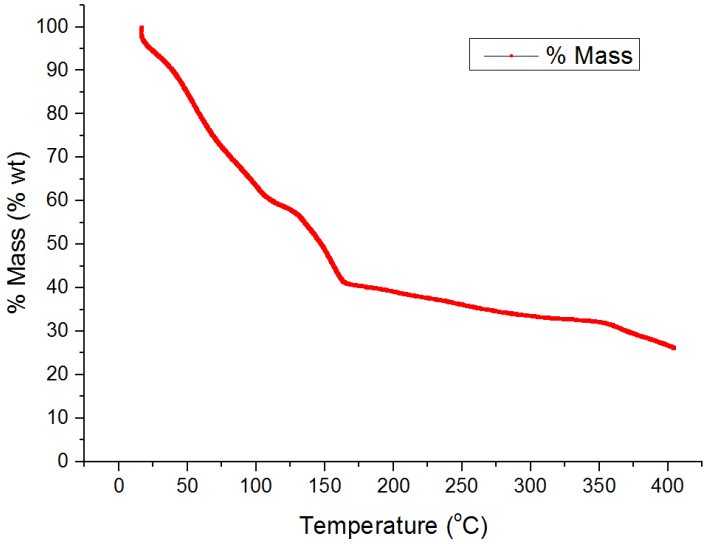

Figure E.3. IRMOF-3 B1 TGA test from 20 to 400 °C, 5 °C min^{-1} under nitrogen.

Figure E.3 shows three steps of weight loss of 40, 20 and 10 % respectively prior to the final thermal decomposition of IRMOF-3 at around 350 °C. The first step of weight loss (20-100 °C) was assigned to the loss of DEF, water and other possible organics present in the lab. The second step (100-150 °C) was believed to be due to water remnants and DEF still trapped in the pores that take longer to leave the framework. The third step was thought to be solely to DEF still trapped in the pores. IRMOF-3 showed a stability plateau in the range of 300-350 °C. The material was not solvent exchanged before the TGA test, although the samples were solvent exchanged with $CHCl_3$ as it was done in literature [1]. Literature shows that heating the sample at 125 °C was enough to activate it, showing a plateau area from 20 to 375 °C [1].

IRMOF-9

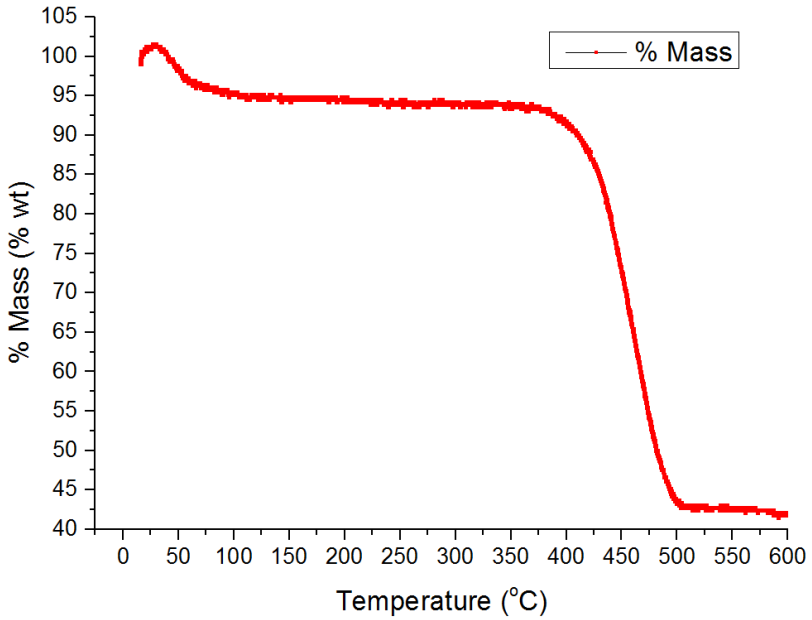

Figure E.4. IRMOF-9 B1 TGA test from 20 to 600 °C, 5 °C min^{-1} under nitrogen.

Figure E.4 shows one step of weight loss of 5 % prior to the final thermal decomposition of IRMOF-9 at around 400 °C. The small step of weight loss (20-75 °C) was assigned to the loss of $CHCl_3$ from the solvent exchange and possible organics present in the lab. The lack of further steps of weight loss confirmed the non-existence of DEF in the pores because of the solvent exchange process. IRMOF-3 showed a stability plateau in the range of 75-400 °C.

ZIF-7

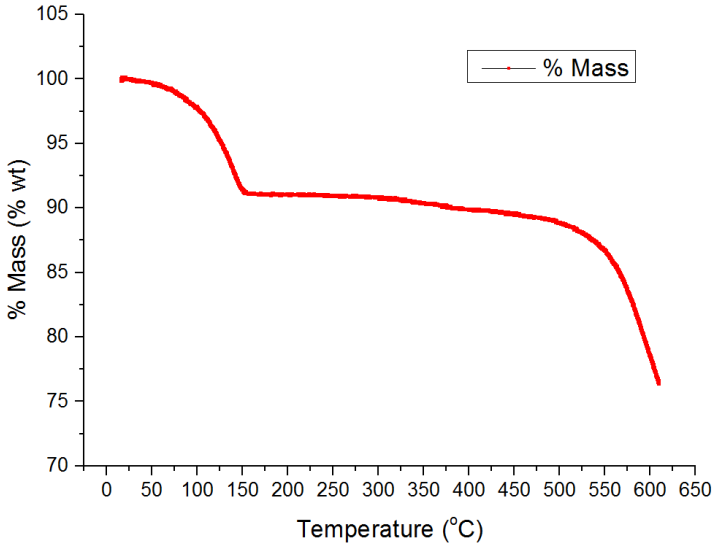

Figure E.5. ZIF-7 TGA test from 20 to 600 °C, 5 °C min^{-1} under nitrogen.

Figure E.5 shows one step of weight loss of 10 % prior to the final thermal decomposition of ZIF-7 at around 500 °C. The step of weight loss (20-150 °C) was assigned to the loss of ethanol from the solvent exchange, water and possible organics present in the lab. The reason why the step ended at 150 °C rather than at 100 °C is likely to be due to the small pore windows of ZIF-7, needing the molecules more time to leave the framework, while the temperature kept on increasing. ZIF-7 shows a stability plateau in the range of 150-500 °C.

ZIF-8

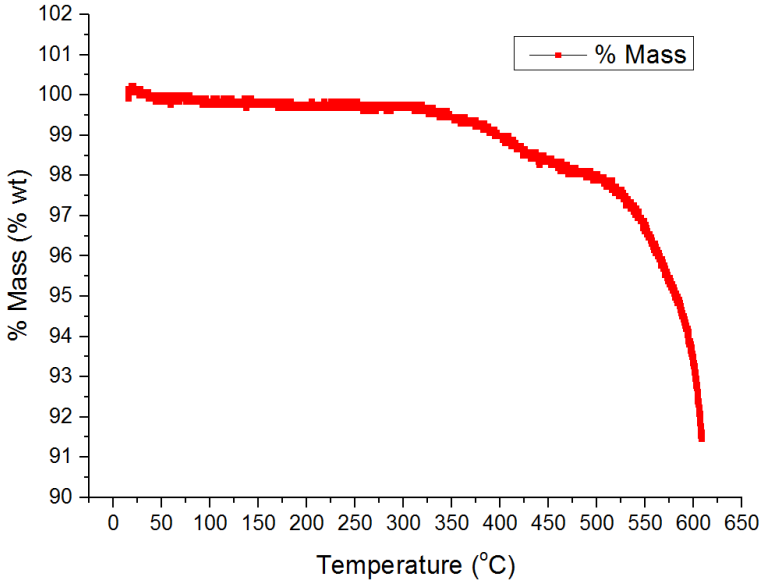

Figure E.6. ZIF-8 TGA test from 20 to 600 °C, 5 °C min^{-1} under nitrogen.

Figure E.6 barely shows any step of weight loss prior to a partial thermal decomposition followed by a higher decomposition of ZIF-8 at around 500 °C. The minimal weight loss observed (20-100 °C) was assigned to the loss of remnants of methanol from the solvent exchange, water and possible organics present in the lab. At 350 °C, a weight loss of 2 % was observed from the decomposition of a small fraction of the sample that was much more perceptible at 500 °C, when a steady mass drop was observed at around 600 °C. At the end of the test, it was observed a black layer of decomposed ZIF-8. Below this layer, a great amount of ZIF-8 with the same white colour was found. The decomposed layer is believed to have protected the rest of the material situated below, hence the low wt % loss at the end of the experiment. ZIF-8 showed a stability plateau in the range of 100-350 °C.

ZIF-9

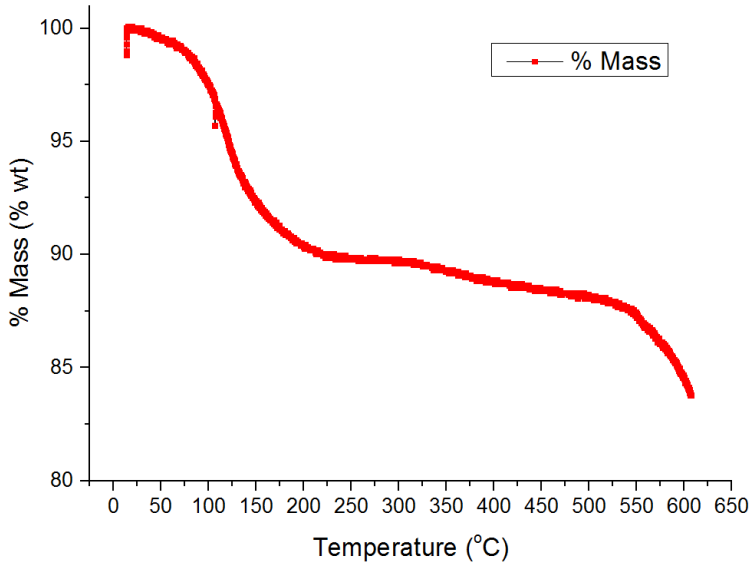

Figure E.7. ZIF-9 TGA test from 20 to 600 °C, 5 °C min^{-1} under nitrogen.

Figure E.7 shows two steps of weight loss of 10 and 3 % respectively prior to the final thermal decomposition of ZIF-9 at around 550 °C. The step of weight loss (20-150 °C) was assigned to the loss of ethanol from the solvent exchange, water and possible organics present in the lab. The reason why the step ended at 150 °C rather than at 100 °C was likely to be due to the small pore windows of ZIF-9, needing more time to get all the molecules out of the framework, while the temperature kept on increasing. A second small weight loss was also observed (350-550 °C), which indicated some thermal decomposition of the material, which became more apparent at 550 °C. ZIF-9 showed a stability plateau in the range of 200-300 °C.

ZIF-11

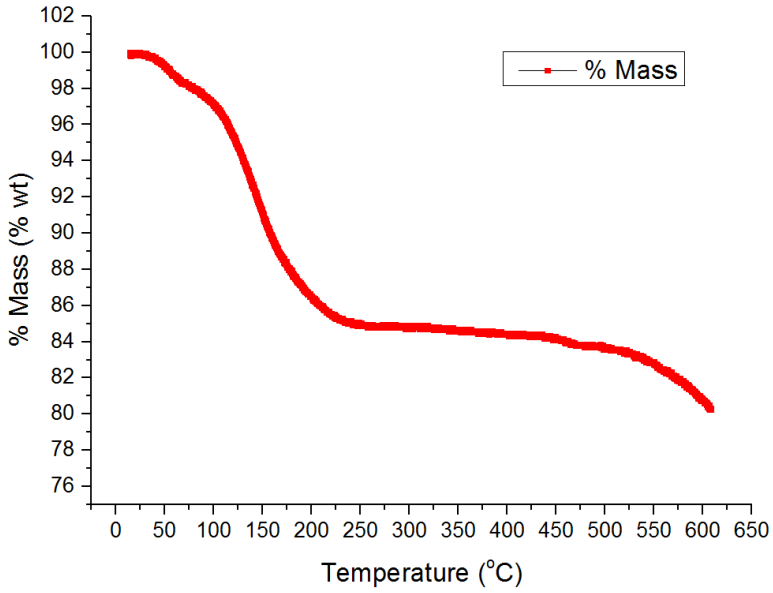

Figure E.8. ZIF-11 TGA test from 20 to 600 °C, 5 °C min^{-1} under nitrogen.

Figure E.8 shows one step of weight loss of 15 prior to the final thermal decomposition of ZIF-11 at around 525 °C. The step of weight loss (20-225 °C) was assigned to the loss of ethanol from the solvent exchange, water, possible organics present in the lab and the possibility of some toluene that could still remain in the pores. The reason why the step ends at 250 °C rather than at 100-110 °C is likely to be due to the small pore windows of ZIF-11, needing the molecules more time to leave the framework, while the temperature kept on increasing. ZIF-11 showed a stability plateau in the range of 250-500 °C.

ZIF-12

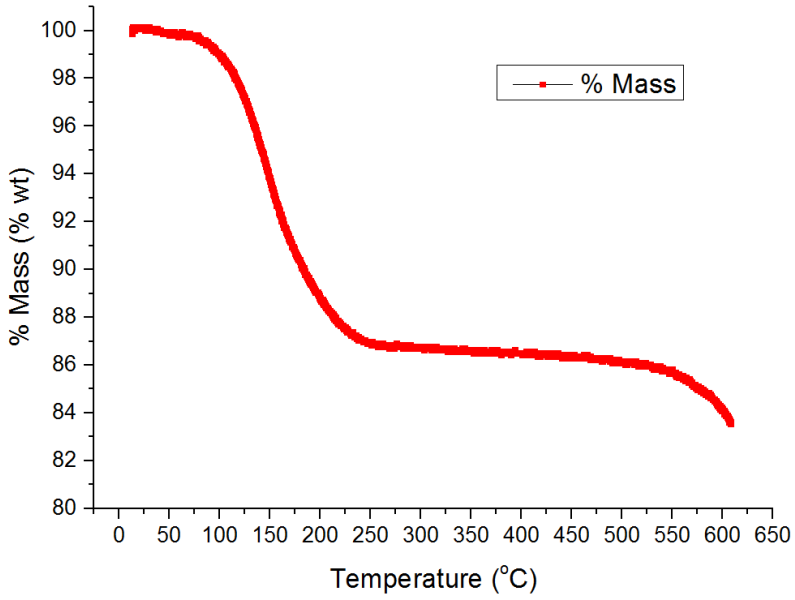

Figure E.9. ZIF-12 TGA test from 20 to 600 °C, 5 °C min^{-1} under nitrogen.

Figure E.9 shows one step of weight loss of 15 % prior to the final thermal decomposition of ZIF-12 at around 525 °C. The step of weight loss (20-250 °C) was assigned to the loss of ethanol from the solvent exchange, remnants of toluene from the synthesis, water and other possible organics present in the lab. The reason why the step ended at 250 °C rather than at 100-110 °C was likely to be due to the small pore windows of ZIF-12, needing the molecules more time to leave the framework, while the temperature kept on increasing. ZIF-12 showed a stability plateau in the range of 275-525 °C.

MIL-101 (Cr)

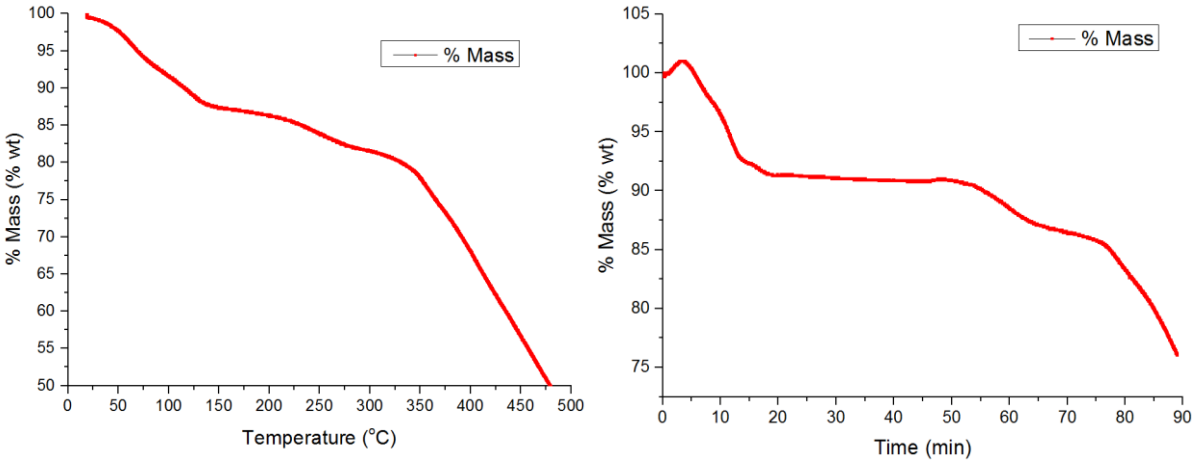

Figure E.10A and E.10B. MIL-101 (Cr) TGA test from 20 to 600 °C and test from 20 to 450 °C, holding temperature at 180 °C for 30 minutes, 5 °C min^{-1} under nitrogen. Checked with literature [2].

Figure E.10A shows two steps of weight loss of 13 % and 5 % respectively prior to the final thermal decomposition of MIL-101 (Cr) at around 350 °C. The weight loss was assigned to the loss of water and possible organics present in the lab. The second weight loss was observed at 250 °C, which indicated the possibility of solvent still leaving the pores or early decomposition of the material. In Figure E.10B, the material was held at 180 °C for 30 min, showing no mass change, confirming stability at that temperature. Based on these results, it was decided to degas de sample at 180 °C, since there existed an indication of early decomposition of the sample at 250 °C. However, literature states stability of MIL-101 (Cr) up to 350 °C [2].

NH_2-MIL-101 (Cr)

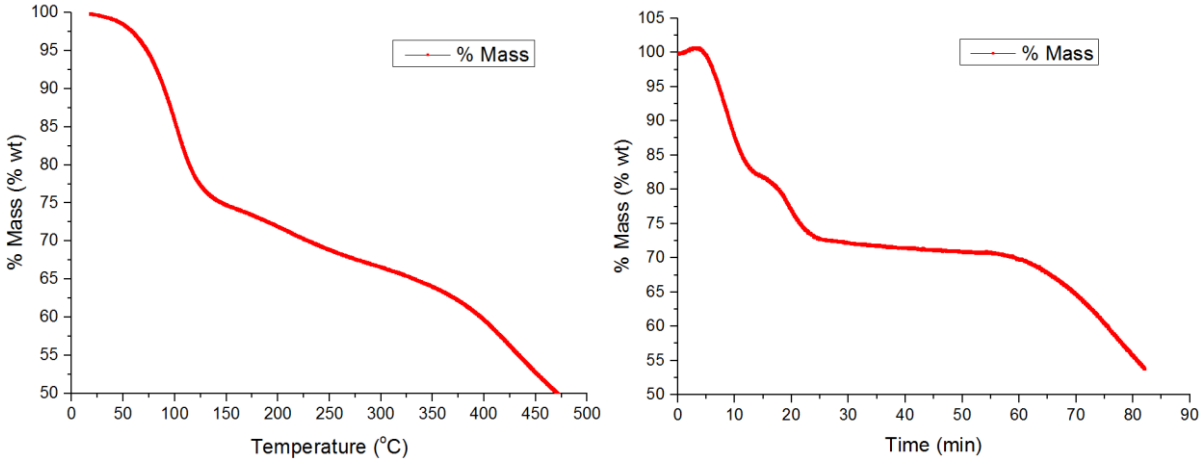

Figure E.11A and E.11B. MIL-101 (Cr) TGA test from 20 to 600 °C and test from 20 to 450 °C, holding temperature at 250 °C for 30 minutes, 5 °C min^{-1} under nitrogen. Checked with literature [2].

Figure E.11A and E.11B shows two steps of weight loss of 25 and 5 % and 12 and 8 % respectively, prior to the final thermal decomposition of NH_2-MIL-101 (Cr) at around 300 °C. The weight loss of the first step was assigned to the loss of ethanol, water and other possible organics present in the lab. In Figure E.11B, temperature was held at 250 °C for 30 min, showing a small weight loss, indicating a possible small thermal decomposition of the material, whose rate is further accelerated at 300-350 °C. A similar trend is observed in literature [3], not being as steep as Figure E.13, showing a stability plateau in the range of 180-250 °C. Based on results from both Figures and literature, it was decided to degas NH_2-MIL-101 (Cr) at 180 °C.

UiO-66

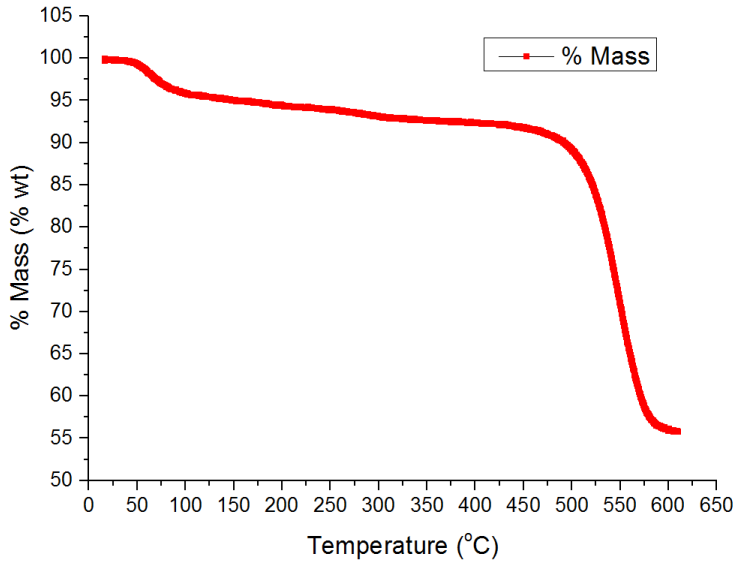

Figure E.12. UiO-66 TGA test from 20 to 600 °C, 5 °C min^{-1} under nitrogen.

Figure E.12 shows two steps of weight loss of 5 % and 2.5 % respectively prior to the final thermal decomposition of UiO-66 at around 475 °C. The sample was activated at 300 °C after the solvent exchange by using TGA literature data [4]. The steps of weight loss (20-100 and 100-300 °C) were assigned to the loss of water and possible organics present in the lab at different rates. UiO-66 showed a stability plateau in the range of 300-475 °C.

UiO-67

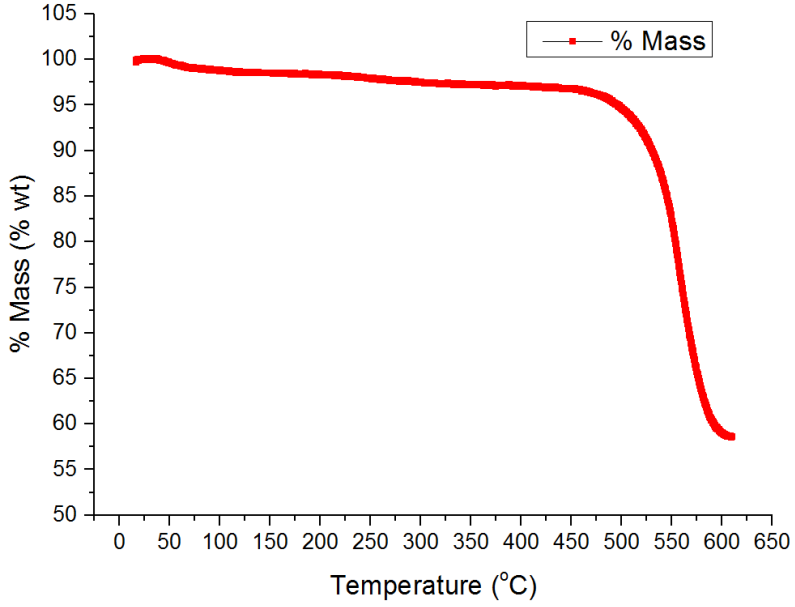

Figure E.13. UiO-67 TGA test from 20 to 600 °C, 5 °C min^{-1} under nitrogen.

Figure E.13 shows one step of weight loss of 5 % prior to the final thermal decomposition of the material at around 475 °C. The sample was previously dried at 200 °C after the solvent exchange by using TGA literature data [4]. The step of weight loss (20-100 °C) was assigned to the loss of water and possible organics present in the lab at different rates. UiO-67 shows a stability plateau in the range of 300-475 °C.

HKUST-1

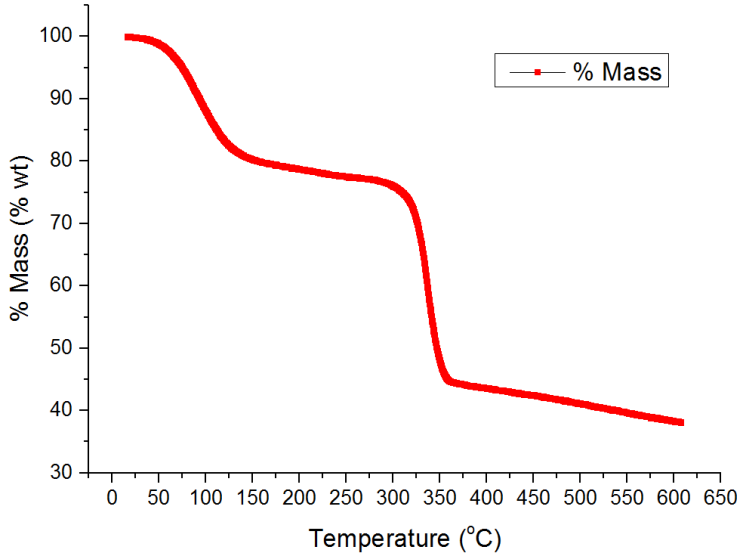

Figure E.14. HKUST-1 TGA test from 20 to 600 °C, 5 °C min^{-1} under nitrogen.

Figure E.14 shows one step of weight loss of around 20 % (20-125 °C), assigned to the loss of water and possible organics present in the lab for the commercial HKUST-1 sample. After that, a slow weight loss rate was seen (125-250 °C), probably also due to water and organics that took longer to leave the framework. HKUST-1 showed a stability plateau in the range of 250-300 °C being this range very similar to literature values (225-325 °C) [5].

TE7_20:

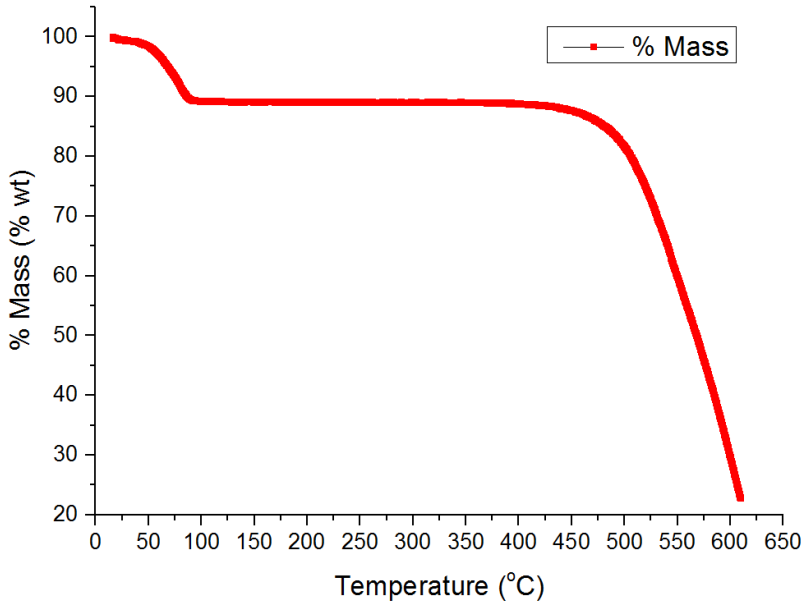

Figure E.15. TE7_20 TGA test from 20 to 600 °C, 5 °C min^{-1} under nitrogen.

Figure E.15 shows one step of weight loss of 10 % prior to the final thermal decomposition of TE7_20 at around 475 °C. The step of weight loss (20-225 °C) was assigned to the loss of water and possible organics present in the lab. TE7_3 showed a stability plateau in the range of 100-475 °C.

TE3

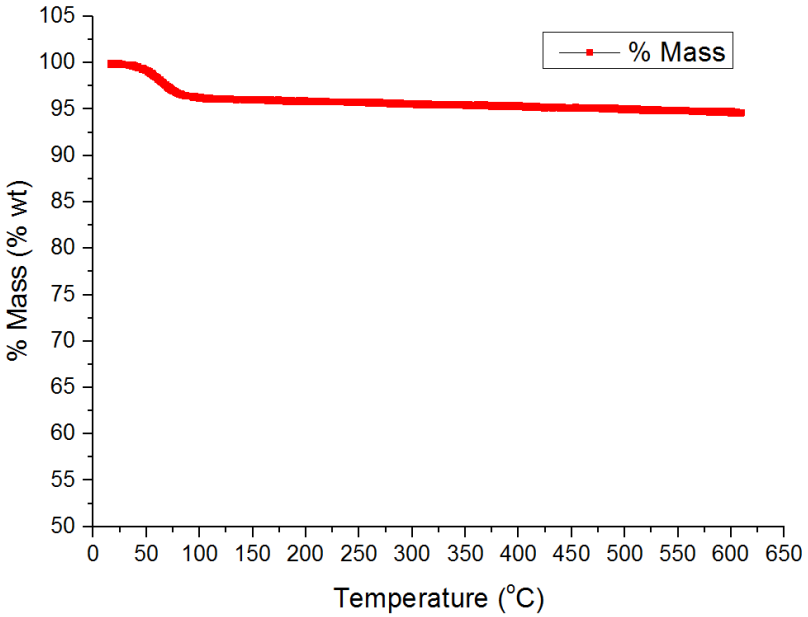

Figure E.16. TE3 TGA test from 20 to 600 °C, 5 °C min^{-1} under nitrogen.

Figure E.16 shows one step of weight loss of 5 % for TE3, showing no signs of decomposition at temperatures up to 600 °C. The step of weight loss (20-100 °C) was assigned to the loss of water and possible organics present in the lab. TE3 showed a stability plateau in the range of 100-600 °C.

AX-21

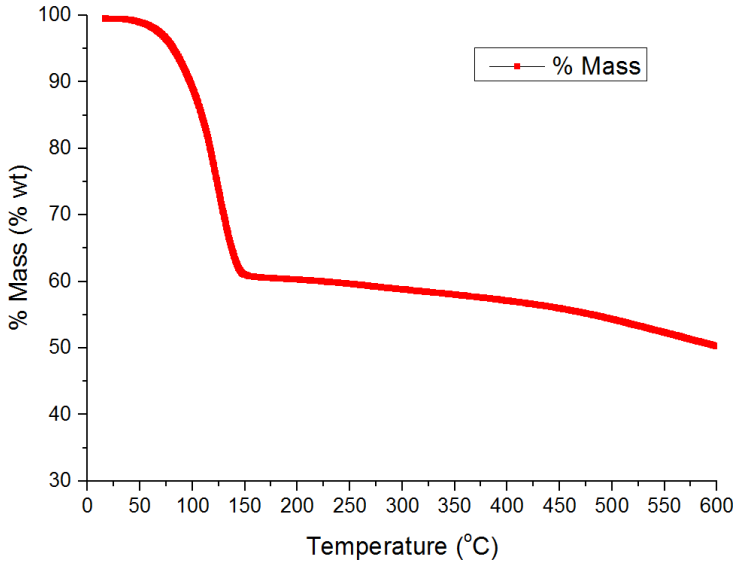

Figure E.17. AX-21 TGA test from 20 to 600 °C, 10 °C min^{-1} under nitrogen.

Figure E.17 shows the TGA data of AX-21. A step weight loss of nearly 40 % (20-150 °C) was seen, showing decomposition at temperatures around 300-400 °C. The step of weight loss was mainly assigned to water. AX-21 showed a stability plateau in the range of 150-300 °C.

OLC-1750

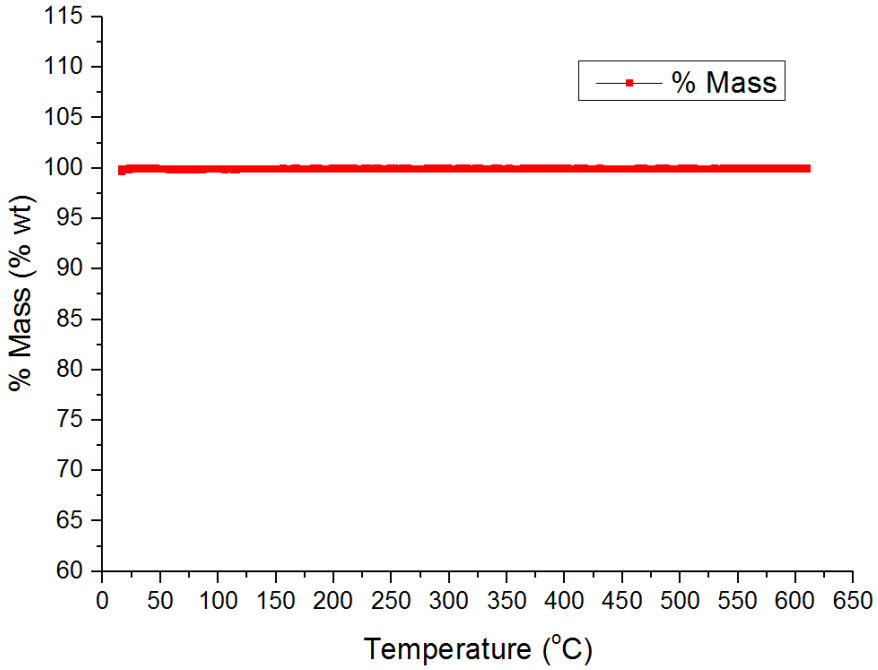

Figure E.18. OLC-1750 TGA test from 20 to 600 °C, 5 °C min^{-1} under nitrogen.

Figure E.18 shows neither real step of weight loss nor sign of decomposition at temperatures up to 600 °C. OLC-1750 shows a stability plateau in the whole range 20-600 °C.

References

1. Millward, A.R. and O.M. Yaghi, *Metal-organic frameworks with exceptionally high capacity for storage of carbon dioxide at room temperature.* Journal of the American Chemical Society, 2005. 127(51): p. 17998-17999.
2. Ferey, G., et al., *A chromium terephthalate-based solid with unusually large pore volumes and surface area.* Science, 2005. 309(5743): p. 2040-2042.
3. Jiang, D.M., et al., *Synthesis and post-synthetic modification of MIL-101(Cr)-NH2 via a tandem diazotisation process.* Chemical Communications, 2012. 48(99): p. 12053-12055.
4. Chavan, S., et al., *H-2 storage in isostructural UiO-67 and UiO-66 MOFs.* Physical Chemistry Chemical Physics, 2012. 14(5): p. 1614-1626.
5. Yan, X.L., et al., *Extremely enhanced CO2 uptake by HKUST-1 metal-organic framework via a simple chemical treatment.* Microporous and Mesoporous Materials, 2014. 183: p. 69-73.

Supplementary information F

Table with the total hydrogen capacity values used for the correlations

Table F.1. Total hydrogen values used for each material used in the correlation. Error bars represent the standard error of the product of $\rho_A * Vp$ to calculate the total capacity.

Material name	Total hydrogen capacity (wt %)	Material name	Total hydrogen capacity (wt %)
IRMOF-1	9.02 ± 0.525	**ZIF-CoNIm**	4.16 ± 0.798
IRMOF-3	7.17 ± 0.419	**NH_2-MIL-101 (Cr)**	7.70 ± 1.67
IRMOF-6	7.40 ± 1.22	**NH_2-MIL-101 (Al)**	9.23 ± 1.45
IRMOF-9	3.16 ± 0.120	**UiO-66**	3.41 ± 0.118
IRMOF-11	5.07 ± 0.626	**UiO-67**	5.46 ± 0.440
IRMOF-20	8.22 ± 1.35	**MOF-74**	6.04 ± 12.0
ZIF-8	4.17 ± 0.119	**MOF-177**	13.51 ± 3.14
ZIF-11	5.24 ± 0.578	**MOF-324**	6.37 ± 3.10
ZIF-12	5.75 ± 0.568	**HKUST-1**	3.84 ± 0.490